AD 673964

AD
SEP 5 1968
A

HUGHES TOOL COMPANY · AIRCRAFT DIVISION

Culver City, California

Reproduced by the
CLEARINGHOUSE
for Federal Scientific & Technical
Information Springfield Va. 22151

HTC-AD 67-3

ROTOR/WING SERIES VI WIND TUNNEL TEST 7-FOOT DIAMETER MODEL IN THE NASA LRC 30-BY-60-FOOT WIND TUNNEL

April 1968

Prepared by: F. J. Briardy
R. E. Head

Contract Number: Nonr-4588(00)
Authority: NR 212-162/12-8-64

An Experimental Research Program Sponsored by Air Programs Office of Naval Research, Naval Air Systems Command, and U.S. Army Aviation Materiel Laboratories

Distribution of this document is unlimited.

HUGHES TOOL COMPANY -- AIRCRAFT DIVISION
Culver City, California

FOREWORD

This report presents the results of aerodynamic testing of a 7-foot-diameter Rotor/Wing model in the 30-by-60-foot wind tunnel at the NASA Langley Research Center, Hampton, Virginia, and may be considered an interim report in the developing technology of the Rotor/Wing concept. The tests reported here are the sixth in a series investigating the external aerodynamics of an aircraft of this VTOL concept that can operate in three steady-state flight modes -- helicopter, autogyro, and airplane -- and whose rotor can also start and stop in flight. Three Rotor/Wing planforms were tested through these modes. Investigations of the conversion maneuver, in general and through the low rotor rpm range of conversion in particular, indicated that no special problems are encountered. Data for the same model from a smaller tunnel, where conventional airplane model wall corrections were included, are compared with data from this large wind tunnel that has no tunnel wall corrections; the data are shown to be equivalent -- at least for this particular aircraft configuration. Analytical methods for predicting performance of full-scale Rotor/Wing aircraft are shown to be well founded on the experimental data.

TABLE OF CONTENTS

	Page
SUMMARY	1
INTRODUCTION	3
DESCRIPTION OF MODEL	11
General	11
Fuselage	12
Empennage	12
Rotor/Wings	12
Rotor/Wing Drive System	20
Rotor/Wing Control System	21
Model Mounting	23
Model Operation	24
Data Recording	24
MODEL TEST PROGRAM	26
MODEL TEST RESULTS	27
Powered Model - Hover Mode	28
Powered Model - Helicopter Mode	32
Autogyro Mode	75
Conversion	76
Airplane Mode	107
ROTOR/WING AERODYNAMIC ANALYSIS	117
Hovering Power Required	117
Fuselage Download	117
Rotor Induced Torque	120
Blade Profile Torque	123
Wing Hover Torque	126
Yaw Fan	128
Ground Effect	129
Vertical Climb	129
Whirl Tower Model Substantiation of Hovering Performance Computational Method	131

Page

Airplane Flight Power Required 132
Helicopter Forward Flight Power Required 146
Autogyro Flight Power Required 156
Conversion Flight Power Required 162
Conversion -- Stability, Control, and Flying Qualities 165
Dynamic Stability in Hover 169
Static Stability in Helicopter and Autogyro Flight 170
Dynamic Stability in Helicopter and Autogyro Flight 170
Static and Dynamic Stability in Airplane Flight 170

RESULTS AND CONCLUSIONS 175

Data Comparison Between Tunnels 175
Rotor/Wing Configuration Comparisons 175
Conversion 175
Analytical Procedures 176
Proposed Areas for Further Investigation 177

REFERENCES 179

APPENDIX - DETAILED TEST RUN SHEETS FOR SERIES VI TESTS 181

LIST OF ILLUSTRATIONS

Figure		Page
1	Rotor/Wing Flight Modes	4
2	Helicopter Flight Mode	8
3	Airplane Flight Mode	9
4	General Arrangement Drawing	13
5	Model Components	15
6	Model Geometry	16
7	Planform Configurations	17
8	Template Locations for Rotor/Wing Airfoil Sections	18
9	Rotor/Wing Airfoil Sections	19
10	Schematic Hydraulic Circuit	20
11	Schematic Control System	21
12	Test Components	22
13	Schematic Model Mount and Systems	23
14	Effect of Rotor/Wing Planform on Hover Performance	29
15	Rotor/Wing Hover Performance	31
16	Rotor/Wing Control Power in Hover	33
17	Helicopter Flight, Trisector Wing, $\mu = 0.15$	35
18	Helicopter Flight, Trisector Wing, $\mu = 0.25$	37
19	Helicopter Flight, Trisector Wing, $\mu = 0.35$	38
20	Comparison of Control Power in Helicopter Flight, Trisector Wing	39
21	Alternating Blade Root and Shaft Bending Moments in Helicopter Flight, Trisector Wing, $\mu = 0.25$	41
22	Alternating Blade Root and Shaft Bending Moments in Helicopter Flight, Trisector Wing, $\mu = 0.35$	42
23	Helicopter Flight, Trisector Wing	44
24	Helicopter Flight, Tricusp Wing	45
25	Helicopter Flight, Triangle Wing	46
26	A_2 Effectiveness, Helicopter Flight, Triangle Wing	47
27	Control Power, Helicopter Flight, Tricusp Wing	48
28	Control Power, Helicopter Flight, Triangle Wing	49
29	Helicopter Flight, Trisector Wing	50
30	Tail Effectiveness in Helicopter Flight, Triangle Wing, $\mu = 0.15$	52

Figure		Page
31	Tail Effectiveness in Helicopter Flight, Triangle Wing $\mu = 0.25$	53
32	Tail effectiveness in Helicopter Flight, Triangle Wing $\mu = 0.35$	54
33	Alternating Blade Root and Shaft Bending Moments in Helicopter Flight, Trisector Wing, $\mu = 0.15$	55
34	Alternating Blade Root and Shaft Bending Moments in Helicopter Flight, Trisector Wing, $\mu = 0.25$	56
35	Alternating Blade Root and Shaft Bending Moments in Helicopter Flight, Trisector Wing, $\mu = 0.35$	57
36	Alternating Blade Root and Shaft Bending Moments in Helicopter Flight, Triangle Wing, $\mu = 0.15$	58
37	Alternating Blade Root and Shaft Bending Moments in Helicopter Flight, Triangle Wing, $\mu = 0.25$	59
38	Alternating Blade Root and Shaft Bending Moments in Helicopter Flight, Triangle Wing, $\mu = 0.35$	60
39	Alternating Blade Root and Shaft Bending Moments in Helicopter Flight, Tricusp Wing, $\mu = 0.15$	61
40	Alternating Blade Root and Shaft Bending Moments in Helicopter Flight, Tricusp Wing, $\mu = 0.25$	62
41	Alternating Blade Root and Shaft Bending Moments in Helicopter Flight, Tricusp Wing, $\mu = 0.35$	63
42	Alternating Blade Root and Shaft Bending Moments in Helicopter Flight, Triangle Wing ($A_2 = 0°$), $\mu = 0.15$	67
43	Alternating Blade Root and Shaft Bending Moments in Helicopter Flight, Triangle Wing ($A_2 = 0°$), $\mu = 0.25$	68
44	Alternating Blade Root and Shaft Bending Moments in Helicopter Flight, Triangle Wing ($A_2 = 0°$), $\mu = 0.35$	69
45	Blades-Off Lift and Torque	71
46	Blades-Off Pitching and Rolling Moments and Shaft Bending Moments	72
47	Autorotation, Trisector Wing	77
48	Autorotation, Tricusp Wing	78
49	Autorotation, Triangle Wing	79
50	Autorotation Tail Effectiveness, Triangle Wing	80
51	Alternating Blade Root and Shaft Bending Moments, Autorotation, Trisector Wing	81
52	Pseudo-Conversion, Trisector Wing	85
53	Pseudo-Conversion, Tricusp Wing	86
54	Pseudo-Conversion, Triangle Wing	87
55	Aircraft Characteristics During Manual Conversion, Trisector Wing	92

Figure		Page
56	Aircraft Characteristics During Manual Conversion, Tricusp Wing	93
57	Aircraft Characteristics During Manual Conversion, Triangle Wing	94
58	Alternating Blade Root and Shaft Bending Moments, Manual Conversion, Trisector Wing	95
59	Alternating Blade Root and Shaft Bending Moments, Manual Conversion, Tricusp Wing	96
60	Alternating Blade Root and Shaft Bending Moments, Manual Conversion, Triangle Wing	97
61	Conversion, Trisector Wing	98
62	Conversion, Tricusp Wing	99
63	Conversion, Triangle Wing	100
64	Center of Pressure Travel During Conversion, Trisector Wing	101
65	Center of Pressure Travel During Conversion, Tricusp Wing	102
66	Center of Pressure Travel During Conversion, Triangle Wing	103
67	Rotor/Wing Shaft-Bending Moments, Triangle Rotor Start-Up	104
68	Rotor/Wing Rolling and Pitching Moments, Triangle Rotor Start-Up	105
69	Full-Scale Rotor/Wing Aircraft Response, Triangle Rotor Start-Up	106
70	Comparison in Airplane Mode, Tail-Off, Trisector Wing	109
71	Comparison in Airplane Mode, Tail-Off, Triangle Wing	110
72	Planform Comparison, Airplane Flight	111
73	Tail Effectiveness, Airplane Flight, Triangle Wing	112
74	Horizontal Tail Characteristics, Airplane Flight	113
75	Yaw and Roll Due to Differential Elevon Deflection, Airplane Flight, Triangle Wing	114
76	Comparison of Yaw and Roll due to Differential Elevon Deflection	115
77	Hover Performance, Power Required	118
78	Hovering Performance, Induced Power	124
79	Hovering Performance, Profile Power	125
80	Dimensional Characteristics, Triangular Model Wing	126
81	Variation of Wing C_Q with r/R, Hovering Conditions	128
82	Ground Effect Test Results	130
83	Comparison, Typical Full-Scale Rotor/Wing Hover Power and Model Test Data	131

Figure		Page
84	Typical Rotor/Wing Aircraft Configuration	132
85	Rotor/Wing Full-Scale CRA Lift-Drag Estimate	134
86	Reynolds Number Effect on Equivalent Skin Friction Drag	136
87	Rotor/Wing Transonic Model Lift-Drag Characteristics	138
88	Reynolds Number Effect on Rotor/Wing Span Efficiency	140
89	Rotor/Wing Span Efficiency Ratios at Lift Coefficients Greater than 0.3 and at Mach numbers less than 0.6	141
90	Rotor/Wing Trim Drag Increment	143
91	Rotor/Wing Mach Number Drag Rise	143
92	Typical Drag Polar, Airplane Mode	147
93	Power Required, Helicopter Forward Flight	148
94	Typical C_L and C_D Curves for Helicopter/Autogyro Mode	150
95	Estimated C_L and C_D for Elevon	152
96	Wing Torque Versus Advance Ratio	155
97	Comparison, Performance Theory and Rotor/Wing Model Data, Helicopter Mode	156
98	Power Required, Autogyro Flight	158
99	Comparison, Performance Theory and Rotor/Wing Model Data, Autogyro Mode	161
100	Typical Power Required and Available	163
101	Rotating Wing Span Efficiency During Conversion	164
102	Rotor/Wing Downwash Distribution During Conversion	166
103	Comparison of Rotor Blade Rolling Moment from Model Test and Theoretical Calculation	167
104	Schematic Rotor/Wing Spring-Mass Representation	169
105	Horizontal Tail Size Statistical Survey	172
106	Vertical Tail Size Statistical Survey	173

LIST OF TABLES

Table		Page
1	Rotor/Wing Wind Tunnel Series VI Test Schedule	26
2	Rotor Shaft Bending Moment Harmonic Analysis, Powered Rotor, Triangle Wing, Tail-Off	64
3	Rotor Shaft Bending Moment Harmonic Analysis, Powered Rotor, Triangle Wing, Blades-Off, Tail-Off	74
4	Rotor Shaft Bending Moment Harmonic Analysis, Autorotation, Triangle Wing, Tail-Off	82
5	Rotor Shaft Bending Moment Harmonic Analysis, Conversion, Triangle Wing, Tail-Off	83
6	Lift and Pitching Moment Comparison, Theory and Test	168

BLANK PAGE

LIST OF SYMBOLS AND DEFINITIONS

ROTOR/WING

A_1 Rotor cyclic pitch angle; see classic blade pitch equation below, degrees

A_2 Second harmonic cyclic pitch angle; see classic blade pitch equation below, degrees

B_1 Rotor cyclic pitch angle; see classic blade pitch equation below, degrees

θ Rotor collective pitch angle; equal to A_0 in classic blade pitch equation below, degrees

ψ Rotor azimuth position, measured from downwind position in the direction of rotation, degrees

Classic Blade Pitch Equation:

$$\theta = A_0 - A_1 \cos \psi - B_1 \sin \psi - A_2 \cos 2\psi - B_2 \sin 2\psi \ldots$$

MODEL

δ_H Horizontal stabilizer incidence, positive nose-up, degrees

$\Delta \delta_H$ Differential horizontal stabilizer incidence, positive right side nose-down, to produce right rolling moment, degrees

α Model angle of attack, degrees (see note, page 36)

β Model yaw angle (zero for this test series), degrees

N_R Model rotor speed, revolutions per minute

R Rotor radius = 3.57 feet

ΩR	Model tip speed, feet per second = 0.374 N_R for this model
μ	Model advance ratio = $V/\Omega R$
e	Wing span efficiency factor
πR^2	Disc area

For an explanation of the preceding Rotor/Wing Test Series, see pages 3 and 4.

For a description of the Series VI model, see pages

TUNNEL

V	Tunnel wind speed, feet per second
ρ	Tunnel air density, slugs per cubic foot
q	Tunnel dynamic pressure, pounds per square foot = $\rho V^2/2$

FORCES AND MOMENTS

L = Lift

D = Drag

Y = Side force

$\mathcal{L}$ = Rolling moment

M = Pitching moment

N = Yawing moment

T = Thrust

Q = Torque

COEFFICIENTS

Lift	$C_L = L/q\pi R^2$	$C_L' = L/\rho(\Omega R)^2 \pi R^2$
Drag	$C_D = D/q\pi R^2$	$C_D' = D/\rho(\Omega R)^2 \pi R^2$
Side Force	$C_Y = Y/q\pi R^2$	$C_Y' = Y/\rho(\Omega R)^2 \pi R^2$
Rolling Moment	$C_{\mathcal{L}} = \mathcal{L}/q\pi R^3$	$C_{\mathcal{L}}' = \mathcal{L}/\rho(\Omega R)^2 \pi R^2$
Pitching Moment	$C_M = M/q\pi R^3$	$C_M' = M/\rho(\Omega R)^2 \pi R^3$
Yawing Moment	$C_N = N/q\pi R^3$	$C_N' = N/\rho(\Omega R)^2 \pi R^3$
Thrust	$C_T = \mu^2 C_L/2$	$= T/\rho(\Omega R)^2 \pi R^2$
Torque	$C_Q = \mu^2 Q/2q\pi R^3$	$= Q/\rho(\Omega R)^2 \pi R^3$

Note that all test data coefficients are based on the rotor disc area πR^2 as the reference area, and on the rotor radius as the reference length. In the Analytical section, the part dealing with airplane performance uses lift and drag coefficients based on the area of the wing plus two blades, thus:

$$C_L = L/qS_W$$

$$C_D = D/qS_W$$

where S_W denotes the planform area of the wing plus two blades.

SHAFT AND BLADE BENDING MOMENTS

$\pm M_{s_\perp}$ Shaft bending moment, about axis parallel to blade spar, inch pounds

$\pm M_{s_\parallel}$ Shaft bending moment, about axis perpendicular to blade spar, inch pounds

$\pm M_H$ Blade bending moment, chordwise, inch pounds

$\pm M_V$ Blade bending moment, flapwise, inch pounds

Blade and shaft bending moments are half the peak-to-peak values measured from the oscillograph records; units are inch-pounds. Coefficients are defined by the following formulas:

$$\pm\overline{M} = \pm M/12\rho(\Omega R)^2 \pi R^3$$

$$\pm\overline{\overline{M}} = \pm M/12LR = \pm M/12C_L q \pi R^3$$

SUMMARY

Wind tunnel tests of a 7-foot-diameter Rotor/Wing aircraft model were conducted in the 30-by-60-foot full-scale wind tunnel at the NASA Langley Research Center (NASA LRC) to further the investigation of the Rotor/Wing concept. These tests were designated Rotor/Wing Series VI, in a continuing program of aerodynamic evaluation. Previous tests of this model in a smaller wind tunnel had demonstrated the feasibility of the Rotor/Wing concept, including the all-important conversion maneuver.

The purpose of the tests reported here was threefold:

1. To check the validity of the data obtained from a model that was quite large relative to the tunnel in which it was tested.
2. To examine more closely the very low rotor rpm region of the conversion.
3. To compare the aerodynamic characteristics of Rotor/Wings of three different planforms.

The tests showed that the data obtained from both tunnels compared well when the rotor advance ratio was 0.15 or higher, and when conventional airplane-type tunnel wall or jet boundary corrections were made to the data from the small tunnel.

Conversion tests showed that except for the first or last 1/2 revolution as the Rotor/Wing starts or stops in flight, conversion is a straightforward maneuver that can be easily accomplished. During the critical 1/2-revolution time

period, these tests with the rigid Concept Model showed that the rotor develops a pitch-up and rolling tendency, but these are of a magnitude that can be balanced by the elevons.

Tests of the three Rotor/Wing planforms showed the trisector wing with straight blades and the triangle wing with tapered blades to have approximately equivalent performance, whereas the tricusp wing with tapered blades was noticeably inferior for the helicopter flight modes.

An analytical procedure for predicting Rotor/Wing performance and flying qualities is shown to be applicable through comparisons of theoretical and experimental data.

INTRODUCTION

The Rotor/Wing high-speed VTOL concept is based on a dual-purpose lifting device that is a powered rotor for hover and low-speed flight, and a fixed-wing lifting surface in the high-speed flight mode. Power, in the form of gas generator exhaust, is piped to the Rotor/Wing blade tips where it exhausts through tip nozzles to drive the rotor during the helicopter flight mode; alternatively, this exhaust may be piped to a conventional turbojet nozzle at the rear of the fuselage, where its energy is converted to the thrust necessary to propel the aircraft in the autogyro and airplane flight modes. The transfer of power for the different flight modes consists of simply operating a pneumatic valve to divert the hot gas from one path to another.

The various flight modes appropriate to the Rotor/Wing concept are shown schematically in Figure 1 and are summarized below.

1. Helicopter
   Hover and low-speed flight mode where the rotor is powered by Hot Cycle propulsion system. Aircraft control is by conventional helicopter collective and cyclic rotor blade pitch. No reaction to main rotor torque is present, but a small yaw fan is required for directional control.

2. Autogyro
   Intermediate flight mode, where power is diverted to conventional turbojet nozzles and the Rotor/Wing autorotates at a low collective pitch setting. Aircraft control is by rotor blade cyclic pitch, augmented by the horizontal tail elevon action and the rudder on the vertical tail.

3. Airplane

   The stopped Rotor/Wing is locked to the fuselage, and retractable fairings and seals are in place. Propulsive force is supplied by the exhaust through the turbojet nozzle. Control is by tail surface deflection only. In this configuration, the aircraft is capable of flight into the high subsonic speed regime.

4. Conversion/Reconversion

   The rotor is stopped and started in flight, using aerodynamic torque, with some assistance from a brake for final stopping. Small control motions which combine the rotor cyclic pitch controls and the elevons are used in a straightforward manner to effect the conversion and reconversion.

Since 1962, Hughes Tool Company - Aircraft Division has been actively engaged in a program of research and model testing of the Rotor/Wing concept. These tests, covering the speed range from hover to Mach = 0.9, are summarized below:

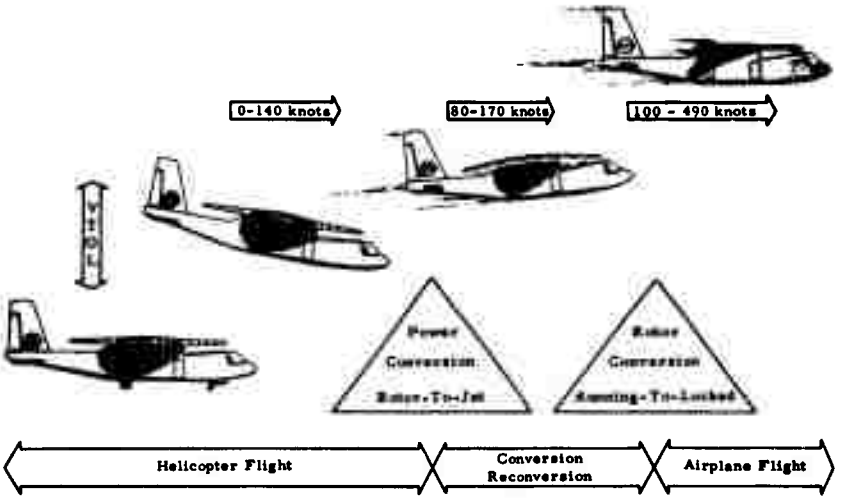

Figure 1. Rotor/Wing Flight Modes

Rotor/Wing Series I Whirlstand Test, May 1963

Initial tests of Rotor/Wing concept at HTC-AD whirlstand facility; determined feasibility of the large center-body in the hover flight mode. Tests included variation of planform shapes, pneumatically-driven by tip-jets.

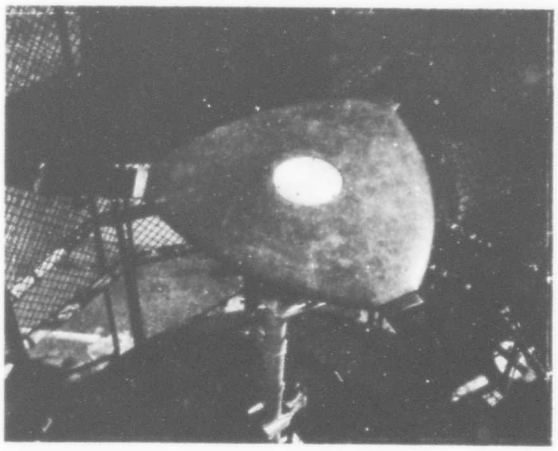

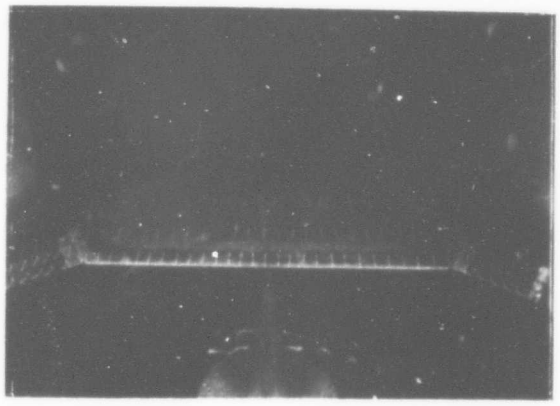

Rotor/Wing Series I Wind Tunnel Test, October 1964

First wind tunnel tests in the subsonic wind tunnel at the Navy Ship Research and Development Center (NSRDC) Aerodynamics Laboratory (then David Taylor Model Basin), to determine loads with the rotor in various azimuth positions. Two planforms tested in the stopped-rotor mode without a fuselage. Tests reported in Reference 1.

Rotor/Wing Series II and III Wind Tunnel Test, March and June 1965

Extensive tests in helicopter, autogyro and airplane flight modes in NSRDC subsonic wind tunnel. Proved ability to start and stop the rotor and trim the aerodynamic forces. Only one planform tested: the trisector. Tests reported in References 2 and 3.

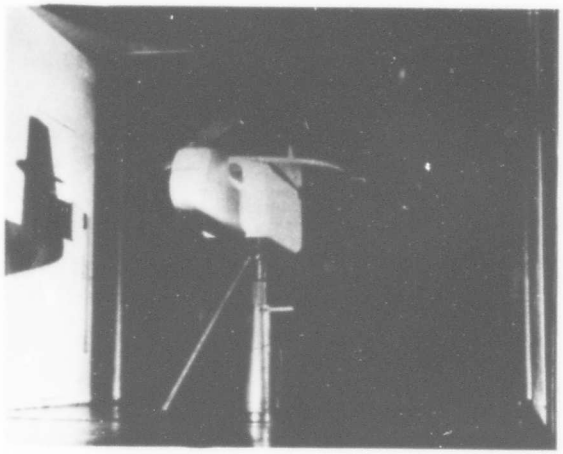

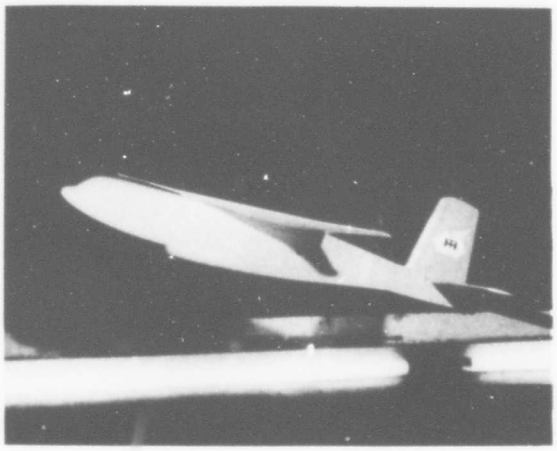

Rotor/Wing Series IV Wind Tunnel Tests, January 1966

Low-speed tests in the Douglas Aircraft Corporation wind tunnel in the airplane flight mode determined influence of nose configuration and low horizontal tail position on longitudinal stability and drag. Extensive tuft photos of triangular wing with tapered blades were obtained.

Rotor/Wing Series II Whirlstand Tests, March 1966

Additional hover tests at the HTC-AD whirl test facility of three Rotor/Wing planforms. Determined performance and control power available and provided extensive model checkout.

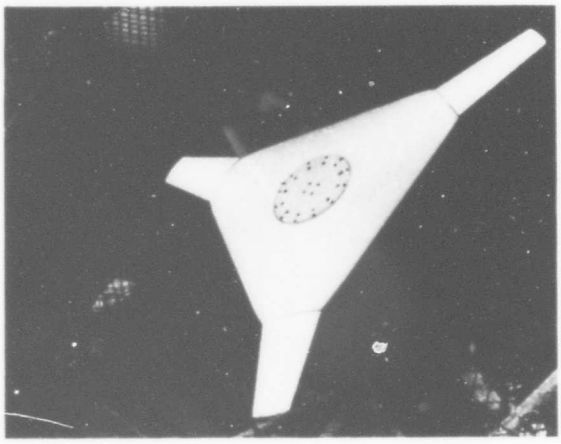

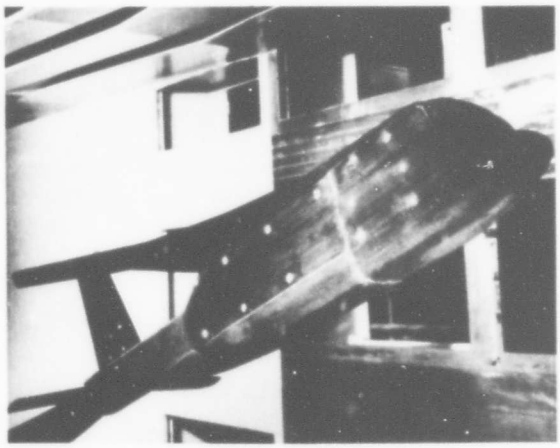

Rotor/Wing Series V Wind Tunnel Tests, April 1966

Determined high-speed performance and stability parameters in airplane flight mode. Tested at NSRDC in the transonic wind tunnel up to M = 0.90.

The test series described in this report was conducted in the full-scale 30-by-60-foot wind tunnel at NASA Langley Research Center (LRC) (Reference 4) in September 1966. These tests are designated Rotor/Wing Series VI Wind Tunnel Test.

The purpose of this test was:

1. For the same Rotor/Wing model, compare the test data from the full-scale tunnel with data previously obtained in the small NSRDC wind tunnel (Rotor/Wing Series I, II, III), where the tunnel walls have an unknown influence on the validity of the test. (This influence would be expected to be greatest at low tunnel speeds and high rotor speeds.)
2. Evaluate the complexity of the conversion maneuver, particularly in the very low rotor speed range.
3. Evaluate the aerodynamic characteristics of three planform shapes applicable to the Rotor/Wing concept in all flight modes.

Figures 2 and 3 show the model installed in the wind tunnel. Figure 2 shows general views taken during helicopter flight mode tests. Figure 3 illustrates the three planforms tested.

This report includes the results of the Series VI tests, and where logical comparisons with the data from previous tests can be made, these are included. The test data are presented in the following order:

Powered-rotor hover (V = 0)
Powered-rotor helicopter mode
Autorotation mode
Conversion/Reconversion (including powered-rotor pseudo-conversion)
Airplane mode (locked rotor)

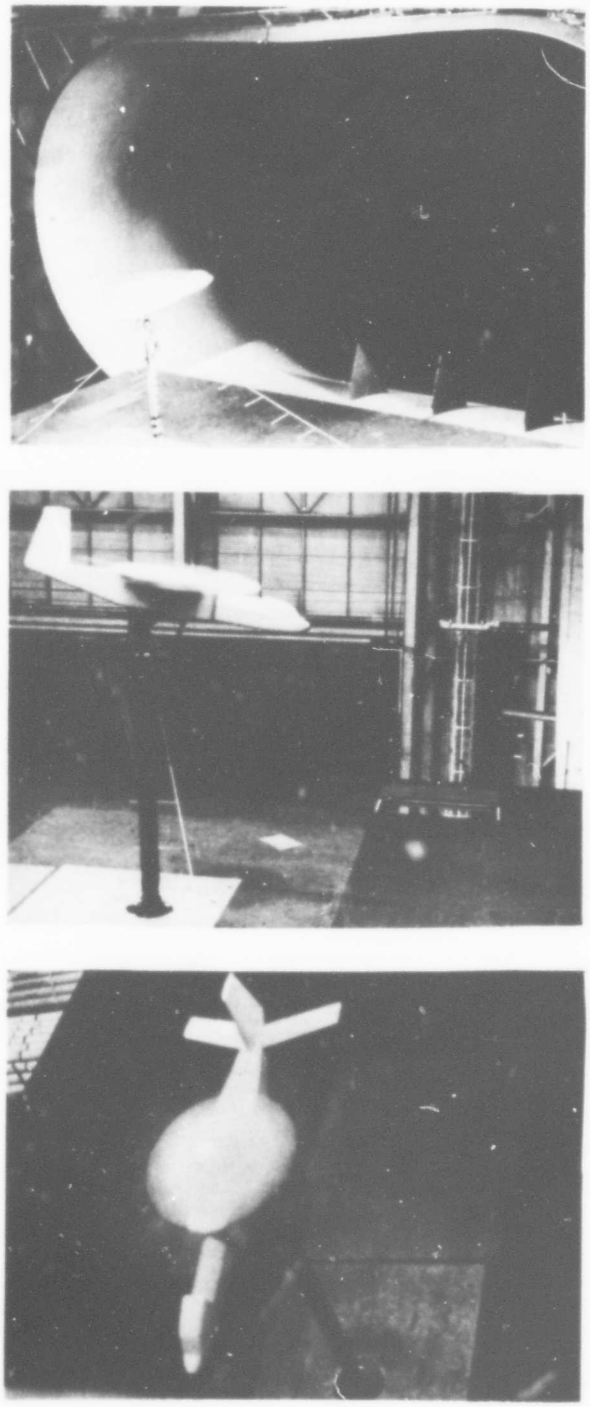

Figure 2. Helicopter Flight Mode

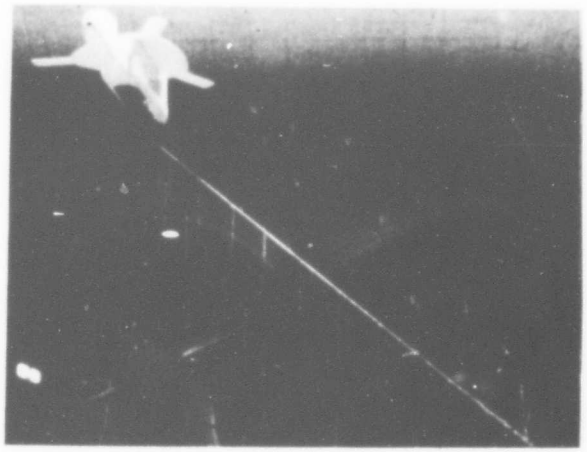

Trisector

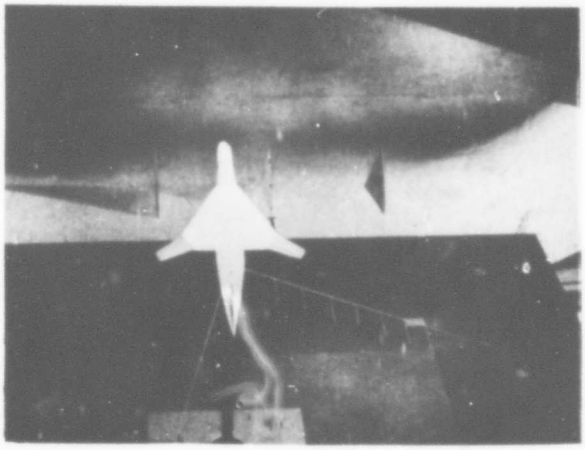

Triangle

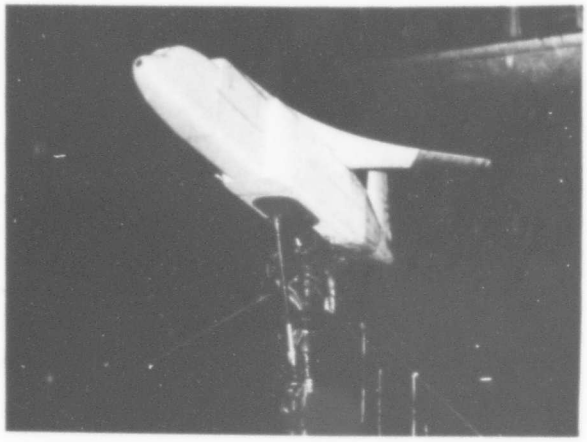

Tricusp

Figure 3. Airplane Flight Mode

BLANK PAGE

DESCRIPTION OF MODEL

GENERAL

In 1962, Hughes Tool Company - Aircraft Division designed and built a series of Rotor/Wing models, and conducted whirlstand tests to determine their hovering performance. The optimum model configuration from this test series was chosen as the Rotor/Wing for the complete wind tunnel model sponsored by the Office of Naval Research and the Naval Air Systems Command (at that time the Bureau of Naval Weapons). This configuration, the trisector wing with straight blades, was tested in the 8-by-10-foot subsonic wind tunnel at the Naval Ship Research and Development Center (NSRDC) (at that time the David Taylor Model Basin - DTMB). The results of that test and the first whirlstand test are summarized in Reference 2.

For the present test series in the 30-by-60-foot wind tunnel, two additional Rotor/Wings were supplied that could be mounted on the existing model chassis. These were the triangle and tricusp planforms, both with tapered blades. The new Rotor/Wing configurations were tested, along with the existing trisector planform, in the hover flight mode at the HTC-AD whirlstand facility. This second whirlstand test served the purpose of model, instrumentation, and systems checkout prior to this wind tunnel test.

The three-view drawing of Figure 4 shows the general arrangement of the Rotor/Wing Concept Model. It consists of a fuselage, empennage, miscellaneous small fuselage fairings, and the three Rotor/Wing planform configurations.

FUSELAGE

The fuselage was basically a structural box built of aluminum plate and covered with mahogany to provide the external contours. Located within the box were the rotor support bearings, hydraulic driving motor, rotor control mechanism, instrumentation and model-mounting structure. Detail drawings, essentially unchanged from previous tests, are shown in Reference 2. Photographs of these components are shown in Figure 5.

EMPENNAGE

The vertical tail surface was bolted to the top of the aft fuselage structure and was in place for all testing because its weight relieved a nose-heavy model situation that would have seriously limited the range of testing.

The horizontal tail was attached to the aft fuselage tail cone instead of near the top of the vertical tail, as in the previous tests with this model, because tests with other models had shown this low position to be preferable from an aerodynamic as well as a structural standpoint. The tail incidence could be set manually, both sides together for pitch control or differentially for roll control. Empennage dimensions are given in the table on Figure 4.

ROTOR/WINGS

The three Rotor/Wings tested had equal diameters -- 86.7 inches -- and the same ratio of blade root radius to tip radius -- 59 percent. The trisector wing and blades were tested previously and were not modified for this test. The triangle wing was adapted from the triangular configuration used in Series I whirlstand tests. The tricusp wing was new for this test and was constructed in the same manner as the previous models: mahogany, covered with fiberglass.

ROTOR/WING		Trisector	Triangle	Tricusp
Diameter	85.90 in.			
Disc area	40.30 sq ft			
Wing span (rotor locked)	77.00 in.			
Wing area (hub + 2 blades)		13.87 sq ft	12.48	11.11
Aspect ratio (hub + 2 blades)		2.98	3.29	3.72
Collective pitch	-10 to +20 degrees			
Cyclic pitch				
Lateral	±15 degrees			
Longitudinal	±15 degrees			
Blade chord, root		6.66 in.	10.65	10.65
Blade chord, tip		6.66 in.	6.30	6.30
Blade thickness ratio	15 percent			
Blade airfoil section	Modified circular arc			

HORIZONTAL TAIL	
Span	54.00 in.
Area	4.17 sq ft
Root Chord (Theoretical)	12.00 in.
Aspect ratio	4.50
Taper ratio	0.83
Leading edge sweepback	20 degrees
Tail length (to ℄ rotor)	52.41 in.
Airfoil section	
Root	NACA 0015
Tip	NACA 0012

VERTICAL TAIL	
Span	25.00 in.
Area	2.88 sq ft
Root chord	21.20 in.
Aspect ratio	1.50
Taper ratio	0.57
Leading edge sweepback	5 degrees
Tail length (to ℄ rotor)	50.57 in.
Airfoil section	
Root	NACA 0019
Tip	NACA 0012

FUSELAGE

1. Tandem cockpit forward of blade tip; leading edge faired into fuselage.
2. Tandem cockpit forward of blade tip; open for blade clearance.

Tricusp
11.11
3.72
10.65
6.30

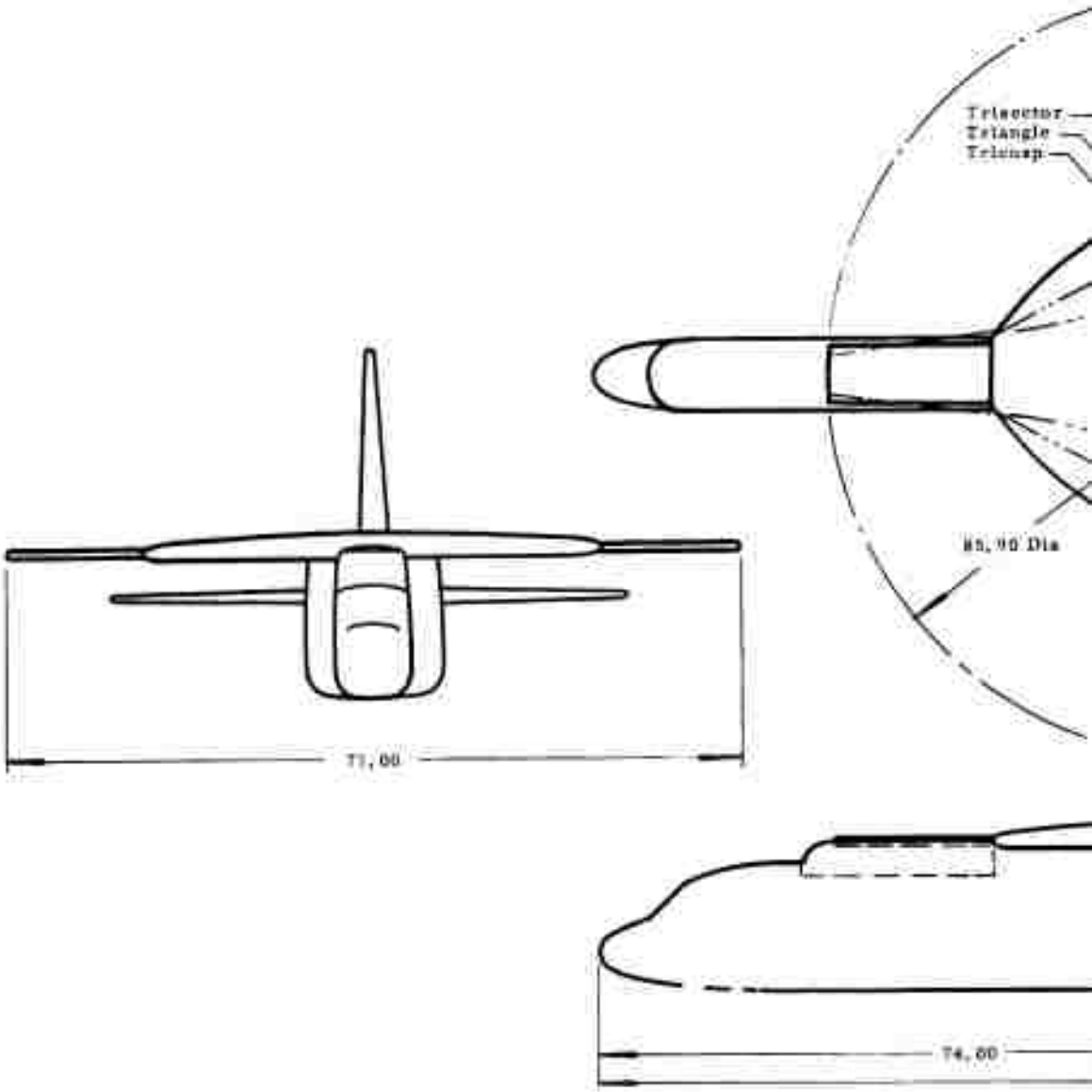

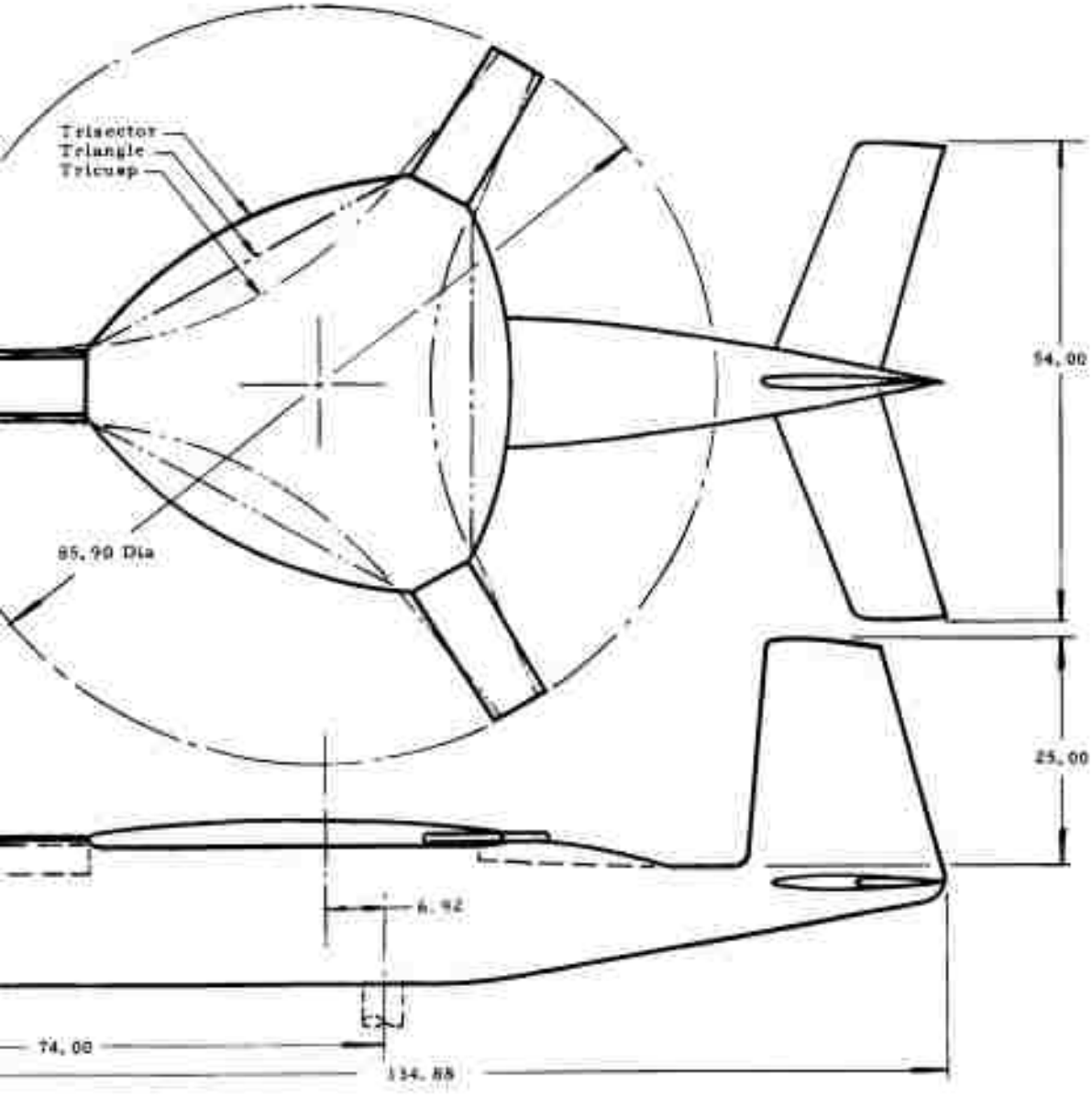

Figure 4. General Arrangement Drawing

BLANK PAGE

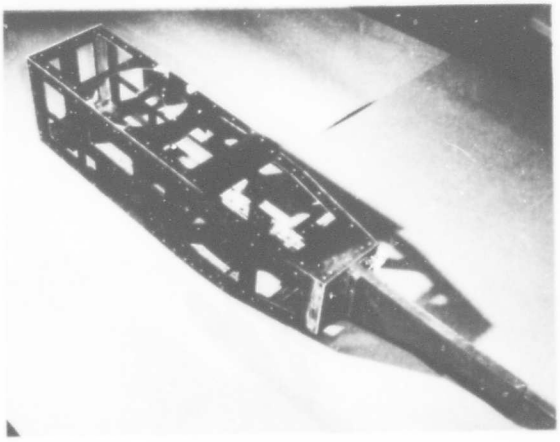

Model Structural Box

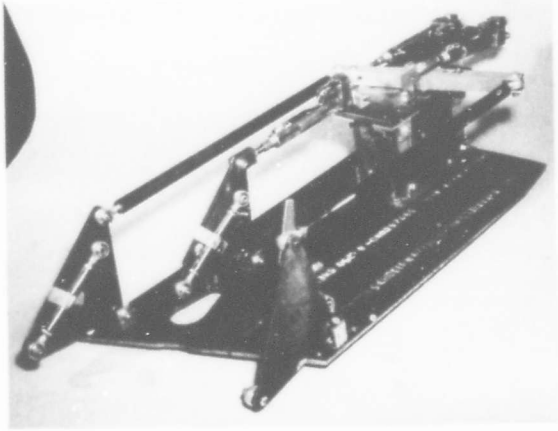

Cyclic and Collective Control System

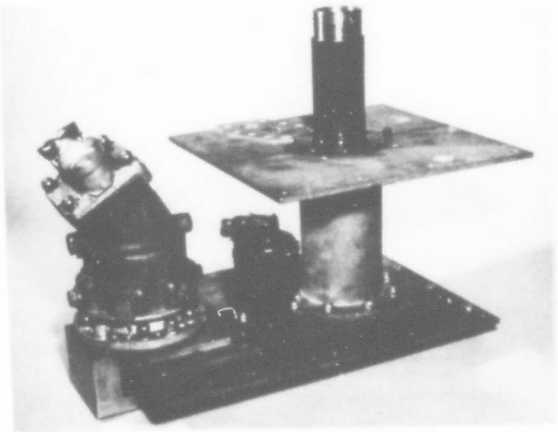

Rotor Mast and Drive Motor

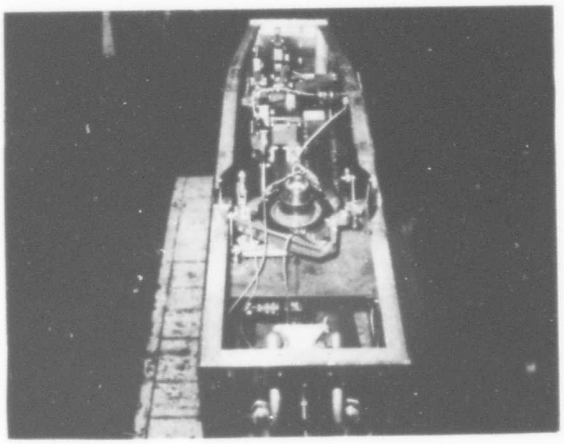

Fuselage Assembly

Figure 5. Model Components

The straight blades, used only on the trisector wing, were not changed for this test series. The tapered blades were new, being built of balsa wood covered with fiberglass for light weight. There was a metal rib at the blade root and at the blade tip to transfer torsion loads to the tubular blade spar. The blade tip, outside the metal rib, was mahogany. The new tapered blades and the old straight blades had circular arc airfoils with parabolic leading and trailing edges, and were double-ended uncambered sections, completely

symmetrical about the mid-chord point of the chordline. Figure 6 presents the blade and wing planform geometry of each configuration for comparison. The photographs of Figure 7 show these planforms mounted on the model chassis for the Series II whirlstand test.

After the tests were completed, measurements were made of the airfoil contours of the Rotor/Wing. Figure 8 shows the template locations of the airfoil sections and Figure 9 shows the sections of the three Rotor/Wings. For scale comparison, the rectangular bar above each model's profile is 12 inches long.

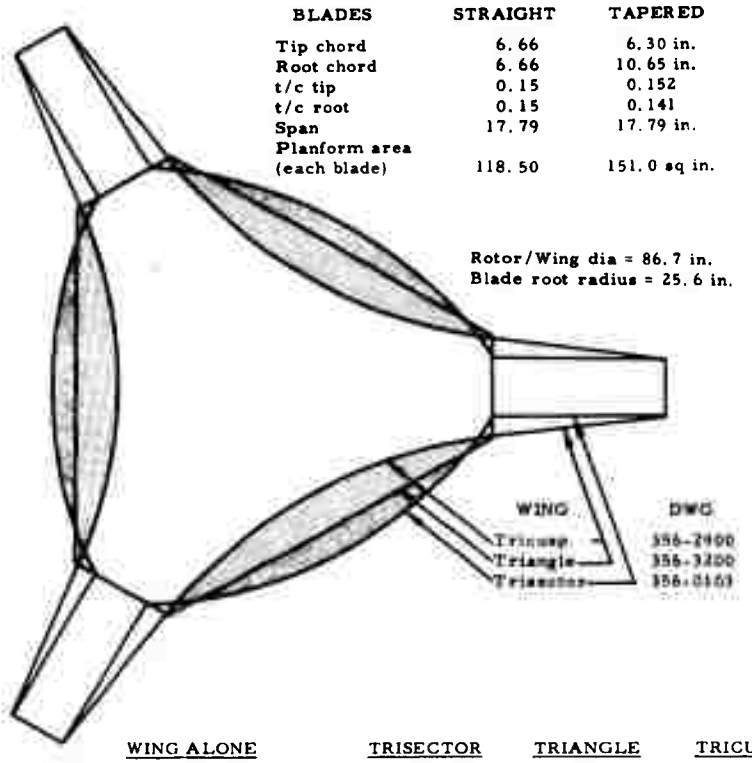

BLADES	STRAIGHT	TAPERED
Tip chord	6.66	6.30 in.
Root chord	6.66	10.65 in.
t/c tip	0.15	0.152
t/c root	0.15	0.141
Span	17.79	17.79 in.
Planform area (each blade)	118.50	151.0 sq in.

WING ALONE	TRISECTOR	TRIANGLE	TRICUSP
Radius of edge in planform	48.52	∞	-50.0 in.
Planform area	1630.0	1483.0	1300 sq in.

Figure 6. Model Geometry

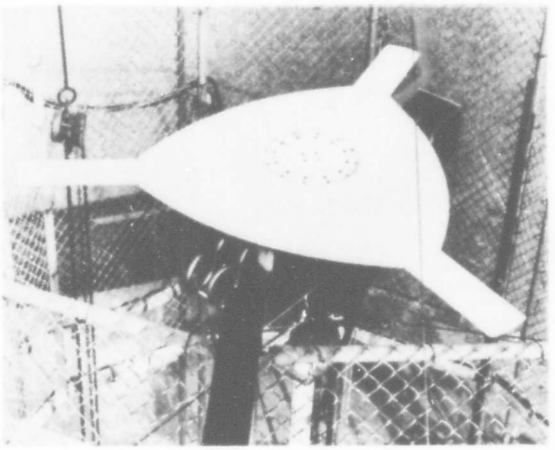

Trisector wing with straight blades. This configuration was tested previously during the Rotor/Wing Series I Whirlstand test.

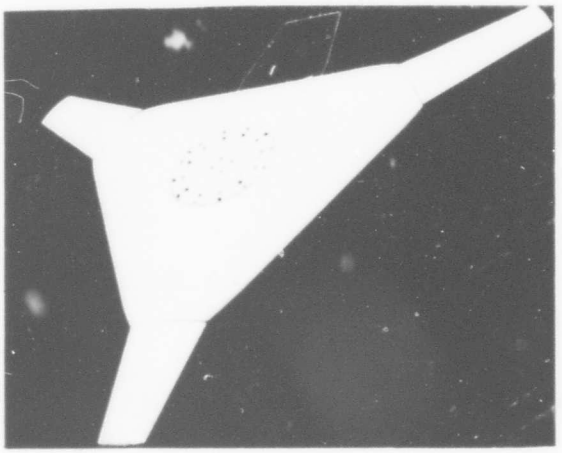

Triangle wing with tapered blades. This configuration is similar to that proposed for CRA application.

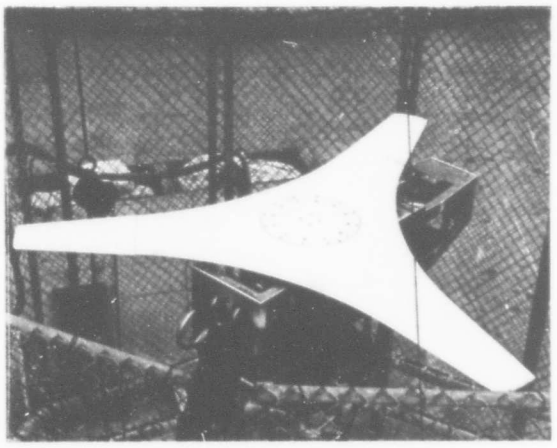

Tricusp wing with tapered blades. This configuration has a higher aspect ratio during stopped-rotor airplane flight.

Figure 7. Planform Configurations

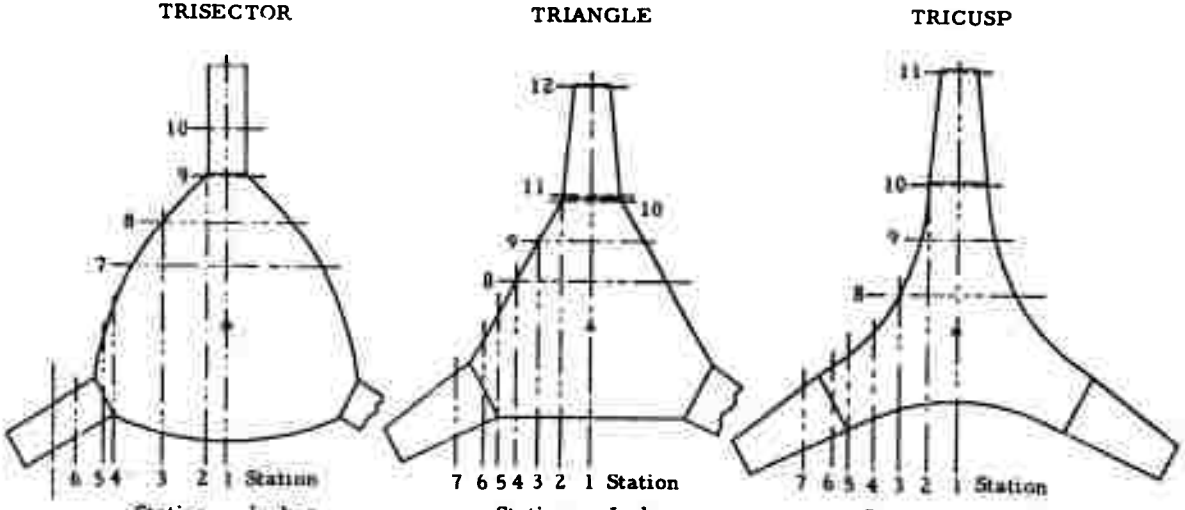

Station	Inches
1	0
2	5.18
3	12.42
4	17.95
5	22.20
6	29.56
7	9.83
8	17.20
9	24.57
10	-

Station	Inches
1	0
2	6.21
3	11.00
4	15.50
5	19.50
6	22.00
7	26.75
8	8.70
9	16.53
10	24.36
11	26.36
12	1 from tip

Station	Inches
1	0
2	5.43
3	11.68
4	15.68
5	19.50
6	22.00
7	26.75
8	6.68
9	15.50
10	24.56
11	1 from tip

Template location for Rotor/Wing planform as tested in full-scale tunnel. Dimensions are in inches and are measured from the center of the hubs. 5-18-67 JPS

Figure 8. Template Location for Rotor/Wing Airfoil Sections

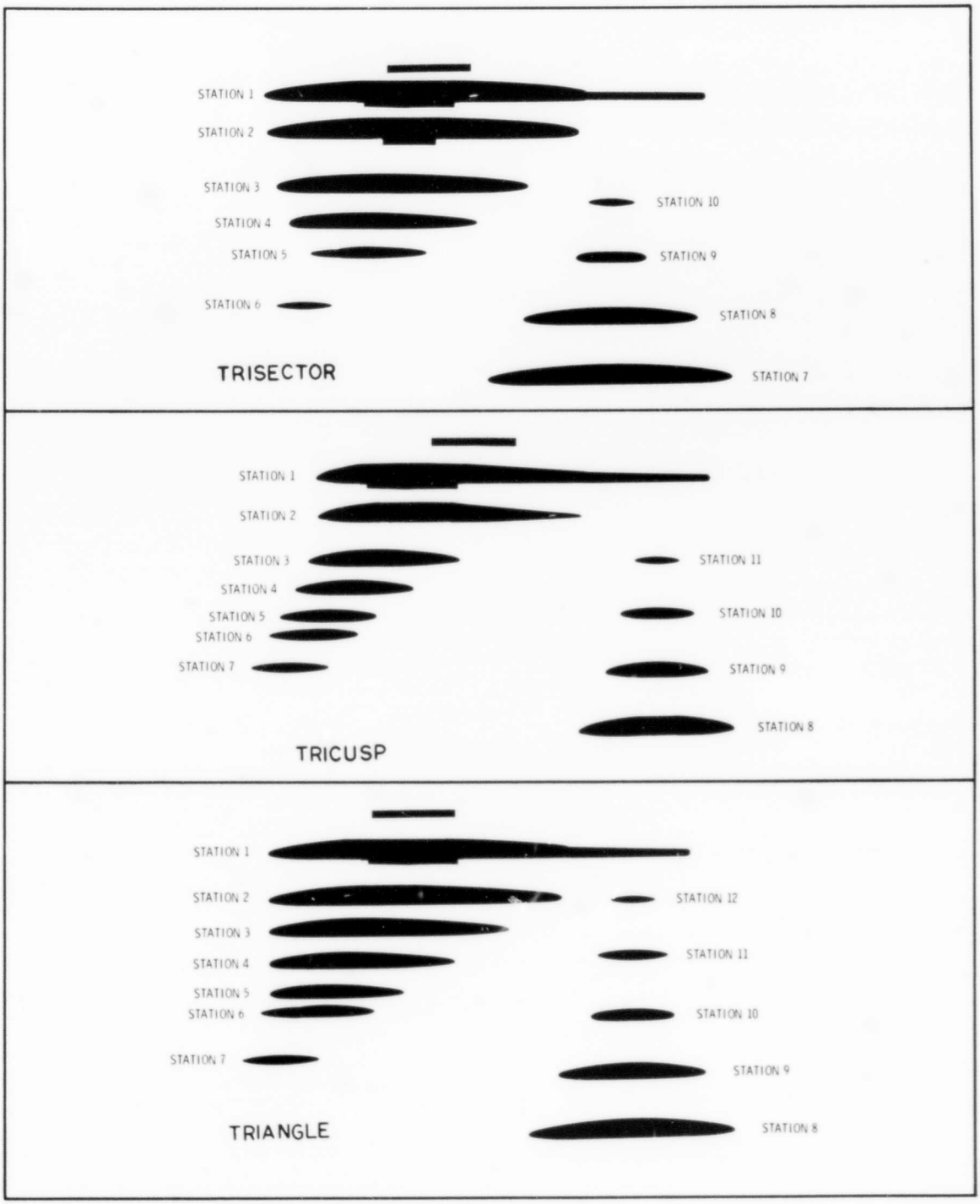

Figure 9. Rotor/Wing Airfoil Sections

ROTOR/WING DRIVE SYSTEM

The hydraulic motor and drive system are unchanged from the description given in Reference 2. The motor is a Vickers Model MF 40-3918-30Y-4 whose displacement is 2.349 cubic inches per revolution. A roller chain drive connects the motor to the Rotor/Wing, providing a gear reduction ratio of 1.5294 to 1.0. The chain drive was removed for autorotation tests to minimize mechanical and hydraulic restrictions to free rotation.

A variable-displacement hydraulic pump supplied the power to drive the model. This pump was the same unit, described in Reference 2, that was used at NSRDC. The hydraulic lines between this pump and the model were arranged to minimize their influence on the strain gage balance system. A schematic of the hydraulic circuit is shown in Figure 10.

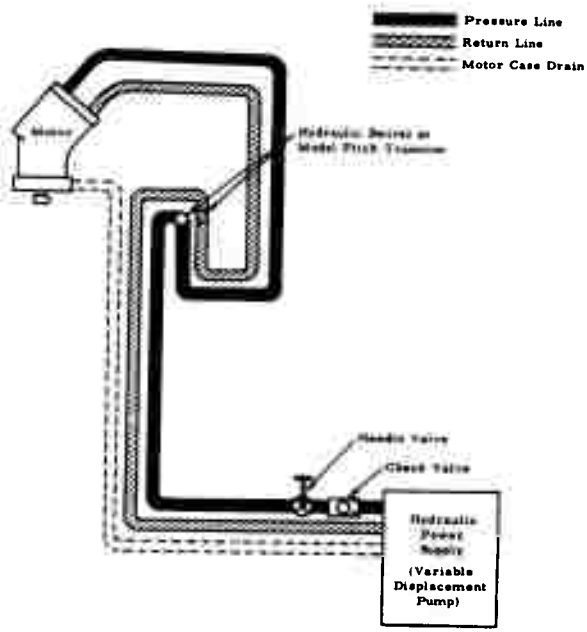

Figure 10. Schematic Hydraulic Circuit

ROTOR/WING CONTROL SYSTEM

The control system was unchanged from that described previously, Reference 2, and shown in the photograph of Figure 5. Schematically, the system is shown on Figure 11.

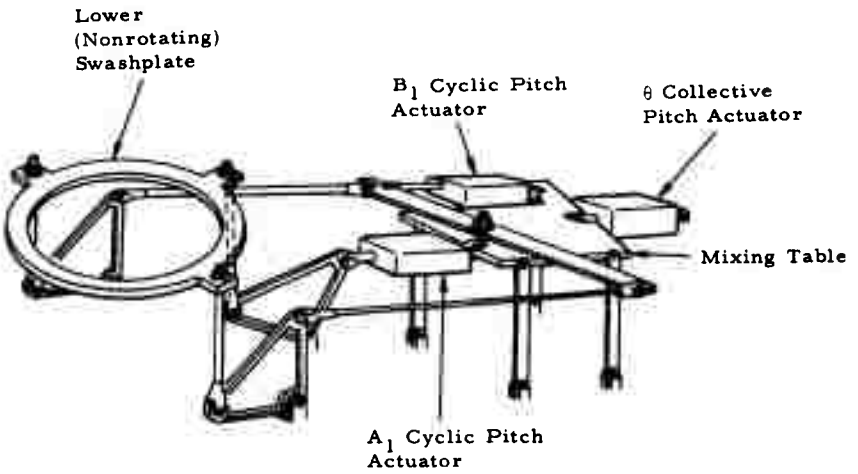

Figure 11. Schematic Control System

The swashplate used for most testing was the $A_2 = 2.5°$ configuration. This swashplate, shown in the upper photograph of Figure 12, was built with a wave in its track, such that the followers riding in the track caused the blades to cycle 5 degrees, double amplitude, twice each revolution of the rotor. This is equivalent to an $A_2 = 2.5°$ blade-feathering motion in the classic blade pitch equation below:

$$\theta = A_0 - A_1 \cos \psi - B_1 \sin \psi - A_2 \cos 2\psi - B_2 \sin 2\psi - \ldots$$

The $A_2 = 0°$ swashplate is similar in construction and operation except that the wave is, of course, omitted.

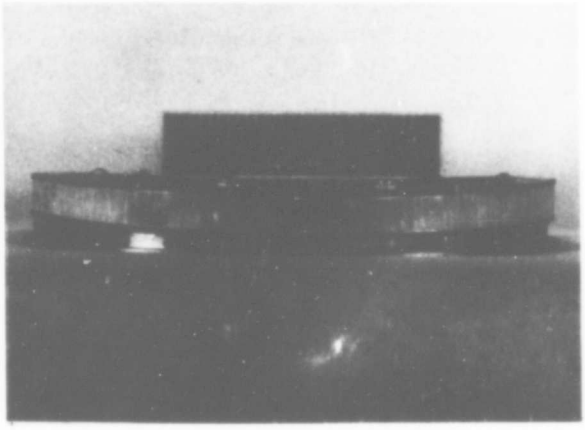

$A_2 = 2.5°$ swashplate, provides 2.5 degrees of cyclic pitch, twice each rotor revolution.

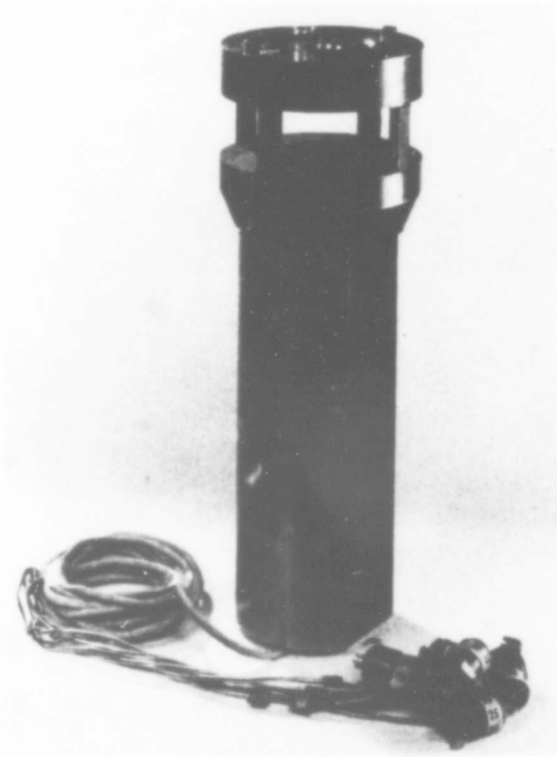

Strain-gage balance system, used to measure six component forces and moments imposed on the model. This is the property of NASA, Langley Research Center.

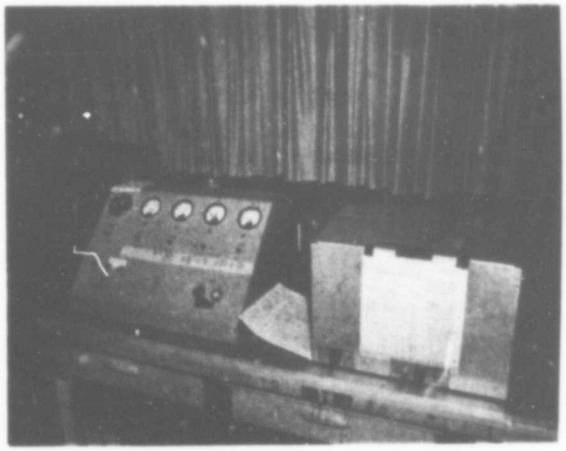

Control panel, providing full cyclic and collective blade pitch control.

Figure 12. Test Components

The blade pitch for each of the Rotor/Wings was controlled remotely by electric actuators that positioned the swashplate. A_1 and B_1 cyclic pitch in the equation above was controllable between ±16 degrees; collective pitch, θ, was controllable between -11 and +21.5 degrees.

MODEL MOUNTING

The second photograph of Figure 12 shows the strain gage balance used to measure forces on the model. This component, the property of NASA-Langley Research Center, was mounted between the model and the model mast in the wind tunnel. The balance measured the conventional six component forces and moments about the balance center, located in the middle of the flat surface at the top of the balance. Figure 13 shows schematically how the balance was installed and located within the test setup. All forces applied to the model above the balance were measured, and the balance signals were recorded by one of several modes.

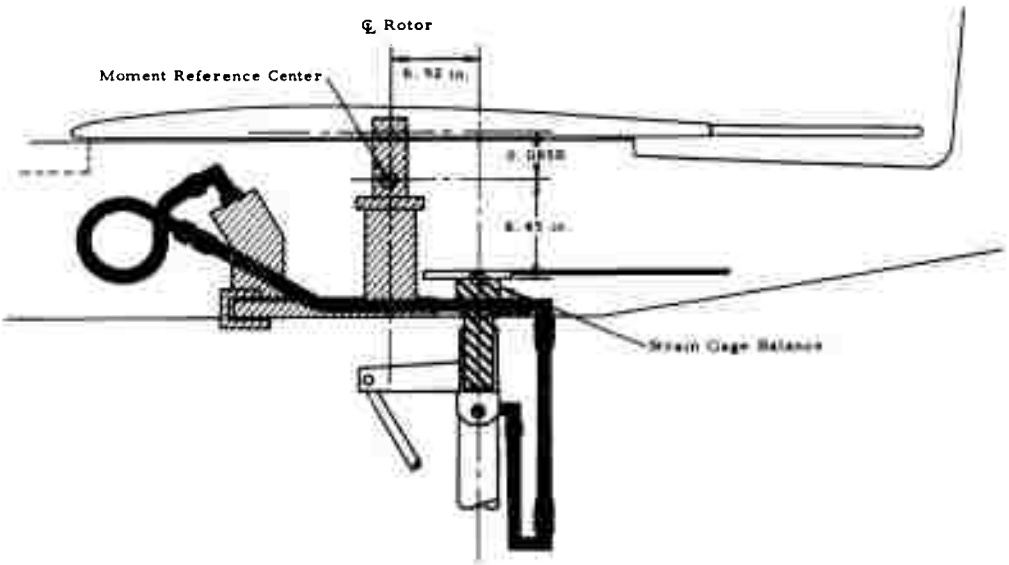

Figure 13. Schematic Model Mount and Systems

The lower portion of the balance fitted into a steel cylinder welded to the hydraulic knuckle that was the model pitch axis. Thus, the balance system sensed forces and moments in the model axis reference system. The model mounting-mast was stayed to the tunnel's ground plane by three steel cables. The tension in these cables was tuned to avoid mechanical resonance when the Rotor/Wing was at its primary operating speed, 600 rpm. The total height of the mast, hydraulic knuckle balance, and fuselage placed the Rotor/Wing 13 feet above the ground plane. This location was nearly in the center of the tunnel's open-throat test section.

MODEL OPERATION

The console shown in the lower photograph of Figure 12 was used to operate the model's control system and angle of attack. The console provided indications of collective pitch, cyclic pitch, and angle of attack. A tachometer gave an indication of rotor speed. Manual control of the model through this panel was made for all tests, including conversion.

DATA RECORDING

Besides giving an indication of the operator's control panel, the signals from the potentiometers that sensed control position were also recorded by an 18-channel oscillograph. In addition, this oscillograph recorded signals from two accelerometers mounted in the model fuselage, two rotor shaft bending strains, the inlet and outlet pressures of the hydraulic motor, and two blade spar-bending strains. A rotor azimuth signal was also recorded, and when compared to the paper's timing lines, indicated rotor speed.

The signals from the six-component balance system were recorded manually from digital readout equipment and on magnetic tape for steady-state data points. Data from the transient tests (conversion to and from the stopped-rotor mode) were recorded on a second oscillograph. A high-speed electronic

digital computer was used to convert the magnetic tape data to meaningful aerodynamic coefficients.

Each data point was assigned a run number and a test-point number. A summary of the run numbers and test-point numbers is shown in Table 1; more details may be found in Appendix A.

MODEL TEST PROGRAM

The program followed in the Series VI wind tunnel tests of the Rotor/Wing Concept Model is presented in Table 1. Detailed run sheets may be found in Appendix A.

Table 1. Rotor/Wing Wind Tunnel Series VI Test Schedule

(NASA Langley Research Center 30-by-60-Foot Wind Tunnel)

Model Configuration	Flight Mode	Run Number	Test-Point Number
Trisector - A_2 = 2.5°			
Tail-Off	Hover	4	86-290
	Helicopter	5-36	291-574
	Autogyro	37-56	576-782
With Blade Fairing	Airplane	57	828-836
Without Blade Fairing	Airplane	143	1807-1822
Tricusp - A_2 = 2.5°			
Tail-Off	Hover	62	984-1001
	Helicopter	63-83	1002-1146
Blades-Off	Helicopter	216-219	2705-2724
	Autogyro	60-61	946-953
		85-90	1192-1215
With Blade Fairing	Airplane	59	897-905
Triangle - A_2 = 2.5°			
Tail-Off	Hover	96	1337-1354
Tail-Off	Helicopter	97-117	1355-1457
Tail-On		151-168	1920-1991
Tail-Off	Autogyro	132-143	1656-1806
Tail-On		169-176	2047-2090
Tail-Off	Airplane	178-179	2151-2168
Tail-On		180-186	2169-2213
Triangle - A_2 = 0°			
Tail-Off	Hover	187	2320-2332
	Helicopter	188-209	2333-2456
Blades-Off	Helicopter	211-214	2632-2652
Fuselage Alone		210	2522-2582

MODEL TEST RESULTS

This section describes the results of the Rotor/Wing Series VI wind tunnel tests.

This was the first test for the strain gage post balance in this wind tunnel, and the first test for the magnetic tape recording equipment. A number of problems resulted in a delay of nearly seven months following the conclusion of the tests before all the test data were finally available for analysis. Hence, discrepancies that are sure to arise with new equipment were not discovered until much too late to repeat the tests. Areas where there are problems in data analysis because of this procedure are pointed out in the discussion.

Aerodynamic tare and support interference tests were not made for this model because the use of the post-balance support minimizes most tare effects and because of the inconvenience of measuring tares in this particular tunnel. It is known that a drag component of unknown magnitude is included in the test data because a portion of the hoses supplying hydraulic power to the model were in the metrical system and were exposed to the airstream. A number of different methods were used in trying to correlate the Series VI drag data with that from previous tests of comparable configurations, but no consistent pattern could be established. It is concluded that because of this lack of consistency, it is preferable not to show any drag data in this report.

Rotor blade root bending moments and rotor shaft bending moments were measured during all the running-rotor tests. These are a good measurement of the aerodynamic loading on the Rotor/Wing, except for the few cases in

conversion where model resonance interfered. The values measured here must be used only for indicating trends, not absolute levels, for an actual aircraft because the model was heavy, stiff, and dynamically similar to nothing but itself. More accurate measurement of applicable structural loads must await the testing of a dynamically-scaled Rotor/Wing model. The lighter and more flexible Rotor/Wing of the dynamic model or a full-scale aircraft is expected to experience a lower level of moments, than this heavy, stiff concept model.

POWERED MODEL - HOVER MODE

One of the discrepancies mentioned in the previous section occurred during tests in the hover mode and concerns the rotor-torque measurement. Rotor torque was related to the hydraulic pressure difference between the input and outlet side of the rotor's drive motor. These pressures were measured by transducers and recorded on both the magnetic tape and oscillograph records, and the rotor-torque was calculated using the appropriate constants, tares, and calibration factors. The results were not very realistic and seemed to show a general increase in the torque required to drive the rotor as time progressed. Quite possibly the friction in the drive system changed as the testing progressed as a result of wear and tear on the model, in which case no accurate comparisons between rotor configurations can be made.

Fortunately, these rotors were previously tested in the hover mode at the Hughes whirlstand in Culver City. These tests are reported in Reference 17, and the appropriate data are repeated here in Figure 14.

Figure 14 presents the performance comparison of the three planforms, out of ground effect, with the $A_2 = 0$ swashplate. The triangular and tricusped wings, with the same tapered blades, sustain the parabolic nature of the curves to higher thrust coefficients than does the trisector wing with its

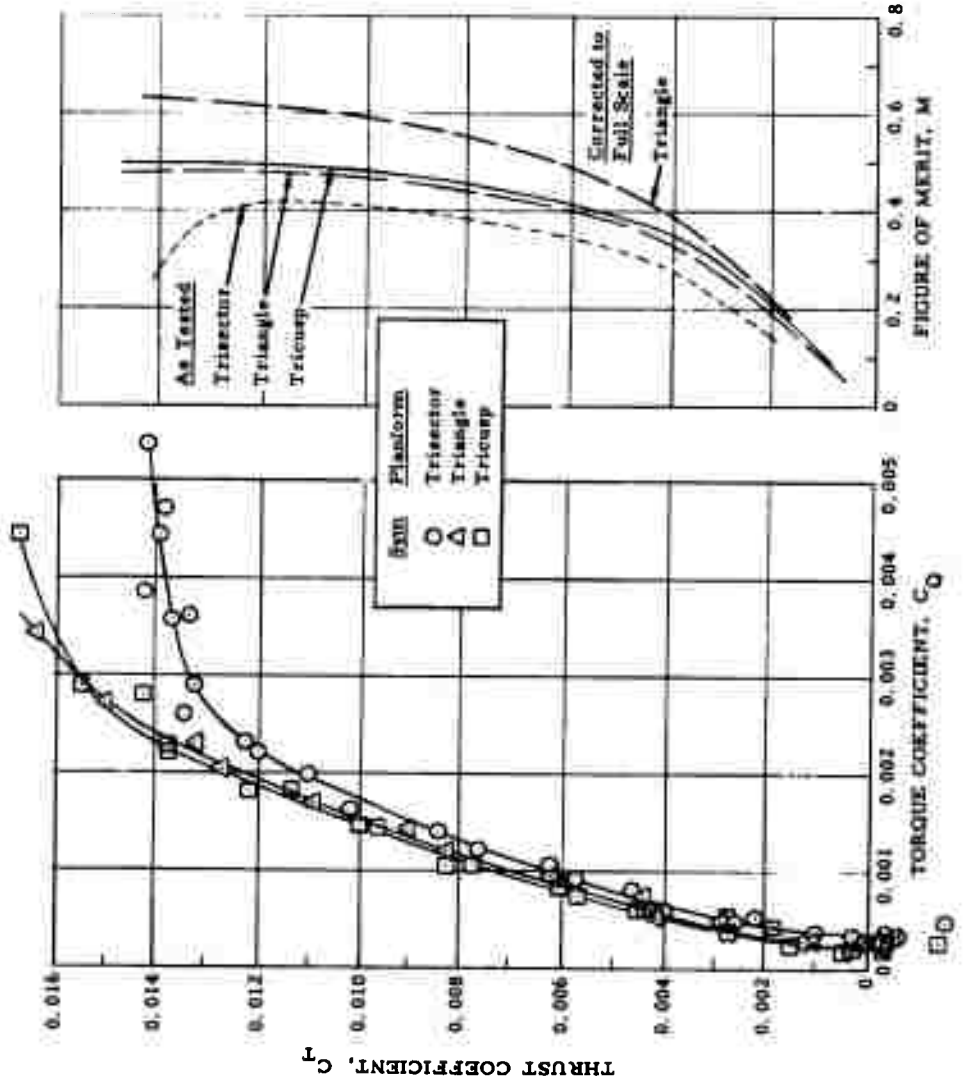

Figure 14. Effect of Rotor/Wing Planform on Hover Performance

narrow, straight blades. The coefficients shown on the figure are based on total disc area, but, since all three configurations have the same swept annulus area, coefficients based on this parameter will present the same relative picture. For the three configurations to produce equal thrust, the trisector blades, which have lower solidity, have to operate at a higher blade lift coefficient, and, as thrust is increased, these blades will stall earlier than the tapered blades. This is suggested by the break that occurs in the trisector curve (circle symbols) of Figure 14 above $C_T = 0.012$.

The following comparison among the three planforms will be restricted to the region of the curves below blade stall. Figure 14 shows that the tricusped Rotor/Wing performs slightly better than the triangular shape in the hover flight mode. At all torque coefficients, the tricusped wing exhibits 4 or 5 percent more thrust for the same power. The maximum figures of merit of the two model rotors are 0.502 and 0.480, again in favor of the tricusped planform.

An empirical method of extrapolating model hover data to full-scale characteristics was developed during the Rotor/Wing Series I whirlstand tests. Essentially, the correction is the product of the measured whirlstand data for the Rotor/Wing blades and the ratio of full-scale data using NACA 0015 blades to model test data with the same blade sections. Additional small Reynolds number corrections apply to the torque required to drive the wing. The figure of merit plot of Figure 14 shows the triangular wing extrapolated to full-scale where the maximum M equals 0.63. The tricusp and trisector rotors will show essentially the same full-scale relationships to each other as they do in model-scale.

As tested, both the tricusp and triangle wings are significantly better than the trisector planform with its straight, narrow-chord blades. A more realistic comparison is shown in Figure 15, where the model data for the

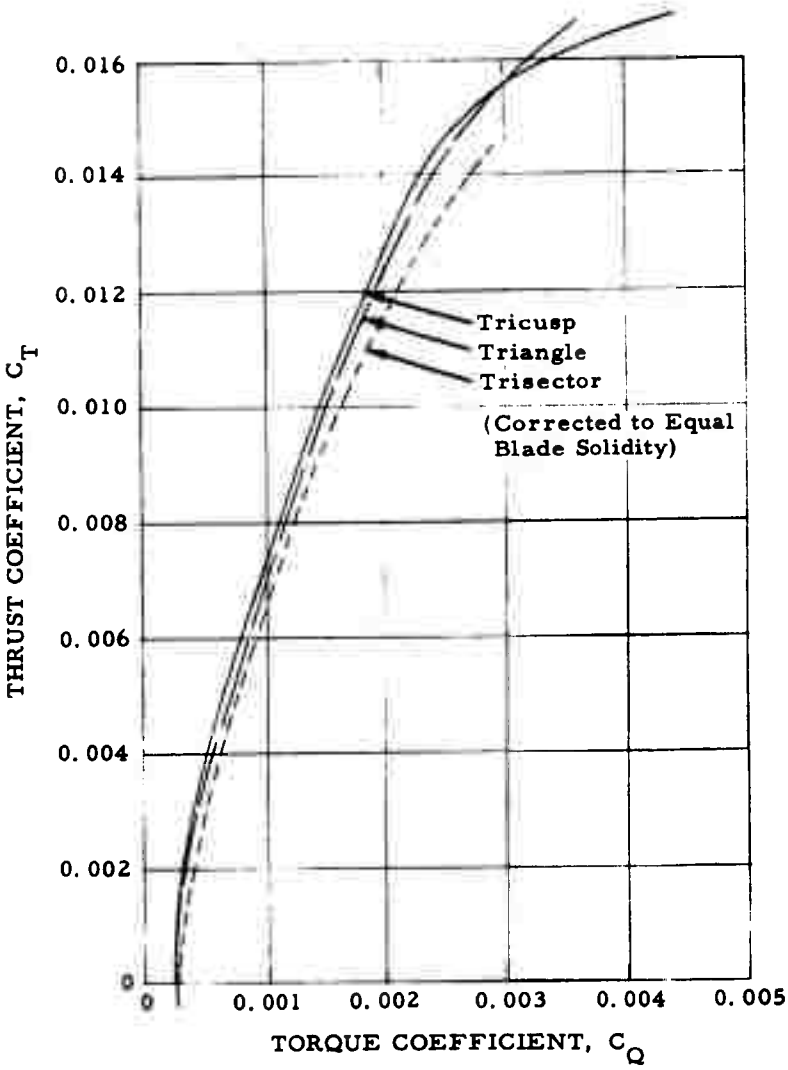

Figure 15. Rotor/Wing Hover Performance

trisector wing has been corrected for blade solidity so that differences in performance are due to wing planform only. Again, the tricusp planform is 4 or 5 percent better than the triangle and some 12 to 13 percent better than the trisector planform. This difference in hover performance is attributed directly to the torque required to drive the wings, which, in turn, is related to the wing's area.

While the tricusp planform exhibits superior hover performance compared with the other planforms tested, other factors such as the wing area required to support the aircraft during transition must be considered before a final planform selection can be made.

There can be no direct comparison with the hover data obtained in the DTMB 7-by-10-foot tunnel, because the model in that tunnel was less than one diameter from the tunnel ceiling; additionally, the tunnel wall constraints induced a considerable airflow around the tunnel circuit.

The control power in hover for pitch- and roll-cyclic-control inputs is plotted in Figure 16. The pitching- and rolling-moments for 5-degree cyclic-pitch inputs are almost identical for the three rotors.

POWERED MODEL - HELICOPTER MODE

TEST DATA COMPARISON - SAME MODEL IN TWO WIND TUNNELS

It has been shown by several studies, such as that reported in Reference 5, that the testing of conventional rotor models may be accomplished satisfactorily in relatively small wind tunnels if the rotor does not span more than about 70 percent of the width of the test section, and the rotor advance ratio is 0.15 or higher. Under these conditions, conventional airplane-type tunnel

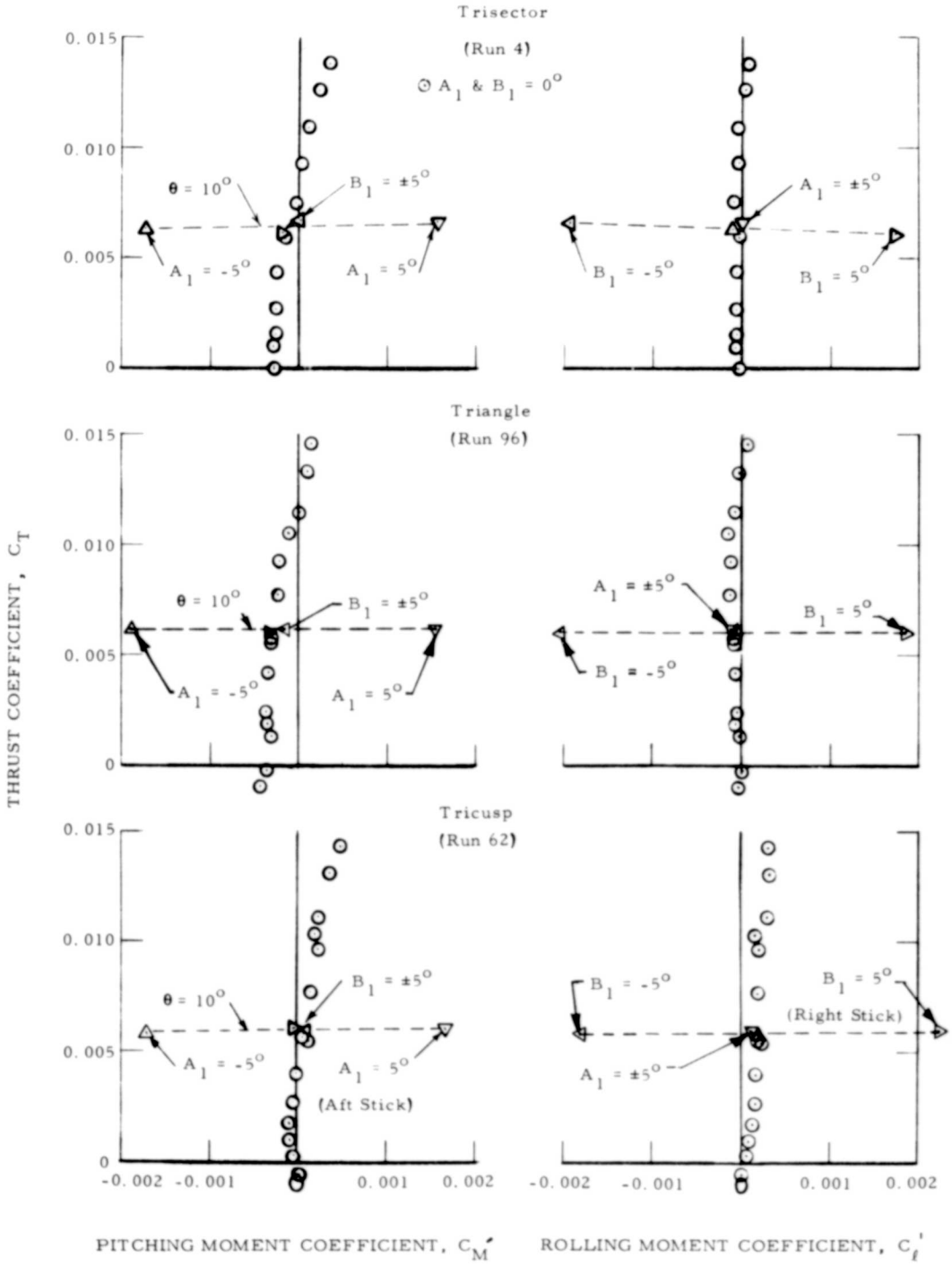

Figure 16. Rotor/Wing Control Power in Hover

wall corrections may be used. The Rotor/Wing model tested in the 8-by-10-foot NSRDC Aerodynamics Laboratory wind tunnel was just at the boundary of this limitation; therefore, a major purpose of the present tests was to compare data obtained from the same model in the two tunnels.

Comparisons of the data are made for the trisector planform Rotor/Wing for three rotor advance ratios: 0.15, 0.25, 0.35.

At $\mu = 0.15$, Figure 17, a point-by-point comparison is not possible, because comparable test conditions were not measured in both tunnels; however, the comparison by inference outlined below shows good agreement. At NSRDC, Series II, the model had to be operated at 1000 rpm because of a tunnel speed limit; at LRC, Series VI, the rotor speed was held to 600 rpm to avoid resonances in the model support. NSRDC tests were made with a 2-per-rev cyclic input of 0 degrees while the tests at LRC were made only for 2.5 degrees of 2-per-rev cyclic pitch. Examining Figure 26 for the aerodynamic characteristics of the triangle wing at $\mu = 0.15$, it is seen that the effect of A_2 is negligible on the external aerodynamic characteristics of the Rotor/Wing, and the implication then is that the difference in A_2 for the two tests shown in Figure 17 may also be considered negligible. The differences would then be attributable to rotor-speed or tunnel-wall effects.

The effect of rotor speed would be expected to influence the rotor-torque coefficient to the greatest extent with the slower-turning LRC rotor having the greater torque coefficient because it operates in a lower Reynolds number environment where the blade section drag coefficients should be higher. The lift of the blades would not be appreciably changed by Reynolds number in the range involved. This, indeed, is the result of the comparison: little change

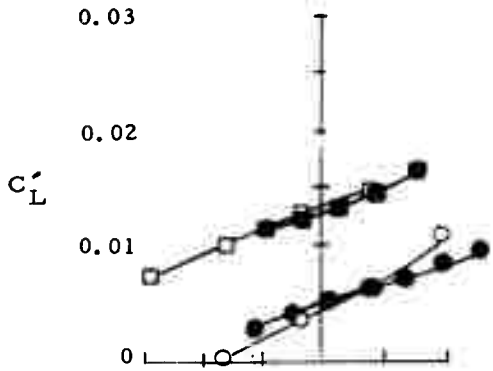

Trisector Wing

μ0.15, $A_1 = 0^o$

Tail-Off

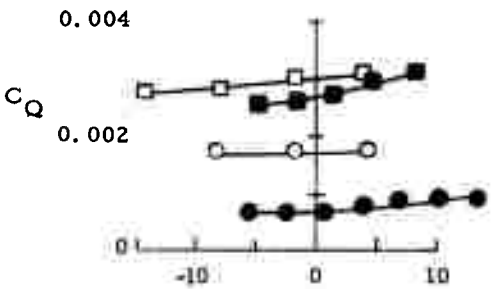

○ $\theta = 5^o$

□ $\theta = 15^o$

Open LRC Series VI

$A_2 = 2.5^o$, 600 rpm

Solid NSRDC Series II

$A_2 = 0^o$, 1000 rpm

α – DEGREE

Increase α for Series VI by 3 degrees.

Figure 17. Helicopter Flight, Trisector Wing, $\mu = 0.15$

in lift coefficient, but a large increase in torque coefficient at the low rotor speed.

The data thus appear to agree fairly well except for a shift of the LRC Series VI data in the negative angle of attack direction. There appears to be a consistent discrepancy of approximately 3 degrees in the model angle of attack in the 30-by-60-foot tunnel. Confirmation of this condition could not be investigated, because it was discovered long after the model had been removed from the tunnel. The same angle shift shows up throughout all the test data where comparisons may be made: powered rotor and unpowered rotor, both autorotating and stopped (the specific comparisons will be pointed out below). The data appear to be consistent within the Series VI tests, but include this fixed angle of attack incident.

NOTE

All angle of attack values given for the Series VI tests must be increased by 3 degrees from the plotted values.

Direct comparisons are made of the aerodynamic test data for the trisector Rotor/Wing from the two tunnels for advance ratios of 0.25 and 0.35 in Figures 18 and 19. Here the tests were conducted at rotor speeds of 600 rpm and it is seen that good agreement exists for lift, torque, pitching moment, and lateral cyclic pitch control, except for the negative 3 degree shift in the angle-of-attack values of the LRC data, as compared with the NSRDC data.

A comparison between the control power measured in the two tunnels is shown for the trisector configuration in Figure 20. Here, for a condition near level flight at $\mu = 0.25$, 5-degree inputs of A_1 and B_1 cyclic pitch from the basic trim condition are applied. The pitching and rolling moment data are quite comparable.

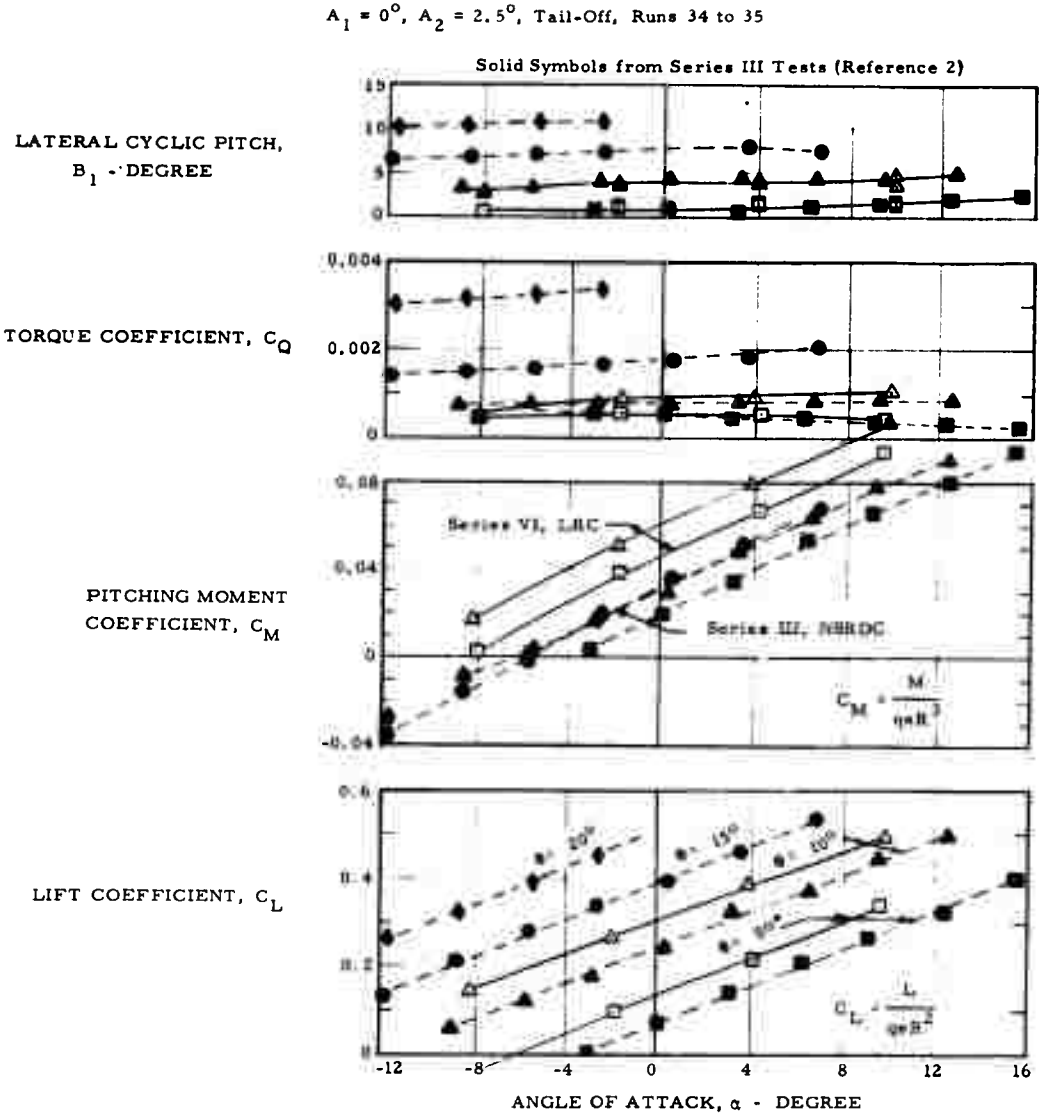

Increase α for Series VI by 3 degrees

Figure 18. Helicopter Flight, Trisector Wing, $\mu = 0.25$

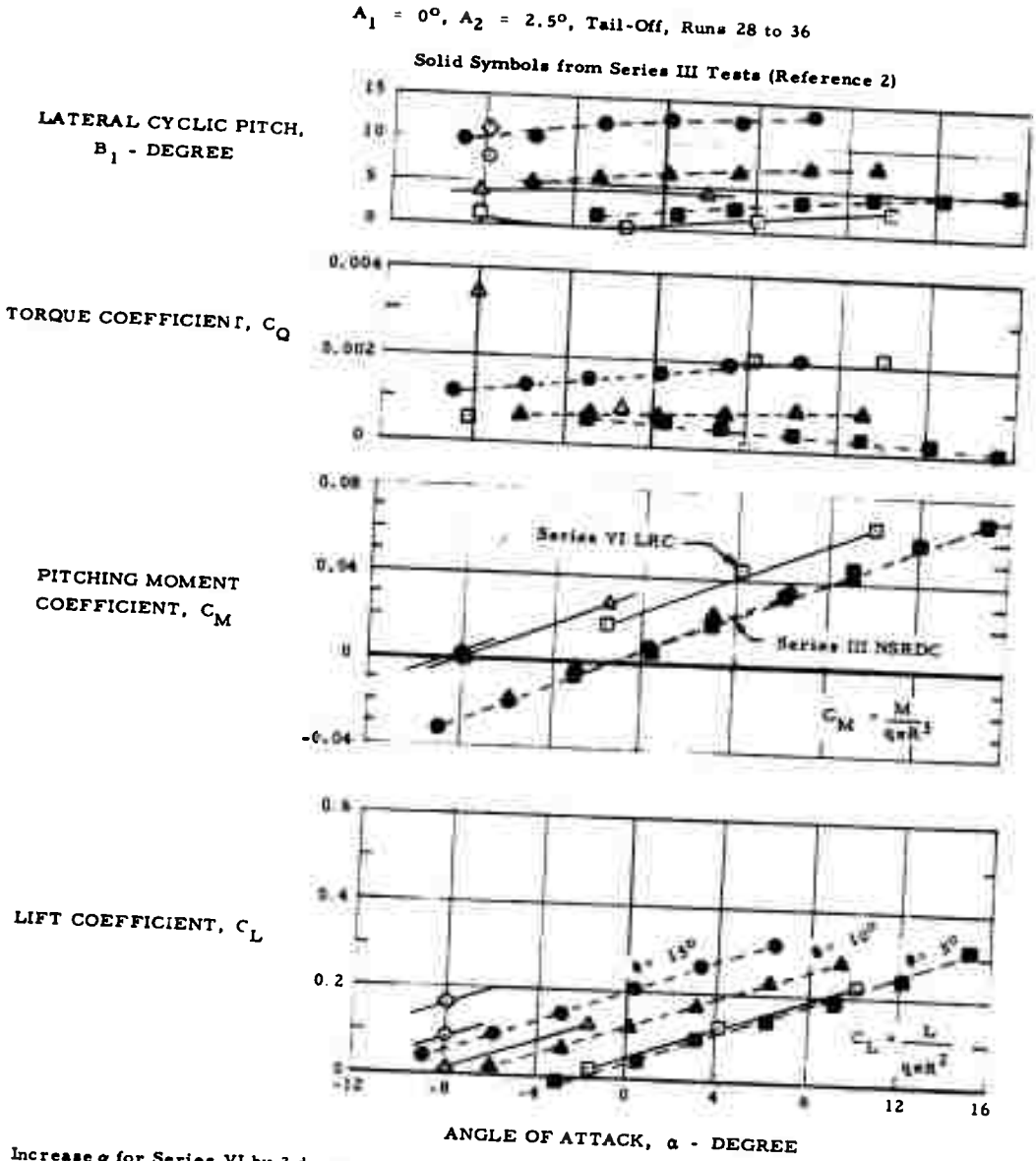

Increase α for Series VI by 3 degrees

Figure 19. Helicopter Flight, Trisector Wing, μ = 0.35

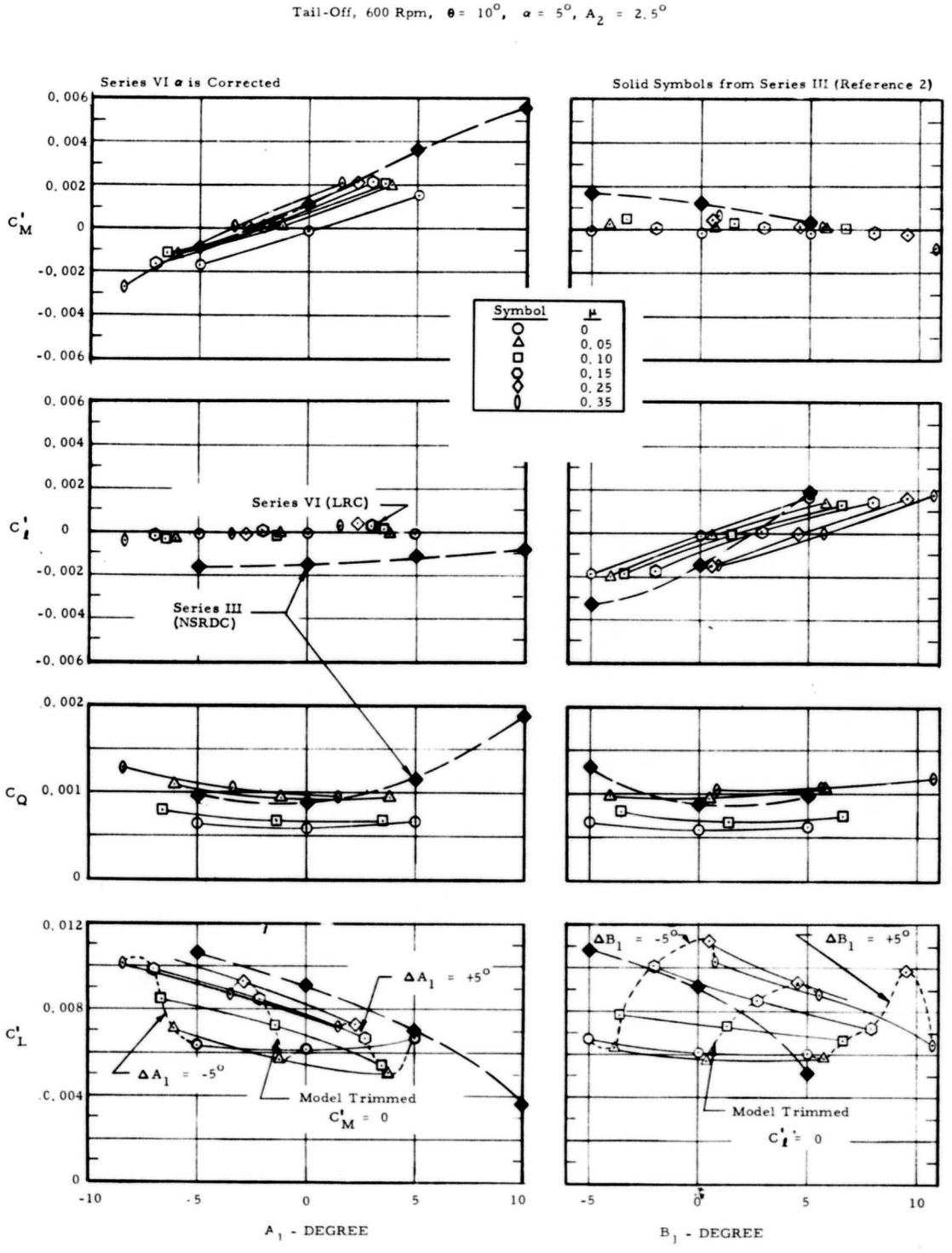

Figure 20. Comparison of Control Power in Helicopter Flight, Trisector Wing

Another comparison between data from tests in the two tunnels is with respect to the blade root and rotor shaft alternating bending of the trisector Rotor/Wing moments. Figures 21 and 22 show these moments made non-dimensional by dividing by rotor lift and rotor radius. The moments were not measured at $\mu = 0.15$, but at the higher advance ratios, the data from the two tests fall within the expected scatter bands. It should be pointed out that in these plots the cyclic pitch angle, A_1, was held at zero degrees because the only comparable data from the NSRDC tests were for this same condition of $A_1 = 0°$. Therefore, there is included a large 1-per-rev component of moment in the shaft bending moment that would not normally be present in trimmed flight. These data are presented only to bolster the comparison of data between the two wind tunnels and should not be taken as indicative of actual Rotor/Wing flight conditions. For a comparison of Rotor/Wing moments with A_1 and B_1 trimmed, see Figures 34 and 35.

Therefore, the two test series confirm that the 8-by-10-foot NSRDC subsonic wind tunnel is satisfactory for testing this particular powered rotary-wing configuration in models up to 86 inches diameter at advance ratios of 0.15 or greater when regular airplane type boundary corrections are applied. This reaffirms the observation of Reference 5 that powered rotor models that span no more than 70 percent of the test section and operate at advance ratios of 0.15 or more may be tested satisfactorily, using regular boundary corrections.

TEST DATA COMPARISON - THREE MODELS IN LRC 30-BY-60-FOOT WIND TUNNEL

The trisector, tricusp, and triangular Rotor/Wings were tested in sequence in the LRC full-scale tunnel at rotor advance ratios from 0 (hover) to 0.35 (maximum helicopter flight speed). All tests were made at a constant rotor speed of 600 rpm and the airspeed was varied to accomplish the desired advance ratio. For these tests the $A_2 = 2.5°$ swashplate was installed; $A_2 = 0°$

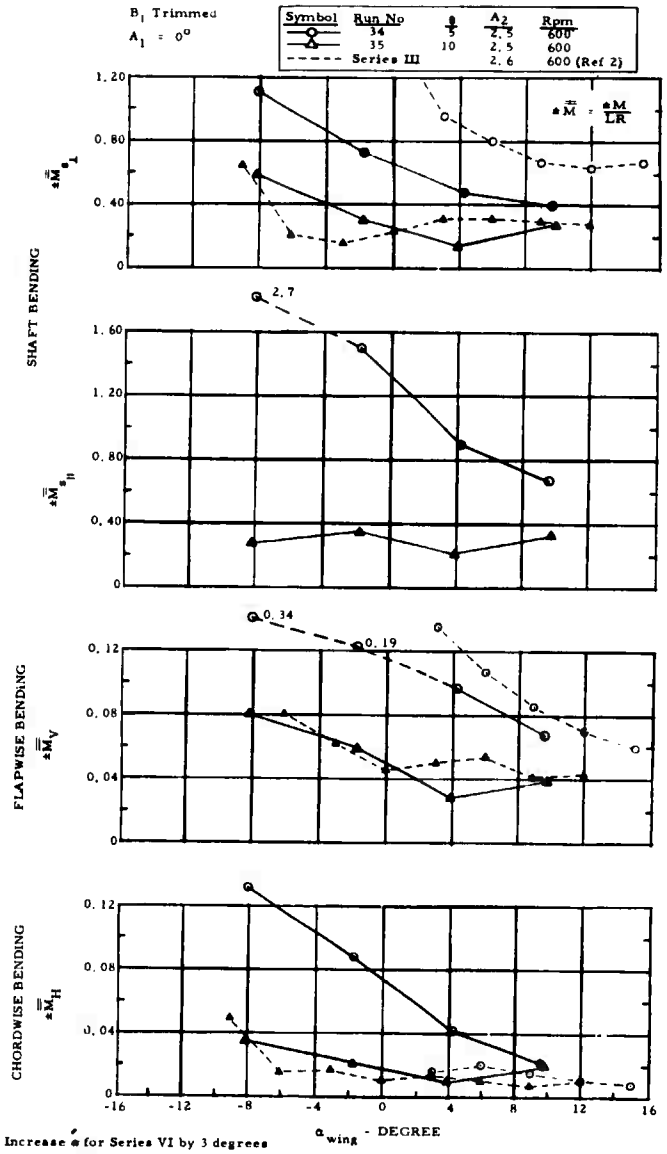

Figure 21. Alternating Blade Root and Shaft Bending Moments in Helicopter Flight, Trisector Wing, $\mu = 0.25$

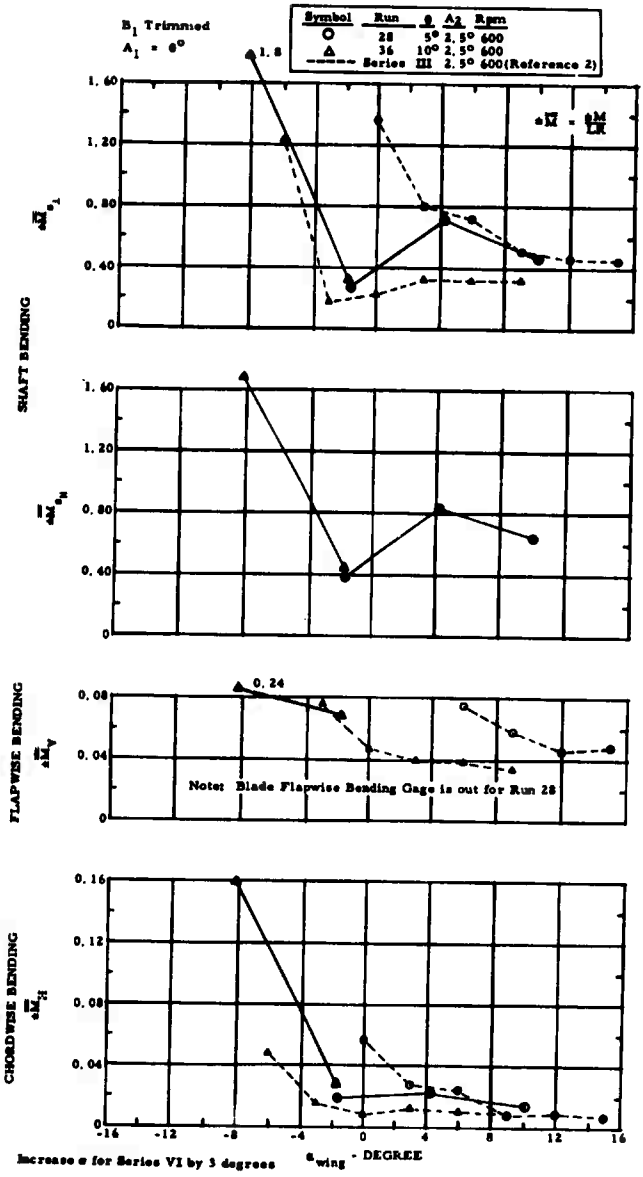

Figure 22. Alternating Blade Root and Shaft Bending Moments in Helicopter Flight, Trisector Wing, μ = 0.35

was tested in the triangle Rotor/Wing only. The horizontal tail was off for the basic tests, and the model's pitching and rolling moments about the model moment center were trimmed to zero by application of A_1 and B_1 cyclic pitch for most of the test points.

Figures 23 through 25 show the aerodynamic characteristics of the three Rotor/Wings. There is little difference between the performance of the triangle and tricusp rotors; both produce approximately the same lift for a given rotor torque at equivalent collective pitch and angle of attack. The trisector rotor produces less lift at the same angles of collective pitch and angle of attack, but also requires less torque. On a basis of (thrust coefficient/torque coefficient) for steady 1 g flight at the design gross weight condition, all three Rotor/Wing planforms are nearly identical.

The effect of second harmonic cyclic-pitch input on the aerodynamic characteristics is shown in Figure 26 for $A_2 = 0°$ and $A_2 = 2.5°$. Lift is affected only very slightly.

Control power in pitch and in roll throughout the helicopter flight speed range is shown in Figures 20, 27, and 28 for the three rotors, beginning from a point near trimmed level flight. Little cross-coupling between pitch and roll for this rigid model that is held rigidly on the support strut is evident, and there is practically no change in the level of moment per degree of cyclic-control input over the advance ratio range from $\mu = 0$ to 0.35; there is essentially no change in the control power going from one configuration to the others.

Tests were made with the trisector Rotor/Wing to ascertain the effects on rotor characteristics when the A_1 cyclic pitch was adjusted to trim the longitudinal pitching moment to zero, or was set at zero cyclic pitch. Figure 29 shows the comparison. When the pitching moment was trimmed to zero,

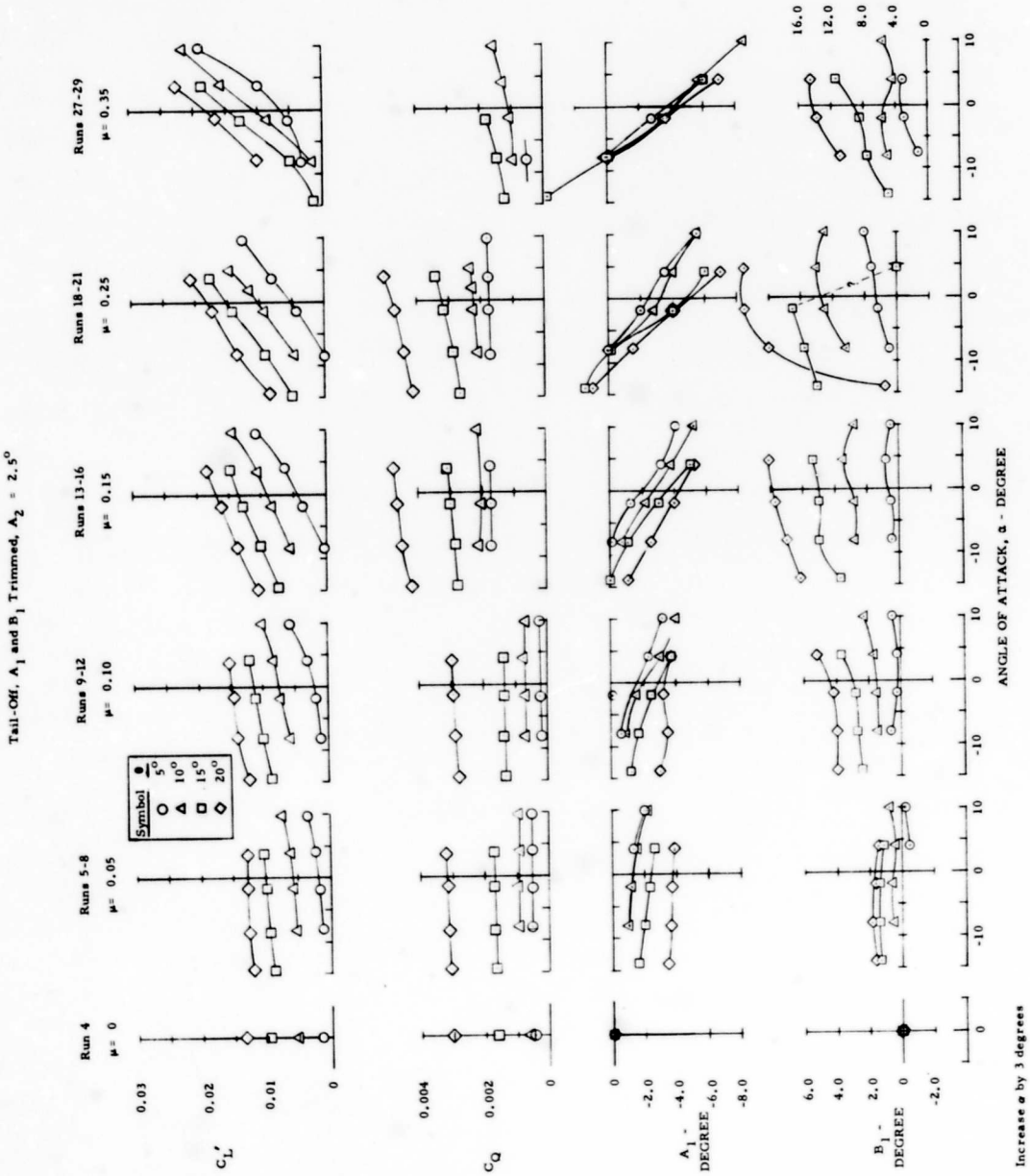

Figure 23. Helicopter Flight, Trisector Wing

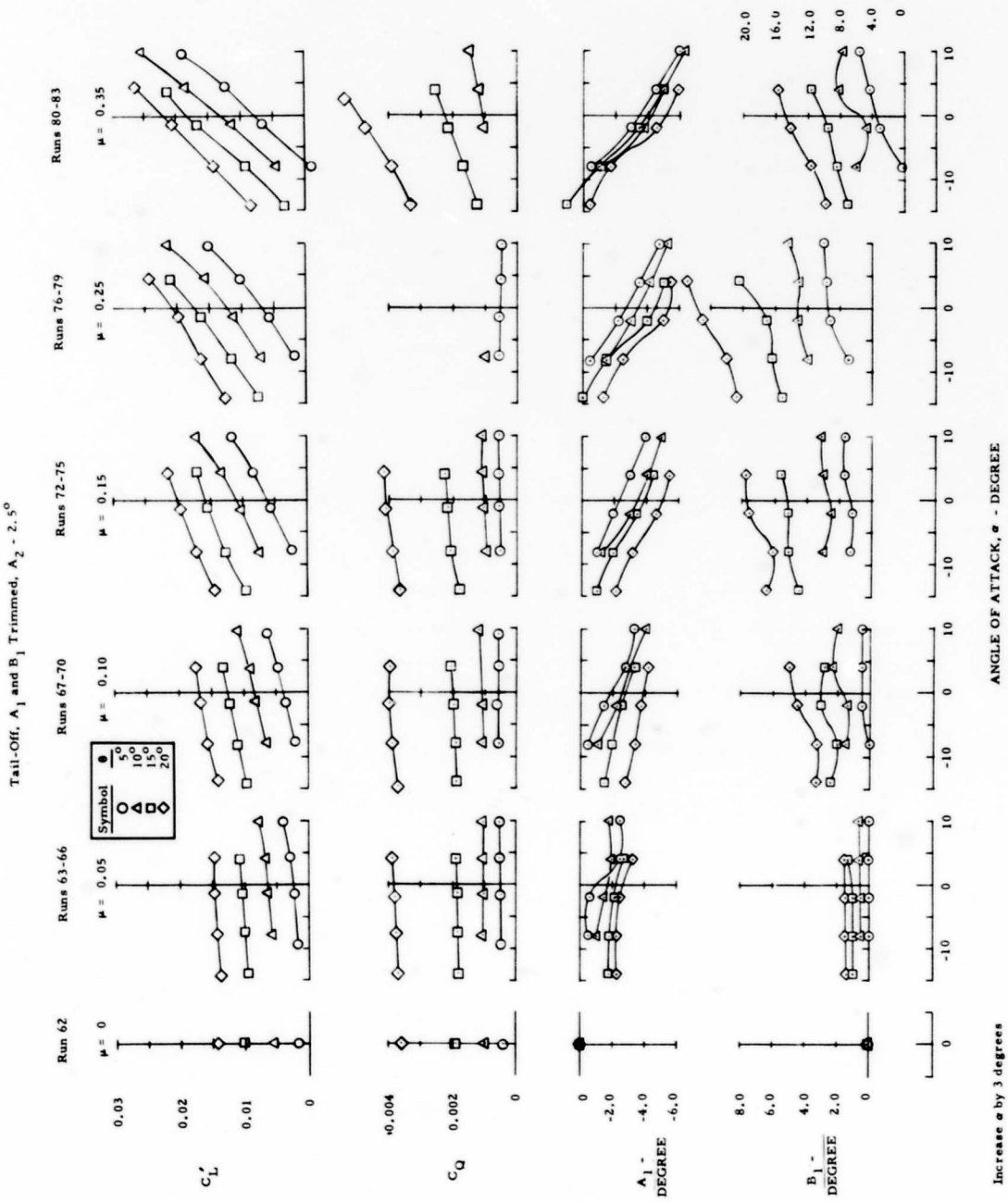

Figure 24. Helicopter Flight, Tricusp Wing

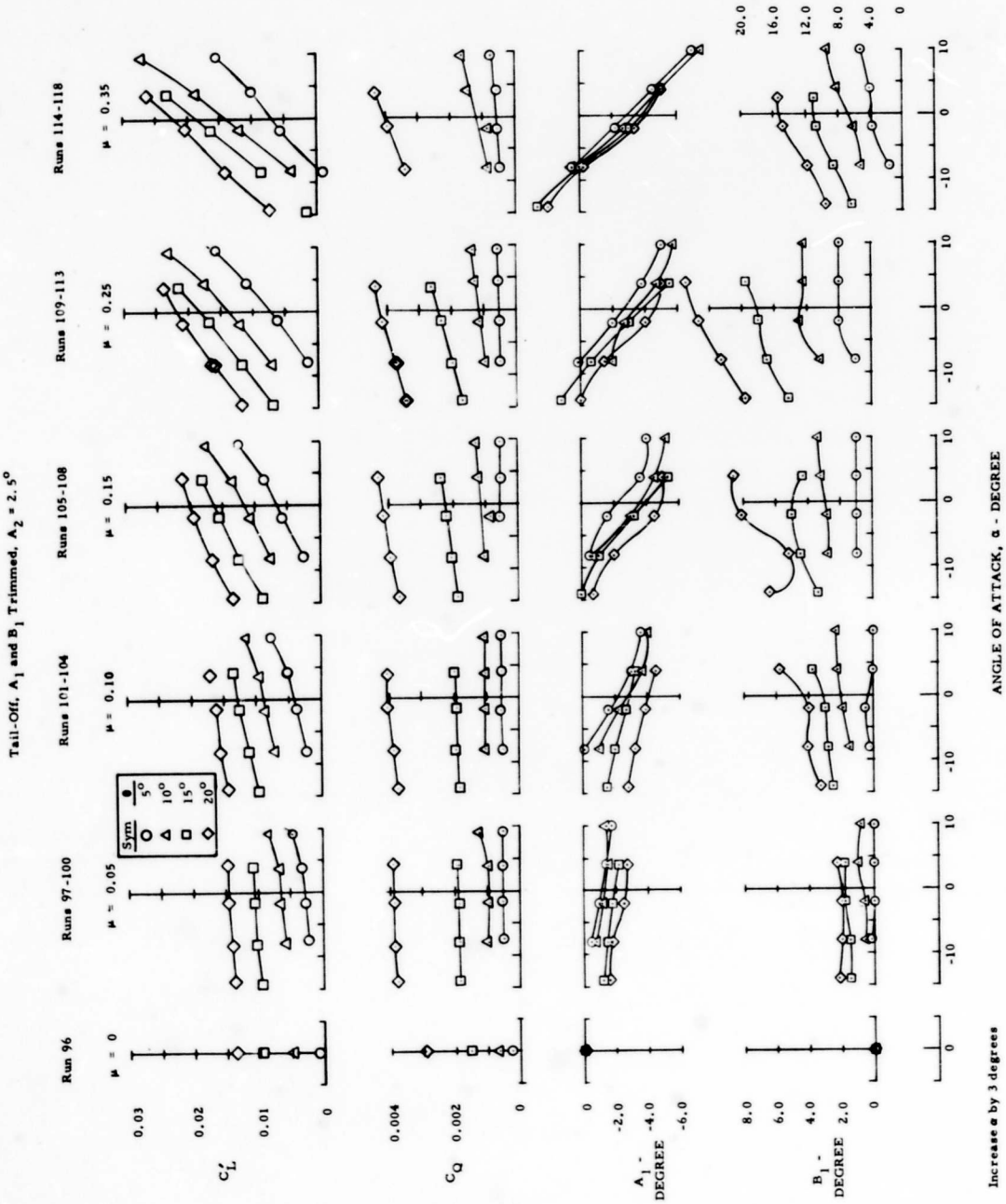

Figure 25. Helicopter Flight, Triangle Wing

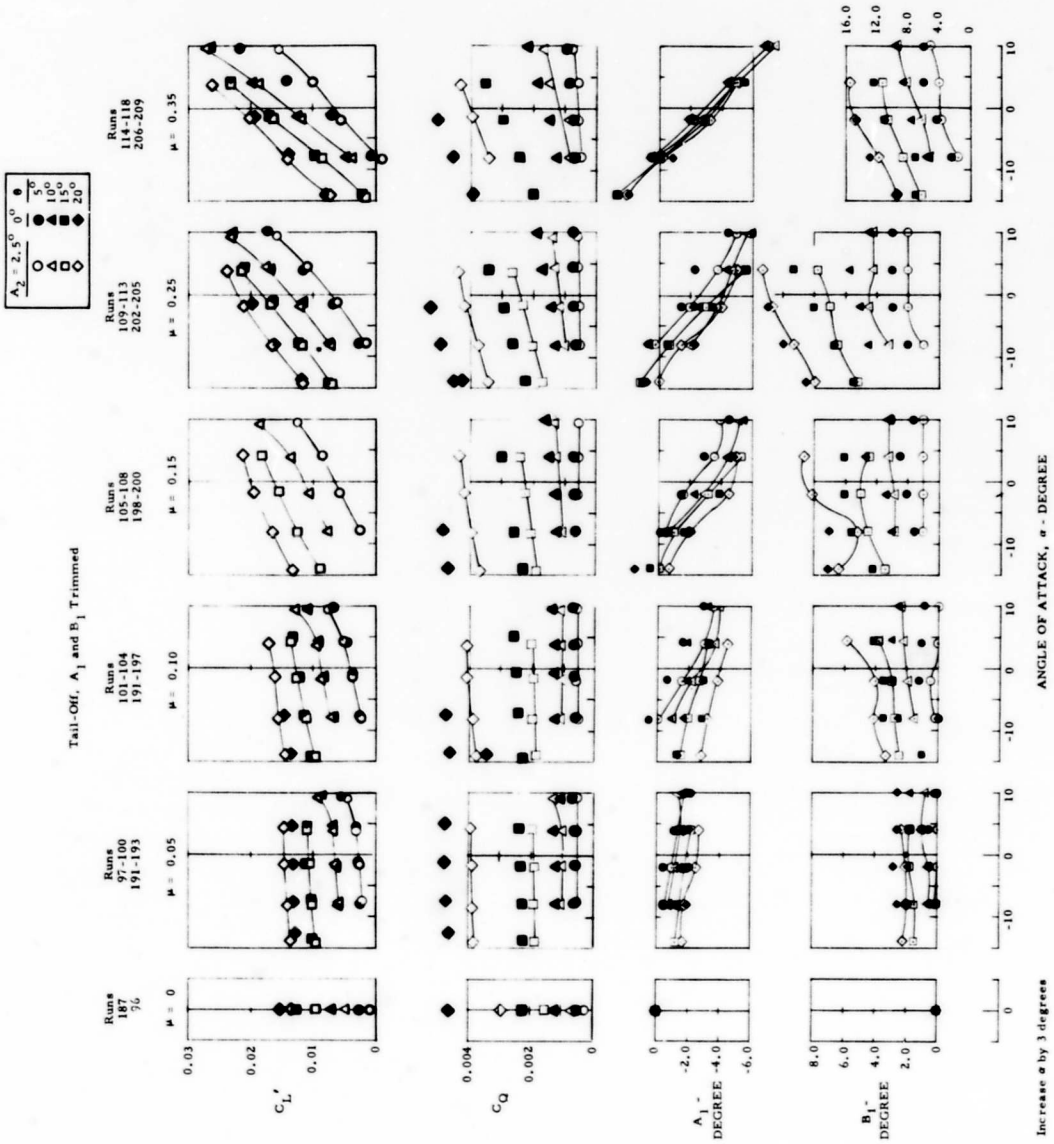

Figure 26. A_2 Effectiveness, Helicopter Flight, Triangle Wing

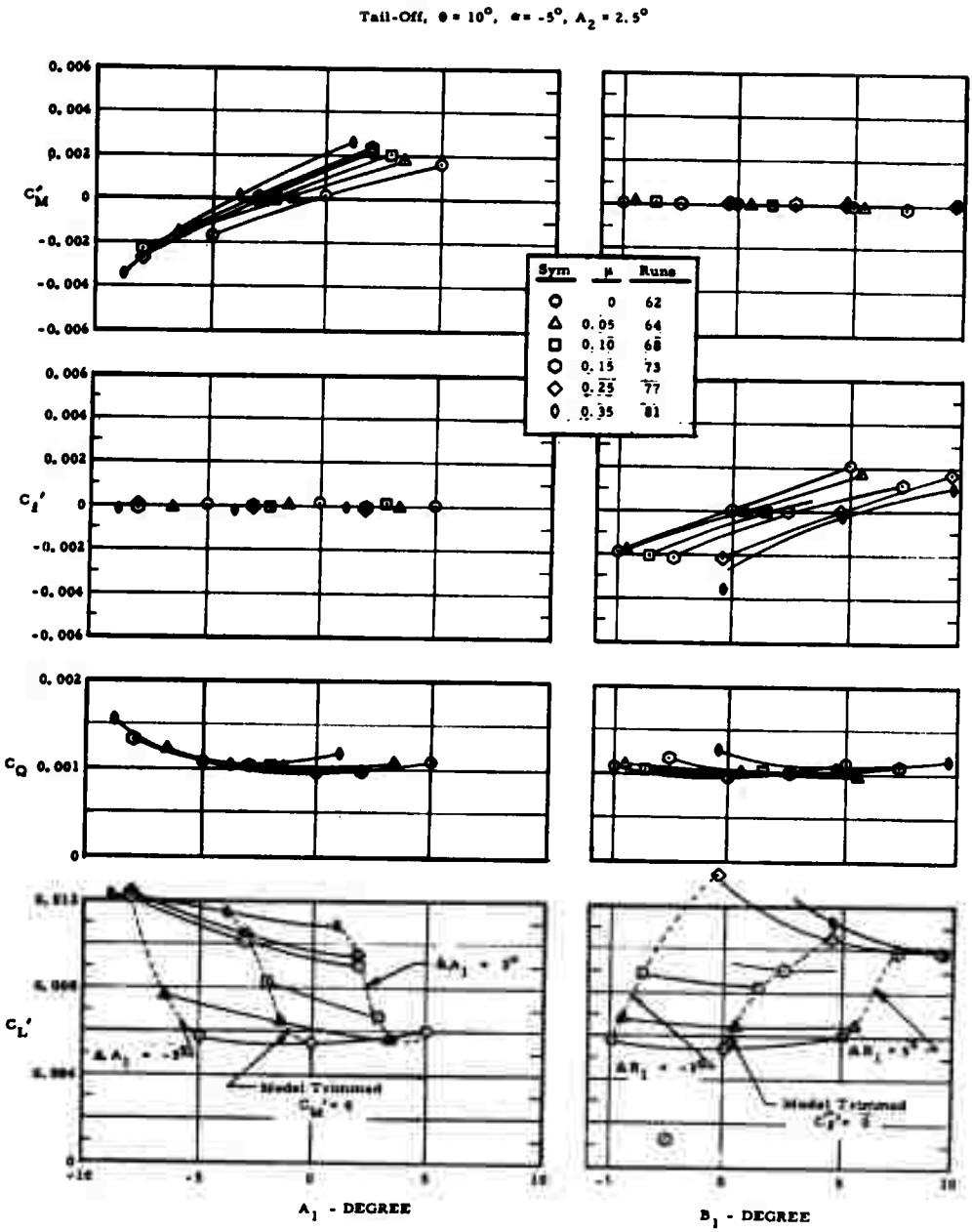

Figure 27. Control Power, Helicopter Flight, Tricusp Wing

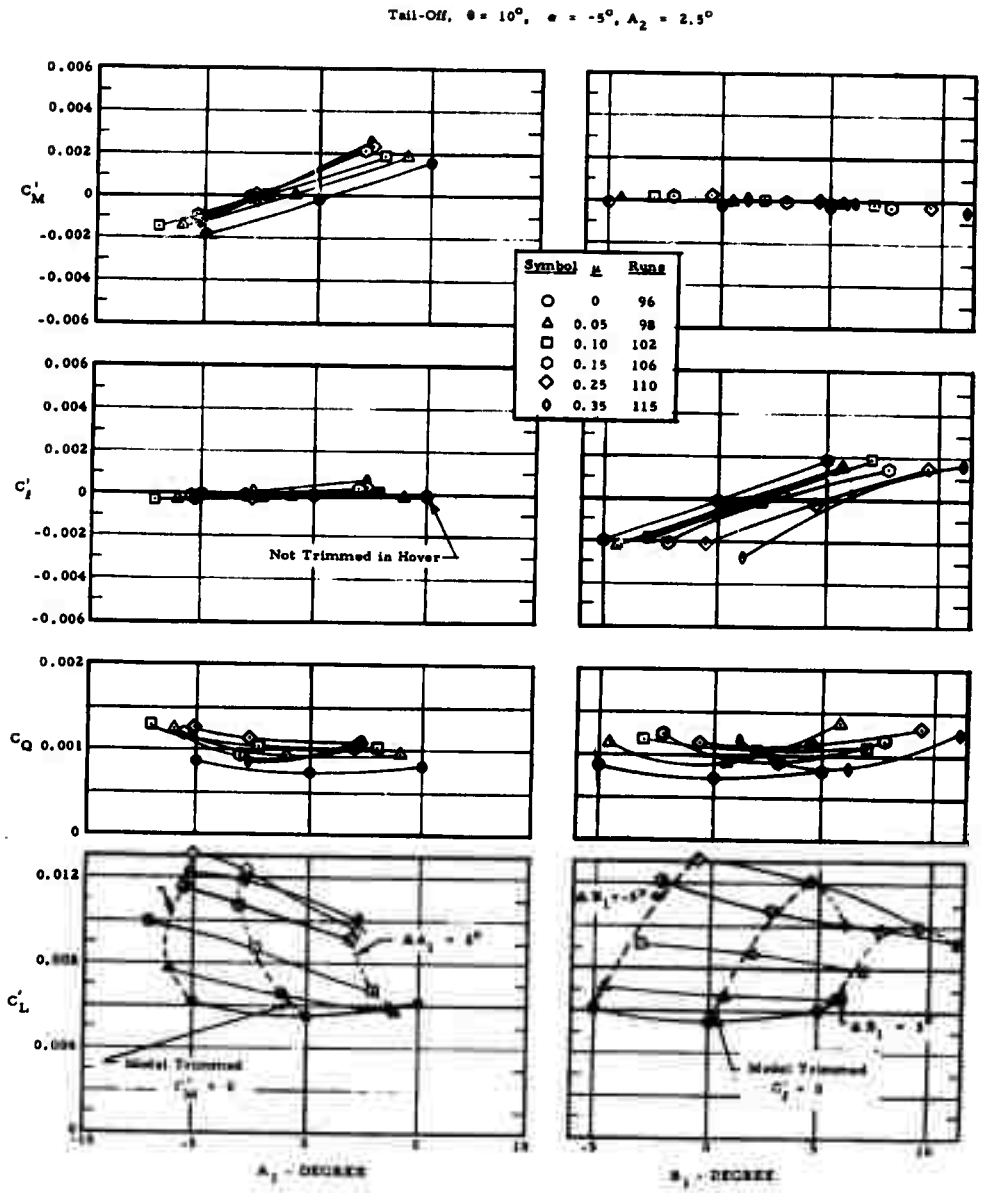

Figure 28. Control Power, Helicopter Flight, Triangle Wing

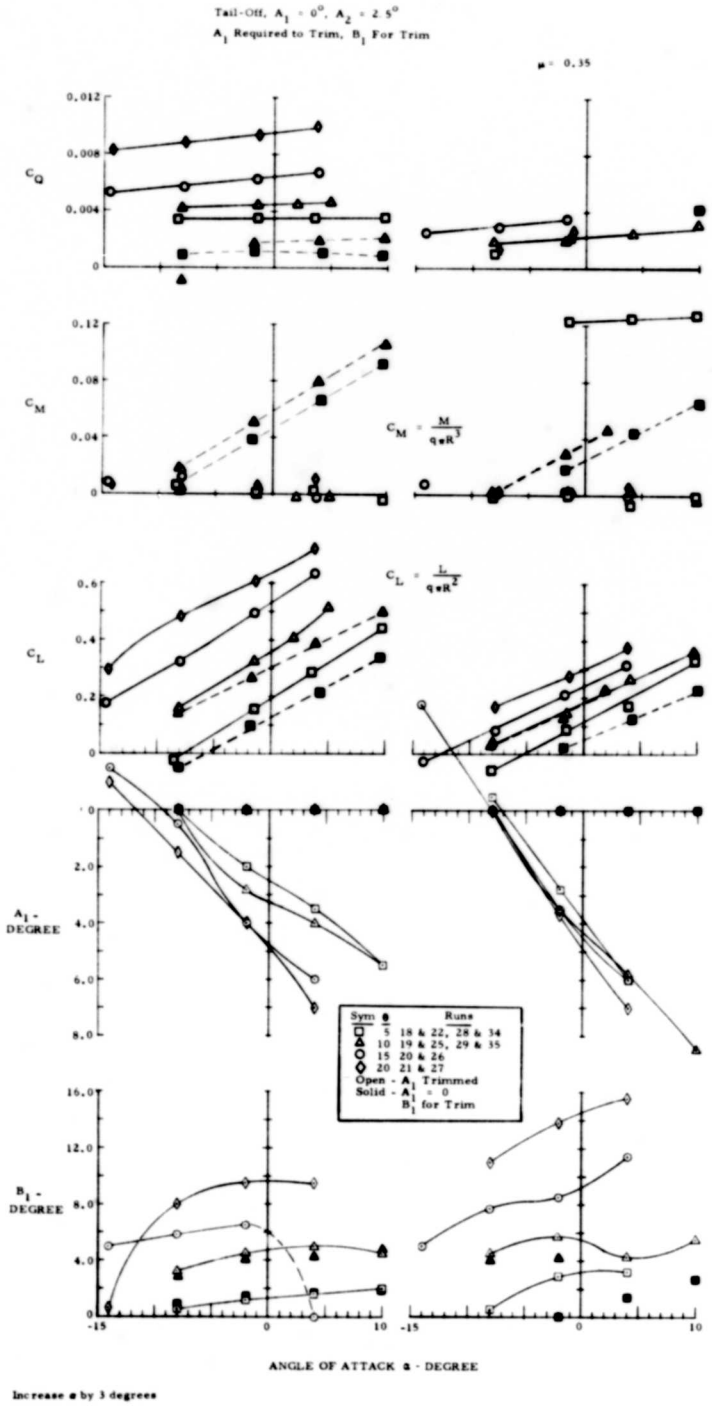

Figure 29. Helicopter Flight, Trisector Wing

the Rotor/Wing developed greater overall lift, but also required the input of higher torque.

The effectiveness of the horizontal tail was measured in forward flight for the triangle Rotor/Wing. Figures 30 through 32 show the results of these tests for μ = 0.15, 0.25, and 0.35, respectively. The tail effectiveness increases with advance ratio as would be expected. In comparison with the tail effectiveness measured in the Series II and III tests at NSRDC, the present tail is about 20 percent more effective than the tail mounted on the top of the vertical tail, and about 30 percent more effective than a smaller horizontal tail mounted near the mid-span of the vertical.

Peak-to-peak rotor shaft bending moments and blade root bending moments were measured for the three Rotor/Wing configurations. These moments are made non-dimensional by dividing the moment by rotor lift and rotor radius. Because the lift can go through zero for some combinations of α and θ, the non-dimensional moments can appear quite large; however, these conditions are never reached in normal flight. In a similar vein, the non-dimensionalized moments tend to decrease with increasing collective pitch and/or angle of attack because of the increase in lift for these conditions. This means that although the moments increase with α and θ, they do not increase as rapidly with these angles as the lift does. A more meaningful assessment of rotor shaft bending moments is presented in Table 2 where harmonic analyses are reported for Rotor/Wing steady level flight cases. In these, a better idea of the actual moments to be expected inflight may be had.

All rotors incorporated the A_2 = 2.5° cyclic pitch input, and the triangle Rotor/Wing was also tested with A_2 = 0° for comparison. In comparison, Figures 33 through 41 show that the rotor shaft oscillating bending moments are quite comparable for all three rotors when A_2 = 2.5°. For all conditions the model rolling and pitching moment was trimmed to zero by cyclic pitch.

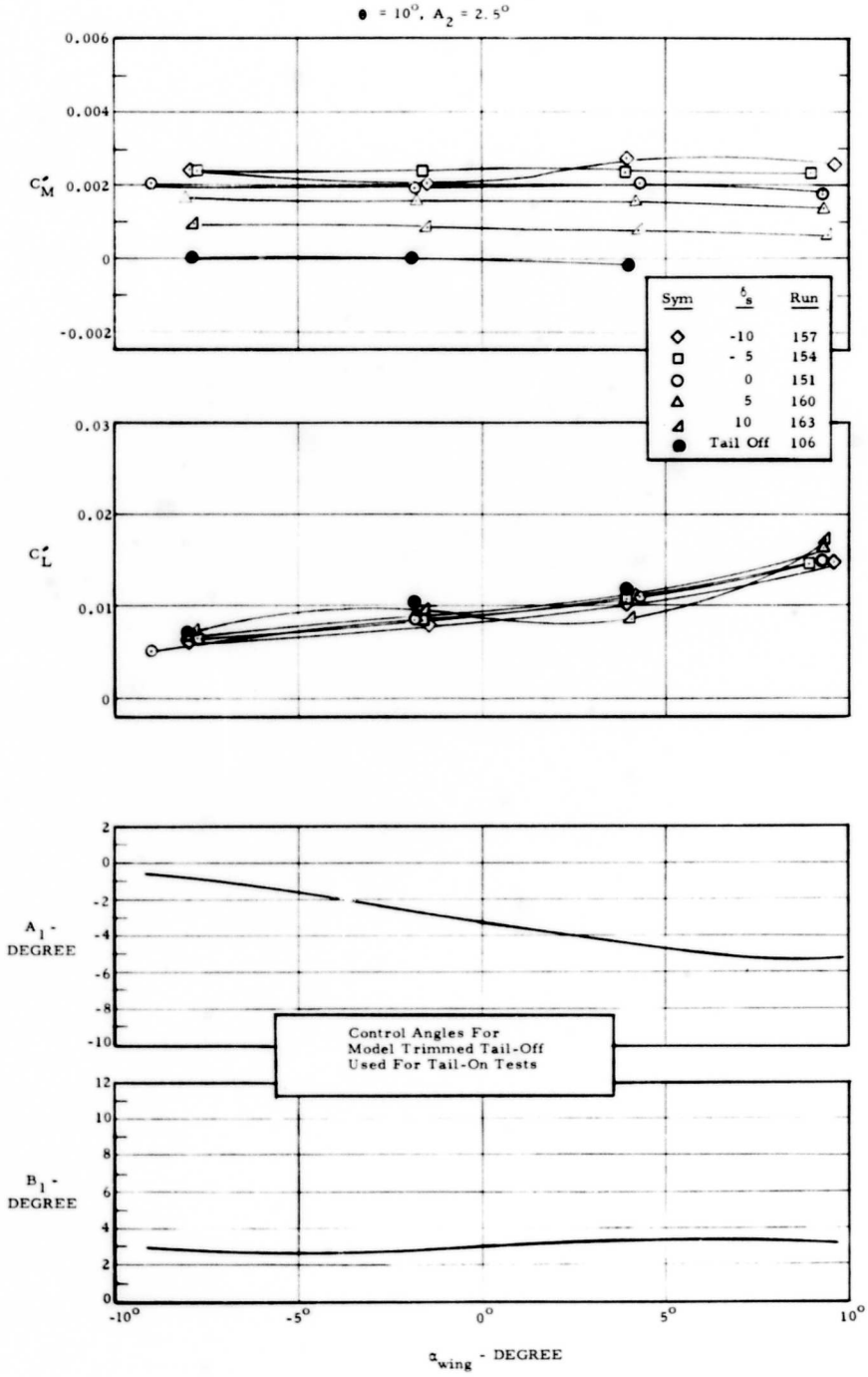

Increase α by 3 degrees

Figure 30. Tail Effectiveness in Helicopter Flight, Triangle Wing, μ = 0.15

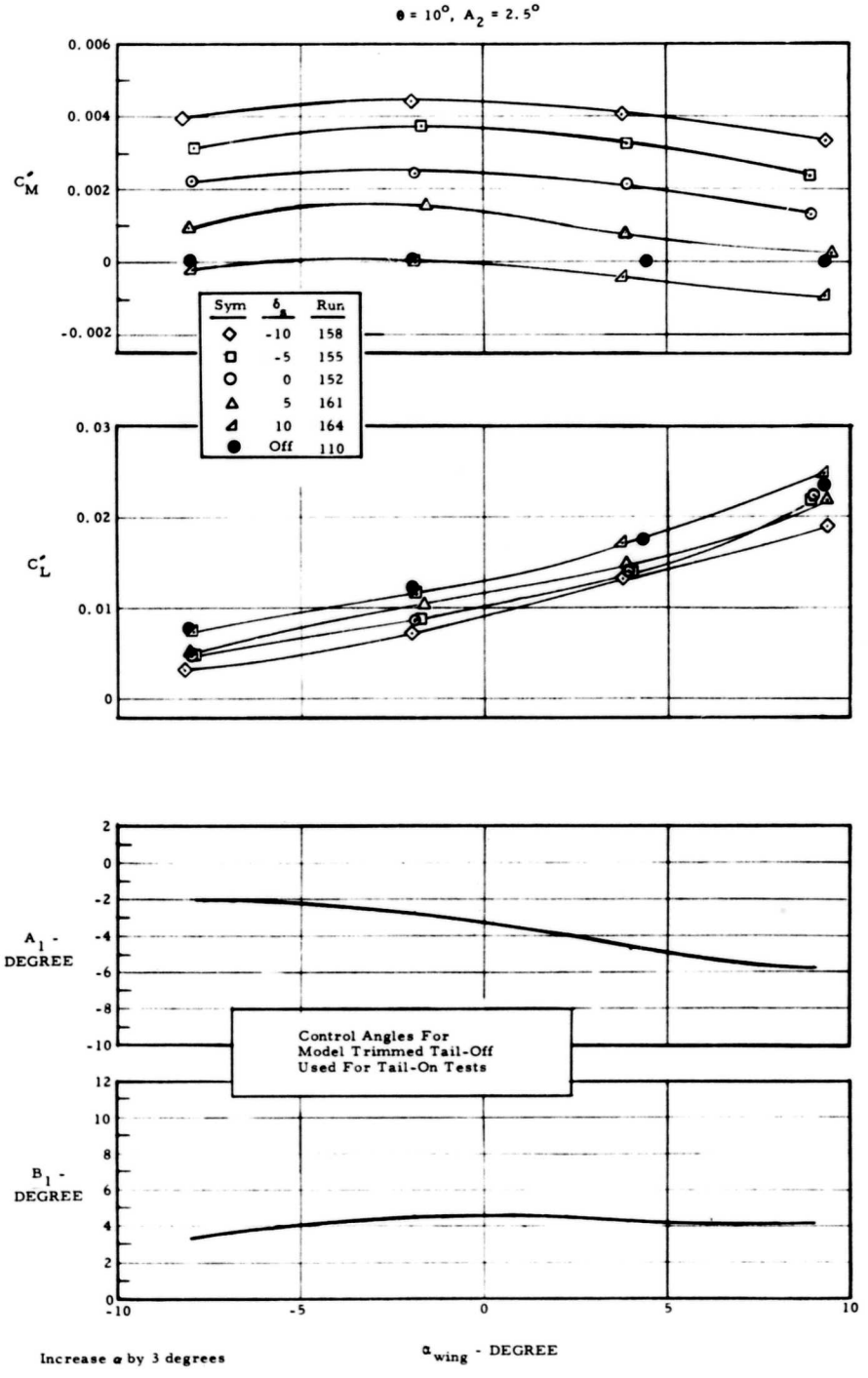

Figure 31. Tail Effectiveness in Helicopter Flight, Triangle Wing, μ = 0.25

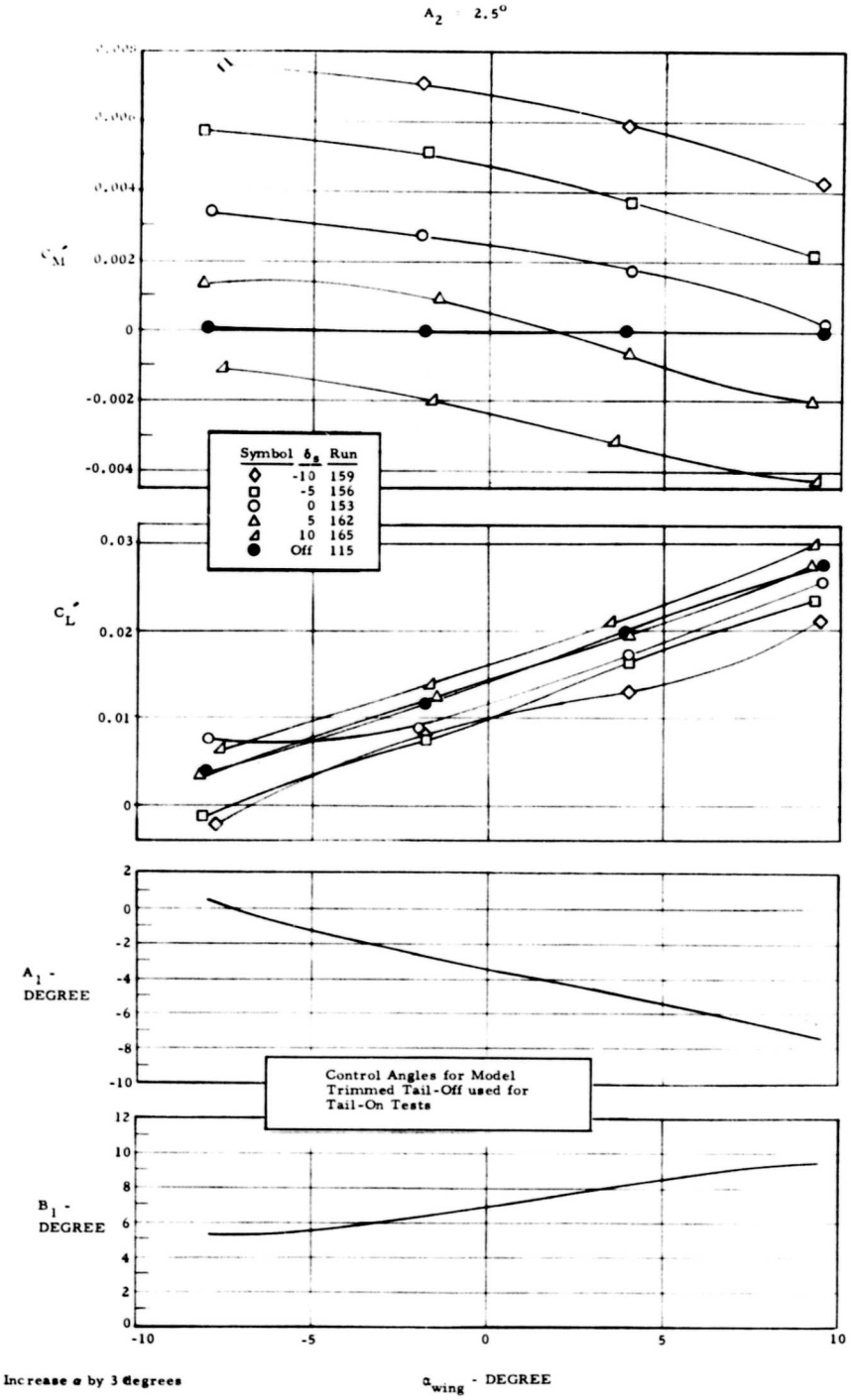

Figure 32. Tail Effectiveness in Helicopter Flight, Triangle Wing, μ = 0.35

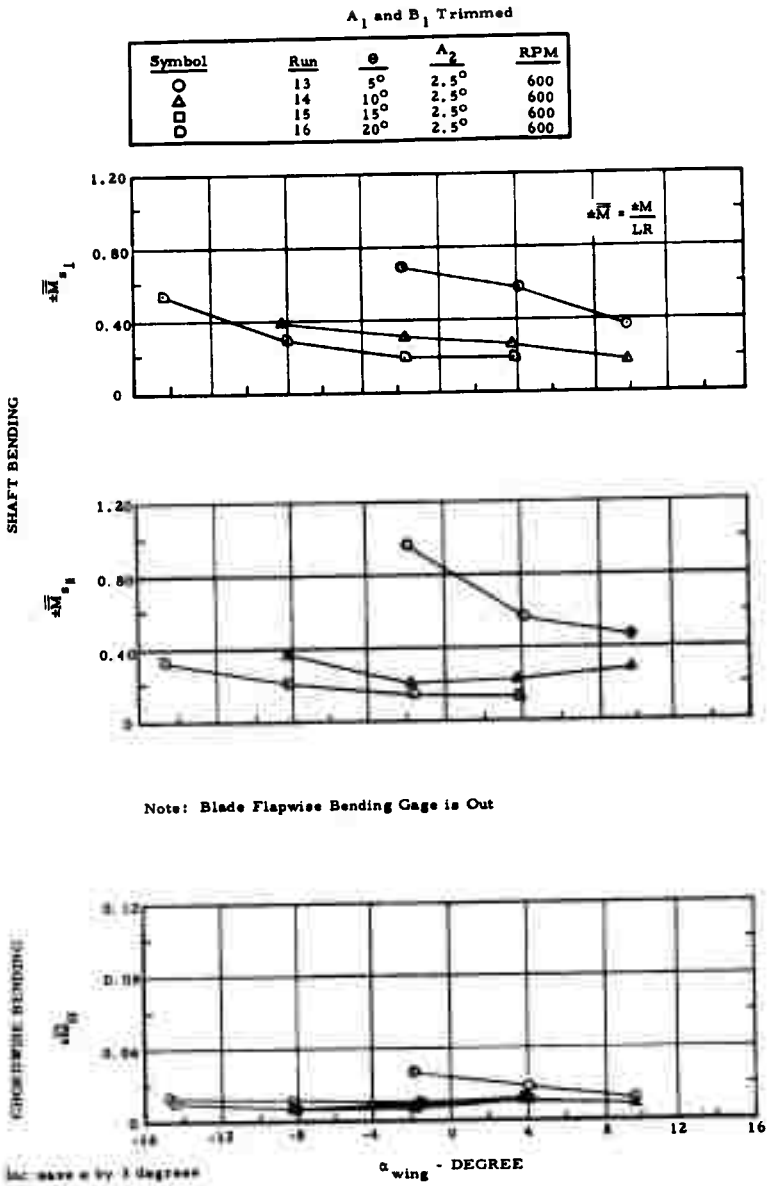

Figure 33. Alternating Blade Root and Shaft Bending Moments in Helicopter Flight, Trisector Wing, μ = 0.15

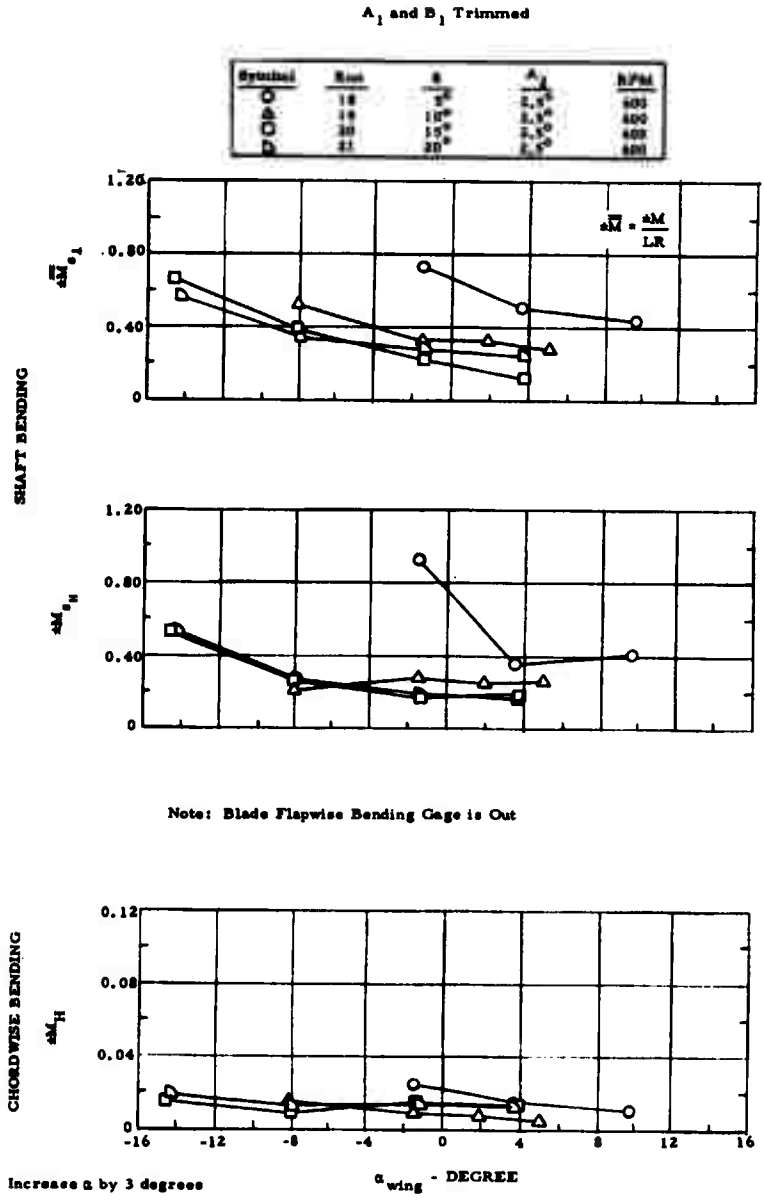

Figure 34. Alternating Blade Root and Shaft Bending Moments in Helicopter Flight, Trisector Wing, μ = 0.25

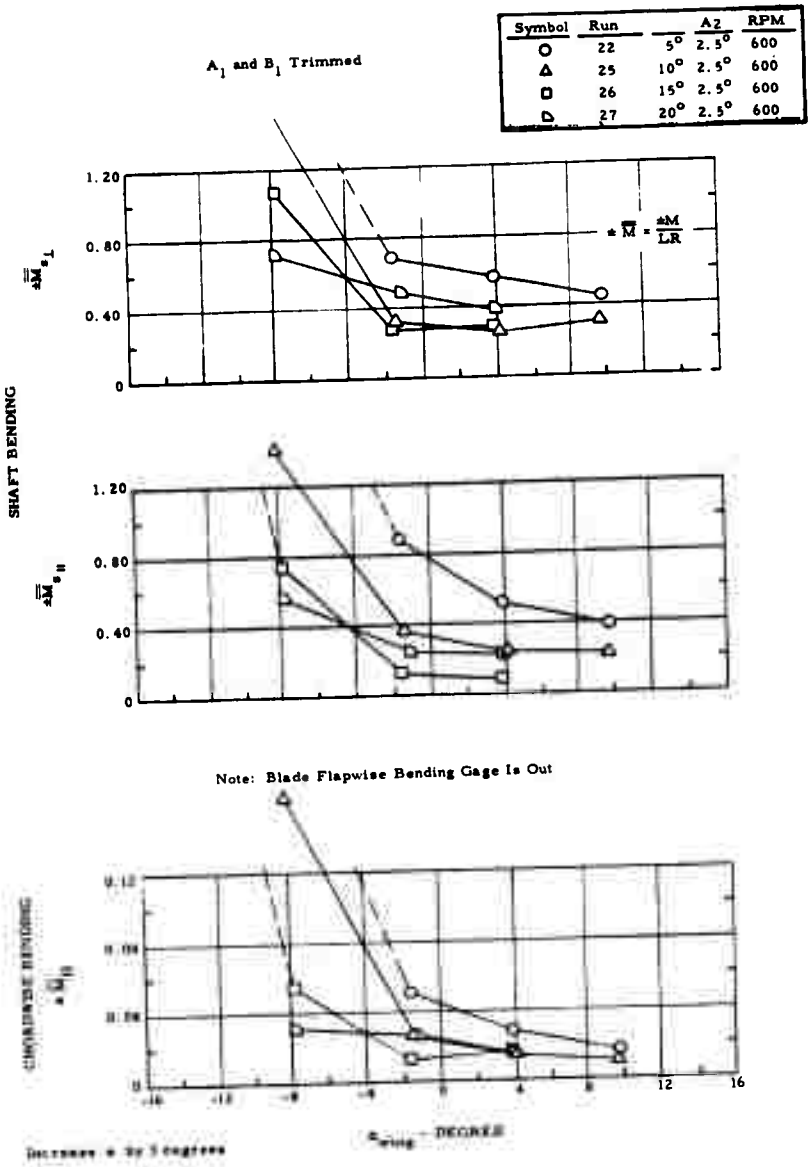

Figure 35. Alternating Blade Root and Shaft Bending Moments in Helicopter Flight. Trisector Wing, μ = 0.35

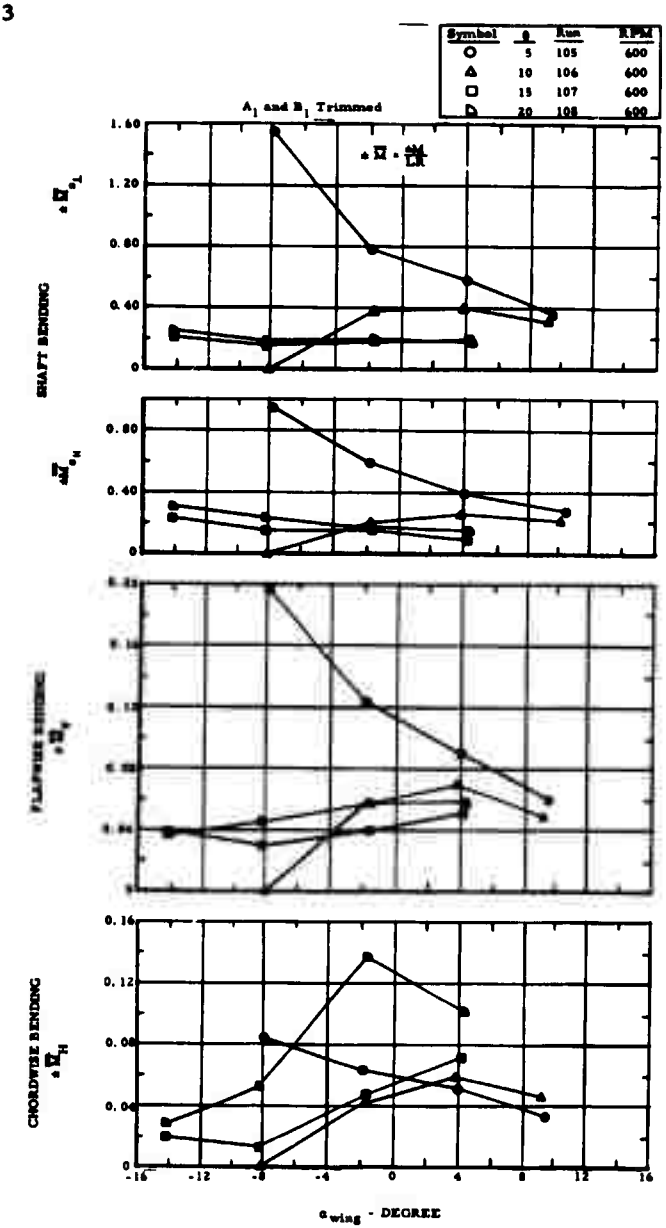

Increase α by 3 degrees

Figure 36. Alternating Blade Root and Shaft Bending Moments in Helicopter Flight, Triangle Wing, μ = 0.15

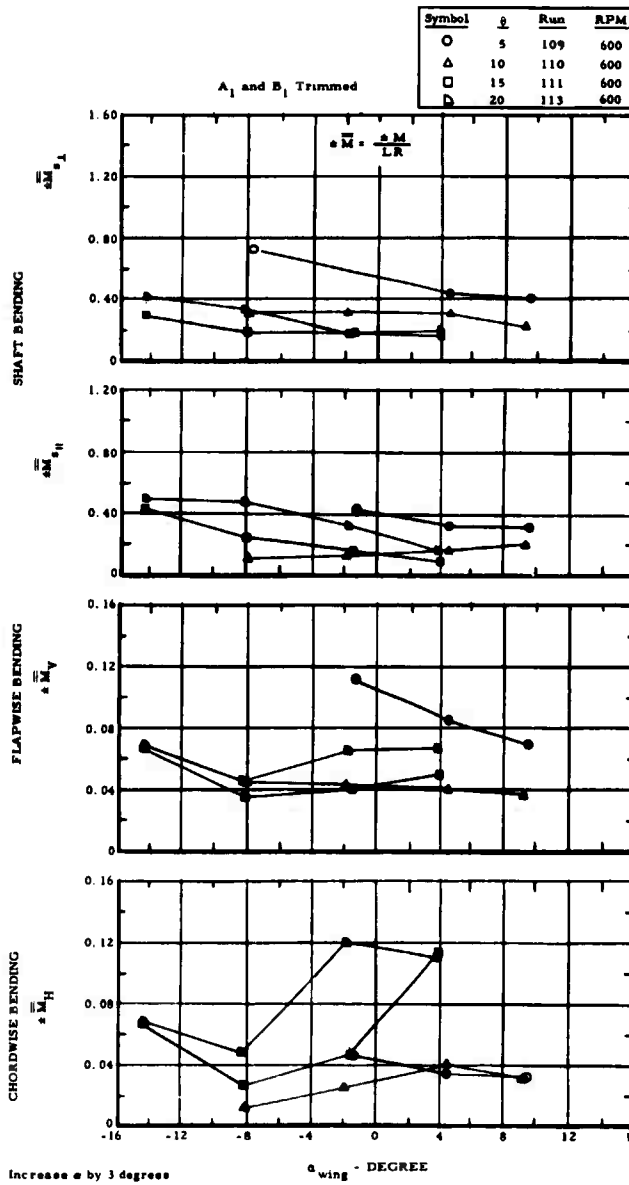

Figure 37. Alternating Blade Root and Shaft Bending Moments in Helicopter Flight, Triangle Wing, μ = 0.25

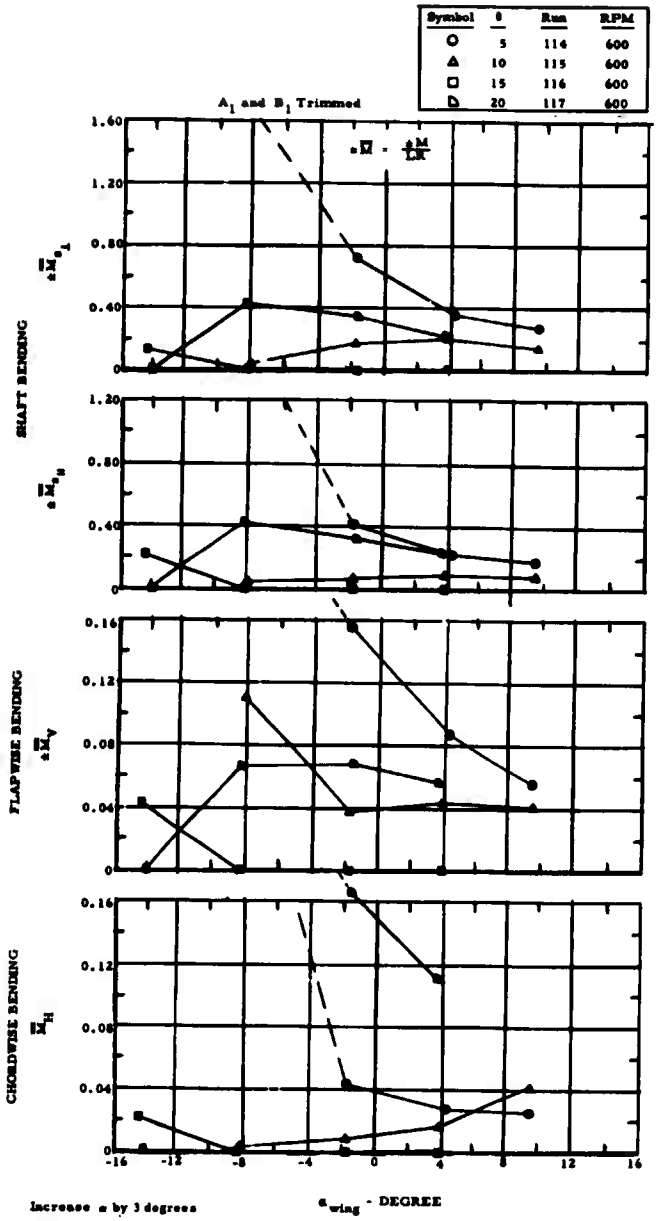

Figure 38. Alternating Blade Root and Shaft Bending Moments in Helicopter Flight, Triangle Wing, μ = 0.35

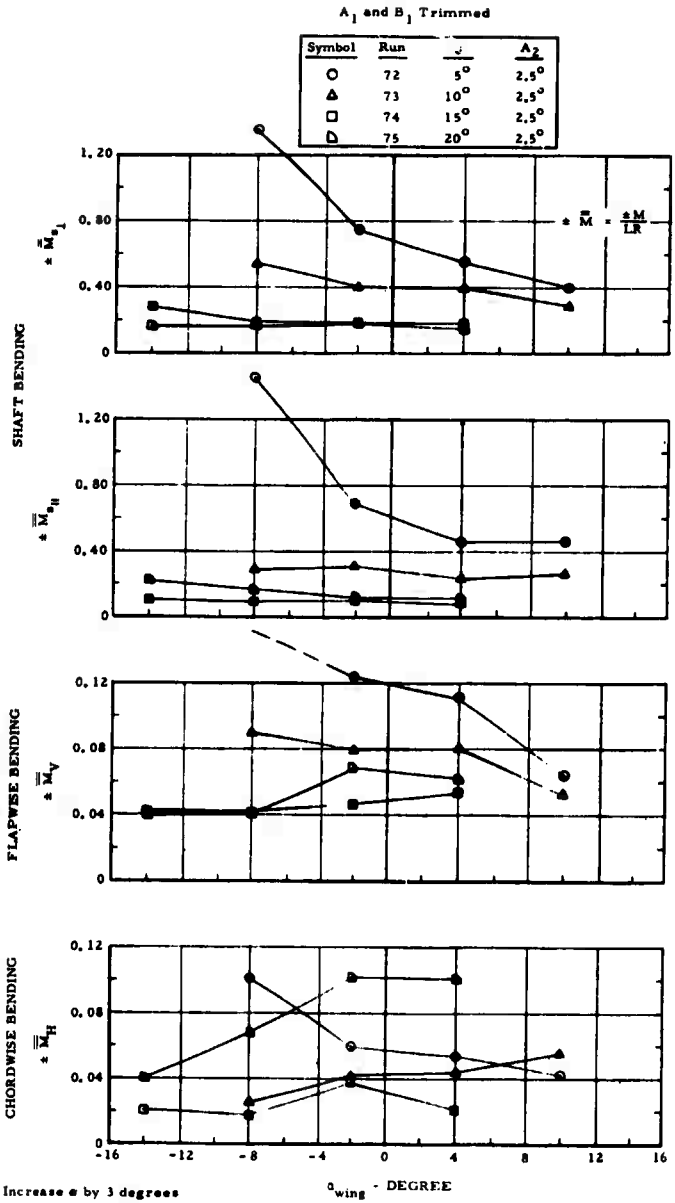

Figure 39. Alternating Blade Root and Shaft Bending Moments in Helicopter Flight, Tricusp Wing, μ = 0.15

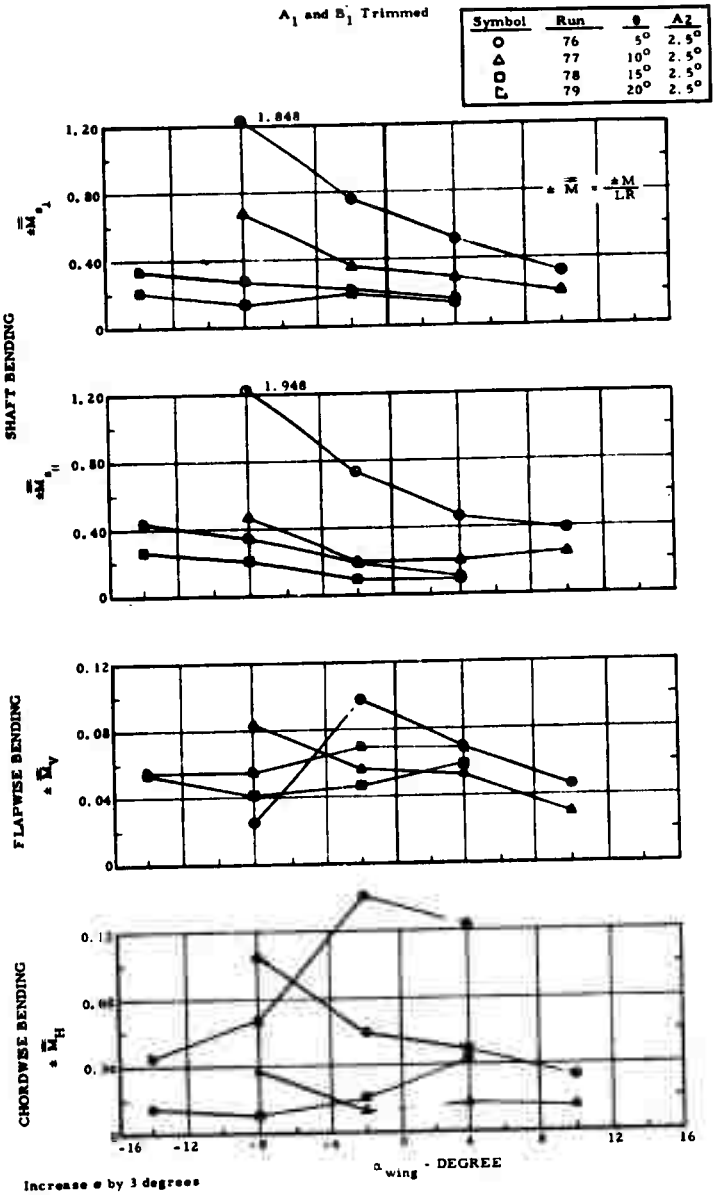

Figure 40. Alternating Blade Root and Shaft Bending Moments in Helicopter Flight, Tricusp Wing, μ = 0.25

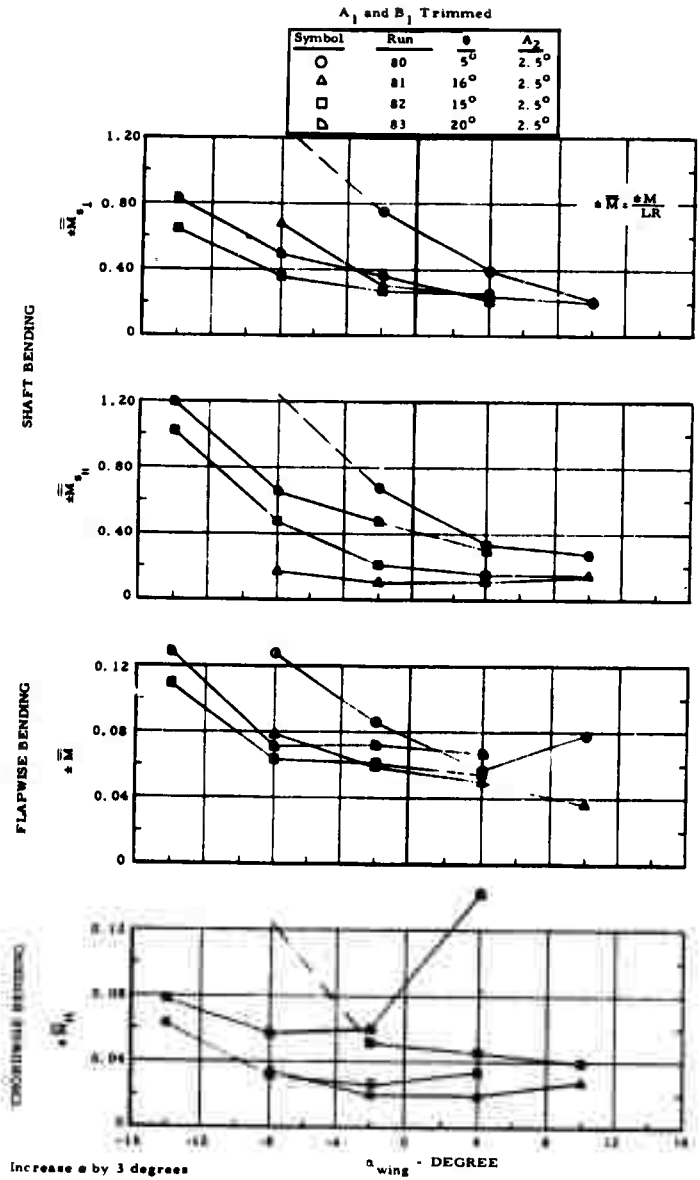

Figure 41. Alternating Blade Root and Shaft Bending Moments in Helicopter Flight, Tricusp Wing, μ = 0.35

Table 2. Rotor Shaft Bending Moment Harmonic Analysis, Powered Rotor, Triangle Wing, Tail Off

$\delta = 15°$, $\alpha = 11°$ (corrected), A_1 and B_1 Trimmed

$\overline{\overline{M}} = \frac{M}{LR}$

Moment	Advance Ratio	Run No.	First Harmonic*		Second Harmonic		Third Harmonic		Fourth Harmonic	
			$A_2 = 0°$	$A_2 = 2.5°$	$A_2 = 0°$	$A_2 = 2.5°$	$A_2 = 0°$	$A_2 = 2.5°$	$A_2 = 0°$	$A_2 = 2.5°$
$\overline{\overline{M}}_{s_\perp}$	0.15	200/107	0.076	0.080	0.138	0.120	0.060	0.021	0.044	0.030
	0.25	204/111	0.044	0.044	0.114	0.094	0.026	0.030	0.052	0.028
	0.35	208/116	0.026	0.044	0.188	0.098	0.015	0.007	0.047	0.021
$\overline{\overline{M}}_{s_\parallel}$	0.15	200/107	0.063	0.029	0.236	0.079	0.032	0.022	0.064	0.038
	0.25	204/111	0.030	0.014	0.209	0.126	0.034	0.040	0.048	0.045
	0.35	208/116	0.059	0.013	0.268	0.140	0.048	0.022	0.028	0.024
$\sqrt{\overline{\overline{M}}_{s_\perp}^2 + \overline{\overline{M}}_{s_\parallel}^2}$	0.15	200/107	0.098	0.085	0.274	0.144	0.068	0.030	0.078	0.048
	0.25	204/111	0.053	0.046	0.238	0.157	0.042	0.050	0.071	0.053
	0.35	208/116	0.064	0.046	0.327	0.171	0.050	0.023	0.055	0.033

*First harmonic principally represents fuselage plus tail moment balanced by the Rotor/Wing.

Since the fuselage and vertical tail contribute a certain moment by themselves, this zero model moment does not mean the rotor shaft first harmonic moment is zero. The blade root inplane bending moments are similar for the triangle and tricusp rotors, and both average about 25 percent higher than those measured for the trisector rotor. Flapwise bending moments cannot be compared in all cases, because a broken strain gage on the trisector blade spar prevented measuring this parameter. Flapwise bending moments for the triangle and tricusp rotors are comparable.

Figures 42 through 44 show the blade and shaft moments for the triangle Rotor/Wing and the $A_2 = 0°$ cyclic pitch input. When compared with Figures 33 through 41 for the $A_2 = 2.5°$ rotor, each case shows the shaft bending moments and the blade root bending moments are significantly reduced when 2.5 degrees of second harmonic cyclic pitch is introduced.

When going to an actual aircraft or a dynamically-scaled model, the flexibility of the Rotor/Wing and its supports to the fuselage are expected to account for a significant reduction in the rotor moments. Values of A_2 second harmonic cyclic pitch other than those tested will also contribute to reduced moments.

Harmonic analyses have been made of the rotor shaft bending moments measured during the powered-rotor tests of the triangular Rotor/Wing. The data were taken near a condition representing level flight: specifically, the collective pitch was 15 degrees, fuselage angle of attack was about level, and the cyclic pitch was trimmed to zero rolling and pitching moments. Table 2 presents the harmonic content of the shaft bending moment (made non-dimensional by dividing the total lift and rotor radius) for two moments mutually perpendicular to each other, whose orientations are:

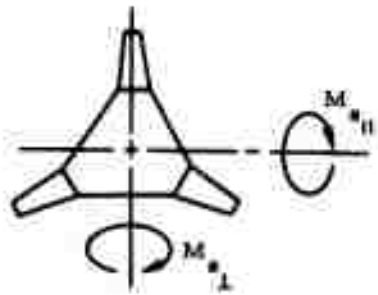

and for the root mean square of these moments:

$$\sqrt{\bar{M}_{s_{\perp}}^{2} + \bar{M}_{s_{11}}^{2}}$$

The moments were measured in the rotating rotor system. Since moments transfer into the stationary fuselage-based reference system at a frequency of one-plus or one-minus the harmonic in the rotor, the two rotor-based harmonics of most interest are the first and second.

The first becomes a steady moment in the stationary system, and would have been zero if the rotor moments alone were zero; however, the model condition set was model-minus-horizontal tail moments trimmed to zero, so the fuselage moment contribution had to be balanced by the rotor -- hence, the one-per-rev shaft moment.

The second harmonic moment would transfer into the fuselage as a 3-per-rev moment. The second harmonic moment is quite large for the $A_2 = 0°$ swashplate, as indicated by the

$$\sqrt{M_{s_{\perp}}^{2} + M_{s_{11}}^{2}}$$

values. When the $A_2 = 2.5°$ swashplate is installed, these bending moments reduce by a factor to two. This fact was also shown in the NSRDC Series II and III tests of the trisector Rotor/Wing.

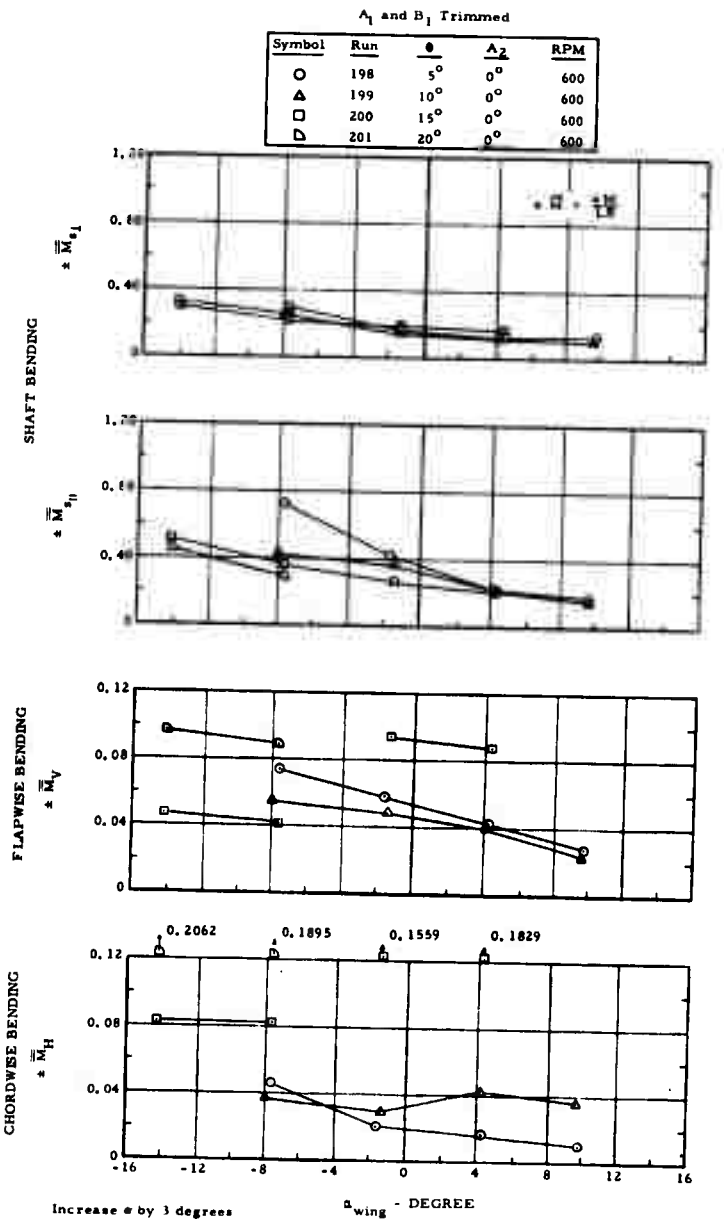

Figure 42. Alternating Blade Root and Shaft Bending Moments in Helicopter Flight, Triangle Wing (A_2 = 0°), μ = 0.15

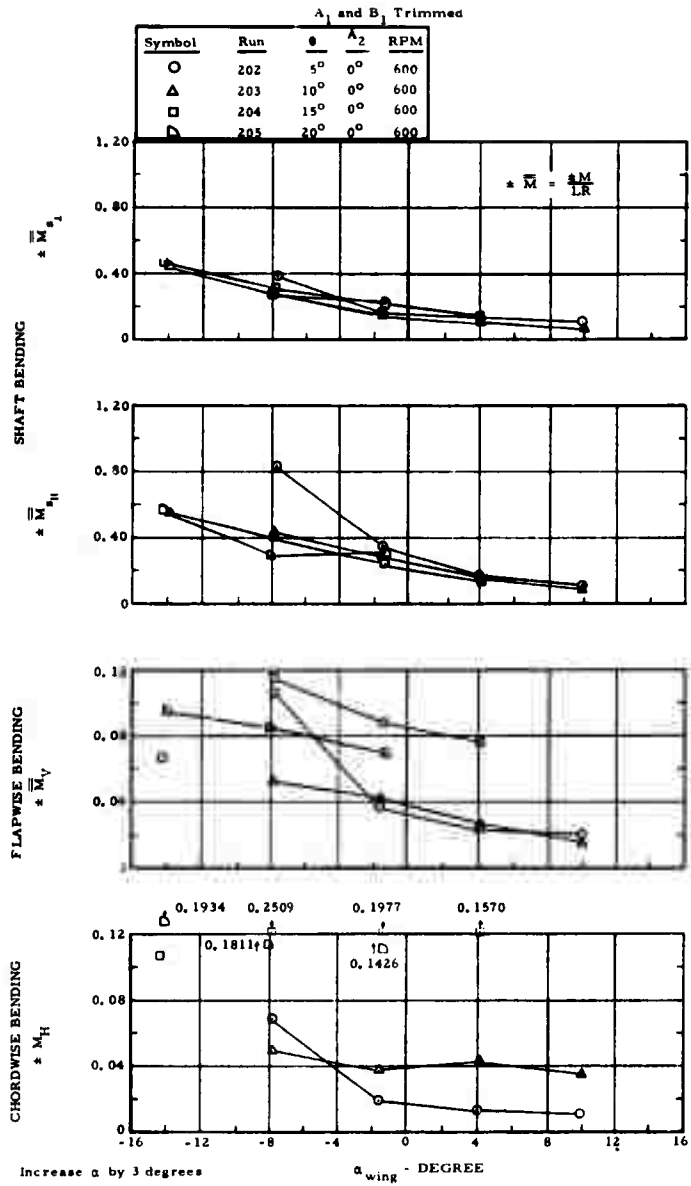

Figure 43. Alternating Blade Root and Shaft Bending Moments in Helicopter Flight, Triangle Wing (A_2 = 0°), μ = 0.25

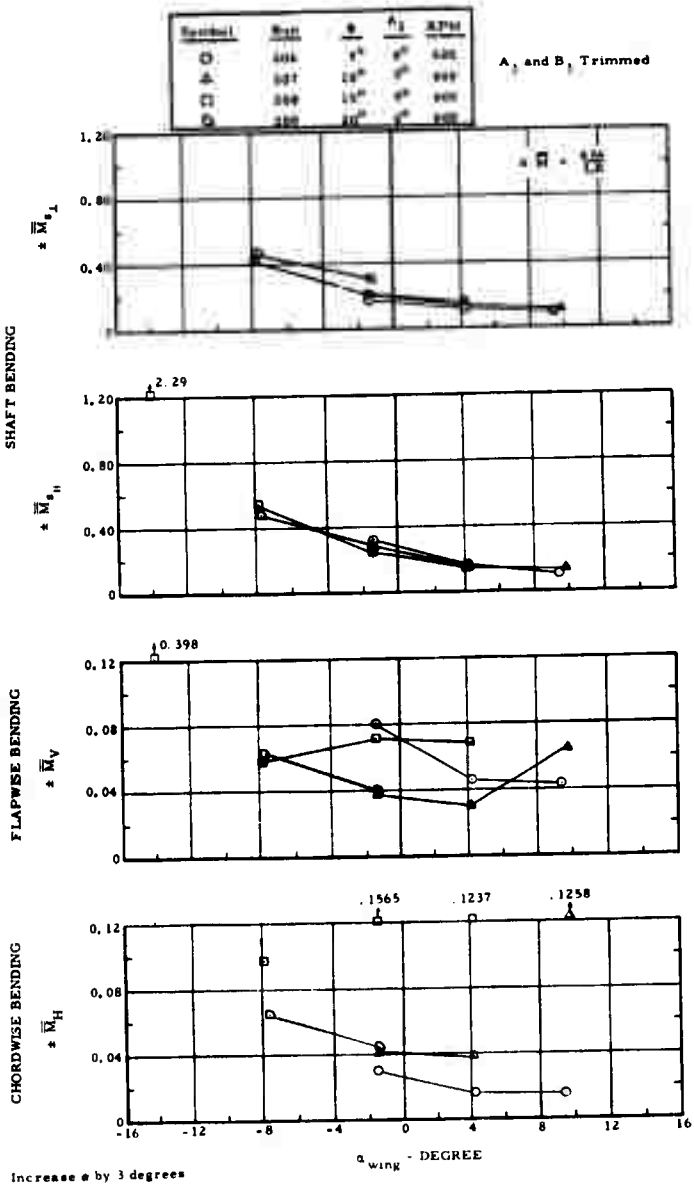

Figure 44. Alternating Blade Root and Shaft Bending Moments in Helicopter Flight, Triangle Wing ($A_2 = 0°$), $\mu = 0.35$

HELICOPTER MODE -- BLADES OFF

The triangle Rotor/Wing model was tested with the blades off over the same advance ratio range tested with blades on, or more specifically, the rotor rpm/tunnel speed ratios were the same. Figures 45 and 46 show the results of these tests. The rolling moment data are in question, first because of the magnitude which is about 10 times greater than calculations indicate, and secondly, because the sense of the moment is in the wrong direction. Series III tests of the trisector wing alone (Reference 2, Figure F-9) and calculations indicate a low level of rolling moment for the wing alone, and this should be a rolling moment to the left ($-C_{\mathcal{L}}$).

If rolling moment were plotted versus rotor advance ratio, as in the sketch below, for the wing alone (also for the complete Rotor/Wing with zero cyclic and collective pitch), it should be zero at $\mu = 0$ (high rpm . . . zero airspeed) because there is no dissymmetry of flow from side to side; it should also be zero at $\mu = \infty$ (high airspeed . . . zero rpm) because again there is no dissymmetry of flow. At intermediate μ's there should be a rolling moment to the left because of the familiar condition of high relative airspeed on the advancing side and low relative airspeed on the retreating side, thus:

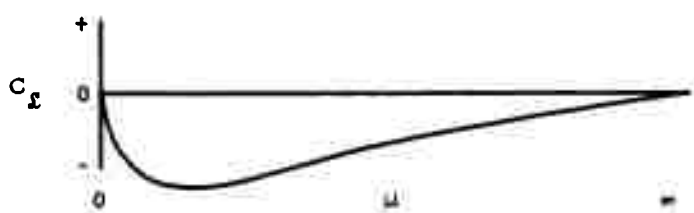

This is indeed the pattern measured in the Series III NSRDC tests for the trisector wing alone. The Series VI LRC data for the triangle wing appear to contain an uncompensated steady right rolling moment that was not eliminated by weight tare corrections. If a constant moment is subtracted from the Series VI data, they, too, show the anticipated trend of $C_{\mathcal{L}}$ versus μ.

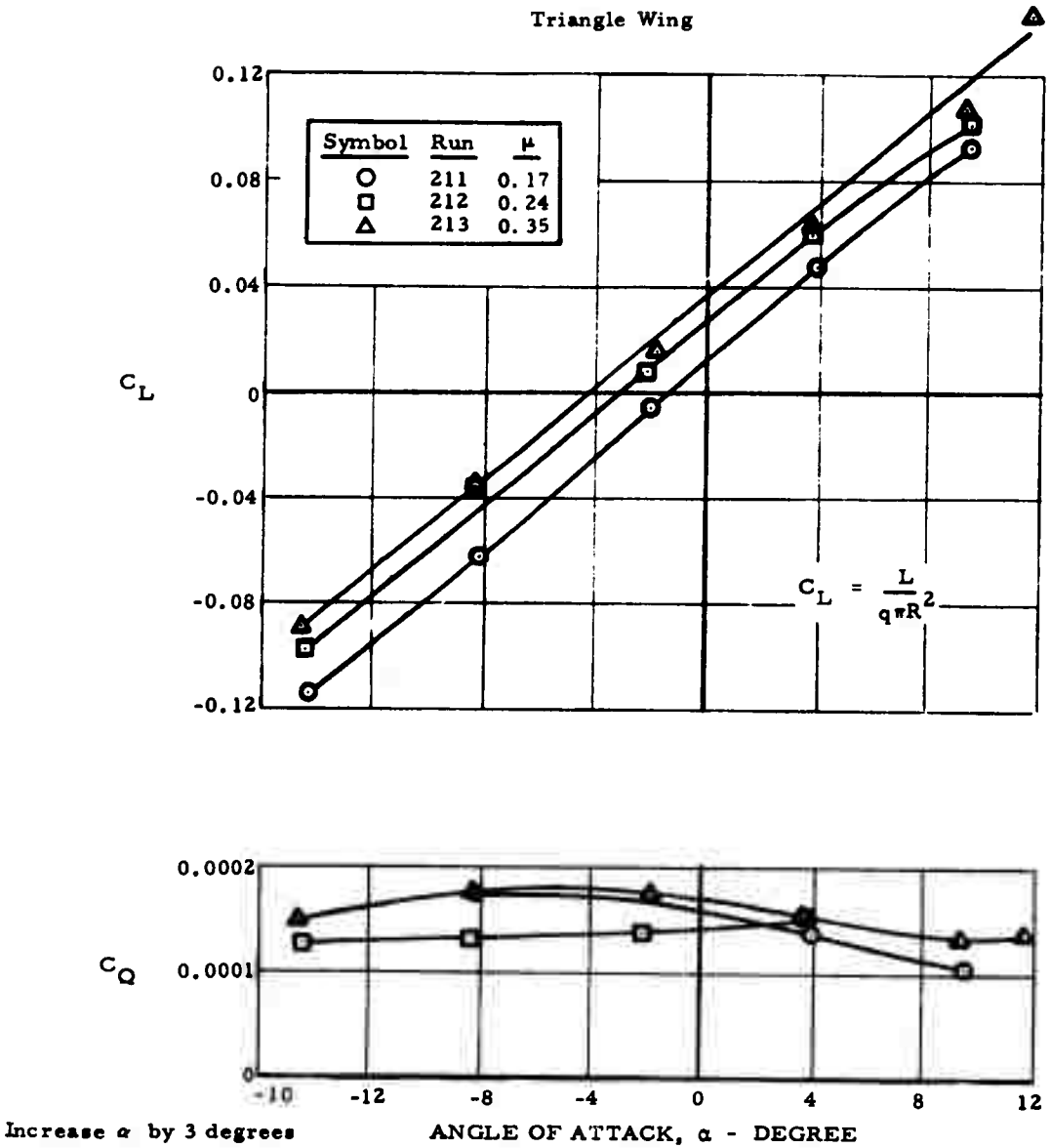

Figure 45. Blades-Off Lift and Torque

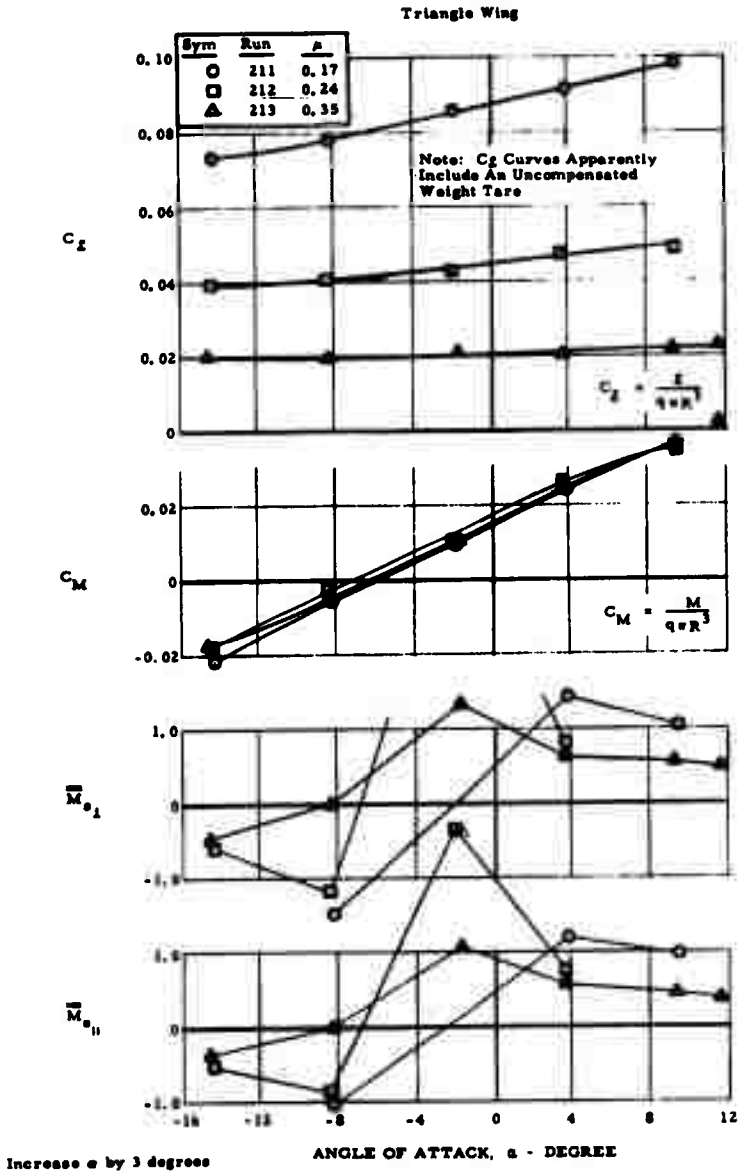

Figure 46. Blades-Off Pitching and Rolling Moments and Shaft Bending Moments

Rotor shaft bending moments measured in the blade-off tests of the triangle Rotor/Wing have been harmonically analyzed in Table 3 for an angle of attack of 14.6 degrees, approximately the angle encountered in autorotation and in conversion. The moments are nondimensionalized by dividing by the wing lift and the rotor radius to the blade tip. This table shows a one-per-rev moment that is quite steady with increasing advance ratio and a two-per-rev moment that decreases quickly with increasing advance ratio. Undoubtedly, this 2-per-rev hub moment is a large contributor to the moments that will be described later for the autogyro case.

The one-per-rev moment can be mostly accounted for by the simple procedure of calculating the aerodynamic center of a triangle. It can easily be shown that for a wing of equilateral triangle planform, the quarter-chord of the MAC is 3/8 of the root chord forward of the centroid of the wing, whether one point of the triangle points into the wind or away from it. Since the MAC equals 2/3 of the root chord for the symmetrical positions of the triangle, the quarter chord of the MAC is 25 percent of the distance from triangle centroid to triangle tip forward of the center. The tip of the equivalent triangle falls at 82 percent* of the model Rotor/Wing radius; hence, in terms of the $\overline{\overline{M}}$ coefficients this contribution to the one-per-rev shaft bending should be:

$$\overline{\overline{M}} = 0.25r \times 0.82 \frac{R}{r} \times \frac{1}{r}$$

$$\overline{\overline{M}} = 0.205$$

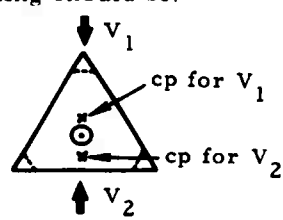

The difference between this value and that shown for the first harmonic in Table 3 is attributed to the effect of truncated tips of the triangle, camber in the wing, and nonuniform flow around the rotating wing.

*Blade root radius equals 59 percent of tip radius.

Table 3. Rotor Shaft Bending Moment Harmonic Analysis, Powered Rotor, Triangle Wing, Blades Off, Tail Off

$\alpha = 14.6°$ (corrected), $A_2 = 2.5°$

$\overline{\overline{M}} = \frac{M}{LR}$

Moment	Run No.	Advance Ratio	First Harmonic	Second Harmonic	Third Harmonic	Fourth Harmonic
$\overline{\overline{M}}_{s_\perp}$	213	0.35	0.220	0.220	0.061	0.059
	214	0.70	0.212	0.046	0.025	0.098
		1.46	0.211	0.063	0.015	0.011
		2.25	0.204	0.057	0.005	0.019
$\overline{\overline{M}}_{s_\parallel}$	213	0.35	0.211	0.157	0.109	0.025
	214	0.70	0.238	0.023	0.022	0.072
		1.46	0.223	0.063	0.005	0.006
		2.25	0.216	0.051	0.011	0.013
$\sqrt{\overline{\overline{M}}_{s_\perp}^2 + \overline{\overline{M}}_{s_\parallel}^2}$	213	0.35	0.305	0.270	0.125	0.065
	214	0.70	0.319	0.051	0.034	0.122
		1.46	0.307	0.089	0.016	0.012
		2.25	0.297	0.077	0.012	0.023

This analysis indicates that a sizable one-per-rev will always occur in the shaft because of the forward offset of the center of pressure, regardless of the wing planform shape. A way to avoid the moment arising from the forward center of pressure appears to be the use of considerable camber in the wing. The nose-down moment created by the camber would compensate for the lift vector offset. Tests have been proposed to investigate the effect of camber.

AUTOGYRO MODE

Autorotation tests were made with the rotor drive chain removed and the Rotor/Wing autorotating freely. The trisector and tricusp models were tested at one collective pitch setting: $\theta = 2°$ (Figures 47 and 48); the triangle model was used to investigate the effect of collective pitch setting from 0 to 2 degrees as plotted in Figure 49. Two rotor speeds were tested, nominally 600 and 500 rpm. A comparison of test data for the trisector model in autorotation obtained in the NSRDC and in the LRC tunnels is shown in Figure 47. Reasonably good agreement again indicates the small NSRDC tunnel is satisfactory for testing rotary-wing models.

Autorotation tests were made with the steady rolling moment trimmed to zero, by adjustment of the lateral cyclic pitch. Longitudinal cyclic pitch, A_1, had to be held to zero degrees because application of A_1 to trim out the steady pitching moment resulted in greatly reduced rotor rpm that could not be tolerated. Hence, all the autorotation data show a steady nose-up pitching moment of a magnitude that may be easily trimmed out with the horizontal tail. This A_1 effect on rotor speed, when the rotor cyclic pitch is coupled to the elevon controls, must be evaluated in the Rotor/Wing dynamic model tests.

All models were tested tail-off; the triangle model was tested in conjunction with the tail to determine tail effectiveness in the autogyro mode. Figure 50

shows that the tail effectiveness measured in helicopter flight (see Figures 30, 31, and 32), is only about 85 percent as effective as in the airplane mode (compare with Figure 73).

There is little to choose between the three Rotor/Wings as far as lift, pitching moment, control, and angle of attack characteristics are concerned.

Figure 51 pr· sents the half-amplitude values of the peak-to-peak rotor shaft bending and blade flapwise and chordwise bending data for the trisector configuration. The loads measured in the Series III tests at NSRDC are shown for comparison.

Table 4 shows the results of harmonic analysis of the shaft bending moments, $\overline{\overline{M}}_{s_\perp}$ and $\overline{\overline{M}}_{s_\parallel}$, and also the root mean square of these for the triangle Rotor/Wing. This table shows the moments to be higher in autorotation than in the powered-rotor condition (Table 2), especially the second harmonic at the lower advance ratio. The level decreases rapidly with advance ratio, approaching the values measured in the lower rpm's of conversion (Table 5). Tests with the trisector model at NSRDC (Reference 2) showed A_2 to have little influence on the rotor loads in the autogyro mode, so the moments shown here are representative of the loads associated with A_2 values in the zero to 2.5 degree range. The first harmonic in the shaft bending is due to the wing contribution discussed previously, and to the fact that A_1 was zero for these tests and could not aid in reducing this component.

CONVERSION

Conversion tests were made with all three Rotor/Wings: trisector, triangle, and tricusp. For each, the $A_2 = 2.5°$ swashplate was used; no tests were made in this series with $A_2 = 0°$.

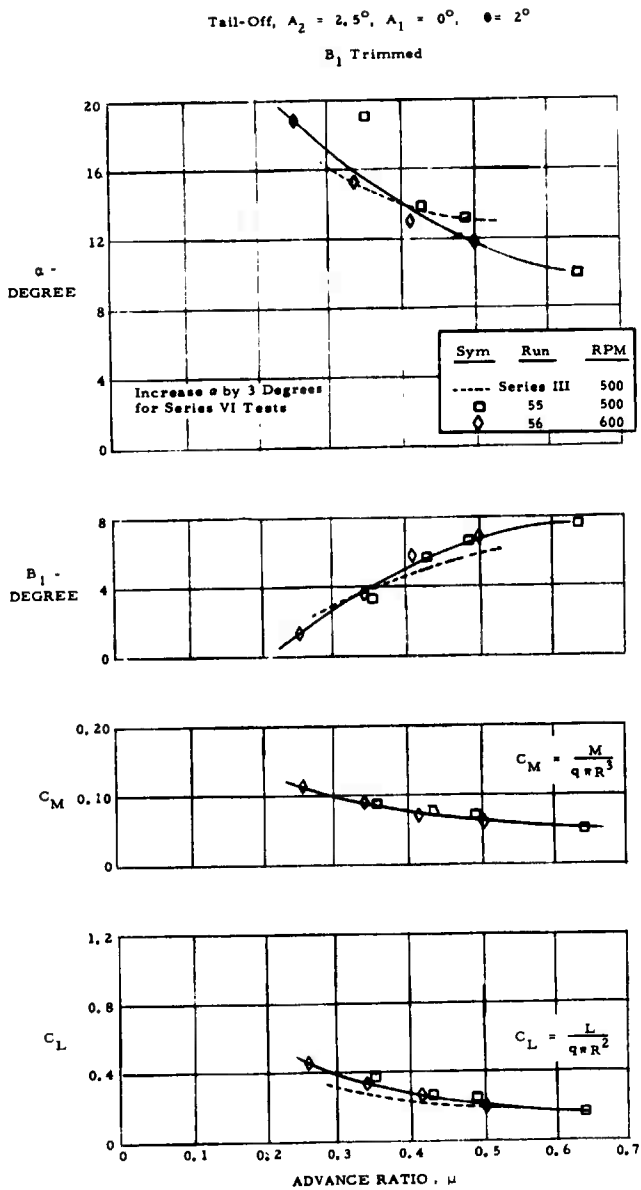

Figure 47. Autorotation, Trisector Wing

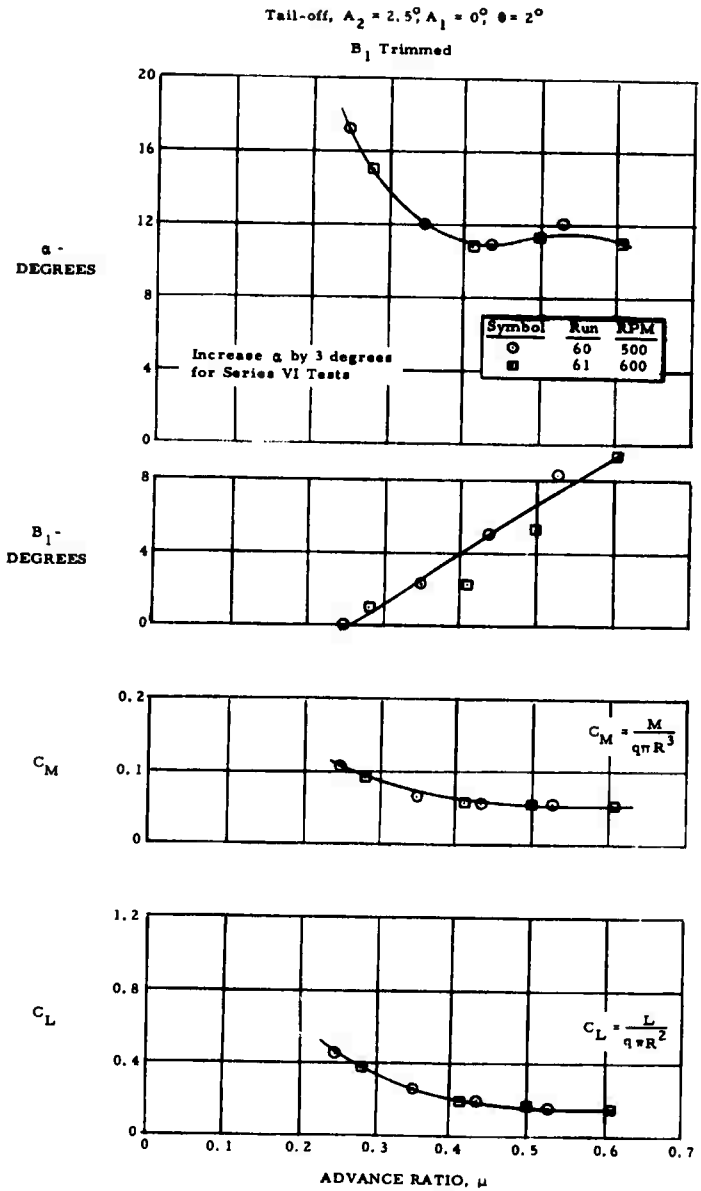

Figure 48. Autorotation, Tricusp Wing

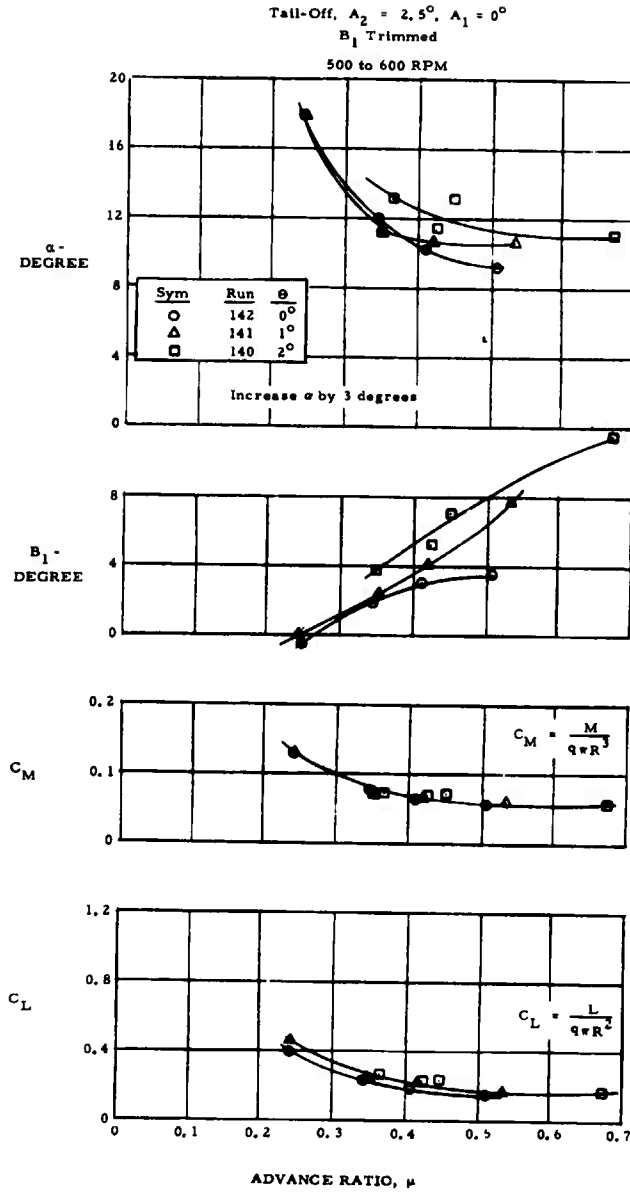

Figure 49. Autorotation, Triangle Wing

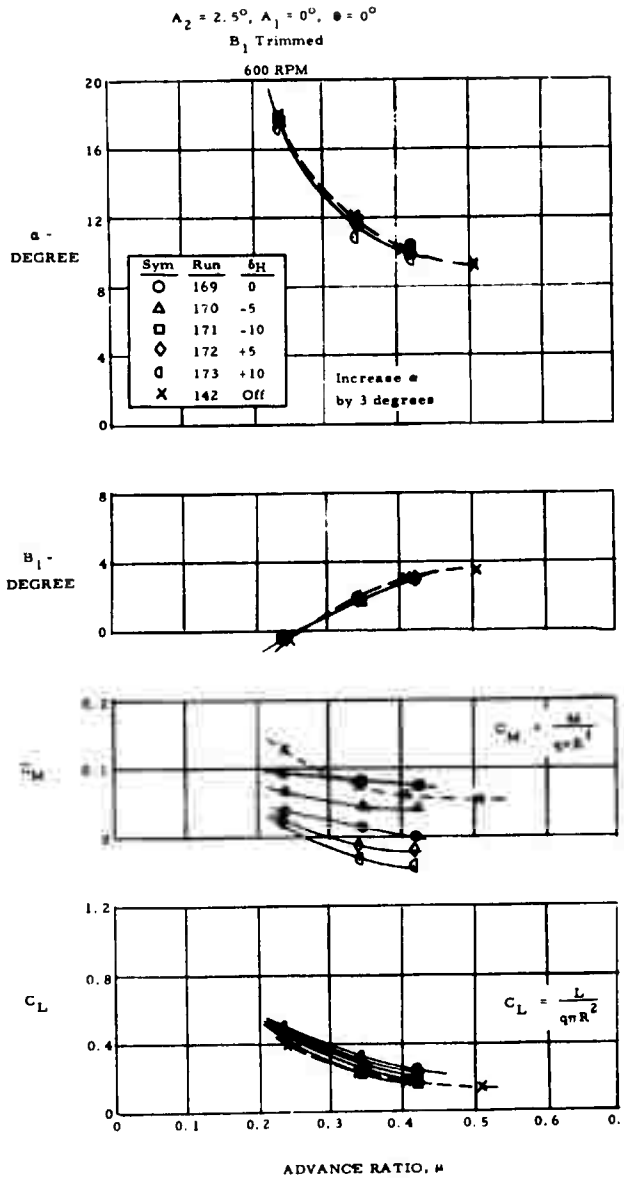

Figure 50. Autorotation Tail Effectiveness, Triangle Wing

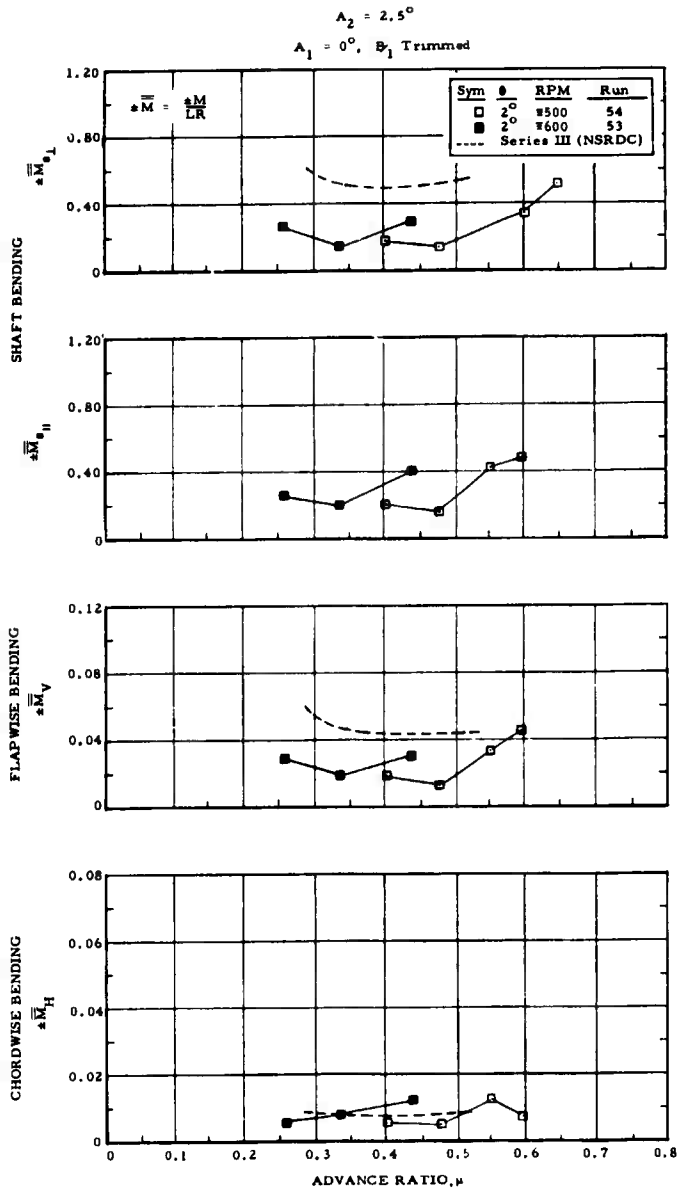

Figure 51. Alternating Blade Root and Shaft Bending Moments, Autorotation, Trisector Wing

Table 4. Rotor Shaft Bending Moment Harmonic Analysis, Autorotation, Triangle Wing, Tail Off

$A_2 = 2.5°$, $\theta = 0°$, $A_1 = 0°$, B_1 Trimmed, $\alpha = 16°$ (Corrected)

$\overline{\overline{M}} = \frac{M}{LR}$

Moment	Run No.	Advance Ratio	First Harmonic	Second Harmonic	Third Harmonic	Fourth Harmonic
$\overline{\overline{M}}_{s_\perp}$	124	0.411	0.262	0.161	0.008	0.017
	140	0.672	0.238	0.042	0.032	0.046
$\overline{\overline{M}}_{s_\parallel}$	124	0.411	0.254	0.164	0.011	0.024
	140	0.672	0.235	0.027	0.004	0.025
$\sqrt{\overline{\overline{M}}_{s_\perp}^2 + \overline{\overline{M}}_{s_\parallel}^2}$	124	0.411	0.365	0.230	0.014	0.029
	140	0.672	0.334	0.050	0.032	0.053

Table 5. Rotor Shaft Bending Moment Harmonic Analysis, Conversion, Triangle Wing, Tail Off

$A_2 = 2.5°$, $A_1 = 0°$, B_1 Trimmed

$\overline{M}_s = \frac{M}{LR}$

Mode	Run No.	Moment	Rotor RPM	First Harmonic	Second Harmonic	Third Harmonic	Fourth Harmonic
Pseudo Conversion	122	$\overline{\overline{M}}_{s_\perp}$	122	0.215	0.107	0.046	0.050
			195	0.231	0.127	0.007	0.038
		$\overline{\overline{M}}_{s_\parallel}$	122	0.206	0.093	0.011	0.003
			195	0.240	0.125	0.017	0.047
		$\sqrt{\overline{M}_{s_\perp}^2 + \overline{M}_{s_\parallel}^2}$	122	0.298	0.141	0.047	0.050
			195	0.333	0.178	0.018	0.060
Manual Conversion	138	$\overline{\overline{M}}_{s_\perp}$	30	0.192	0.104	0.040	0.020
			66	0.185	0.121	0.013	0.023
			123	0.179	0.097	0.018	0.011
			195	0.216	0.093	0.017	0.014
		$\overline{\overline{M}}_{s_\parallel}$	30	0.200	0.088	0.035	0.013
			66	0.211	0.117	0.027	0.026
			123	0.206	0.095	0.004	0.031
			195	0.222	0.075	0.015	0.026
		$\sqrt{\overline{M}_{s_\perp}^2 + \overline{M}_{s_\parallel}^2}$	30	0.277	0.136	0.053	0.024
			66	0.281	0.168	0.030	0.035
			123	0.273	0.136	0.019	0.033
			195	0.310	0.118	0.023	0.030

PSEUDO-CONVERSION TESTS

Tests were made for each Rotor/Wing in the pseudo-conversion mode to determine model control programs as a function of rotor speed that may be used in the actual conversion tests, where only aerodynamic forces start or stop the rotor. The technique here was to power the rotor, select a rotor lift force, and for a series of rotor speeds from 600 rpm down to about 100 rpm, find the combinations of model angle of attack, collective pitch, and lateral cyclic pitch that maintain constant lift and zero rolling moments. Longitudinal cyclic pitch was held at zero for all the pseudo-conversion runs. Initial tests showed that the longitudinal control power deteriorates rapidly with decreasing rotor speed at constant airspeed, and below a rotor speed of approximately 500 rpm even full nose-down cyclic pitch of 15 degrees could not balance the nose-up pitching moment of the wing at the angles of attack needed to maintain lift. This is due to the small chordwise velocity vector across the blades when they sweep the forward and aft sectors of the rotor disc (the region where the blades create a rotor pitching moment), and the resulting small blade lift components created. It was observed that the horizontal tail was capable of trimming the resulting Rotor/Wing moment; therefore, to simplify testing, A_1 was held at zero degrees throughout.

Figures 52, 53, and 54 show the control position maps established for the three Rotor/Wings at the design lift force, which is 50 pounds. Zero torque boundaries are plotted on these maps for the triangle and tricusp planforms. Because of an obvious zero shift in the recorded hydraulic pressure data, no boundaries are shown for the trisector wing. Inside the boundary, an accelerating torque is created; outside, a decelerating torque exists.

FULL CONVERSION TESTS

The conversion tests were run twice for each configuration: once, through the rpm range up to about 520 rpm, which is 85 percent of design helicopter

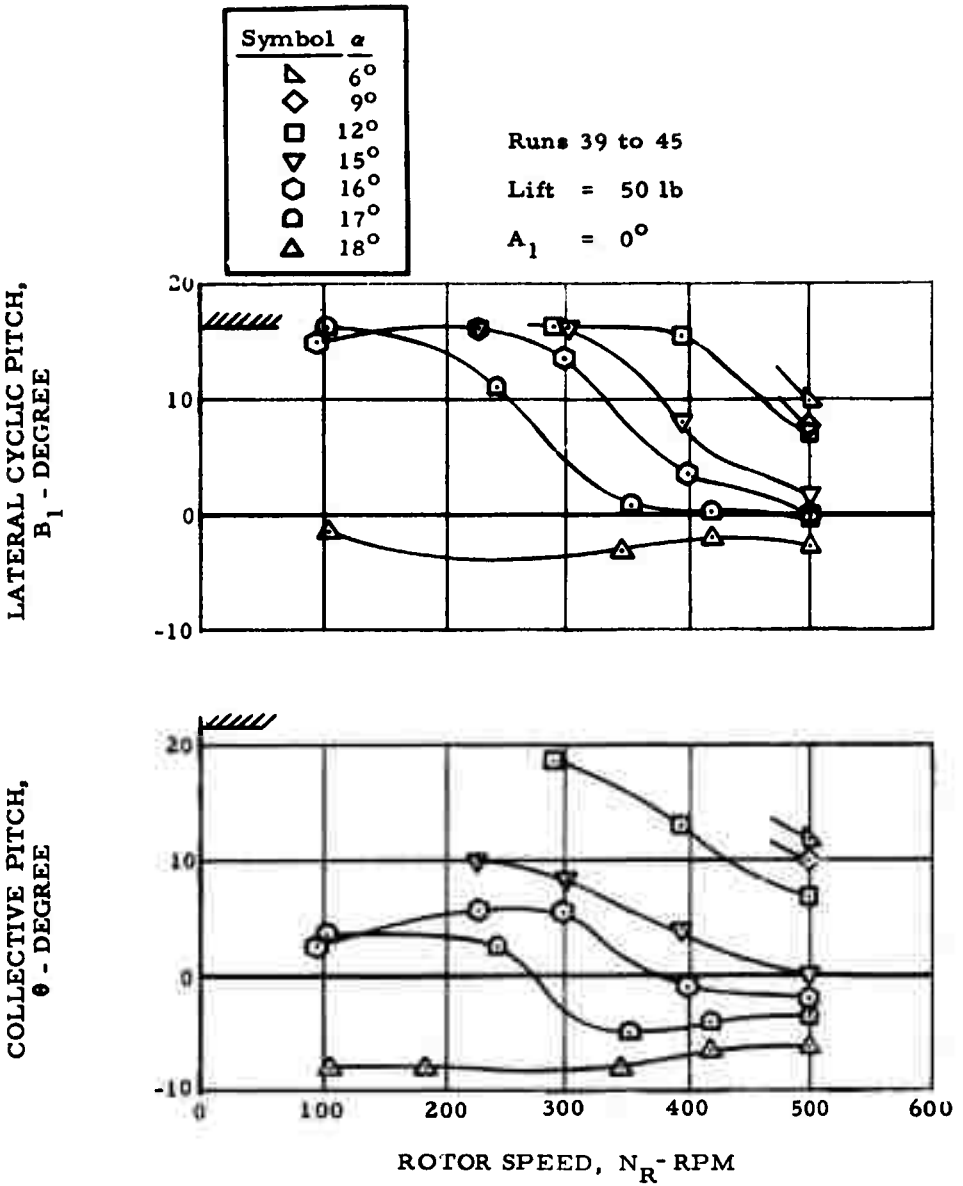

Figure 52. Pseudo-Conversion, Trisector Wing

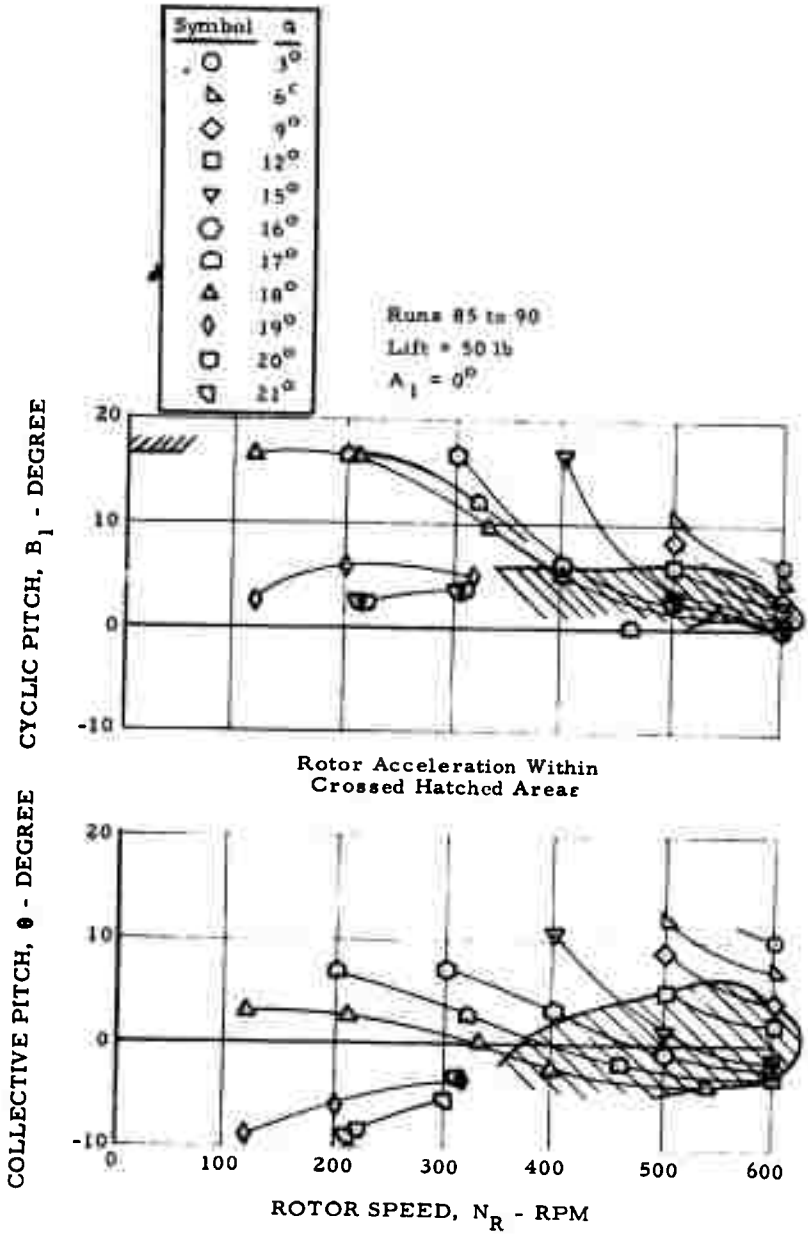

Figure 53. Pseudo-Conversion, Tricusp Wing

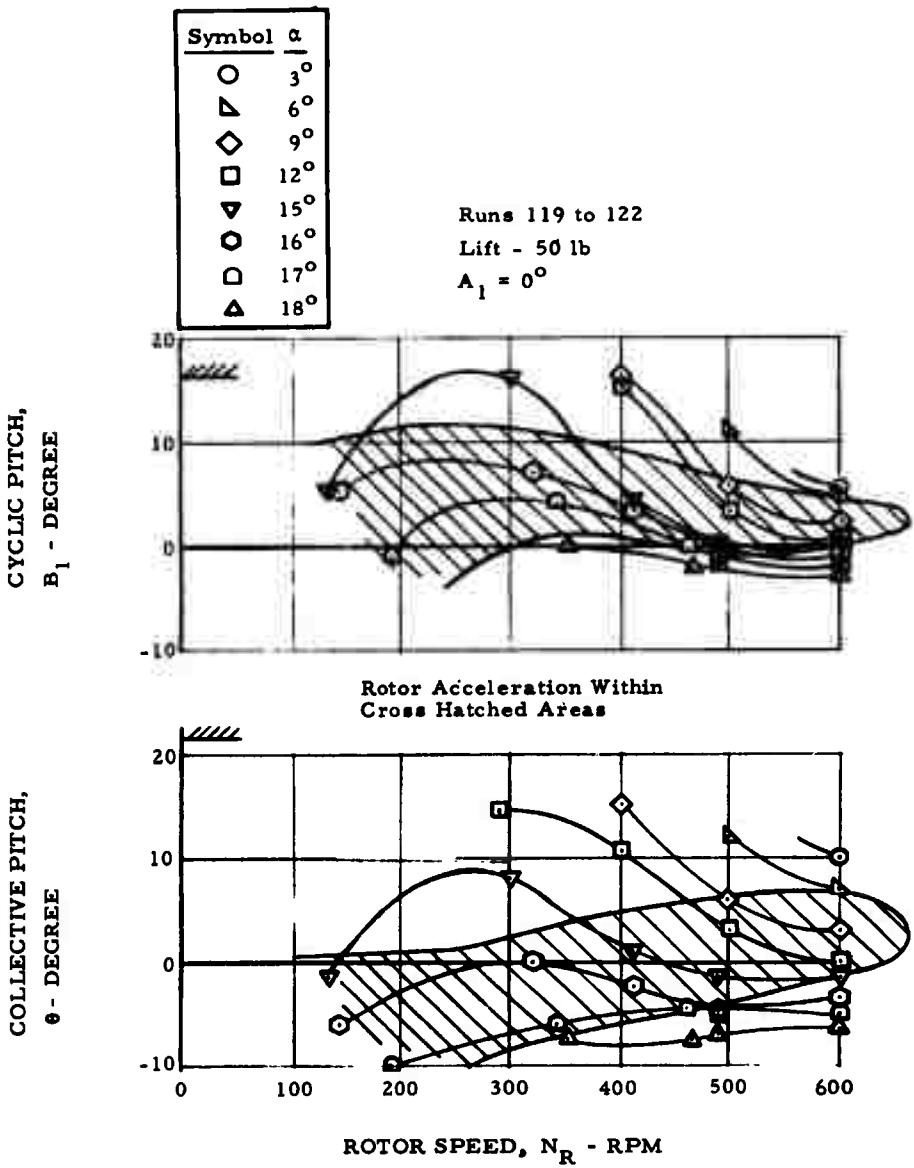

Figure 54. Pseudo-Conversion, Triangle Wing

rpm -- the rpm selected for autogyro flight while recording the strain gage post balance data on an oscillograph; and a second time through the 0 to 100 rpm range while recording the strain gage output on a digital magnetic tape at a reading rate of 30 times per second.

Time histories of the conversions, as read from the oscillograph, are plotted in Figures 55, 56, and 57 for the three Rotor/Wings. That the lift, pitching moment, and rolling moment were not exactly on schedule is not considered of too great importance, because by very small changes in the control inputs, the rolling moment and lift could have been brought to the required condition of zero rolling moment and constant lift. The pitching moment excursions are well within the balancing capability of the horizontal tail.

A comparison of trisector Rotor/Wing conversion in the two wind tunnels is shown in Figure 55. The data are similar.

The blade root and shaft bending moments are shown in Figures 58 through 60. Figure 58 shows that the measured moments are similar for the trisector model in both the NSRDC and the 30-by-60-foot tunnel. Tests to observe resonances in the model and support showed that these occurred at approximately 250, 350, and 500 rpm; hence, data points near these rotor speeds are not shown.

The magnetic tape data were recorded 30 times per second, and from this the six-component coefficients were calculated on a basis of averaging over 10 data points and over 60 data points. Trial plots of the 10- and 60-point data showed little variation in curves plotted versus rotor speed; therefore, the 60-point data are shown in the plots of Figures 61, 62, and 63. In all three of these figures, the lift, drag, and side force are shown to be quite constant over this critical 0- to 100-rpm range. The mean rolling moment is near zero, and mean pitching moment is relatively constant, as shown in the

oscillograph data of Figures 55, 56, and 57. The RMS values shown for lift, roll, and pitch are a measure of the amplitude of these coefficients from the mean. They are calculated from

$$\sqrt{C_{L_{total}}^2 - C_{L_{mean}}^2} \; .$$

The lift RMS amplitude is equal to about 1/20 of the mean lift in Figures 55, 56, and 57, and indicates an almost uniform ±0.05 g acceleration across this rpm.

Generally, the magnetic tape recorded data are considered a better record of the conversion maneuver, because the oscillograph record was too sensitive to be read accurately. Six-component balance oscillograph data are used for indicating trends only.

The pitching and rolling moment oscillations are more easily visualized in Figures 64 through 66, where the pitching and rolling moments are combined with the lift to indicate the location of the center of pressure in the fuselage-oriented, nonrotating coordinate system, as it makes a 3-per-rev excursion in a more or less elliptical pattern centered on the longitudinal axis of the aircraft and somewhat forward of the rotor center. This center of pressure is for the Rotor/Wing alone; the fuselage moments have been removed from the data. Figures 64 and 66 show that there is little basic change in the pattern, whether accelerating or decelerating (with or without a brake), for the trisector and triangle Rotor/Wings. The tricusp Rotor/Wing, though, experiences almost three times the fore-and-aft excursion of the center of pressure, compared with the other two, as shown by Figure 65.

A time history of the rotor shaft bending moments -- during the first three revolutions as the rotor starts turning -- is shown in Figure 67 for the

triangle Rotor/Wing. These moments* are in the rotating coordinate system of the rotor. Figure 68 shows these shaft moments transferred into the non-rotating fuselage-oriented coordinate system.

A time history of the aircraft response to these moments has been calculated using the size, inertia, and aerodynamic damping of the HTC-AD/USAAVLABS Composite Research Aircraft. Figure 69 shows the calculated motions of the aircraft as the rotor starts turning. These aircraft motions assume that the pilot trims out the mean moments, but makes no attempt to compensate for the oscillating moments. In actual practice, the pilot (or an auto-pilot) could compensate for the rotor inputs at the very low rotor speeds by deflecting the elevons to maintain straight and level flight.

The rotor moments considered here are based on those generated by the rigid concept model. The more flexible Rotor/Wing of an actual aircraft is not expected to develop such large moments. This will be demonstrated in the forthcoming Rotor/Wing dynamic model tests.

Rotor shaft bending moments were measured during the pseudo-conversion and conversion tests. Table 5 shows the results of a harmonic analysis of the $M_{s_\perp}$ and $M_{s_{||}}$ moments for the triangle wing, made nondimensional by dividing by lift and rotor radius, and also for the root mean square of these moments:

$$\sqrt{\bar{\bar{M}}_{s_\perp}^{\,2} + \bar{\bar{M}}_{s_{||}}^{\,2}} \quad ;$$

these moments are measured in the rotating coordinate system of the Rotor/Wing. The first harmonic moment is principally due to the forwardly located

*The moments here are of the opposite sense to those reported in Figure 37 of Reference 2, and Figures 4 through 8 of Reference 3. It has been found that a sign error occurred in plotting the data of the Series II and Series III tests, and that the aforementioned plots should have the signs changed in both pitch and roll.

lift vector that acts mainly on the wing and causes a steady nose-up moment that would be reacted by the horizontal tail in an actual aircraft. The second harmonic of shaft bending would be felt as a 3-per-rev moment in the fuselage.

Table 5 shows that, in the lower rotor rpm range, the second harmonic root mean square moment is relatively constant, and very nearly the same as that measured in powered rotor flight (Table 2). These data are for the $A_2 = 2.5°$ swashplate. No tests were made with $A_2 = 0°$, but the Series II and Series III Rotor/Wing tests (Reference 2) showed that for the trisector wing, the second harmonic shaft bending moments were slightly lower when the $A_2 = 2.5°$ swashplate was used.

It must be remembered that the moments were measured on the rigid concept model, and that they are not necessarily the same as those expected on a more flexible aircraft. Other factors -- besides the rotor support flexibility that would alleviate the rotor shaft bending moment problem -- are variation of A_2 or B_2 second harmonic cyclic pitch and wing camber, as discussed previously. A better indication of the true situation should be given by the forthcoming Rotor/Wing dynamic model program.

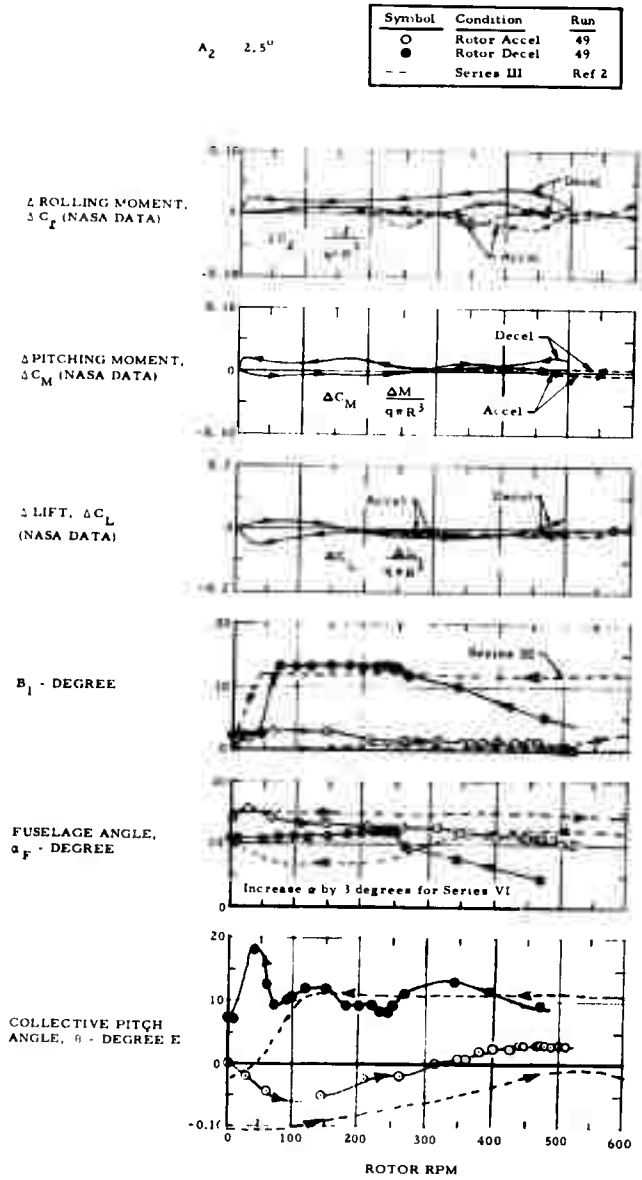

Figure 55. Aircraft Characteristics During Manual Conversion, Trisector Wing

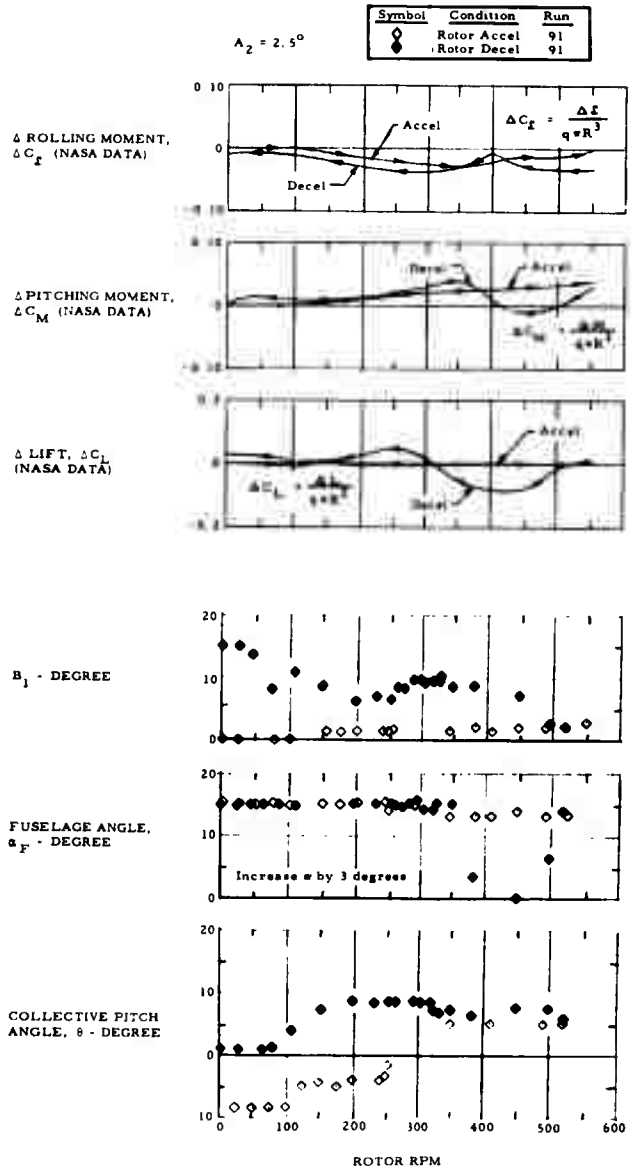

Figure 56. Aircraft Characteristics During Manual Conversion, Tricusp Wing

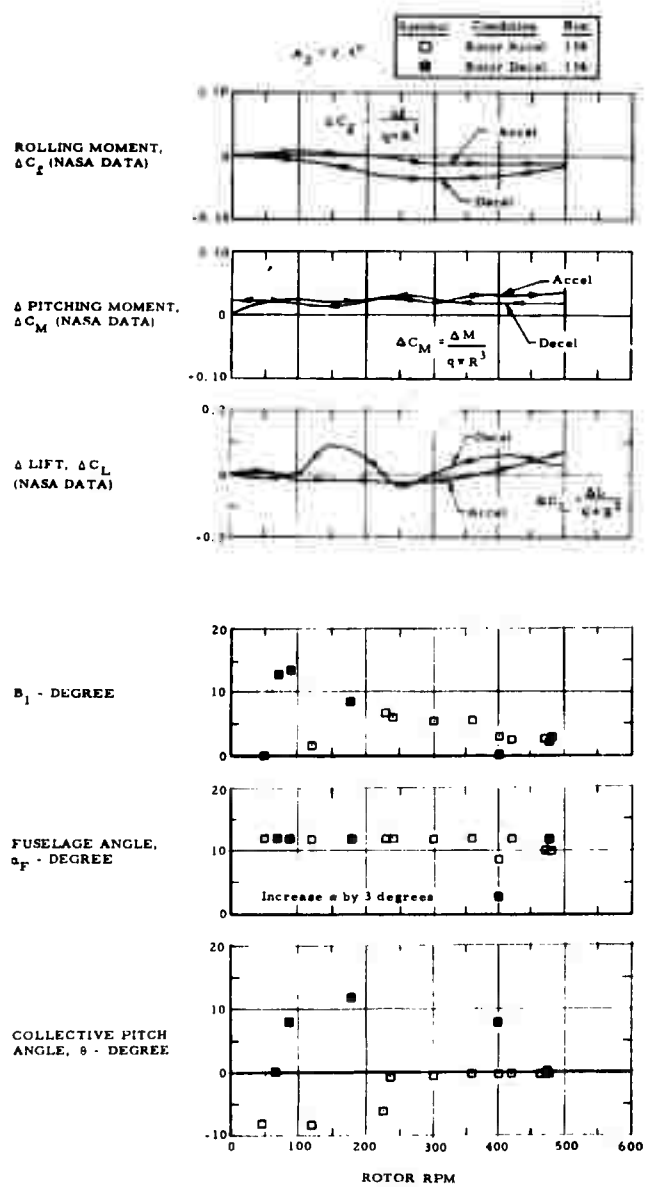

Figure 57. Aircraft Characteristics During Manual Conversion, Triangle Wing

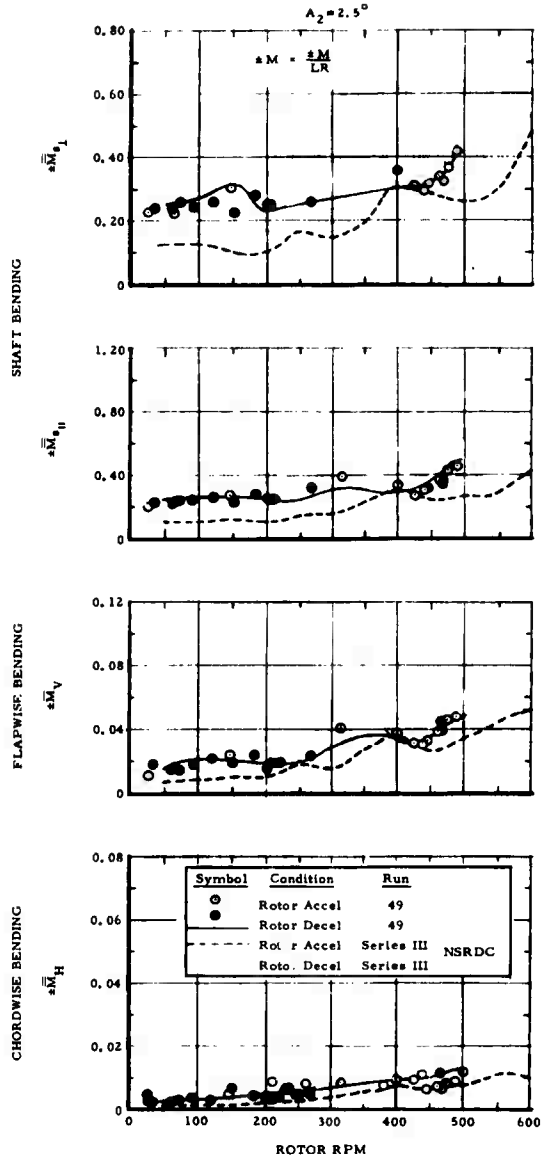

Figure 58. Alternating Blade Root and Shaft Bending Moments, Manual Conversion, Trisector Wing

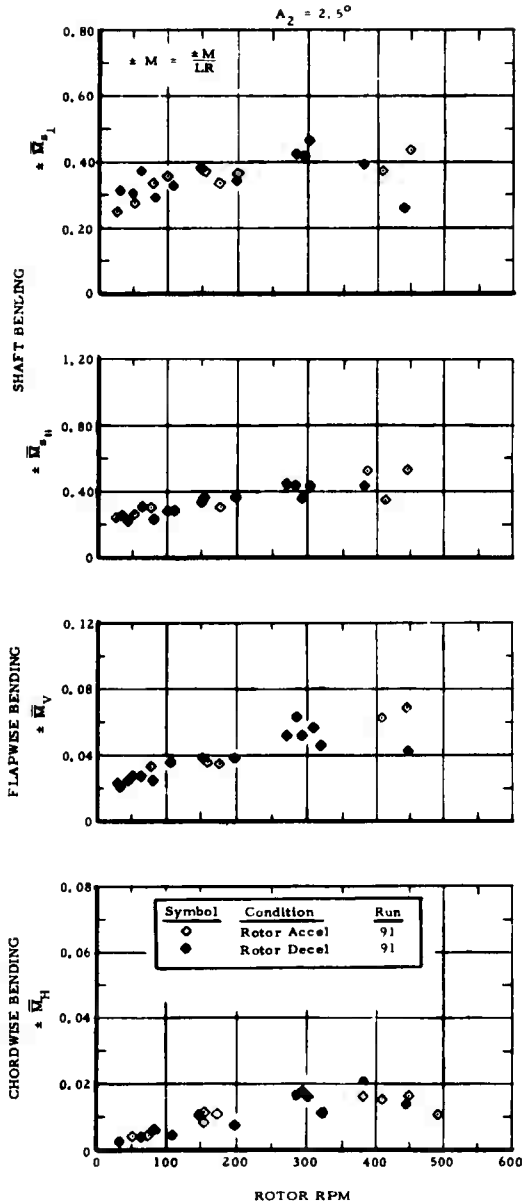

Figure 59. Alternating Blade Root and Shaft Bending Moments, Manual Conversion, Tricusp Wing

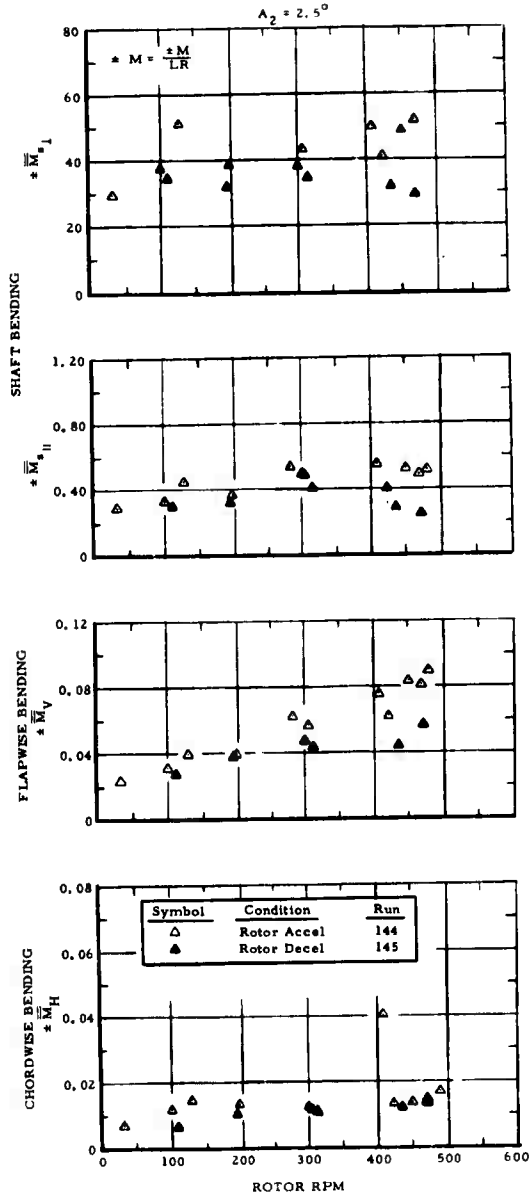

Figure 60. Alternating Blade Root and Shaft Bending Moments, Manual Conversion, Triangle Wing

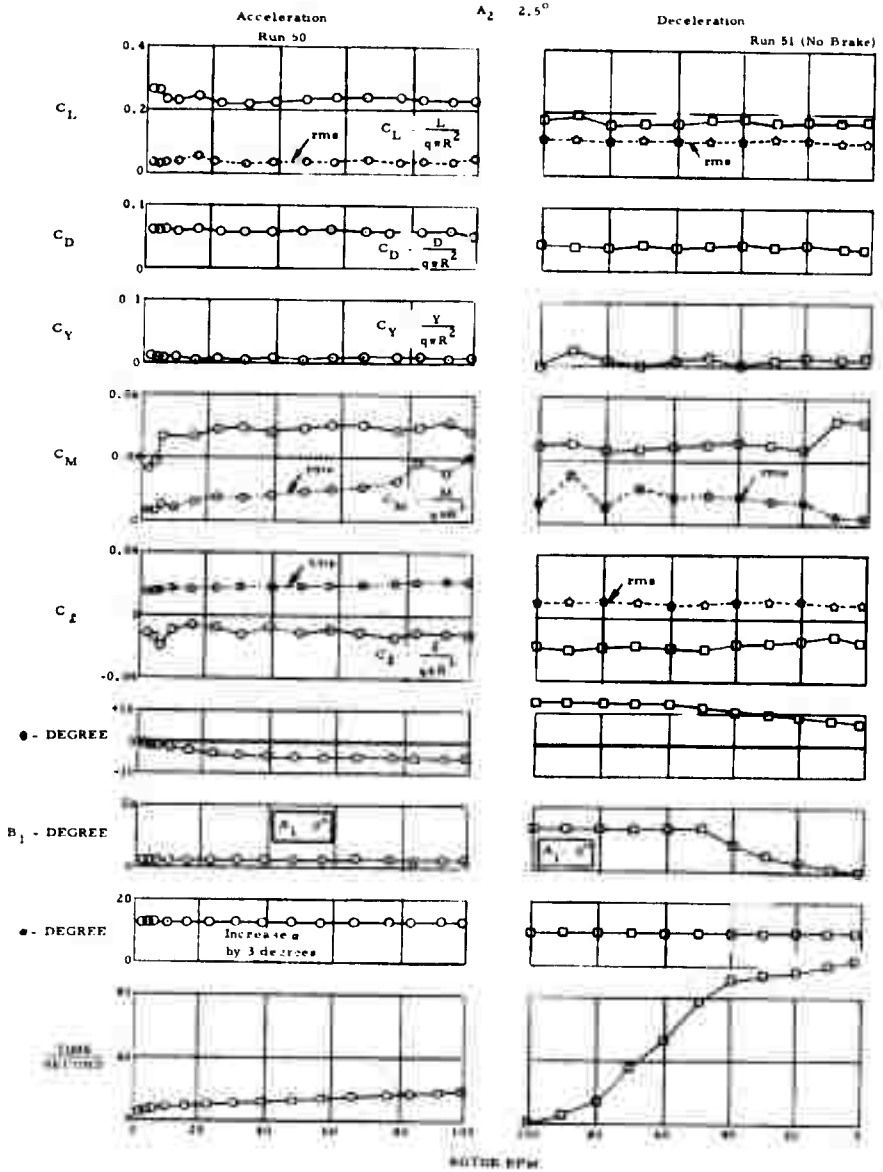

Figure 61. Conversion, Trisector Wing

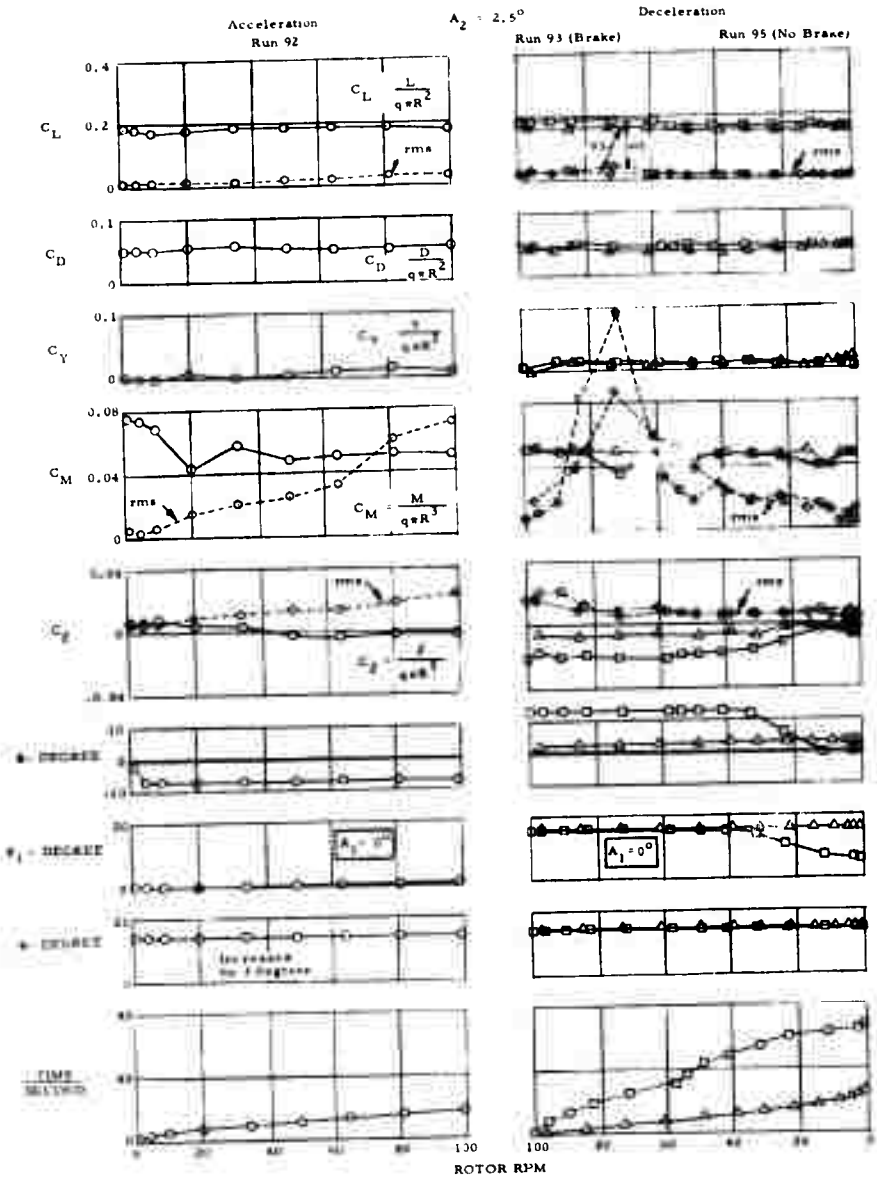

Figure 62. Conversion, Tricusp Wing

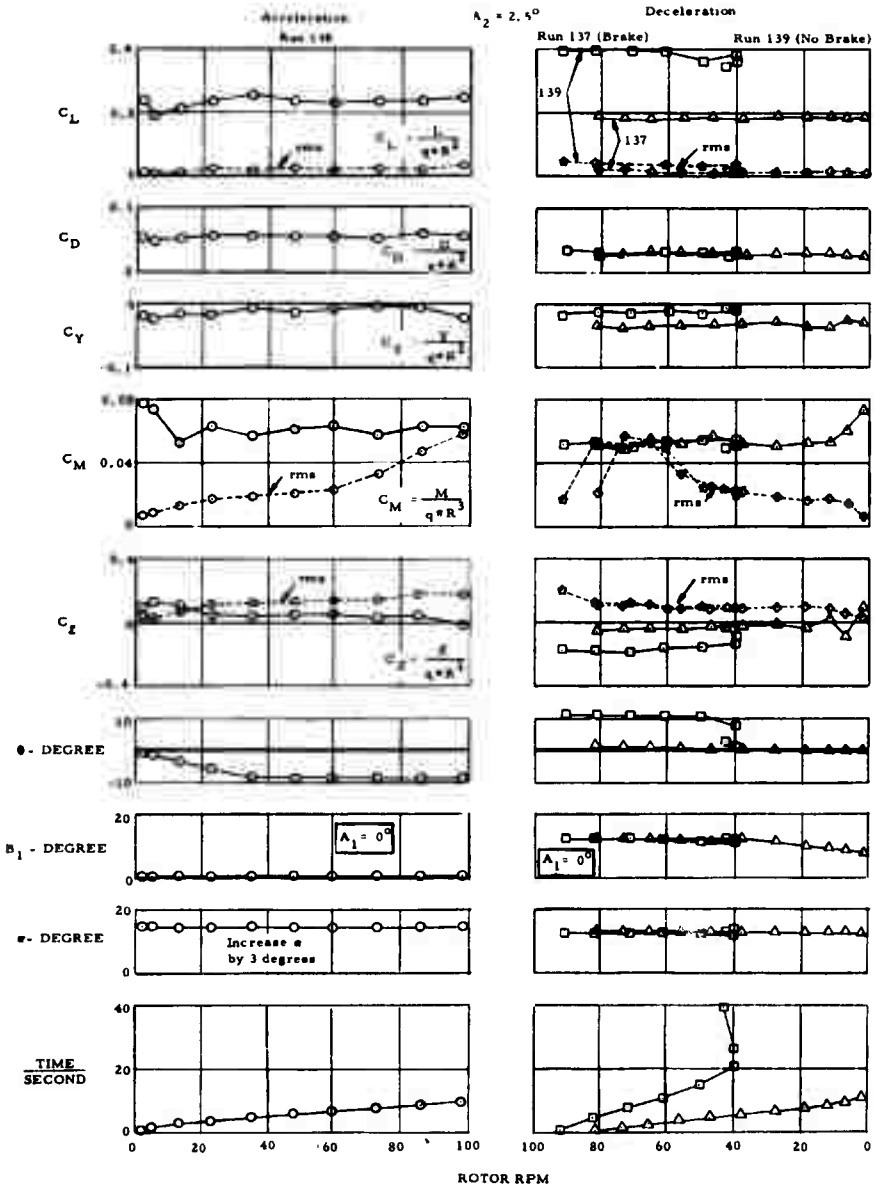

Figure 63. Conversion, Triangle Wing

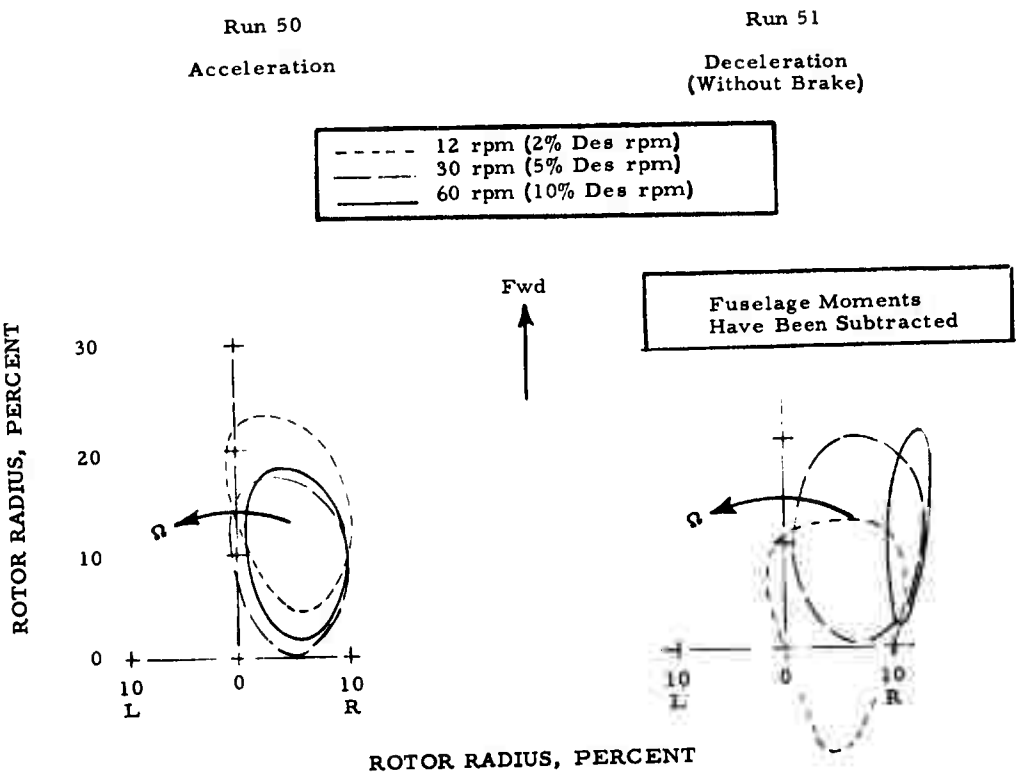

Figure 64. Center of Pressure Travel During Conversion, Trisector Wing

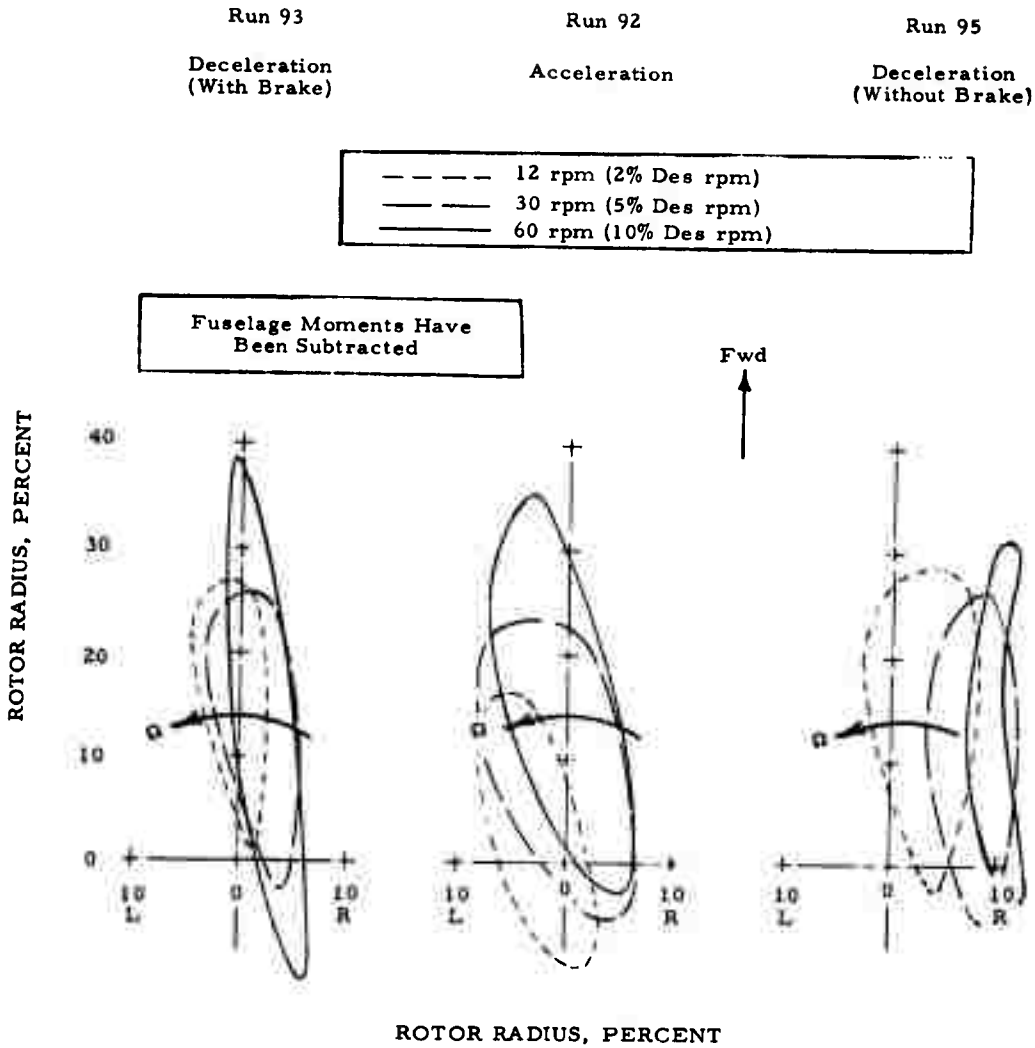

Figure 65. Center of Pressure Travel During Conversion, Tricusp Wing

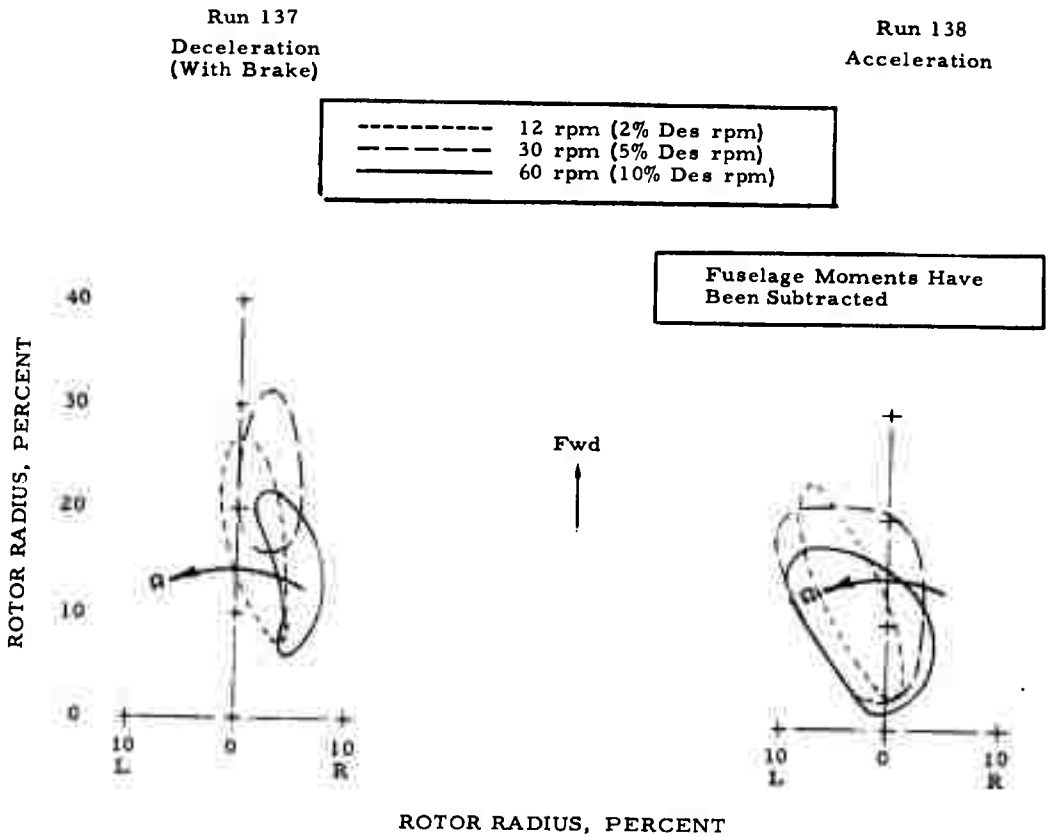

Figure 66. Center of Pressure Travel During Conversion, Triangle Wing

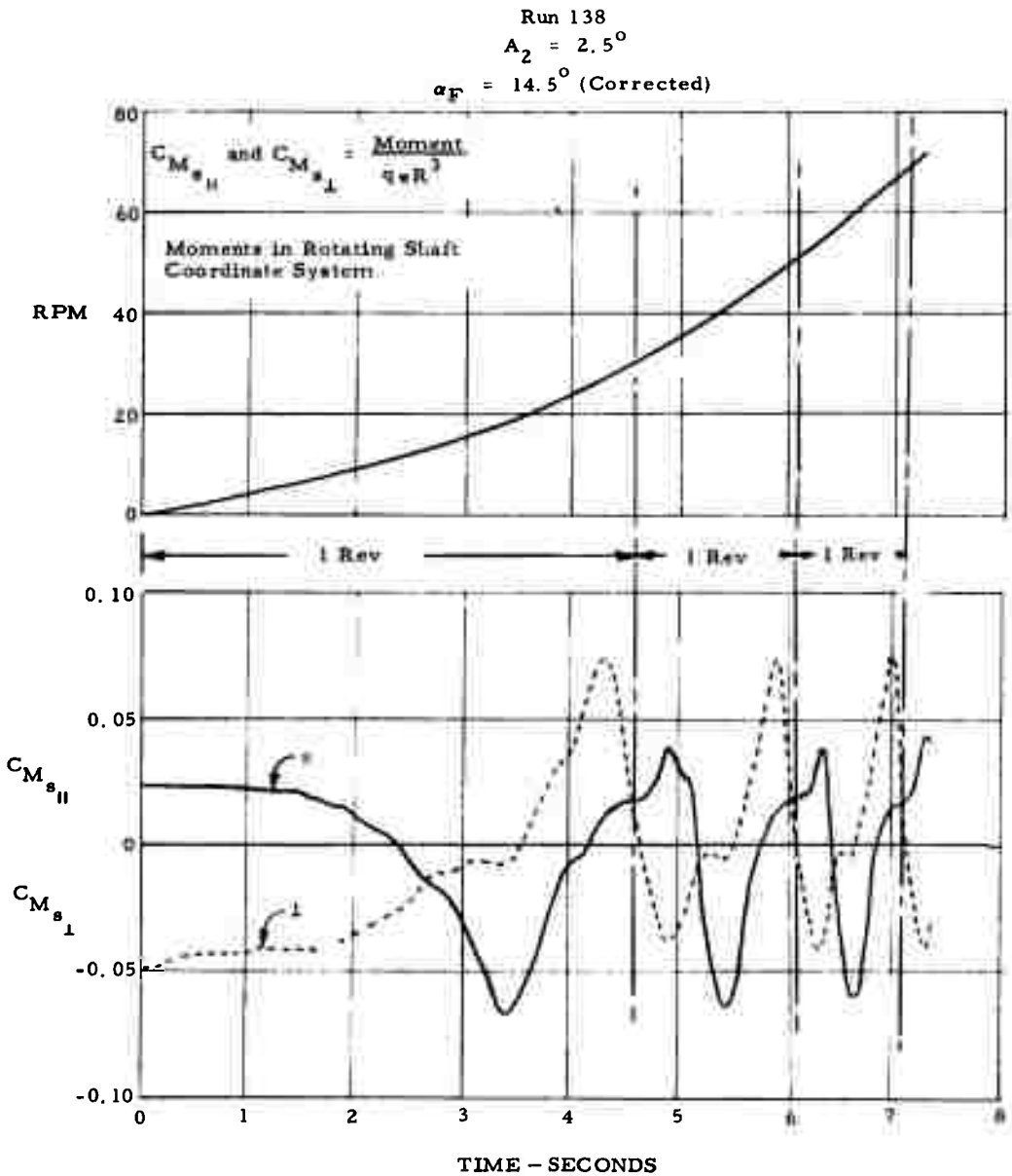

Figure 67. Rotor/Wing Shaft-Bending Moments, Triangle Rotor Start-Up

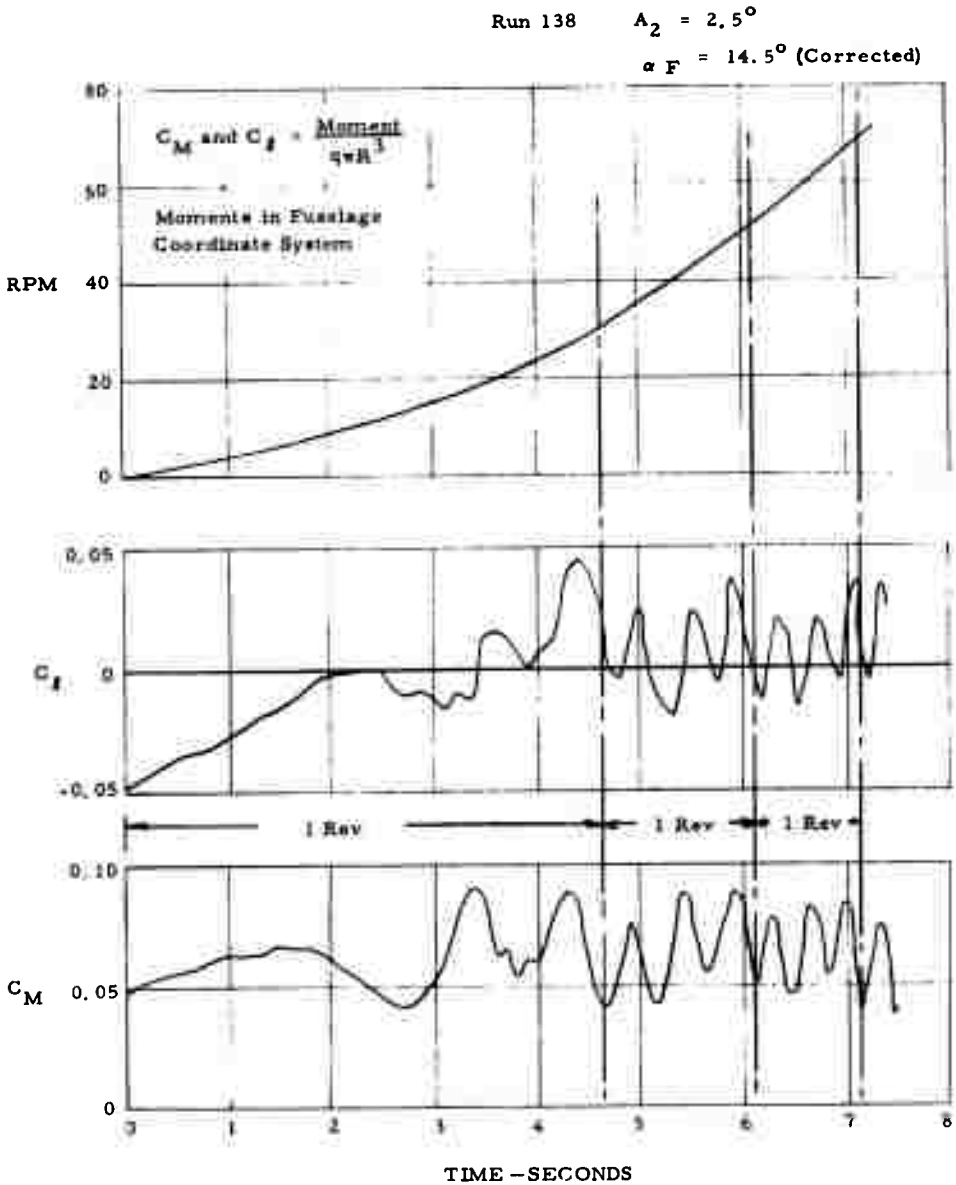

Figure 68. Rotor/Wing Rolling and Pitching Moments, Triangle Rotor Start-Up

Triangle Wing Start-Up
Based on Run 138

$A_2 = 2.5^{\circ}$

$\alpha_F = 14.5^{\circ}$ (Corrected)

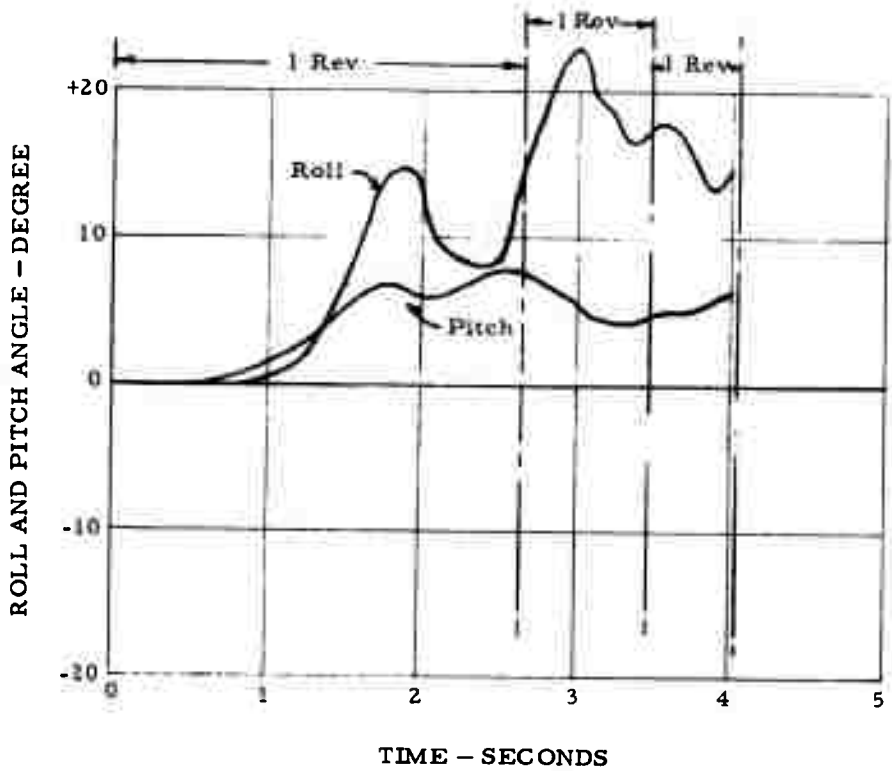

Figure 69. Full-Scale Rotor/Wing Aircraft Response, Triangle Rotor Start-Up

AIRPLANE MODE

The model was tested in the various configurations indicated in Figure 3. The Rotor/Wing was locked and sealed to the fuselage, a fairing block was sealed between the top of the fuselage and forward rotor blade, and a second fairing block was sealed between the wing and the aft portion of the fuselage.

As described previously on page 36, there is an angle of attack shift between the data measured in the Langley tunnel and in two different tunnels at NSRDC. Figure 70 shows a comparison of the concept model data for the trisector Rotor/Wing in the LRC 30-by-60-foot tunnel and in the 8-by-10-foot subsonic NSRDC tunnel. There is a shift in angle of attack of approximately -3 degrees for the LRC data, going from conditions of equal lift and pitching moment. Figure 71 shows a similar shift in the test data for triangle Rotor/Wing models when going from the NSRDC 7-by-10-foot transonic tunnel to the LRC 30-by-60-foot tunnel.

The lift and pitching moment characteristics of the three Rotor/Wing configurations are compared in Figure 72.

Tail effectiveness, that is, the lift and pitching moment increments developed by the horizontal tail in conjunction with the triangle Rotor/Wing, is plotted in Figure 73. Figure 74 compares the effective tail lift coefficient

$$\left[q_t/q \times C_{L_T}\right]$$

with values measured in Series III, IV, and V tests. All are quite similar.

The downwash angle at the horizontal tail is also shown in Figure 74. The downwash angle is a little greater than measured previously, but the slope with angle of attack is smaller; thus, the tail is more efficient.

The effectiveness of the horizontal tail in functioning as a roll control device, through differential deflection of the two sides, is shown in Figure 75. The roll control effectiveness increases with increasing angle of attack; this trend is the same as measured in the Series V transonic tests with the low-mounted horizontal tail, and just opposite the trend measured in the Series III tests for a high-mounted horizontal tail. A favorable yawing moment occurs with differentially deflected elevons on this low-mounted tail, rather than the more conventional adverse yaw that accompanies elevons on the T-tail or wing-mounted ailerons.

Figure 76 compares the yawing and rolling moments developed by differential horizontal tail deflection at a corrected fuselage angle of attack of +2 degrees. The tail effectiveness is similar for all cases except for the adverse yaw of the T-tail of Series III, and the Series VI yawing and rolling moments recorded at zero elevon deflection. This latter effect is thought to result from an error in the data recording, because with zero differential elevon deflection, the model was nominally symmetrical and could not develop moments of this magnitude. The adverse yaw for the T-tail and favorable yaw for the conventional tail differential deflection is explained by the positive and negative pressures that the deflected elevons develop. These are created in the presence of the vertical tail and act on the vertical tail in a manner to create the observed yawing moment.

An attempt was made to obtain tuft photographs to visualize the flow patterns on the three Rotor/Wings, but trouble with camera focus and exposure prevented obtainment of any meaningful pictures. The visually observed patterns for all three Rotor/Wings were quite similar to those reported in Reference 2 for the trisector wing.

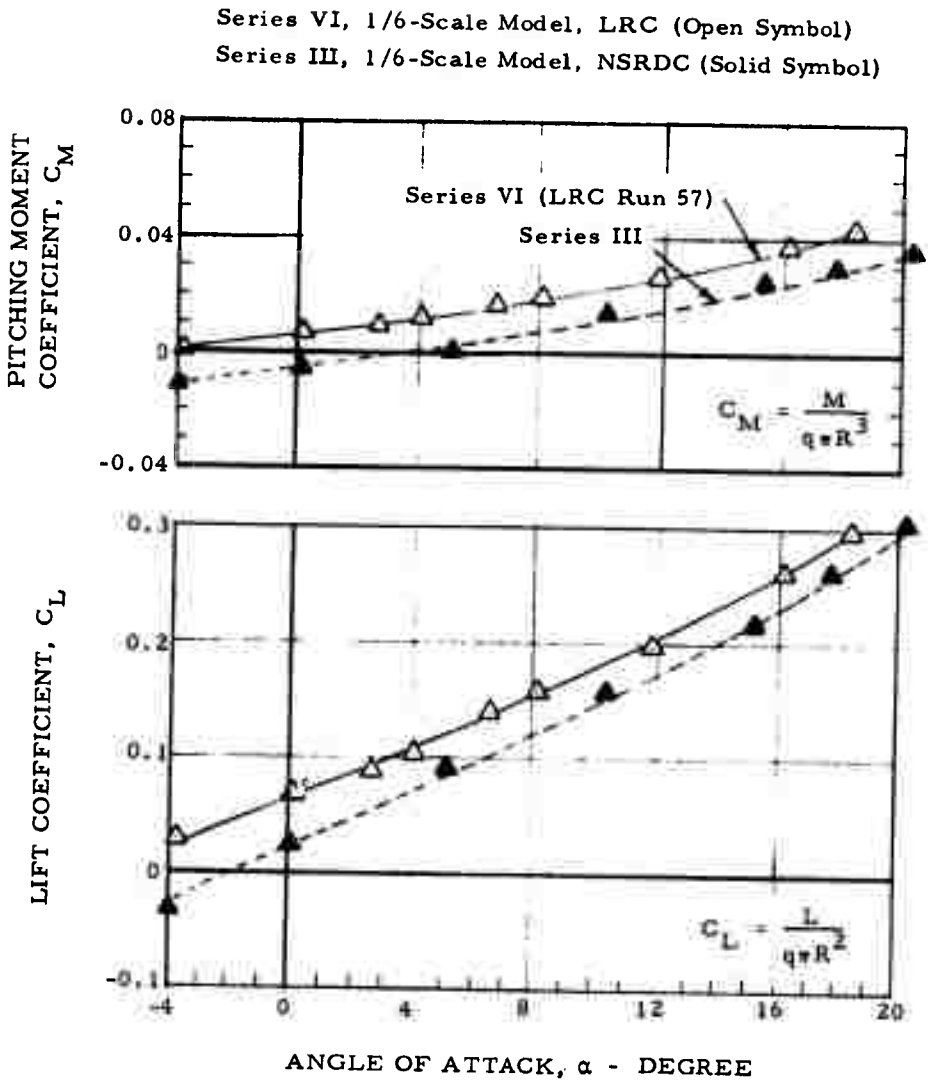

Increase α for Series VI by 3 degrees

Figure 70. Comparison in Airplane Mode, Tail-Off, Trisector Wing

Series VI, 1/6-Scale Concept Model, LRC (Open Symbol)
Series V, 1/15-Scale Transonic Model, NSRDC (Solid Symbol)

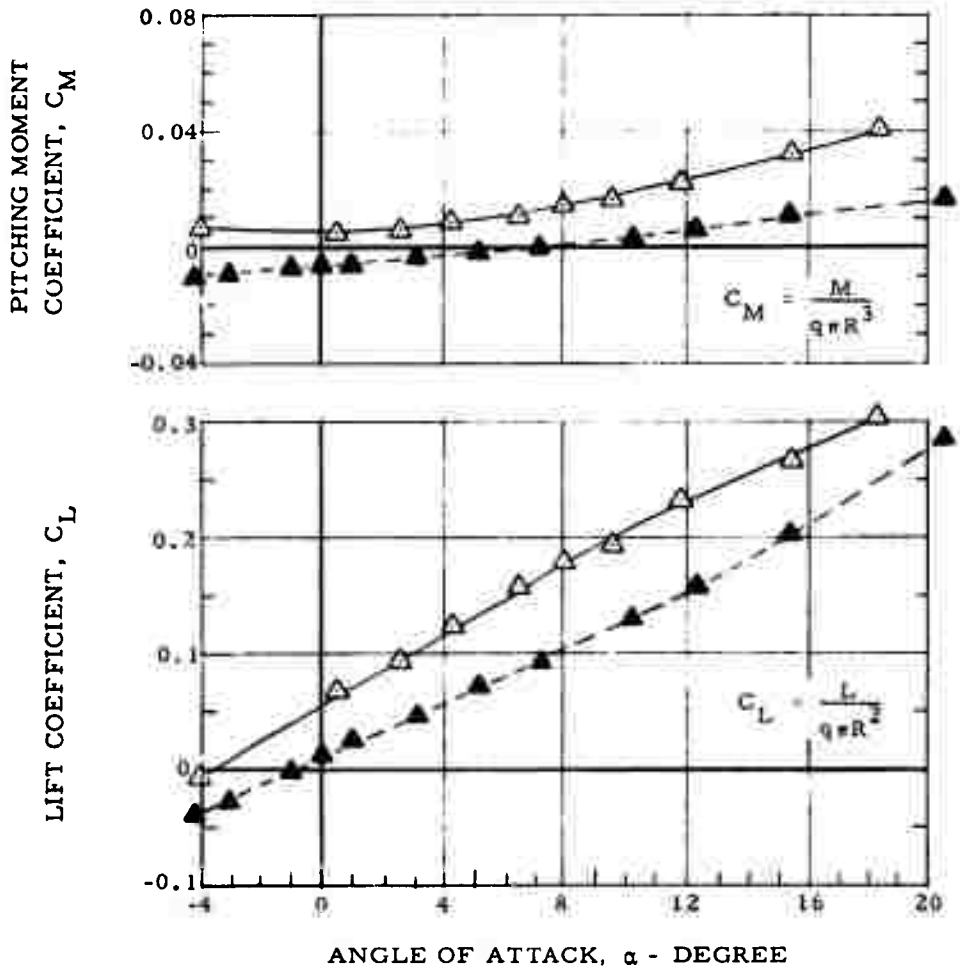

·Increase α for Series VI by 3 degrees

Figure 71. Comparison in Airplane Mode, Tail-Off, Triangle Wing

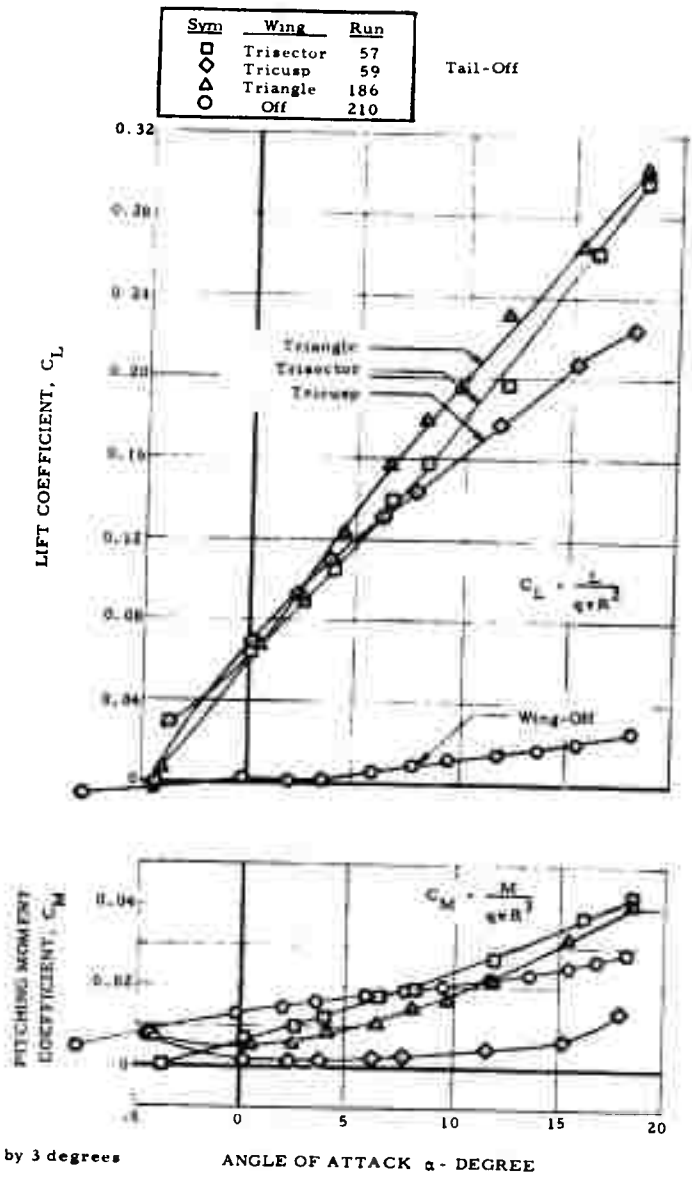

Increase α by 3 degrees

Figure 72. Planform Comparison, Airplane Flight

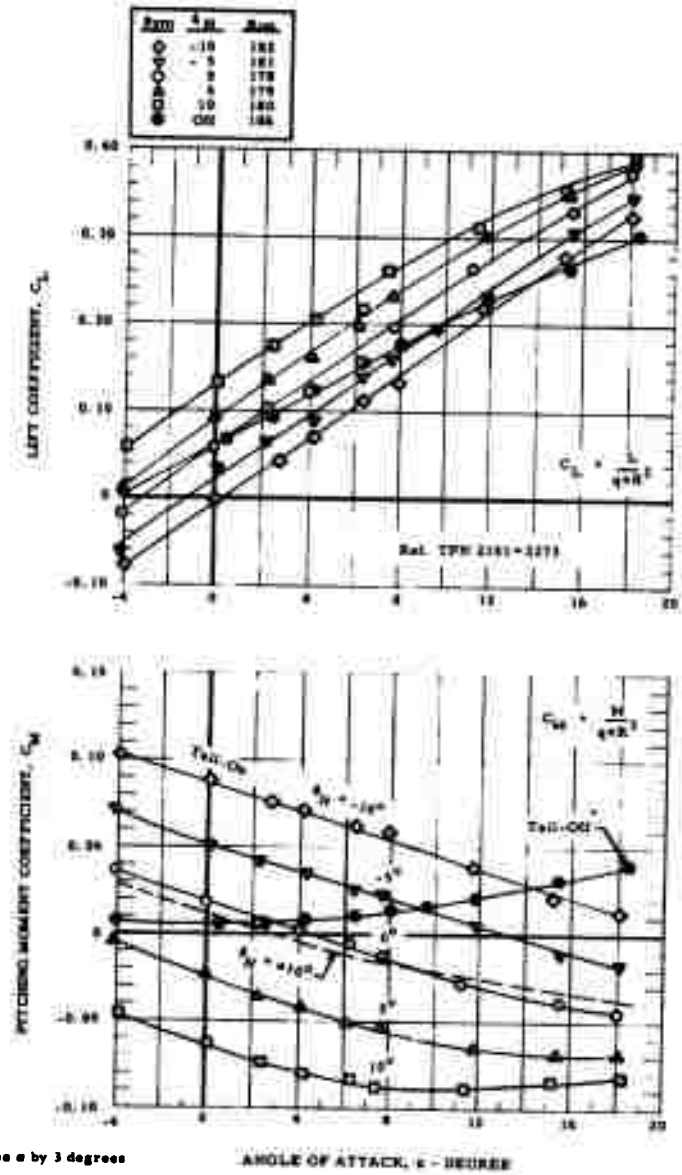

Figure 73. Tail Effectiveness, Airplane Flight, Triangle Wing

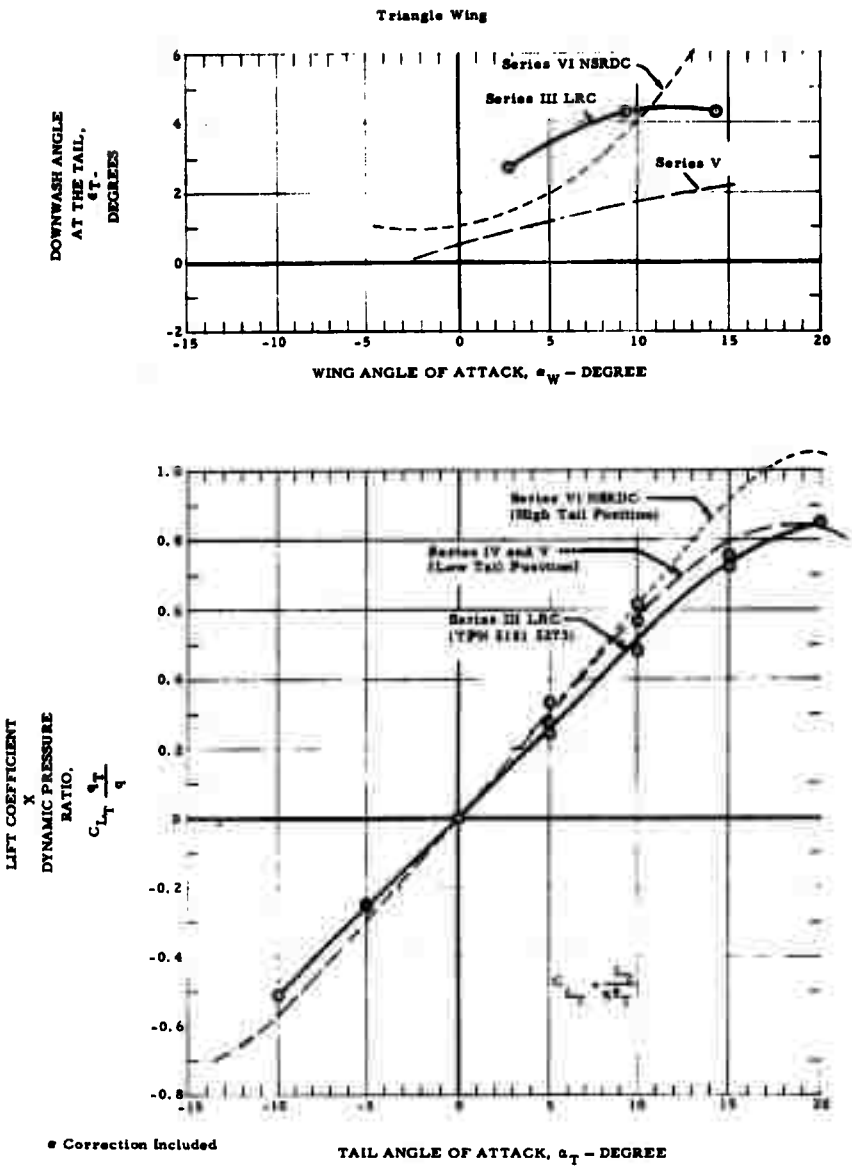

Figure 74. Horizontal Tail Characteristics, Airplane Flight

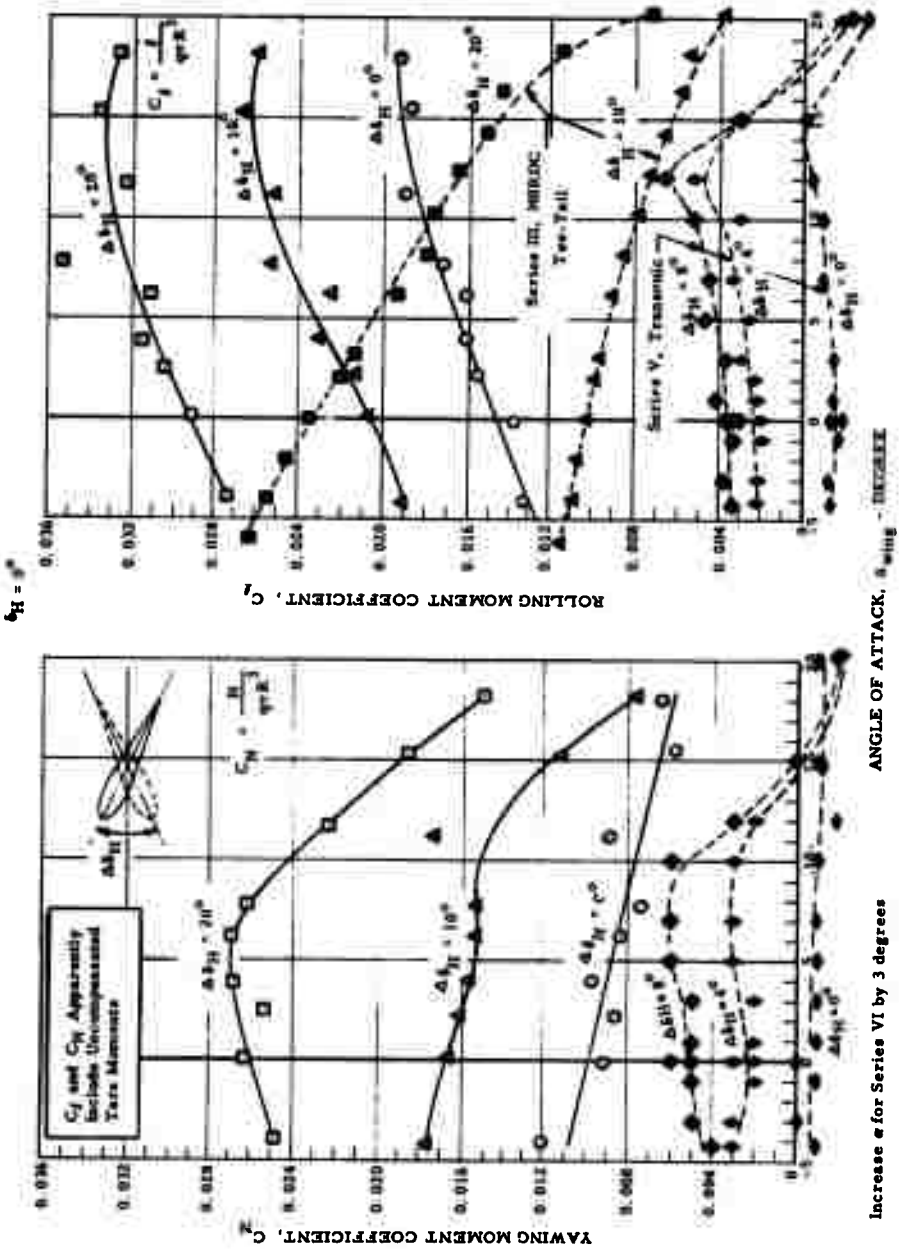

Figure 75. Yaw and Roll Due to Differential Elevon Deflection, Airplane Flight, Triangle Wing

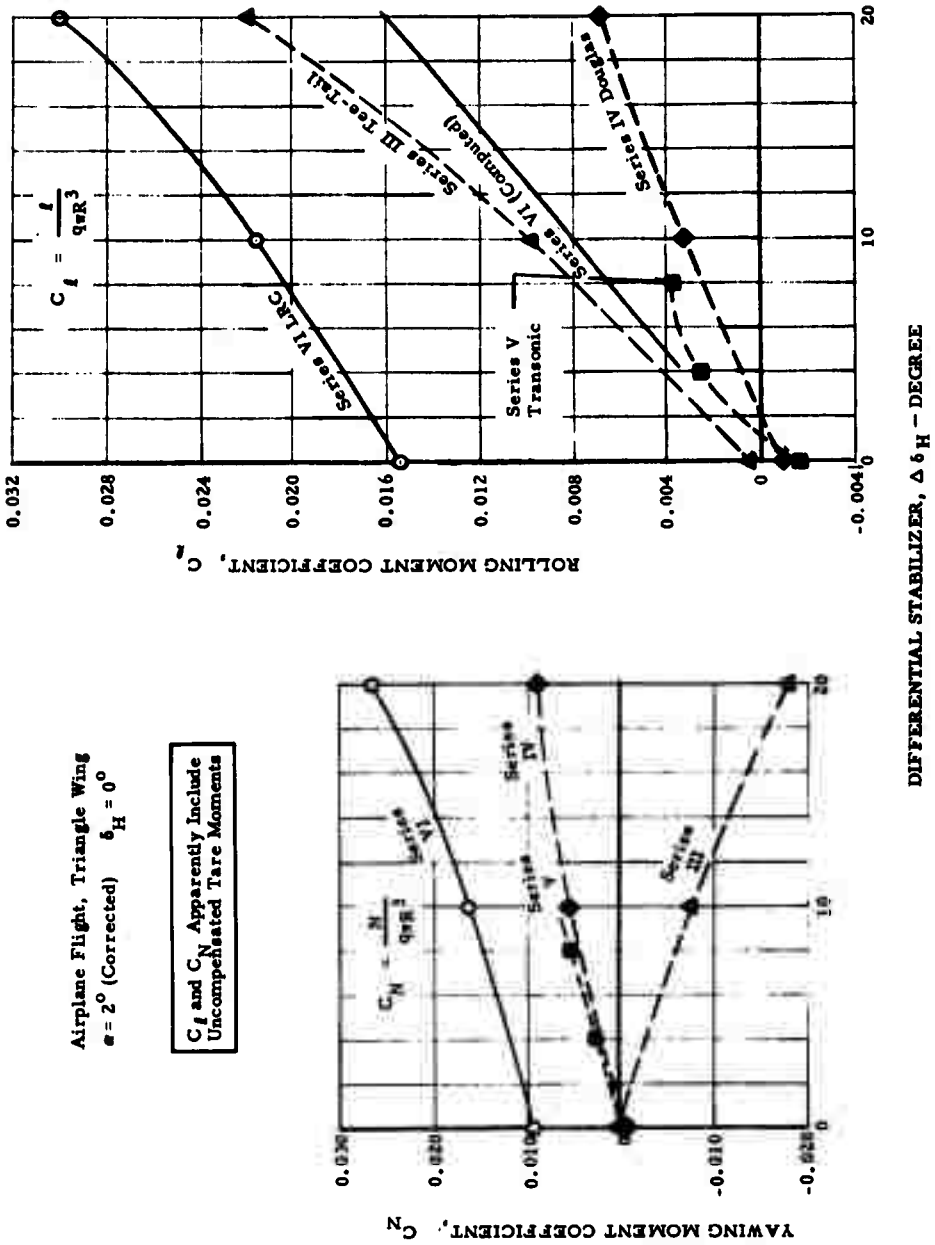

Figure 76. Comparison of Yaw and Roll Due to Differential Elevon Deflection

BLANK PAGE

ROTOR/WING AERODYNAMIC ANALYSIS

HTC-AD has studied the application of analytical methods for predicting aerodynamic performance and flying qualities of Hot Cycle Rotor/Wing aircraft, and has adopted methods that basically follow the classical methods established for conventional airplanes, helicopters, and autogyros, with special consideration given to the unique features of the Rotor/Wing. These methods are substantiated by the Rotor/Wing model test data available.

HOVERING POWER REQUIRED

Hovering power required for the aircraft is computed according to the method of Reference 6, but modified to handle the large centerbody of the Rotor/Wing. The method has been verified by whirlstand tests of model Rotor/Wings and of a conventional rotor. The calculation procedure has been programmed for an electronic digital computer. Figure 77 outlines the entire procedure.

FUSELAGE DOWNLOAD

The fuselage download arises from the impingement of the Rotor/Wing slipstream determined by net Rotor/Wing thrust concentrated in an annulus defined by an inner radius equal to that of the blade root and an outer-radius (less tip loss) of 0.97-percent radius. It is assumed that full slipstream velocity has been achieved at the fuselage surface. These Rotor/Wing slipstream characteristics have been generally confirmed by unpublished wake survey measurements made of the Rotor/Wing during the Series I whirlstand tests.

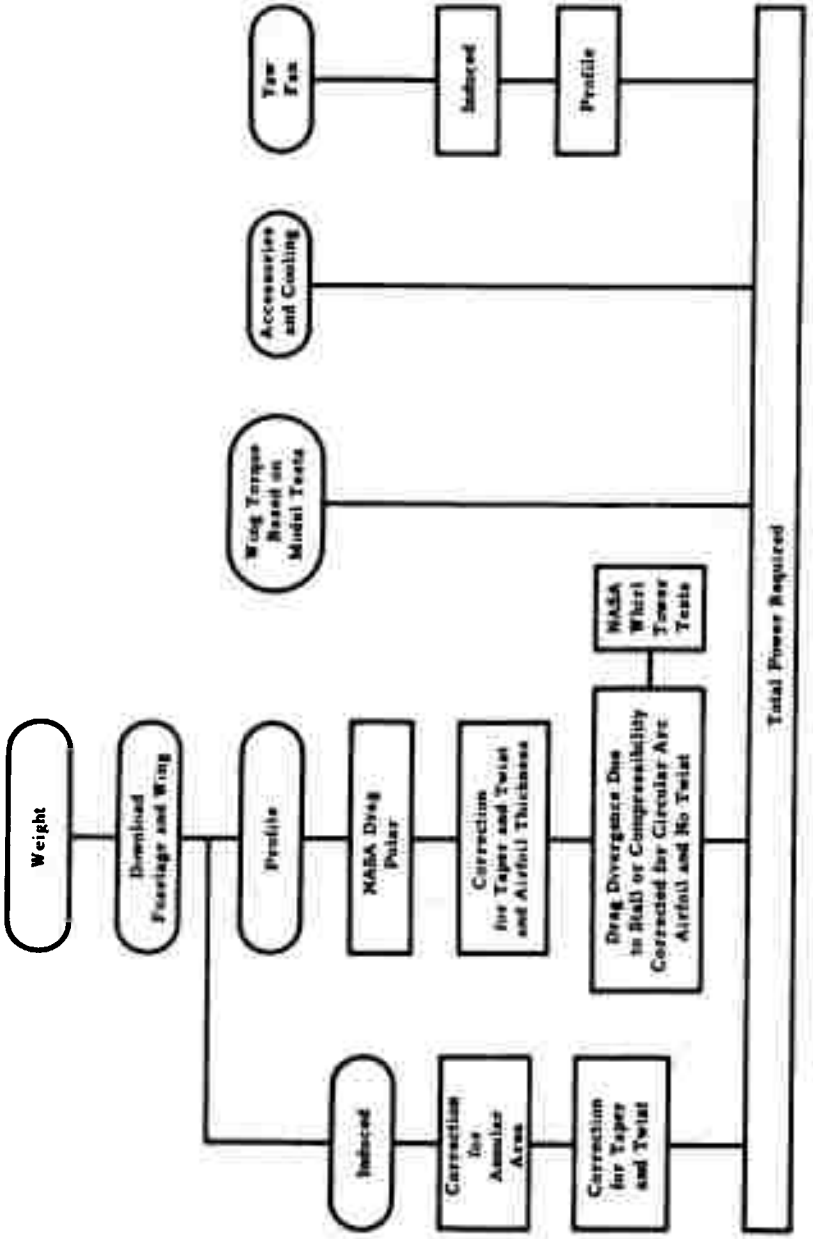

Figure 77. Hover Performance, Power Required

The calculation procedure for fuselage download is as follows:

Wake Velocity and Dynamic Pressure

First, assume the download is, say, five percent

$$T = GW\left(1 + \frac{\text{percent download}}{100}\right)$$

Calculate the slipstream velocity in the wake

$$v_{wake} = 2\sqrt{\frac{T}{2\rho\pi R^2}}$$

and the dynamic pressure in the wake

$$q_{wake} = \frac{T}{\pi(R^2 - e^2)}$$

The Rotor/Wing downwash impinges on a segment of the fuselage near the nose and on another near the tail in the region spanning the annulus swept out by the contracted slipstream, thus creating the hovering download. In these areas, the fuselage is generally a smooth rectangular box with rounded corners. The drag coefficients for the two segments are estimated from Reference 7, using the appropriate fineness ratio, corner radius, and Reynolds number, where RN is based on the fully-contracted slipstream velocity and the equivalent height of the fuselage segment:

$$RN_b = \frac{(h_{equiv})(V_{wake})}{\nu}$$

The download is based on this drag coefficient, the dynamic pressure in the slipstream, and the projected area of the fuselage in the slipstream:

$$DL = q_{wake} \left[C_{D_0}{}_{fwd} S_{fwd} + C_{D_0}{}_{aft} S_{aft} \right]$$

This download, expressed as a percentage of rotor thrust, is used to verify the originally estimated download.

ROTOR INDUCED TORQUE

The Rotor/Wing configuration has a large centerbody that is equivalent to a large root cutout in a conventional rotor. In order to correctly account for this cutout, the induced torque must be integrated from the blade root radius, $\bar{a} = e/R$, to the effective tip radius, BR, instead of the usual range from 0 to BR, where B is the tip loss factor. The derivation of the induced torque equation used in the Rotor/Wing hover analysis is described below; it follows the procedure of Reference 6.

$$T = \int_{\bar{a}}^{b} b \frac{\rho}{2} \Omega^2 R^3 a \times (\theta_t - \phi_t) R dx \quad \text{equation 20, Reference 6}$$

Integrating this equation:

$$T = b \frac{1}{2} \rho \Omega^2 R^3 a (\theta_t - \phi_t) C \left(\frac{B^2 - \bar{a}^2}{2} \right) = C_T \pi R^2 \rho (\Omega R)^2$$

where $\bar{a}$ = (blade root radius/tip radius) ratio

Let $\sigma = \frac{bc}{\pi R}$

Then

$$\frac{C_T}{\left(B^2 - \bar{a}^2\right)} = \frac{\sigma a}{4} (\theta_t - \phi_t)$$

or

$$(\theta_t - \phi_t) = \frac{4\,C_T}{\sigma a\left(B^2 - \bar{a}^2\right)}$$

and

$$\theta_t = \phi_t + \frac{4C_T}{\sigma a\left(B^2 - \bar{a}^2\right)}$$

From equation 15, Reference 6

$$\phi_x = \frac{\sigma a}{16x}\left(-1 + \sqrt{1 + \frac{32\,x\,\theta_x}{\sigma a}}\right)$$

$\phi_t = x\,\phi_x$ and $\theta_t = x\,\theta_x$, assuming ideal twist

Then

$$\phi_t = \frac{\sigma a}{16}\left(-1 + \sqrt{1 + \frac{32\,\theta_t}{\sigma a}}\right)$$

substitute for θ_t in terms of C_T

$$\phi_t = -\frac{\sigma a}{16} + \frac{\sigma a}{16}\sqrt{1 + \frac{(32)\,(4)\,C_T}{\sigma^2 a^2 (B^2 - \bar{a}^2)} + \frac{32\,\phi_t}{a\sigma}}$$

$$\phi_t + \frac{\sigma a}{16} = \sqrt{\frac{\sigma^2 a^2}{16^2} + \frac{(32)\,(4)\,C_T\sigma^2 a^2}{(16)^2\,\sigma^2 a^2 (B^2 - \bar{a}^2)} + \frac{\sigma^2 a^2\,(32)\,\phi_t}{\sigma a\,(16)^2}}$$

squaring both sides and cancelling terms

$$\phi_t^2 + \frac{2\,\sigma a\,\phi_t}{16} + \frac{\sigma^2 a^2}{(16)^2} = \frac{\sigma^2 a^2}{(16)^2} + \frac{C_T}{2\,(B^2 - \bar{a}^2)} + \frac{\sigma a\,\phi_t}{8}$$

$$\phi_t = \sqrt{\frac{C_T}{2(B^2 - \bar{a}^2)}}$$

According to equation 24, Reference 6.

$$Q_i = \int_{\bar{a}}^{B} b \frac{1}{2} \rho \Omega^2 R^4 a \times (\theta_t - \varphi_t) \varphi_t \, cdx$$

$$Q_i = b \frac{1}{2} \rho \Omega^2 R^4 a (B^2 - \bar{a}^2) (\theta_t - \phi_t) \phi_t \, cdx = C_{Q_i} \pi R^2 \rho (\Omega R)^2 R$$

$$C_{Q_i} = \frac{(B^2 - \bar{a}^2)}{4} \sigma a (\theta_t - \varphi_t) \varphi_t$$

substituting for $(\theta_t - \varphi_t)$ and θ_t above

$$C_{Q_i} = \frac{(B^2 - \bar{a}^2)}{4} \sigma a \left(\frac{4 C_T}{a (B^2 - \bar{a}^2)} \right) \sqrt{\frac{C_T}{2(B^2 - \bar{a}^2)}}$$

canceling terms

$$C_{Q_i} = \frac{C_T^{\frac{3}{2}}}{\sqrt{2} \sqrt{B^2 - \bar{a}^2}}$$

This value of induced torque is derived assuming ideal twist or taper. The table on page 96 of Reference 6 presents a correction factor to be used to correct the induced torque for combinations of taper and the lack of twist. Typical Rotor/Wing blades have a 2.3:1 taper ratio, thus a factor C_i of 1.04 is added to the induced power, resulting in:

$$C_{Q_i} = \frac{C_i C_T^{\frac{3}{2}}}{\sqrt{2} \sqrt{B^2 - \bar{a}^2}} = \frac{C_i C_T^{\frac{3}{2}}}{B \sqrt{2} \sqrt{1 - \frac{\bar{a}^2}{B^2}}}$$

or, in another form:

$$\frac{C_{Q_i}}{C_i \, C_T^{3/2}/B\sqrt{2}} = \frac{1}{\sqrt{1 - \frac{\bar{a}^2}{B^2}}}$$

Figure 78 presents a plot of the ratio of induced torque as derived above for a Rotor/Wing to the induced torque for a standard rotor.

BLADE PROFILE TORQUE

The determination of Rotor/Wing blade profile torque is based largely on test data from model and full-scale rotors. The profile torque was determined by subtracting the induced torque (and for the case of the Rotor/Wing model the wing torque) from the total measured torque -- the induced torque being computed in the manner described above and the model wing torque being measured from blades-off whirl tests. Figure 79 shows the hovering profile torque determined from three rotor tests:

1. A small-scale Rotor/Wing model having circular arc blades
2. A small-scale helicopter rotor model having NACA 0015 blades
3. A full-scale helicopter rotor having NACA 0015 blades (Reference 8).

Model test data from the conventional rotor and Rotor/Wing show that both have essentially the same blade profile torque, compared on a blade-loading basis. This indicates that the circular arc blades used on the Rotor/Wing have very nearly the same profile drag characteristics as the more conventional NACA 0015 blades.

The full-scale data were obtained from a NASA Langley Research Center tower test of a conventional helicopter rotor having NACA 0015 blades. Because the model Rotor/Wing exhibits the same profile torque as the conventional rotor model, it follows that the full-scale Rotor/Wing should have a

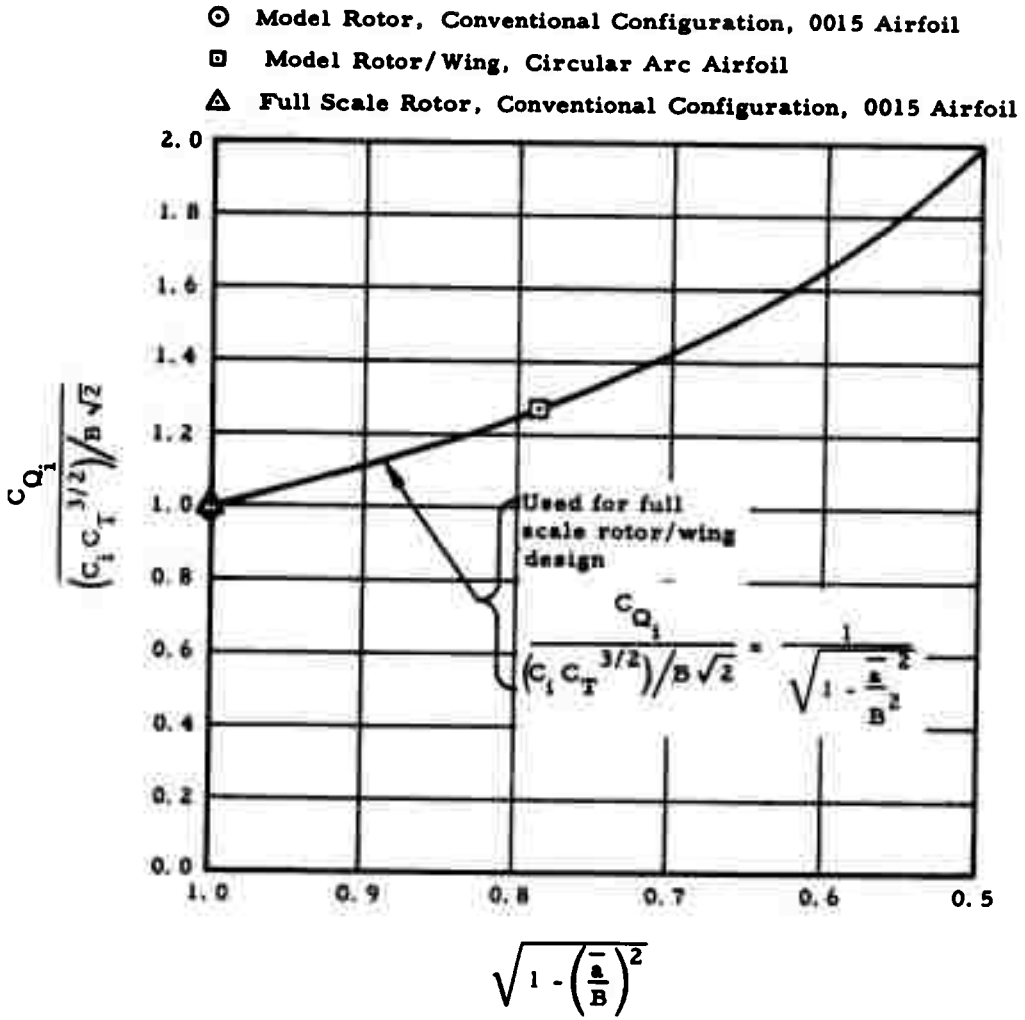

Figure 78. Hovering Performance, Induced Power

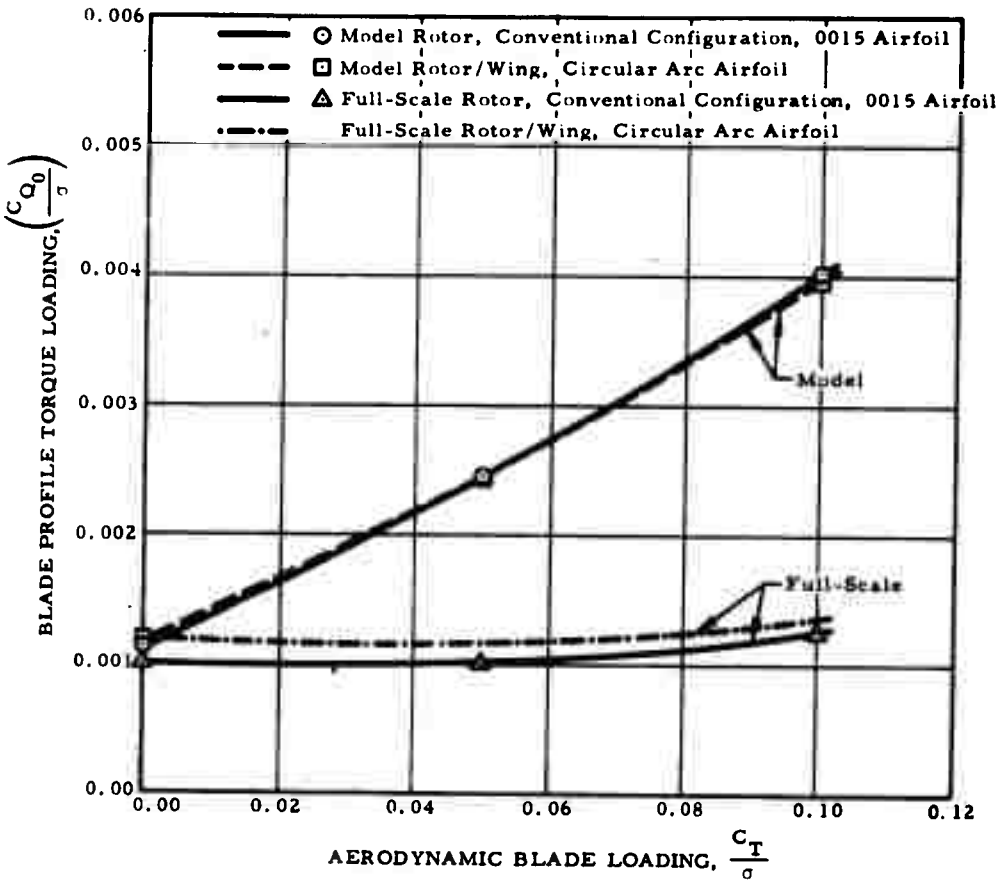

Figure 79. Hovering Performance, Profile Power

profile torque characteristic similar to that of a conventional rotor. However, for initial conservatism with the novel Rotor/Wing, the full-scale Rotor/Wing profile torque is increased slightly above that of the conventional rotor as indicated in Figure 79.

WING HOVER TORQUE

Hovering torque for the wing portion of the Rotor/Wing is derived from whirl tower testing.

The analysis is based on the assumption that the wing may be considered to be made up of a combination of a circular disc centerbody with three blade segments attached, as indicated in Figure 80.

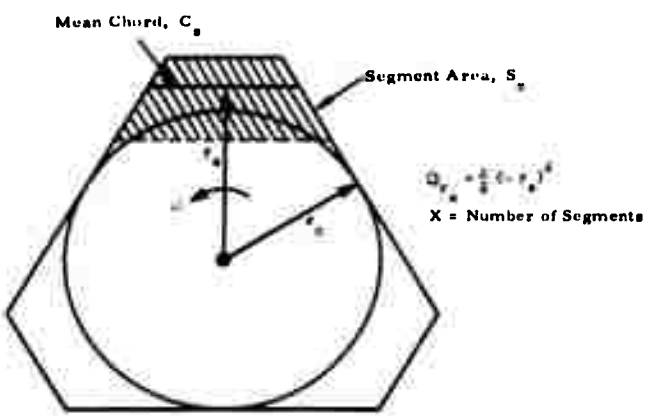

Figure 80. Dimensional Characteristics, Triangular Model Wing

Torque for the circular midsection is calculated using rotating disc theory and data of Reference 9 where Reynolds number based on disc radius is an important parameter.

$$\text{Disc Reynolds number, } RN_{r_c} = \frac{V_{r_c}}{\nu} = \frac{2\pi\, r_c\, n\, r_c}{\nu}$$

Using the equation and terminology of Reference 9 for full turbulent flow, the torque coefficient varies with RN_{r_c}:

$$C_{Q_c} = \frac{0.146}{(RN_{r_c})^{1/5}}$$

from which the disc contribution to centerbody torque is:

$$Q_c = C_{Q_c} \frac{\rho}{2} (\Omega r_c)^2 r_c^3$$

The segment drag coefficient, and consequently the segment torque, is a function of the turbulent flat plate drag of the segment:

$$Q_s = x\ C_{D_0} q_{r_s} S_s r_s$$

and C_{D_0} is determined by the Reynolds number of the segment, as defined by the length of the mean chord of the segment and the rotational velocity of the midpoint of the mean chord:

$$RN_S = \frac{\Omega r_s C_s}{\nu}$$

Comparing model C_{D_0} calculated in this manner with the minimum turbulent section drag coefficient data from Figure 66 of Reference 10, shows the model C_{D_0} to be 2.05 times greater than the classical drag coefficient. This multiplying factor of 2.05 is then used in computing the full-scale Rotor/Wing wing hover torque.

Whirl tower test data for two Rotor/Wing models are shown in Figure 81. The model data were obtained at the r/R values indicated by the data point; the curves were calculated by the above method.

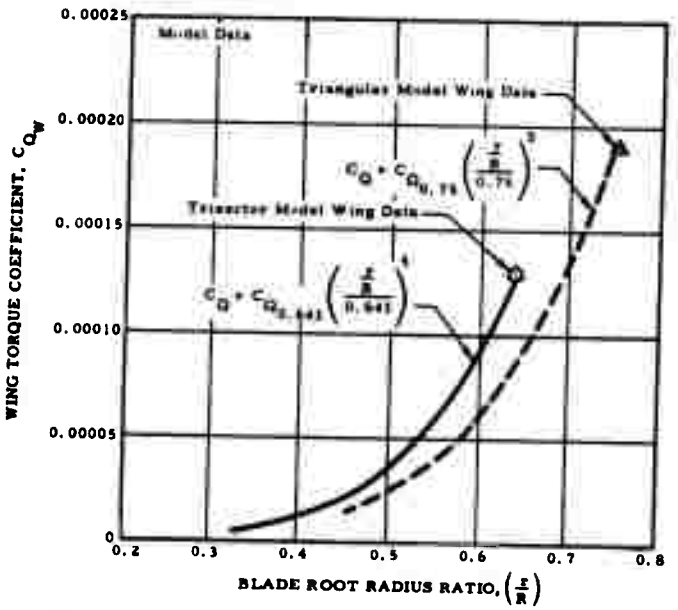

Figure 81. Variation of Wing C_Q with r/R, Hovering Conditions

YAW FAN

The Rotor/Wing also drives a yaw fan for directional control in the running-rotor flight modes. Inasmuch as the Rotor/Wing is tip-driven, the yaw fan thrust during steady flight only counteracts the torque for seal and bearing drag, accessory drive, and the yaw fan itself. By estimating the yaw fan power, the necessary thrust can be computed. The yaw fan power is estimated to be approximately one percent of Rotor/Wing power, assuming a mechanical drive efficiency of 95 percent.

The yaw fan may be considered to be a conventional rotor that is amenable to analysis by classical rotor performance calculation methods such as that of Reference 6. The yaw fan induced power is computed from the method of Reference 6, using an annular area obtained after applying a three percent

radius tip and root loss to the blades. The blades are untwisted and untapered, so the correction factor for twist and taper from Reference 6 is applied to the induced power.

The yaw fan profile power is computed using equation 33 on page 83 of Reference 6. The blade loading is based on a thrust-weighted solidity with a tip and root loss of three percent, and the torque is based on a torque-weighted solidity over the entire blade. A drag divergence factor derived from flight test is used when appropriate.

GROUND EFFECT

Whirl tests of the model Rotor/Wing indicate that the ground effect is greater than that of a conventional rotor as indicated in Figure 82. Rolling takeoffs at elevated gross weight are made in the helicopter mode flying close to the ground and taking advantage of this ground effect.

VERTICAL CLIMB

The vertical climb rate is computed using equation 36 on page 83 of Reference 6, modified to apply to the Rotor/Wing configuration. In this method, the total power required for climb equals the sum of the profile power, induced power reduced to account for the vertical inflow into the Rotor/Wing, and power required to lift the aircraft at the climb velocity. The increased download on the fuselage and elevons is also accounted for.

The profile power computation method is unchanged from the method used during steady hovering flight. The induced torque coefficient is computed by the following equation, which is consistent with the steady hovering analysis:

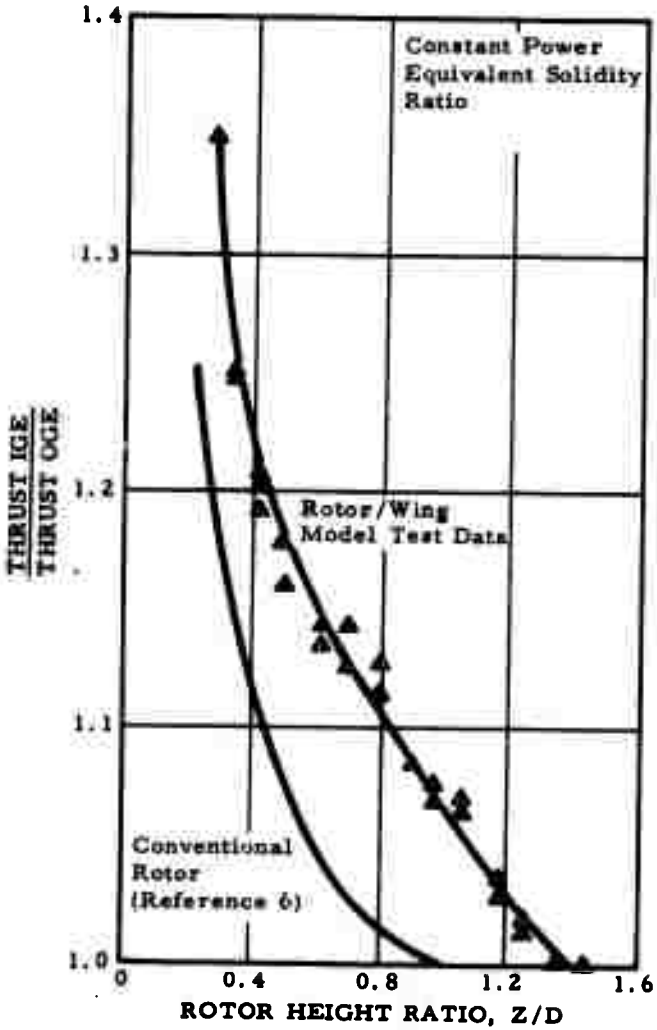

Figure 82. Ground Effect Test Results

$$C_{Q_i} = \frac{1}{4} C_T \sqrt{\left(\frac{V_v}{\Omega R}\right)^2 + \frac{2\,C_T}{\left(1 + \frac{\bar{a}^2}{B^2}\right)}} + \frac{1}{2}\left(\frac{V_v}{\Omega R}\right) C_T$$

where C_T is based on total rotor thrust, including the effects of download.

WHIRL TOWER MODEL SUBSTANTIATION OF HOVERING PERFORMANCE COMPUTATIONAL METHOD

The calculation of overall power required for the model, compared with whirl-stand test data as shown in Figure 83, demonstrates that the above method of determining the power required for hovering is satisfactory. The effect of going to full scale is also indicated.

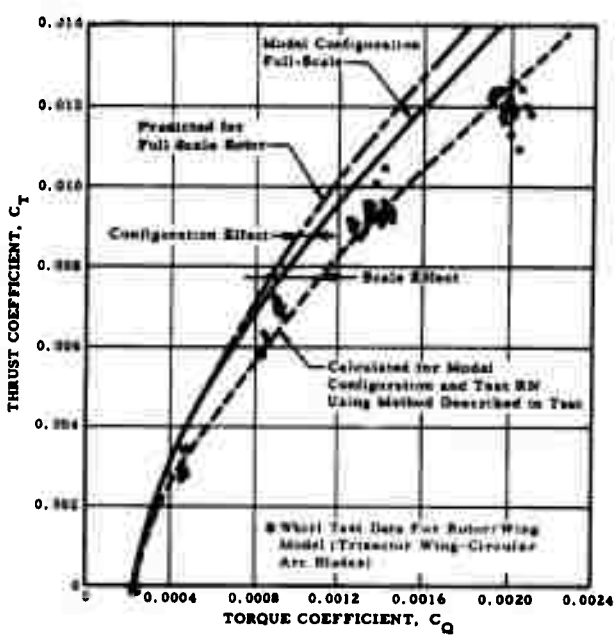

Figure 83. Comparison, Typical Full-Scale Rotor/Wing Hover Power and Model Test Data

AIRPLANE FLIGHT POWER REQUIRED

The power required for flight in the airplane mode is determined in the classical manner of establishing the drag polar of the aircraft and then converting drag and airspeed into power required:

$$HP_{reqd} = \frac{1}{325} C_D q S_w V_{(knots)}$$

The discussion presented here is specifically for a configuration shown schematically in Figure 84; the drag for any other basic configuration, such as a twin tailboom arrangement, would be determined in a similar manner, but with appropriate allowances made for features of the specific configuration.

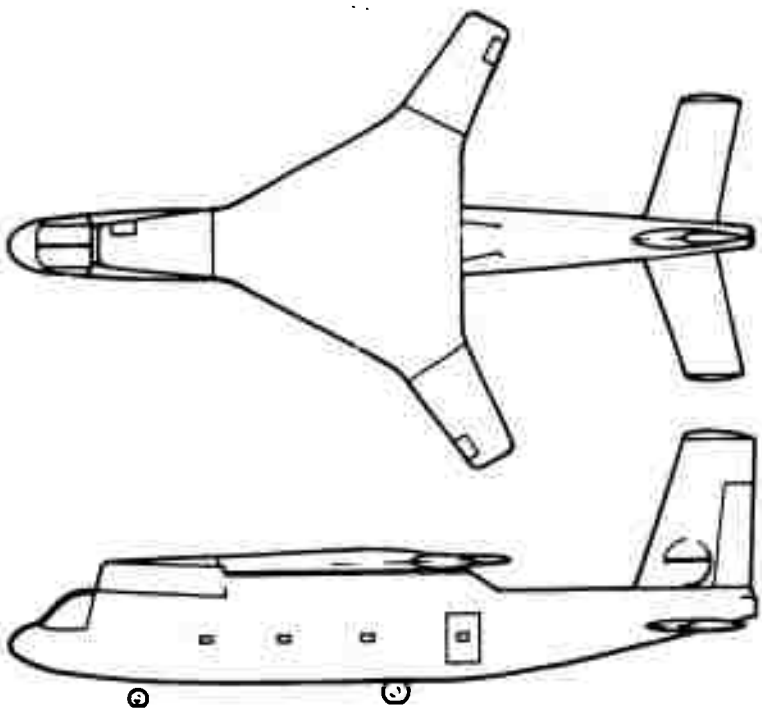

Figure 84. Typical Rotor/Wing Aircraft Configuration

For flight in the airplane mode, the aircraft is assumed to be in the "clean" condition; that is, landing gear retracted, Rotor/Wing locked and faired to the fuselage, yaw fan doors closed, engine inlet in the airplane configuration, and all seals in place.

The approach used in determining the airplane drag polar is to compute a polar using classical methods, match it to data obtained in wind tunnel tests, and then extrapolate to full-scale, using accepted Reynolds number corrections.

DRAG ANALYSIS

In the airplane flight mode, five increments of drag are summed to find the total drag. These are:

1. Parasite drag
2. Induced drag
3. Drag increment due to leading edge vortex separation
4. Trim drag
5. Mach number drag rise

or in equation form:

$$C_D = C_{D_0} + C_{D_i} + \Delta C_{D_{sep}} + \Delta C_{D_{trim}} + \Delta C_{D_M}$$

The first three items are graphically depicted in Figure 85, which is the low speed lift-drag curve for Hot Cycle Rotor/Wing Aircraft depicted in Figure 84. The fourth is an induced drag increment resulting from the horizontal tail lift required to balance the aircraft, while the fifth drag item is the familiar increment of added drag at the higher Mach numbers, beginning around $M = 0.7$, and is a function of both Mach number and angle of attack.

A solid footing for the full-scale Rotor/Wing drag estimation process has been achieved through the Hughes/Office of Naval Research Rotor/Wing

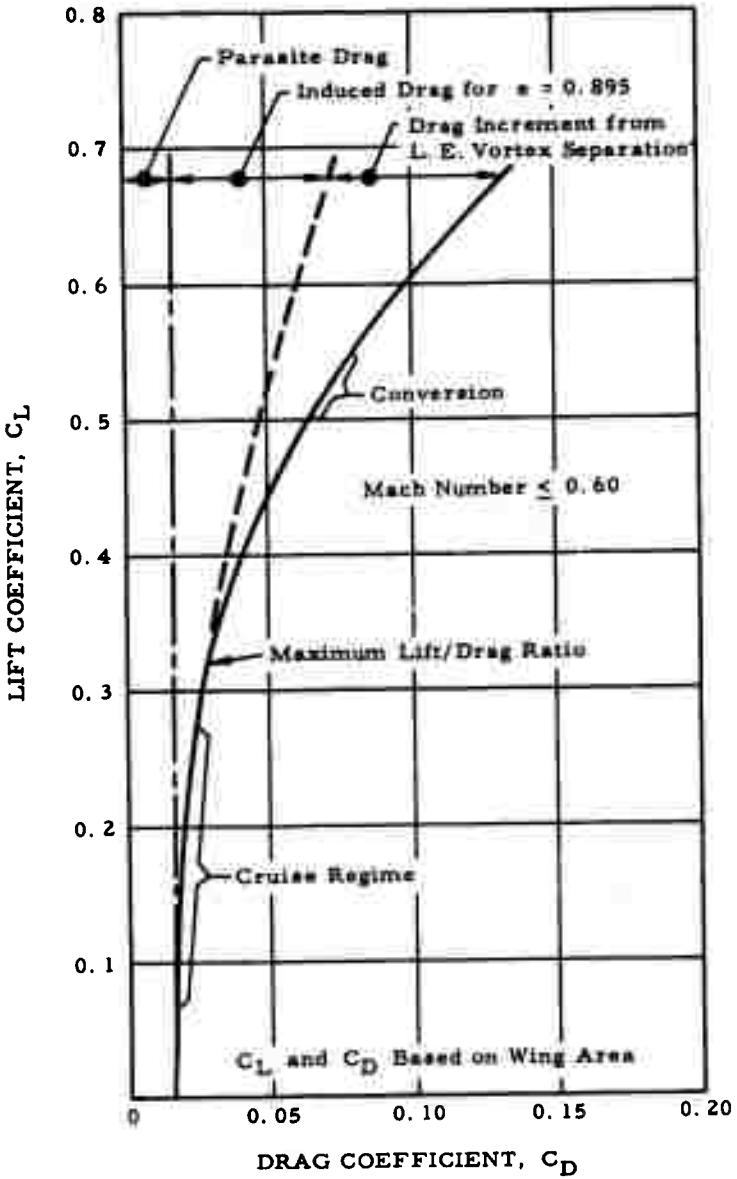

Figure 85. Rotor/Wing Full-Scale CRA Lift-Drag Estimate

research program using several different models in a number of wind tunnels. The data from ten series of tests are used as the basis for drag correlation and for extrapolation to full scale. The following sections describe this process which is founded on well-established methods.

Parasite Drag

The estimated full-scale parasite drag is based on wind tunnel test data obtained for the various Rotor/Wing models tested to date. The parasite drag coefficient is corrected to a skin friction drag coefficient based on the wetted area of the model, and this in turn is compared with the classical skin friction drag coefficient of an equivalent flat plate in turbulent flow. The Reynolds number used in the comparison is a weighted RN in which the RN of each component (wing, fuselage, and so forth) is weighted according to the ratio of its wetted area to the total wetted area of the model.

Figure 86 shows the available model test data compared with flat plate data. A factor of 1.23 applied to the flat plate data conservatively fairs the test data. A further allowance of 15 percent is added to account for the effects of leakage, protuberances, manufacturing irregularities, and so forth that are not simulated in the models. Thus, the full-scale skin friction drag coefficient based on aircraft wetted area is estimated to be 41 percent greater than a flat plate of the same wetted area and at the same equivalent Reynolds number.

The skin friction drag coefficient for a plain flat plate is:

$$C_f = \frac{K}{(RN)^{1/m}} \qquad \text{(Reference 10)}$$

The equivalent equation for the Rotor/Wing aircraft is:

$$C_{f_{R/W}} = \frac{1.415K}{(RN)^{1/m}}$$

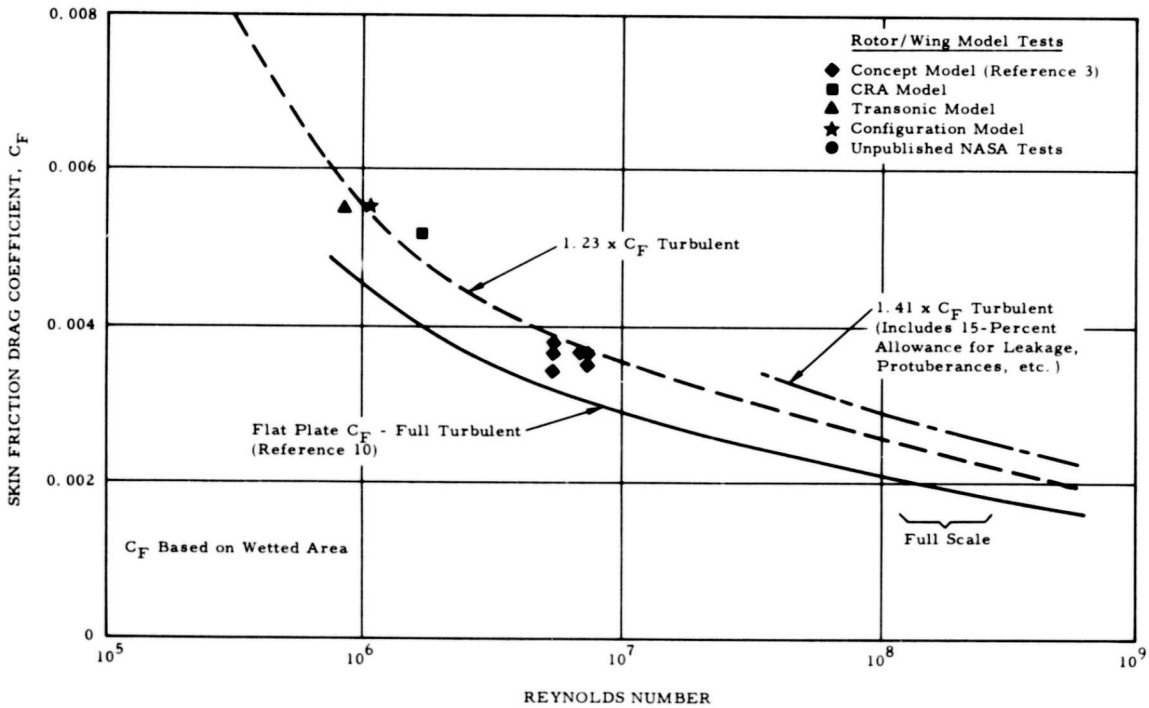

Figure 86. Reynolds Number Effect on Equivalent Skin Friction Drag

K and m are taken from Reference 10 and are found to equal 0.3 and 7.0, respectively, in the Reynolds number range of 10^7 to 10^9 that is expected to be applicable to the full-scale Rotor/Wing aircraft. Therefore, the drag coefficient to be used with the wetted area of each component is:

$$C_{f_{R/W}} = \frac{0.425}{(RN)^{1/7}}$$

and the parasite drag coefficient is:

$$C_{D_0} = C_{f_{R/W}} \times \left(\frac{S_{wet}}{S_{wing}}\right)$$

The effective Reynolds number to be used in this equation for the various components is based on the length of the fuselage for fuselage parasite drag and on the mean aerodynamic chord of the horizontal tail, vertical tail, and Rotor/Wing.

Induced Drag

The induced drag is a function of the aircraft lift, the wing's aspect ratio, and span efficiency factor. It is calculated in the well known manner:

$$C_{D_i} = \frac{C_L^{\,2}}{\pi ARe}$$

Lift coefficient and aspect ratio are easily measured quantities; the span efficiency, e, is calculated from model test data:

$$e = \frac{1}{\pi AR}\left(\frac{dC_L^{\,2}}{dC_D}\right)$$

where the derivative $(dC_L^{\,2}/dC_D)$ is the slope of the lift coefficient squared versus drag coefficient curve of the model.

All the Rotor/Wing model test data, and delta-wing model data, too, show that the $C_L^{\,2}$ versus C_D curve is made up basically of two straight-line elements, one up to $C_L \approx 0.3$, and another at the higher C_L's, as shown in Figure 87, which is taken from Rotor/Wing Transonic Wind Tunnel Tests at a test Mach number of 0.4. This break in the curve occurs near the C_L at which the leading edge vortex of the swept, cranked wing should separate from the wing as described in the following section.

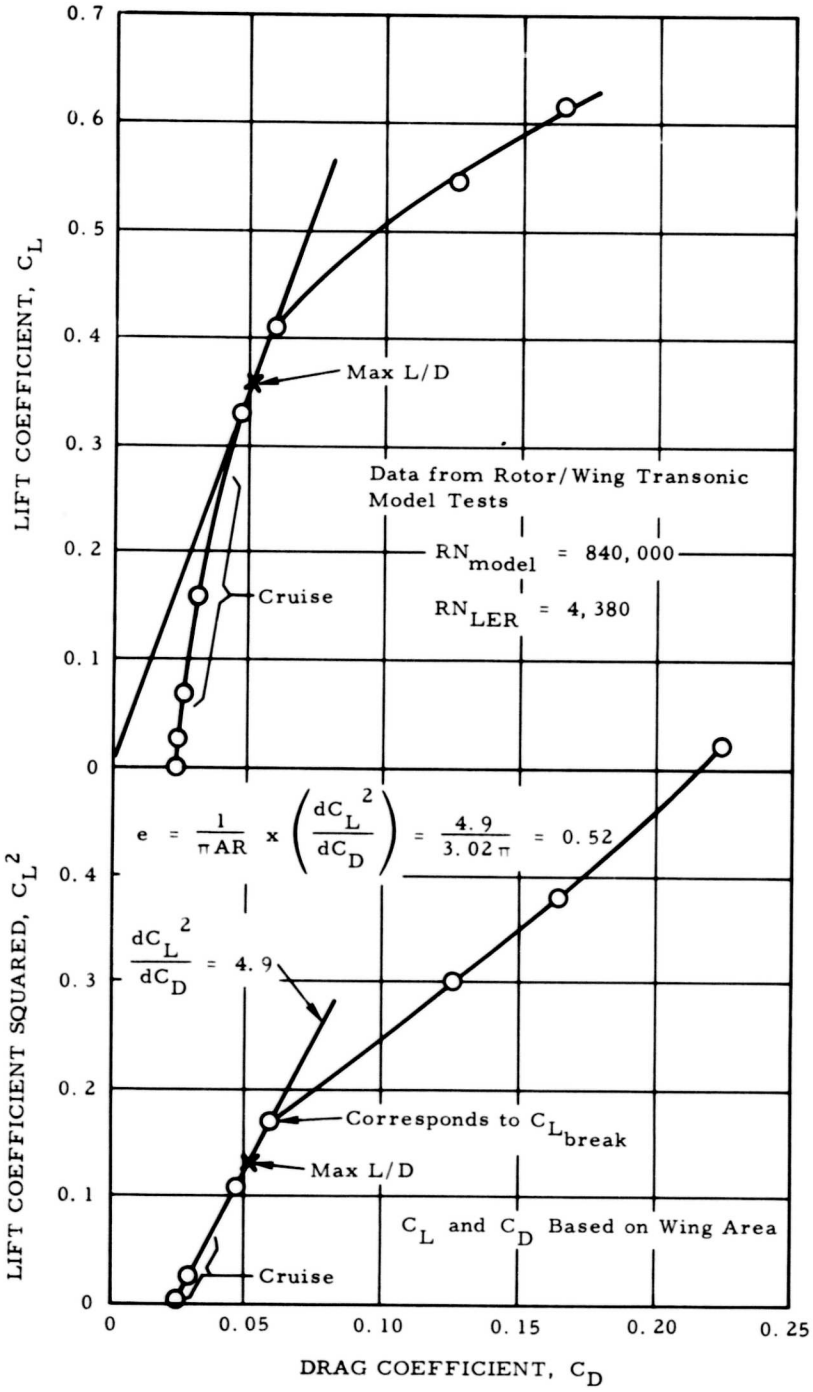

Figure 87. Rotor/Wing Transonic Model Lift-Drag Characteristics

The span efficiency factor, e, for the Rotor/Wing is defined as being based on the $C_L^2 \sim C_D$ curve slope at lift coefficient values below the point at which the curve breaks; this is also in the C_L region that includes the maximum lift/drag ratio and cruise flight lift coefficient (see Figure 87).

Another way to determine span efficiency from model test data is to make use of the equation:

$$(L/D)_{max} = 0.886\ b\ \sqrt{e/f}$$

(Reference 11, page 164)

The maximum L/D ratio; wing span, b; and equivalent flat plate drag area, f, are easily determined quantities from the wind tunnel test data. Therefore, e may be easily calculated.

Figure 88 is a plot of span efficiency, e, determined in the two ways from model tests, with e plotted against a Reynolds number based on the leading edge radius of the wing. The solid symbols denote e calculated from the $C_L^2 \sim C_D$ curves in the C_L region below the break in the curve; the open symbols denote e calculated from $(L/D)_{max}$ and flat plate drag area. Note that both methods give substantially the same value of span efficiency, indicating the validity of determining e from the $C_L^2 \sim C_D$ curve in the C_L range below the point where the break in the $C_L^2 \sim C_D$ curve occurs.

These experimental values of e follow a trend that increases with increasing Reynolds number when the Reynolds number is based on the leading edge radius of the wing. This trend matches very well the trend predicted by Reference 12 in the Reynolds number range covered by the Rotor/Wing model tests. The span efficiency for full-scale Rotor/Wings is fully anticipated to fall on the trend curve predicted by Reference 12.

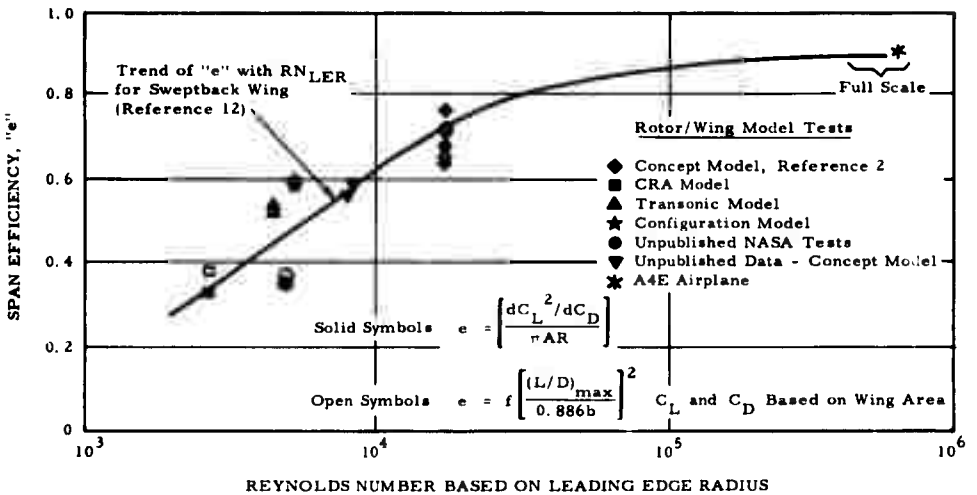

Figure 88. Reynolds Number Effect on Rotor/Wing Span Efficiency

This value of e may be conservatively applied for variations of blade root-to-tip radius ratios between 0.55 and 0.65 as demonstrated by the model test data. Since all the Rotor/Wing configurations currently under study have similar planforms and similar leading edge radius Reynolds numbers, and since they all fall within this blade root radius range, it is anticipated that the value of $e = 0.895$ is applicable to all.

Drag Increment Due to Leading Edge Vortex Separation

One of the most predominant features of flow around a highly swept wing -- such as the Rotor/Wing in its cruise flight mode -- is the development of a strong vortex along the leading edge of the wing. As lift coefficient increases, this vortex remains attached to the wing up to a certain value of C_L; then it detaches and flows above the wing surface. When it detaches, the lift-curve slope usually increases, and a drag increase occurs over and above the drag that would be expected from only the sum of parasite and induced drag.

An empirical method has been established to determine the drag increment due to leading edge vortex separation. Test data from the numerous wing models discussed in Reference 12 show that the curve of lift coefficient squared versus drag coefficient is basically made up of two straight line segments. The ratio of the slopes of these two segments, called e/e^*, is a function mainly of the Reynolds number based on leading edge radius and wing aspect ratio. Figure 89 is a plot of e/e^* for these test data. Also included in Figure 89 are data from the Rotor/Wing test program. The Rotor/Wing has an aspect ratio in airplane flight that is very close to three; therefore, the predicted e/e^* curve for the Rotor/Wing closely follows the AR = 3 line for the wings.

The drag increment due to leading edge separation is calculated for lift coefficients greater than C_L where the slope of the $C_L^2 - C_D$ curve changes, by the equation:

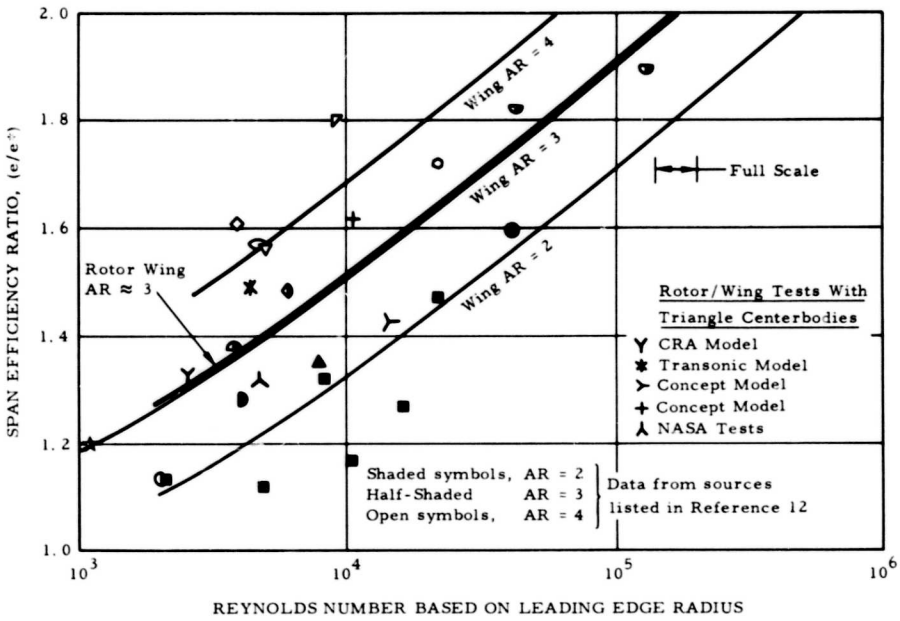

Figure 89. Rotor/Wing Span Efficiency Ratios at Lift Coefficients Greater than 0.3 and at Mach Numbers Less than 0.6

$$\Delta C_{D_{sep}} = \left[\frac{C_L^{\,2} - C_{L_{break}}}{\pi ARe}\right] \times (e/e^* - 1)$$

where C_L is the wing lift coefficient (based on the area of the wing plus two blades); $C_{L_{break}}$ is the lift coefficient at which the slope of the $C_L^{\,2}$ versus C_D curve changes (Rotor/Wing model tests conservatively indicate the use of $C_{L_{break}} = 0.3$); AR is the aspect ratio of the wing plus two blades; "e" is the span efficiency of the wing in the C_L range below $C_{L_{break}}$, and e/e* is defined above.

Trim Drag

The parasite drag of the aircraft includes the drag of the horizontal tail set at zero incidence. When the craft is pitched up to achieve a variation of lift, the resulting wing and fuselage pitching moments must be balanced by horizontal tail lift. This generation of lift produces an induced drag term, called trim drag, that must be included in the overall drag estimation. Tests with models to date have shown the trim drag to be negligible (see Figure 90); this, of course, must be re-verified if any significant changes in configuration occur.

Mach Number Drag Rise

All high-subsonic-speed aircraft suffer an increase in drag coefficient as the flight Mach number goes beyond approximately 0.7. The specific point at which this occurs depends on the configuration of the airframe. Tests with a Rotor/Wing model in a transonic wind tunnel have shown that the Rotor/Wing drag rise begins at M = 0.7. Figure 91 shows the results of these tests. The ΔC_{D_M} increment to be added to the low-speed drag coefficient is shown to be a function of both Mach number and angle of attack.

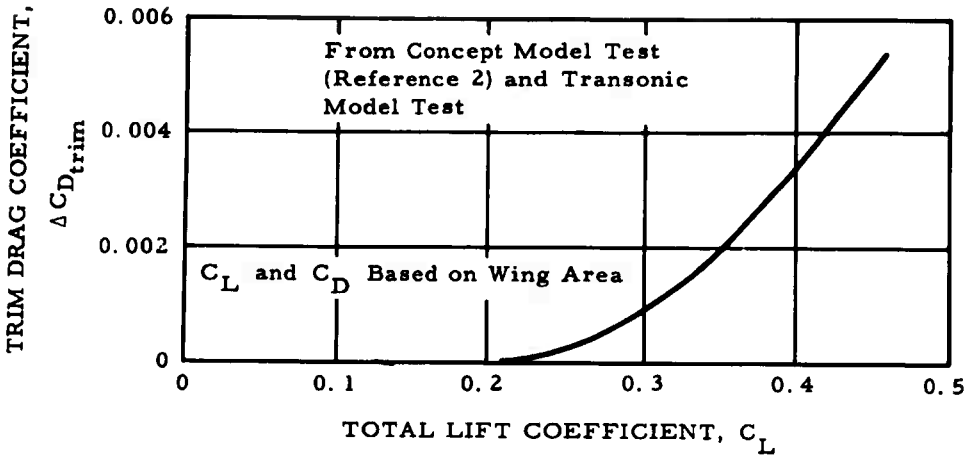

Figure 90. Rotor/Wing Trim Drag Increment

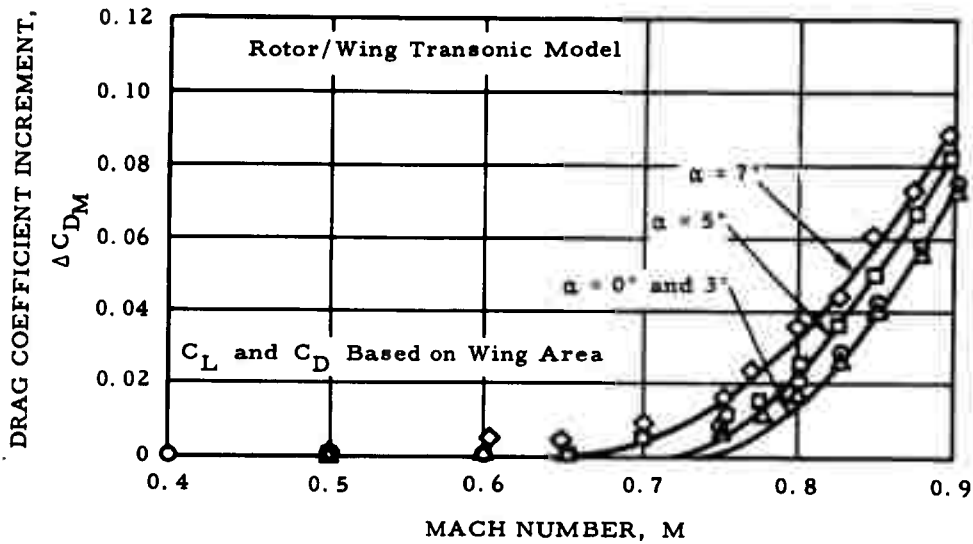

Figure 91. Rotor/Wing Mach Number Drag Rise

The model data may be checked by using an empirical method for determination of drag divergence Mach number for the various portions of an aircraft; the method gives good correlation with flight test. These equations define the drag divergence Mach number for airfoil and body:

$$M_{D_{wing}} = 1.00 - \left[0.15 + \frac{(t/c)}{1.2} - 0.15 e^{-20(t/c)} + 0.13 C_L \right] (\cos \Lambda)^2$$

$$M_{D_{fuselage}} = 0.98 - \left[\frac{0.74}{(\ell/d)} \right]$$

Where (t/c) is the thickness ratio of wing (thickest part) taken normal to the quarter chord:

e = 2.71828

C_L = operating lift coefficient

Λ = leading edge angle of sweep, degrees

ℓ = length

d = maximum width

Thus, for a typical Rotor/Wing:

$(t/c)_{max}$ = 0.213 (blade section)

$C_{L_{S_w}}$ = 0.15 (M = 0.75 at 30,000 feet)

Λ = 35 degrees

$$M_{D_{wing}} = 1 - \left[0.15 + \frac{0.213}{1.2} - 0.15 \times 2.71828^{-20 \times 0.213} + 0.13 \times 0.15 \right] (\cos 35)^2$$

$$= 1 - (0.3448)(0.671)$$

$$= \underline{0.769}$$

For a typical fuselage:

$$(\ell/d) = 10.5$$

$$M_{D_{fuselage}} = 0.98 - \frac{0.74}{10.5} = 0.91$$

$$= \underline{0.91}$$

For a typical horizontal tail:

$$(t/c) = 0.15$$

$$C_{L_{S_{tail}}} = 0.035 \text{ (trim at } M = 0.75,\ 30,000 \text{ feet)}$$

$$\Lambda = 18 \text{ degrees}$$

$$M_{D_{tail}} = 1 - \left[0.15 + \frac{0.15}{1.2} - 0.15 \times 2.71828^{-20 \times 0.15} + 0.13 \times 0.035\right] (\cos 18)^2$$

$$= \underline{0.754}$$

For a typical vertical tail:

$$(t/c) = 0.15$$

$$C_L = 0$$

$$\Lambda = 17 \text{ degrees}$$

$$M_{D_{vt}} = 1 - \left(0.15 - \frac{0.15}{1.2} - 0.15 \times 2.71828^{20 \times 0.15}\right) (\cos 17)^2$$

$$= (0.2675)\ (0.915)$$

$$= \underline{0.755}$$

The critical Mach number is the lowest value calculated for the separate components; hence, a typical aircraft drag divergence Mach number is 0.754. Work on configuration optimization to study tradeoffs between weight and drag divergence Mach number must be done.

In Figure 91 it is noted that drag divergence does begin at $M = 0.75$, as predicted above. Note that the model results are taken literally at C_D greater than 0.02 and that full-scale interpretation does not reflect the tendency of the test points to show a gradual drag increase over the Mach number region of approximately 0.1, just prior to the drag break. This tendency is common to models tested at relatively low Reynolds numbers and is not typical of tests of full-scale airplanes. In fact, full-scale airplane drag tests normally show a decreasing C_{D_0} as Mach number increases toward the drag break as a result of the Reynolds number increase that accompanies the Mach number increase.

It is believed that the satisfactory check of the drag divergence calculations method above -- by the tunnel test -- is indicative that the method may be applied with equal validity to all Rotor/Wing design studies.

ESTIMATED DRAG POLAR-AIRPLANE MODE

A drag polar has been estimated for a typical Rotor/Wing aircraft of the configuration shown in Figure 84 using the foregoing analysis, and is presented in Figure 92.

HELICOPTER FORWARD FLIGHT POWER REQUIRED

The helicopter mode power required during forward flight is computed using the NACA helicopter performance charts of Reference 13, modified to be applicable to the Rotor/Wing configuration. The wing and elevon download, which must be determined to compute power required, is a function of fuselage attitude, which is itself a function of power required. Thus, the computation requires several iterations to determine power required during trimmed flight. The procedure is summarized in Figure 93. Determination of the elements required in the power-required calculation is described in following paragraphs.

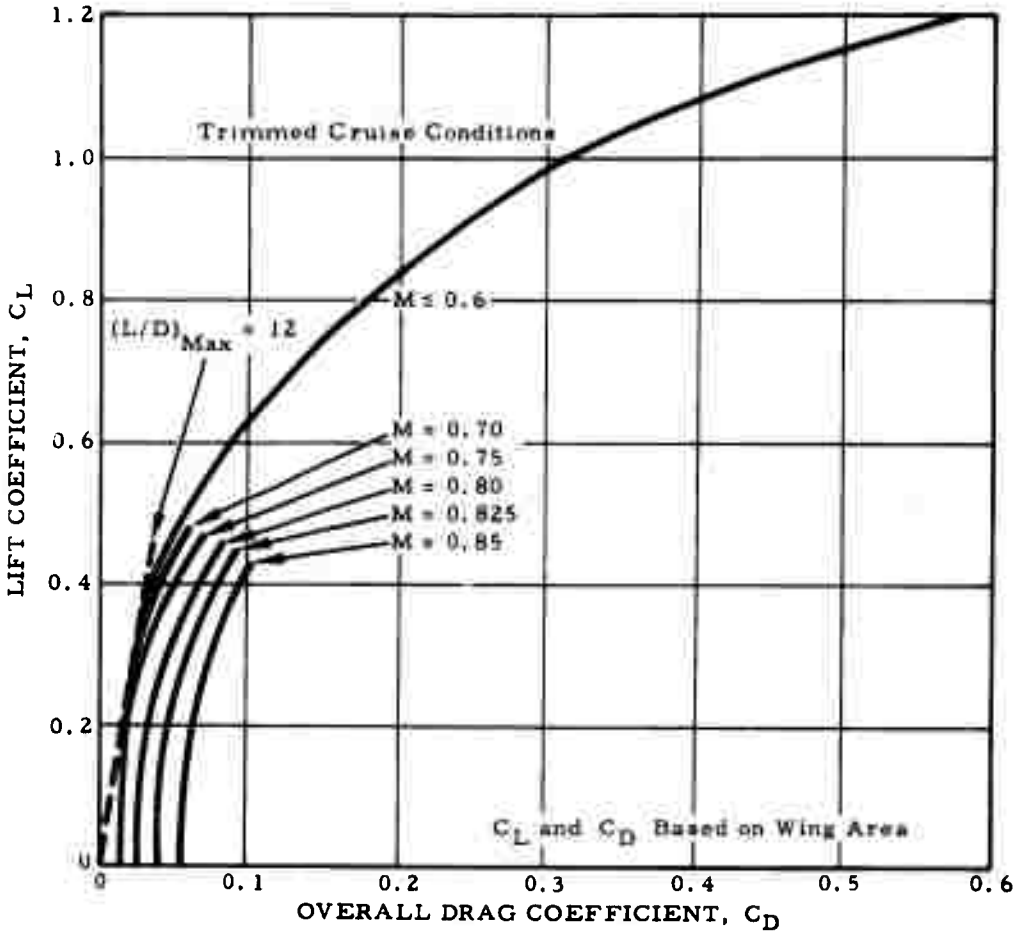

Figure 92. Typical Drag Polar, Airplane Mode

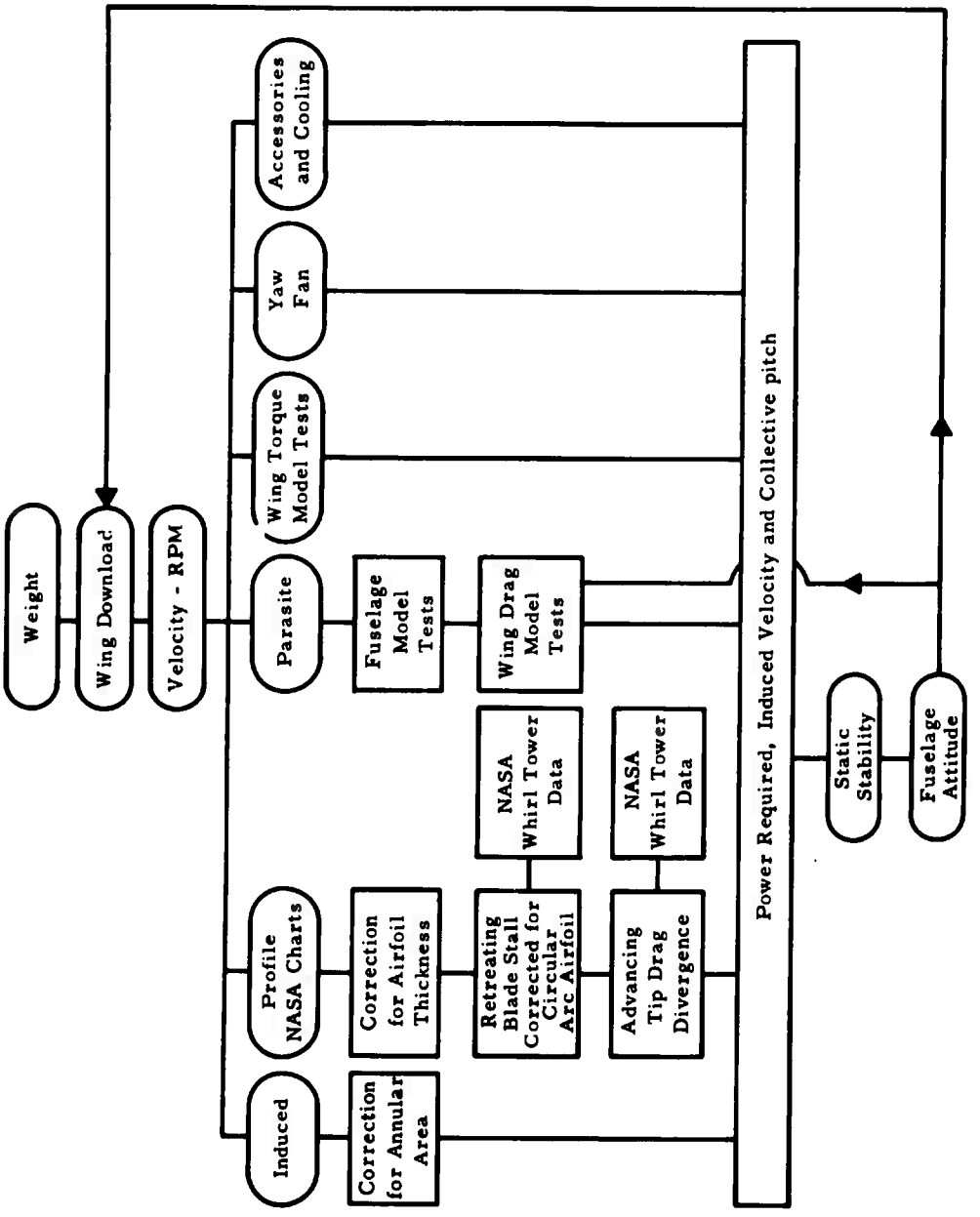

Figure 93. Power Required, Helicopter Forward Flight

LIFT AND DRAG OF WING AND FUSELAGE

The Rotor/Wing aircraft in forward rotating-wing flight will have wing/fuselage seals open, yaw fan doors open, and landing gear up and locked. The conservative approach to determine the drag polars for those configurations is to utilize the available Rotor/Wing wind tunnel test data with corrections to lift for wing size and to drag for trim, open wing seals, open tail fan doors, and other specific modifications such as fuselage shape, tailbooms, and so forth.

The C_L versus α_F curve is based on data from Reference 2. This model test had the tail off, the blades off, and the wing rotating. The ratio of a full-scale wing-to-disc area can be compared directly to the wing-to-disc area ratio of 0.324 in this test to obtain a multiplying factor for the fuselage-plus-rotating wing lift as a function of angle of attack. This is possible since the lift contribution of the fuselage is quite small. A C_L versus α_F curve developed in this manner is shown in Figure 94.

The determination of the aircraft parasite drag is similar to the method described for airplane flight, but with modifications for the special flight condition. Thus, the fuselage drag becomes

$$\left(C_{D_0}\right) = 1.10\, C_{f_f} \left(\frac{S_{f_{wet}}}{S_w}\right) + \Delta C_{D_{gap}}$$

where the 1.10 accounts for added roughness due to the open engine-inlet door, and $\Delta C_{D_{gap}}$ due to the gap that opens when wing pylon seals are retracted. The $\Delta C_{D_{gap}}$ is computed on the basis of a proper drag coefficient of 1.0 acting on an area equal in height to the wing/fuselage gap width times the pylon width.

$$\Delta C_{D_{gap}} = 1.0 \left(\frac{h_{gap} \times W_{pylon}}{S_w}\right)$$

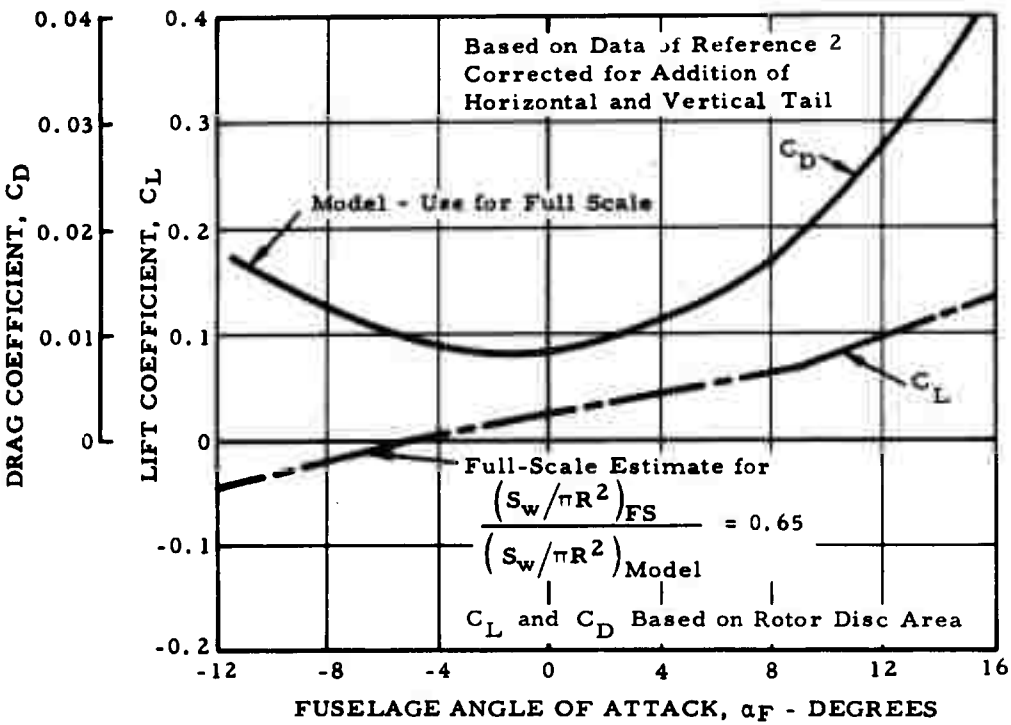

Figure 94. Typical C_L and C_D Curves for Helicopter/Autogyro Mode

Horizontal tail parasite drag is calculated in the same manner as for airplane flight. Vertical tail drag is complicated by the cutout for the yaw fan:

$$C_{D_0} = C_{f_{VT}} \left(\frac{S_{VT_{net\ wet}}}{S_w} \right) + \Delta C_{D_{VT_{cutout}}}$$

The net wetted area of the vertical tail with the yaw fan doors open is equal to the wetted area with doors closed, plus two times the yaw fan disc area. The skin friction coefficient, $C_{f_{VT}}$, remains unchanged.

A proper drag coefficient of 0.07 is applied to an area equal to the cutout area, based on the data of Reference 10.

$$\Delta C_{D_{VT_{cutout}}} = \frac{0.07 \times \pi R^2_{yaw\ fan}}{S_w}$$

Wing parasite drag has been estimated using the helicopter mode wind tunnel data of Reference 2. From these data, it has been found that the blades-off Rotor/Wing drag, nonrotating, is slightly higher than for the wing rotating μ 0.25. Therefore, it is conservative to use the nonrotating wetted area drag characteristic for the wing for the helicopter mode case.

A typical final curve for the untrimmed lift and drag of the aircraft minus rotor blades is given in Figure 94.

The elevon trim angles are obtained from the static stability considerations. Knowing the flow angles at the tail, the lift and drag coefficients of the tail section can be obtained from plots similar to that of Figure 95.* From the incidence of the tail, the components of net lift and drag in the freestream coordinate system are obtained. The tail lift is down; hence, this value must be added to the lift required by the Rotor/Wing blades. In addition, the tail drag must be added to fuselage drag. The tail profile drag is included in the fuselage parasite area, so only the induced drag must be added. The induced drag is the difference between the drag coefficient at the required angle and that at zero angle, as shown on Figure 95.

*When the elevon is stalled, the lift coefficient is taken as 1.0, and the drag coefficient is obtained from tests of an airfoil at large angles of attack (Reference 14).

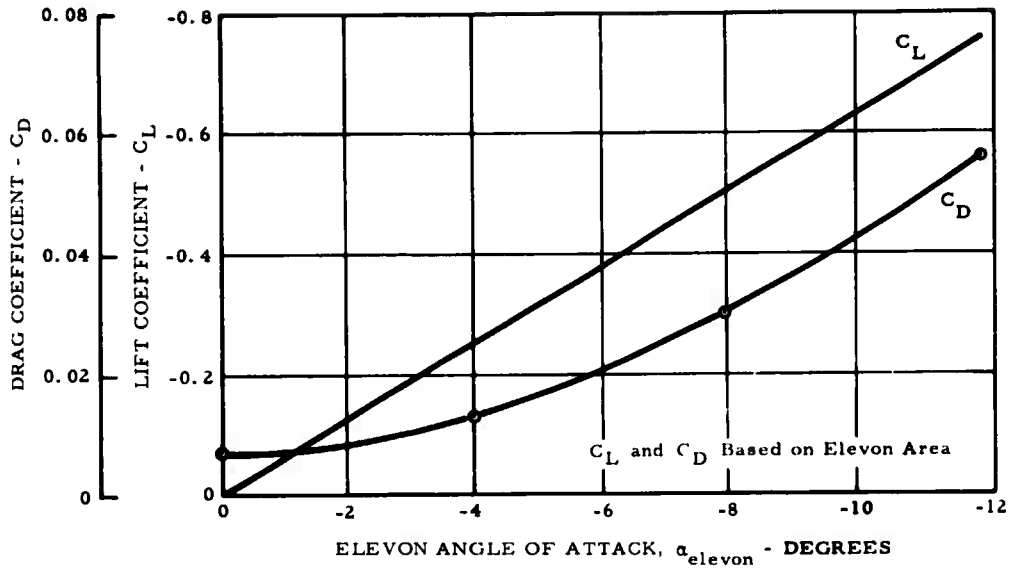

Figure 95. Estimated C_L and C_D for Elevon

Blade Lift

Knowing the angle of attack of the wing, the lift or download of the wing portion of the Rotor/Wing is obtained by using a lift curve similar to Figure 94. For trim, the download is obtained for the elevon. The lift or download of the wing and elevon are subtracted or added to the weight to give the resulting lift that must be carried by the blades.

Parasite Power

The parasite power was obtained from a C_D curve such as that shown in Figure 94 and from the elevon induced drag obtained from trim equations. Using the method of Reference 13 for computing power, the parasite power to thrust coefficient ratio is given by

$$\frac{C_{P_P}}{C_T} = \frac{C_D A q \mu}{L_b}$$

where L_b is the lift required by the blades.

Induced Power

The induced power is based on the annular area of the rotor swept out by the blades, assuming a three percent tip loss on the blades. The equation for the induced power coefficient to thrust coefficient becomes

$$\frac{C_{P_i}}{C_T} = \frac{C_T}{2\mu \left(\frac{A_d}{A}\right) \sqrt{1 + (\lambda / \mu)^2}}$$

Profile Power

The profile power is based on the NACA charts of Reference 13. For each value of μ, the profile power coefficient to thrust coefficient ratio (C_{P_0}/C_T) can be read from charts, knowing $(C_{P_p}/C_T + C_{P_i}/C_T)$ and $(2C_T/\sigma a)$. These charts are based on the NACA polar for the blade section drag coefficient.

As in the hovering analysis, the profile power coefficient is increased by six percent to account for the increased average thickness compared with that of a 12-percent airfoil represented by the NACA polar.

The profile power penalty, if any, due to retreating tip stall and advancing tip drag divergence is obtained using the airfoil data of Reference 14.

The values of C_D for the retreating tip and the advancing tip are obtained from the data in Reference 8, modified to be applicable to the Rotor/Wing. Reference 8 presents the variation of synthesized rotor blade section profile

drag coefficient with angle of attack at various Mach numbers for an NACA 0015 tip airfoil section. The drag coefficients can be obtained from these data, knowing the tip angles of attack and tip Mach numbers.

The tip of the Rotor/Wing blade is the area that is subject to drag divergence. Because the tip of the airfoil may be relatively thick, the Reference 8 data must be modified. Airfoil test data indicate that the drag divergence Mach number is increased by 0.01 for a one percent decrease in thickness ratio. Therefore, when entering the drag coefficient charts of Reference 8 to determine the advancing tip profile power penalty, if any, the effective Mach number must be conditioned by this relationship.

As in the hovering analysis, it is conservatively assumed that the drag rise due to stall for the circular arc airfoil will occur at approximately one degree angle of attack earlier than for an NACA 0015 airfoil. Therefore, when entering the drag coefficient chart of Reference 8 to determine the retreating side stall profile power penalty, if any, the retreating tip angle is increased by one degree.

The maximum speed, as limited by initial blade stall, occurs at a retreating tip angle of attack of 12 degrees. Referring to Reference 6, a retreating tip angle of attack of 12 degrees is the lower boundary for blade stall; thus, this limit is conservative.

Wing Torque

Figure 96 presents a plot of the ratio of wing torque in hovering to the torque in forward flight. The data points shown were obtained from Reference 2. This ratio was used in conjunction with the hovering wing torque to determine wing torque in forward flight.

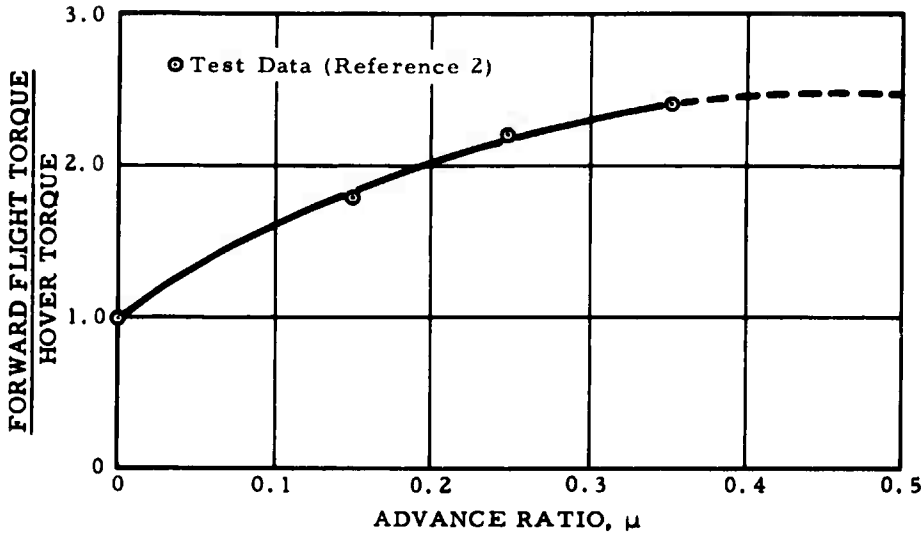

Figure 96. Wing Torque Versus Advance Ratio

Yaw Fan Power

Conservatively, the yaw fan power in forward flight is assumed to be the same as that in hovering (approximately one percent of Rotor/Wing power). The yaw fan thrust required is essentially constant throughout the flight regime; thus, the assumption of constant power is conservative. The power required to overcome the drag of the very slightly deflected rudder is considered to be negligible.

Fuselage Attitude

The fuselage attitude is obtained from static stability equations, knowing the induced velocity and collective pitch, which were obtained from the power required computations.

SUBSTANTIATION OF PERFORMANCE COMPUTING METHOD

Figure 97 presents a comparison of the theoretical and measured torque coefficient of the model wind tunnel tests (Reference 2). The theoretical values of C_Q were computed using the Rotor/Wing performance theory, but including the increased profile power for model scale indicated by Figure 79. Figure 97 shows excellent agreement between full-scale performance theory corrected to model scale and model test data.

AUTOGYRO FLIGHT POWER REQUIRED

The autogyro power required is computed using the NACA charts of Reference 15, modified to be applicable to the Rotor/Wing configuration. The wing and elevon lift must be determined in order to compute thrust required by the Rotor/Wing blades. As the wing and elevon lift are determined from fuselage

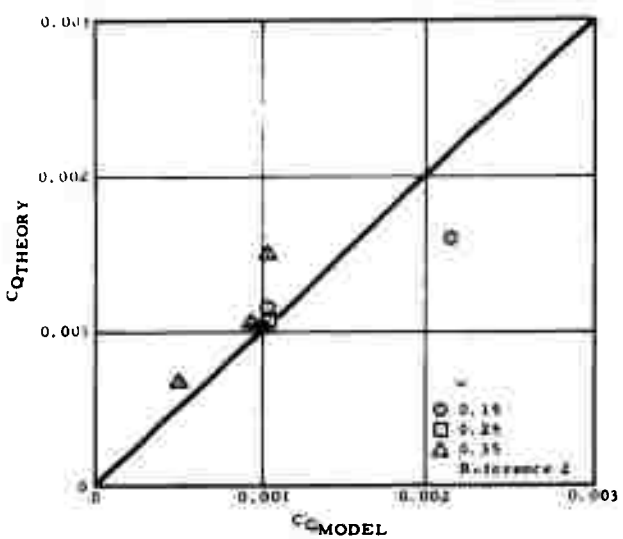

Figure 97. Comparison, Performance Theory and Rotor/Wing Model Data, Helicopter Mode

attitude, which is in itself a function of thrust, the computation requires several iterations, as indicated in Figure 98.

WING AND FUSELAGE LIFT AND DRAG

Autogyro flight C_L and C_D for the wing and fuselage will be similar to those shown in Figure 94. The elevon trim net lift and drag is computed in the same manner as in helicopter mode. Because the induced drag of the wing and blades is computed as a combined lifting system in autorygo flight, the induced drag of the wing is subtracted from the drag curve of Figure 94 when it is used in the autogyro mode.

Rotor/Wing Drag

The Rotor/Wing drag is determined using the NACA charts of Reference 15, with modifications to represent the Rotor/Wing configuration. During autorotation, both the wing and blades are contributing to the lift. Therefore, the induced drag is the same as that for a conventional rotor. The charts of Reference 15 are based on a solidity ratio of 0.1; hence, a correction for the Rotor/Wing solidity must be made, based on pages 23 and 24 of Reference 15. In addition, the six-percent correction factor for average thickness is applied to the profile drag.

In order to obtain the proper value of profile drag, the rotor lift coefficient-solidity ratio used to enter the curves of Reference 15 is based on lift of the blades. However, the induced angle and drag are computed assuming the entire Rotor/Wing combination is acting as a lifting body. Therefore, to correct the Reference 15 chart values of rotor angle and drag, the induced portion must be subtracted from the total drag solidity ratio and added again in the correct form, as follows:

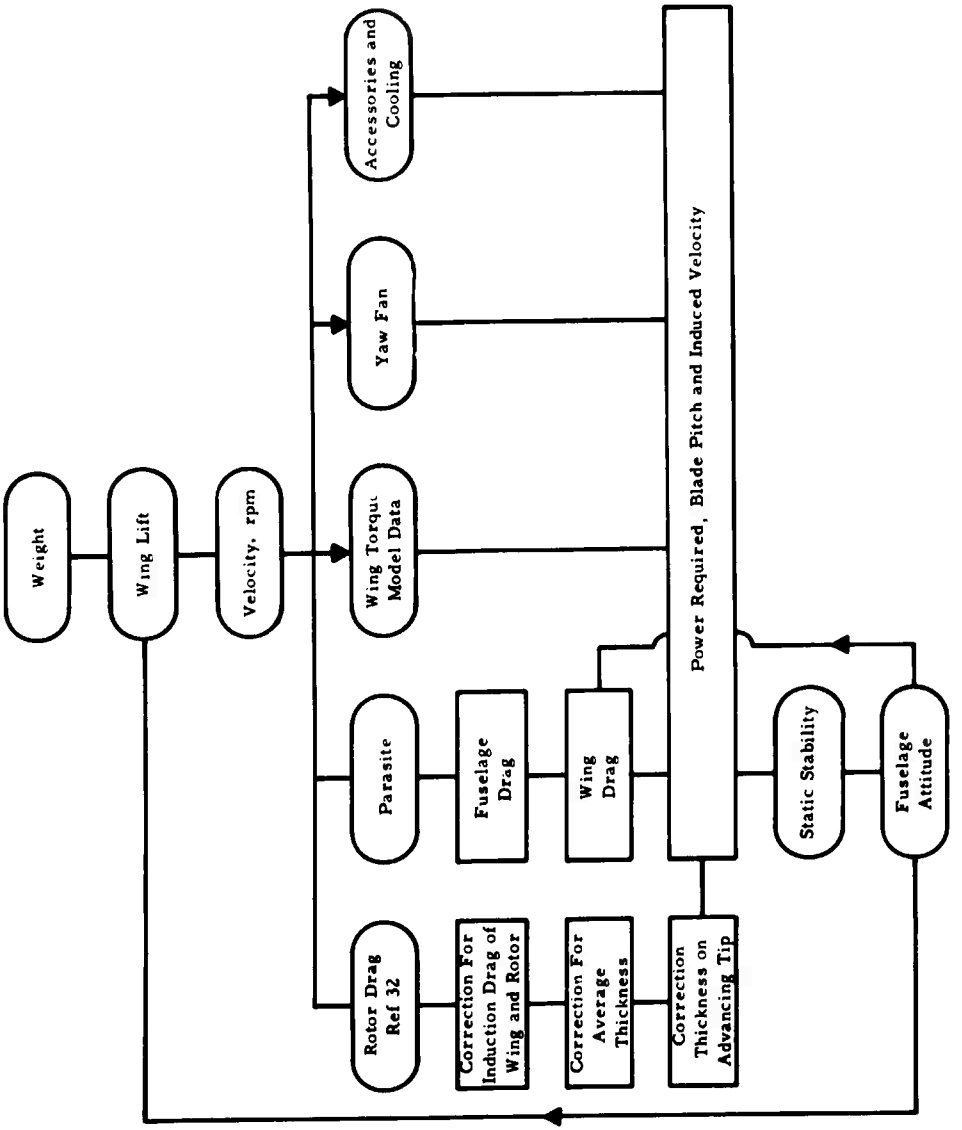

Figure 98. Power Required, Autogyro Flight

The induced angle is given by

$$\alpha_i = \frac{C_L}{2\mu^2} = \frac{\left(\frac{C_L}{\sigma}\right)\sigma}{2\mu^2}$$

The correction to the rotor angle then becomes

$$\Delta\alpha = \frac{\frac{C_L}{\sigma}}{2\mu^2}\left(\frac{W}{T}\sigma - 0.1\right)$$

The induced drag is given by

$$C_{D_i} = \frac{C_L^2}{2\mu^2} \quad \text{or} \quad \frac{C_D}{\sigma} = \frac{\left(\frac{C_L}{\sigma}\right)^2\sigma}{2\mu^2}$$

The total rotor drag/solidity ratio correction for induced drag and the six-percent thickness correction to the profile power become:

$$\frac{C_D}{\sigma} = \left(\frac{C_D}{\sigma}\right)(1.06) + \frac{\frac{C_L}{\sigma}}{2\mu^2}\left(\frac{W}{T}\sigma - (0.1)(1.06)\right)$$

where

W = gross weight

T = lift required by the blades

The charts of Reference 15 contain corrections for drag divergence on the advancing side, assuming a 12-percent thick blade. Test data indicate that the effect of airfoil thickness on drag divergence is equal to a change of 0.01 in Mach number for a 0.01 change in airfoil thickness. To account for tip

thicknesses greater than the chart value, the chart must be entered at a Mach number higher than the actual value.

In autogyro flight, the retreating tip is at a low angle of attack, and therefore unstalled. Thus, the increase in drag due to stall of the circular arc airfoil at high angles of attack does not occur as it may in the helicopter mode.

Wing Torque

The wing torque used in autogyro flight is the same as that used in helicopter flight (see Figure 96).

Yaw Fan Power

As in the helicopter mode, the yaw fan power in forward flight is conservatively assumed to be the same as in hovering flight.

Fuselage Attitude

As in the helicopter mode, the trim fuselage attitude is determined from the static stability equations for the helicopter mode, with the following additions:

1. The angle of attack of the fuselage due to the Rotor/Wing induced flow, $\epsilon_{F_{R_+}} = 0°$
2. The term $T(Z_t)$ is added to the pitching moment equation, where
   T = jet thrust required
   Z_t = vertical distance from jet centerline to rotor.

The derivatives used in these equations were obtained from wind tunnel tests, Reference 16.

SUBSTANTIATION OF PERFORMANCE COMPUTING METHOD

Figure 99 presents a comparison of the theoretical and measured drag coefficient of the model wind tunnel tests (Reference 2). The theoretical values of C_D were computed using the Rotor/Wing performance theory, but including the increase in profile power due to model scale as indicated in Figure 79. The figure shows excellent agreement between full-scale performance theory corrected to model scale and model test results.

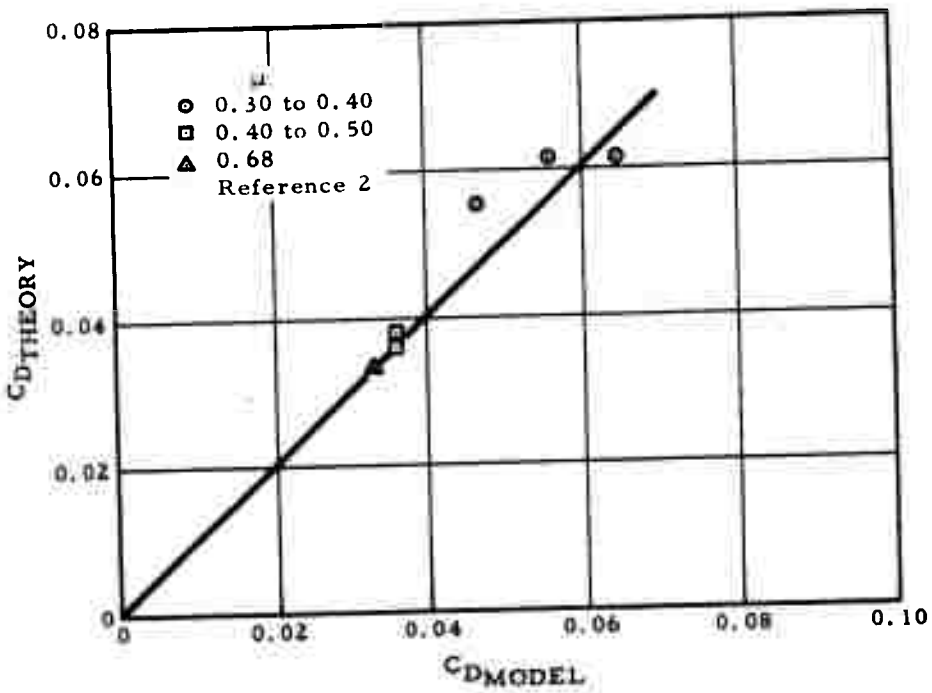

Figure 99. Comparison, Performance Theory and Rotor/Wing Model Data, Autogyro Mode

CONVERSION FLIGHT POWER REQUIRED

The conversion maneuver is the main determining factor in sizing the wing portion of the Rotor/Wing. At the selected conversion speed, the wing size is chosen to support the entire weight of the aircraft while flying at an angle of attack of no more than 10 degrees. If necessary, the area is increased further to reduce the total drag to be within the capacity of the available engine or fan thrust. A check is made of the power required and available in both steady-state autogyro flight and airplane flight to make certain a speed overlap exists between the two, as indicated in Figure 100 for a typical Rotor/Wing aircraft, thus assuring that conversion can be made in a level flight condition.

During the low rpm portion of conversion, the analysis assumes that all the lift is carried by the wing and none by the blades. Hence, all the induced drag is created by the wing. Wind tunnel tests of Rotor/Wings with blades off have been made with several models. Data from Reference 2 and from the present tests give a base point for estimating a span efficiency factor, "e", used in the classic induced drag equation

$$C_{D_i} = \frac{C_L^{\,2}}{\pi ARe}$$

"e" is calculated from the slope of the curve of lift coefficient squared, versus drag coefficient in the lift coefficient range applicable to conversion flight (both being based on the area of the wing), and the aspect ratio is defined by the equation

$$AR = \frac{(2\xi R)^2}{S_{centerbody}} \quad *$$

*See Figure 101 for the definition of ξ.

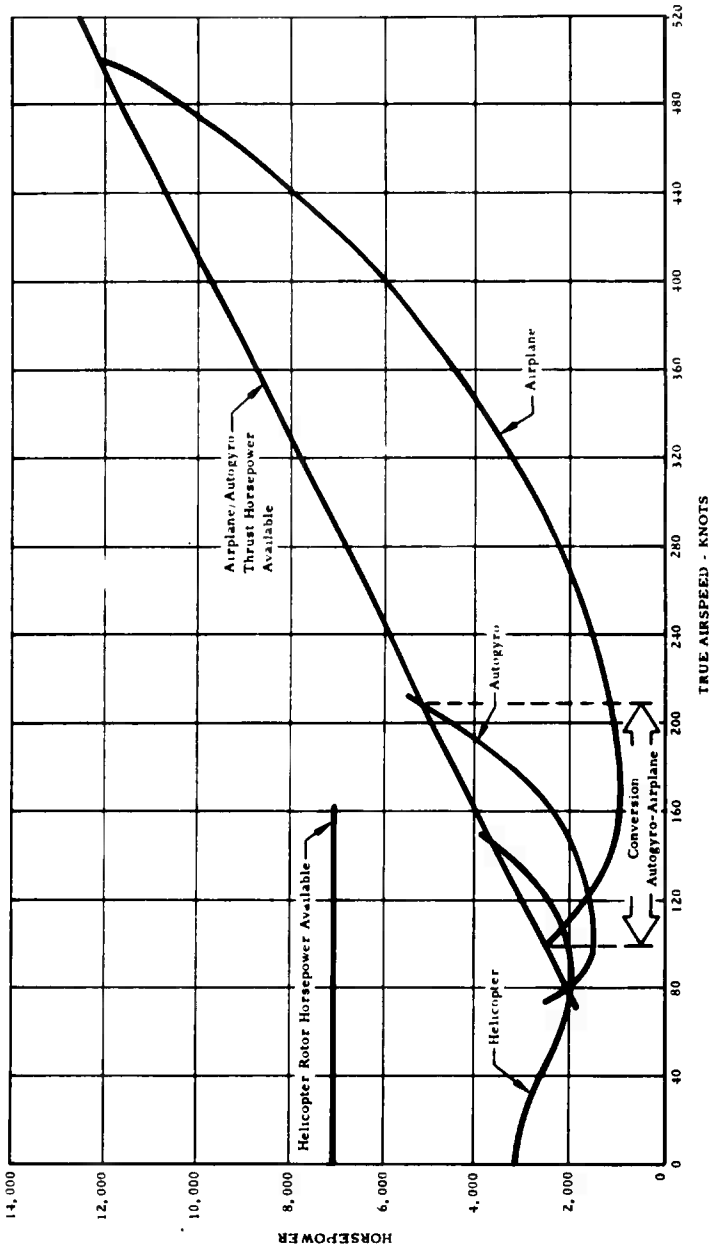

Figure 100. Typical Power Required and Available

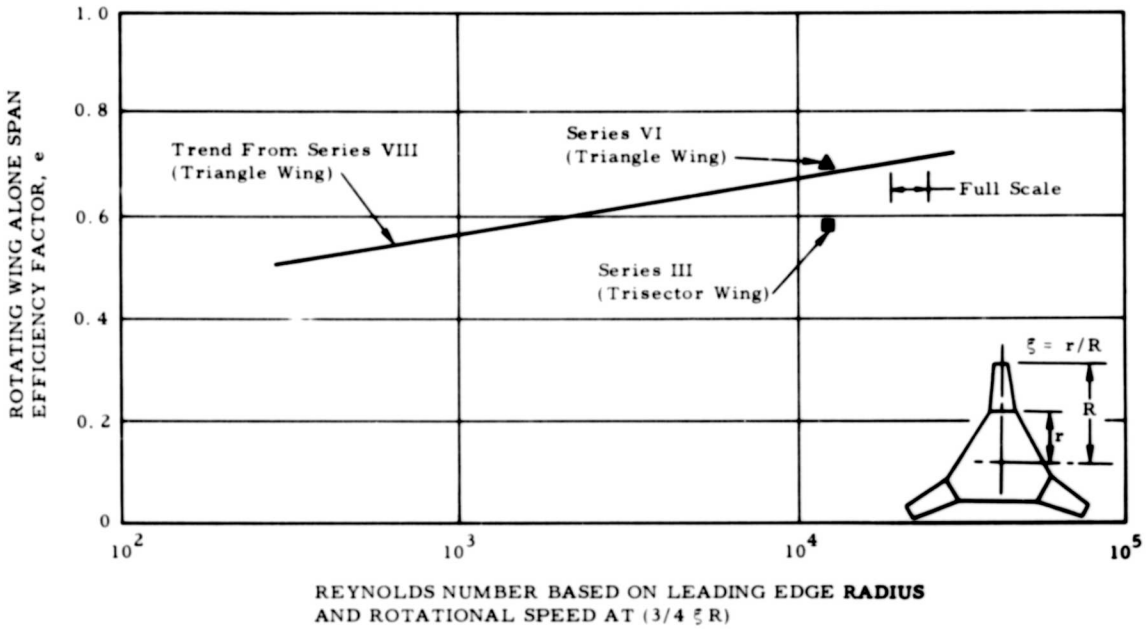

Figure 101. Rotating Wing Span Efficiency During Conversion

"e" is plotted versus Reynolds number, where the Reynolds number is based on the leading edge radius of the wing and the rotational speed of a point on the wing three-quarters of the way out from the center of the rotor to the blade root radius station.

Figure 101 shows points derived from the Series III and VI rotating-wing, blade-off tests at full rotor rpm. Series VIII tests included blade-off rotating rotor tests at several rpm's. The overall level of drag measured in these tests is in question, but the slopes of the C_L^2 versus C_D curves are considered adequate for showing trends. Using this trend and the Series III/VI data, the "e" versus RN_{LER} curve of Figure 101 results. The full-scale RN_{LER} is indicated.

CONVERSION -- STABILITY, CONTROL, AND FLYING QUALITIES

The Rotor/Wing wind tunnel research program has generated a considerable amount of data relative to the conversion regime, and a study has been made to develop a mathematical model that matches this wind tunnel test data. The mathematical model is then used to study the characteristics of full-scale Rotor/Wing aircraft with the assurance of correct results.

The analytical procedure consists of numerically integrating the aerodynamic forces on the blades, using the lift-drag polar determined from tests of a circular arc airfoil. The aerodynamic forces of the wing and fuselage obtained from wind tunnel tests with the blades off are added to the calculated blade forces and moments to give the total forces for comparison with the model conversion data.

The key to obtaining good agreement between the model data and the mathematical model has been found to lie in obtaining a good understanding of the induced velocity in the region of the Rotor/Wing. Figure 102 shows schematically the induced velocity distribution determined in this study.

At low values of rotor speed ($\mu > 0.9$), the wing centerbody provides the bulk of the lift, and the blades operate in the upwash caused by the tip vortices of the centerbody. Theoretically, the upwash is equal to approximately one-half the downwash developed by the wing centerbody. This assumed upwash value has been verified by using it to compute rolling moments due to blade pitch in the stopped mode. Figure 103 shows that this theory gives excellent agreement with the test data. The theory was further verified by theoretically duplicating the lifting and rolling moments obtained from wind tunnel tests of the Rotor/Wing at values of μ greater than 0.95. In order to match the test pitching moments at high values of μ, it is necessary to assume a variable induced velocity -- up at front of the rotor, down at the back, and varying

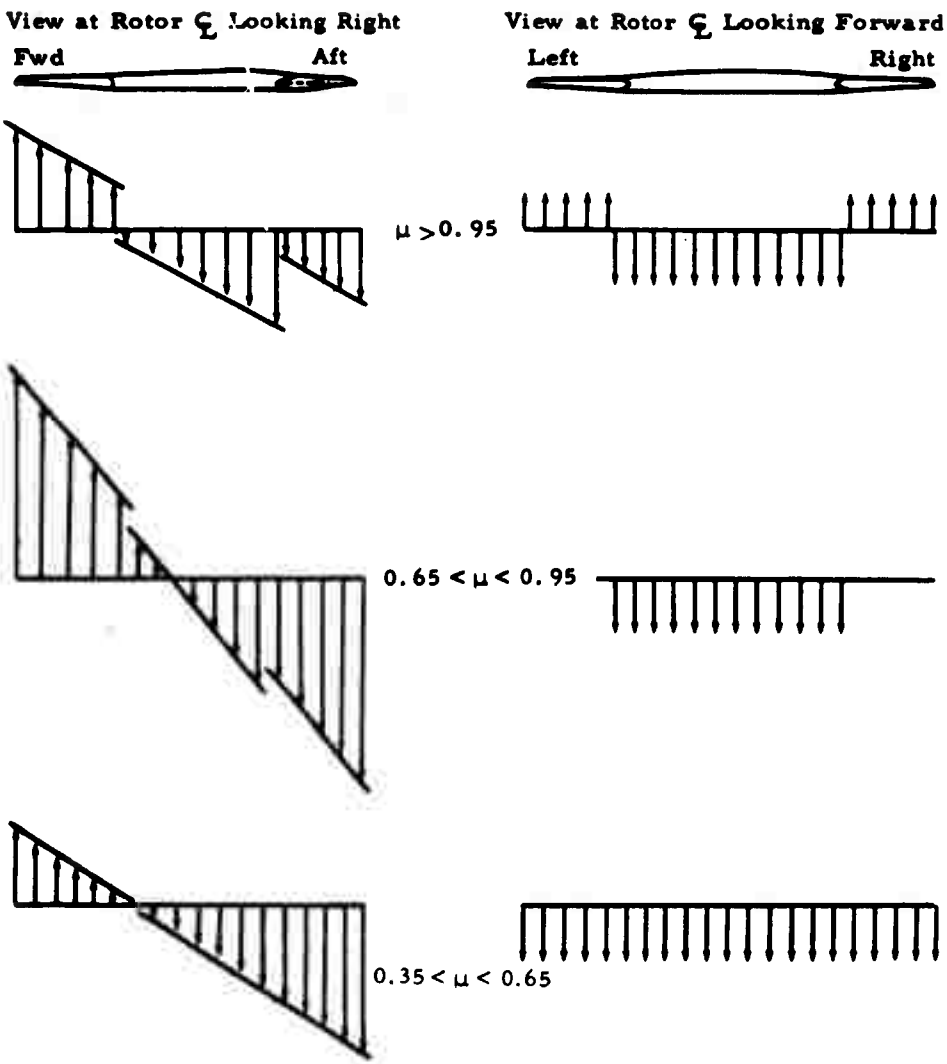

Figure 102. Rotor/Wing Downwash Distribution During Conversion

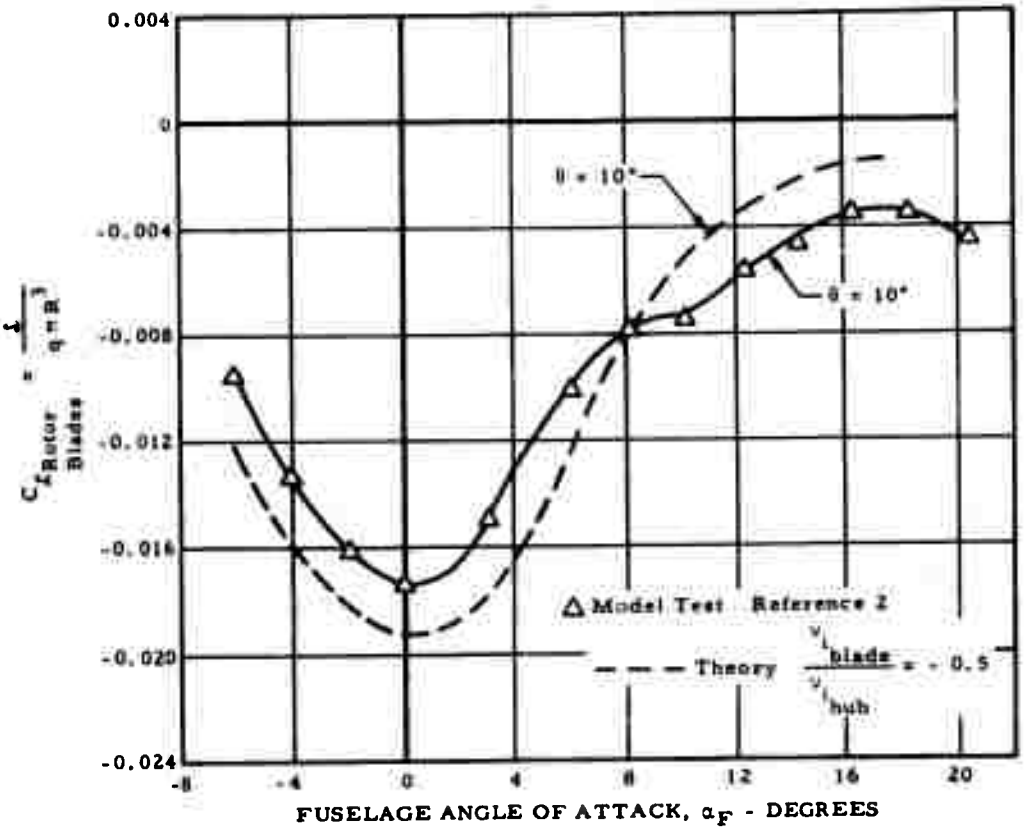

Figure 103. Comparison of Rotor Blade Rolling Moment from Model Test and Theoretical Calculation

linearly with radius and with the magnitude of the variable induced velocity being equal to two times the theoretical downwash average.

At higher values of rotor speed ($\mu < 0.65$), the Rotor/Wing has the characteristics of a helicopter rotor, and the standard method of computing downwash gives good agreement with test data values of lift and rolling moment coefficients. A fore-to-aft variation in induced velocity, equal to three times the

steady value, matches the test pitching moment coefficient. In this μ range, the theoretical induced velocity is based on the rotor area ($v_i/\Omega R = C_T/2\mu$).

At intermediate values of rotor speed ($0.65 < \mu < 0.9$), there is a transition from lift acting over the total rotor disc area to lift acting on the wing only. In this rotor speed range, it has been found that the assumption of zero uniform induced velocity at the blades, and a fore-to-aft variation in induced velocity equal to five times the theoretical induced velocity based on disc area, matches the test data satisfactorily.

Table 6 shows the comparison of theoretical and test values of lift and of pitching and rolling moments.

The downwash distributions deduced from wind tunnel tests are applied to the full-scale Rotor/Wing configuration to obtain the rotor stability derivatives. Then, terms representing the elevon characteristics are added, and the stick positions for steady, trimmed flight at various values of rotor speed are determined. Further, the change in stick position required to produce a steady pitching or rolling velocity is computed.

Table 6. Lift and Pitching Moment Comparison -- Theory and Test

μ	TEST			THEORY		
	C_L	C_ℓ	C_M	C_L	C_ℓ	C_M
1.88	0.1609	-0.0062	0.0371	0.1497	-0.0001	0.0334
0.95	0.0602	-0.0025	0.0402	0.1613	-0.0023	0.0411
1.87	0.1929	-0.0010	0.0471	0.1992	-0.0059	0.0496
1.04	0.1661	-0.0021	0.0464	0.1653	-0.0029	0.0526
0.76	0.1884	-0.0067	0.0528	0.1874	-0.0050	0.0529
0.25	0.1752	-0.0055	0.0609	0.1767	-0.0040	0.0587
0.35	0.1024	-0.0004	0.0291	0.1025	-0.0008	0.0269
0.35	0.1466	-0.0038	0.0216	0.1457	-0.0041	0.0254
0.42	0.1677	-0.0007	0.0489	0.1610	-0.0009	0.0449
0.42	0.1694	-0.0004	0.0578	0.1662	-0.0007	0.0540
0.62	0.1864	-0.0076	0.0510	0.1960	-0.0051	0.0497

At values of $\mu > 2.0$ (rpm < 18% of full rpm), the full-scale Rotor/Wing can be assumed rigid for purposes of aerodynamic analysis; at values of less than 2.0, a modified flapping blade numerical analysis must be used to properly account for the flexibility of the Rotor/Wing. A standard flapping-rotor aerodynamic analysis suffices, with the addition of a spring at the rotor centerline to simulate the stiffness of the hub.

DYNAMIC STABILITY IN HOVER

The hover-flight dynamic-stability-and-control response is calculated by assuming that the rotor blades, wing, and pylon-fuselage combination can be represented by a concentrated mass-spring system (indicated in Figure 104) that represents six degrees of freedom:

Pitch and roll of the fuselage as represented by mass (1)

Pitch and roll of the wing as represented by annular mass (2)

Pitch and roll of the blades as represented by annular mass (3)

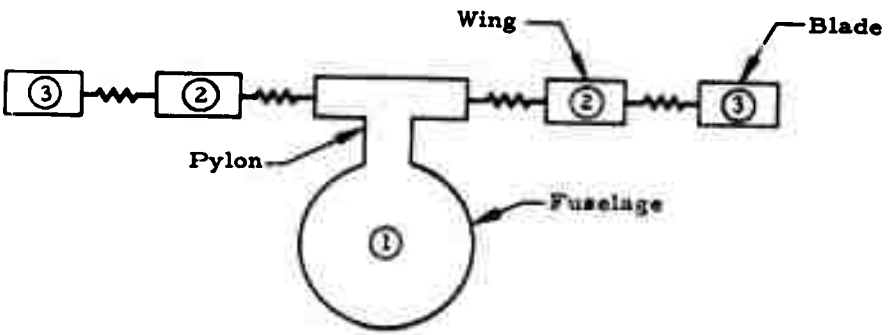

Figure 104. Schematic Rotor/Wing Spring-Mass Representation

STATIC STABILITY IN HELICOPTER AND AUTOGYRO FLIGHT

The Rotor/Wing is a nonarticulated rotor that is really rather flexible. To properly account for this flexibility when calculating static stability, the Rotor/Wing is assumed to act as an articulated rotor with a large offset of the flap hinge. The amount of this effective flap-hinge offset is determined by comparing the dynamic response of the equivalent rotor-with-flap-hinge offset with that computed by the Rotor/Wing hover dynamic stability method described above. Then, using conventional rotor digital computer techniques for this equivalent articulated rotor, the pitching and rolling moment terms are calculated to determine both trim and static stability in the helicopter and autogyro flight regimes.

DYNAMIC STABILITY IN HELICOPTER AND AUTOGYRO FLIGHT

The dynamic stability of the aircraft during the rotor operating modes is studied by using the basic six-degrees-of-freedom system described in the Hover section above, plus vertical and lateral degrees of freedom. The aerodynamic load on all three blades is computed by a strip analysis incorporating the downwash distribution deduced from wind tunnel tests, and the system is numerically integrated for each rotor azimuth. Thus, it becomes a Rotor/Wing simulator that permits an analysis of the response of the vehicle to control inputs. The response includes first-mode vibratory motions as well as rigid-body motions.

STATIC AND DYNAMIC STABILITY IN AIRPLANE FLIGHT

In the airplane flight mode, where the Rotor/Wing is locked and sealed to the fuselage, it is planned to use conventional, well-established analytical methods, such as those outlined in Reference 11 for determining the stability of the aircraft, both statically and dynamically. The information obtained from the extensive wind tunnel program conducted to date and the results of the

currently programmed dynamic model tests will be used as backup information for the aircraft stability studies.

To supplement the model test contributions to the analytical stability investigations, maximum use will be made of appropriate published statistical data. An example of this is the method used to derive the equations for preliminary sizing of the tail areas for Rotor/Wing aircraft. Figure 105 shows how the statistical data, theory, and Rotor/Wing model test results are combined to derive the equation for sizing the horizontal tail area. For current operational fixed-wing aircraft, statistical data of tail volume (tail area times moment arm), $S_H \ell_H$, are plotted versus fuselage volume (fuselage length times height, squared, $\ell_F H_F^2$, plus a wing volume term (wing mean aerodynamic chord times wing area), MAC S_W, showing a well defined relation.

A Rotor/Wing aircraft that was the subject of an intensive preliminary design study had good longitudinal stability and control characteristics, as substantiated by extensive analysis and model tests (neutral point at 68-percent MAC, well aft of the aft center of gravity at 36.6-percent MAC). These are compared with the statistical data in Figure 105. This particular aircraft required less tail volume for a given fuselage volume plus wing volume than current operational fixed-wing aircraft, primarily because of the vertical takeoff design requirements inherent for the Rotor/Wing aircraft. The Rotor/Wing aircraft does not have to make conventional running landings and takeoffs in the airplane mode and, hence, the usually critical elevator requirements for flare in ground effect do not apply; thus, it requires less horizontal tail area than is required by the conventional fixed-wing aircraft. The equation to be used is one that passes through the Rotor/Wing design point, parallel to the statistical data.

The derivation of the equation for sizing the vertical tail is similar and is shown in Figure 106. Model test results show that the required vertical tail

area for Rotor/Wing aircraft is approximately the same as that of the conventional fixed-wing aircraft, and therefore the statistical trend for conventional fixed-wing aircraft is to be used for Rotor/Wing aircraft.

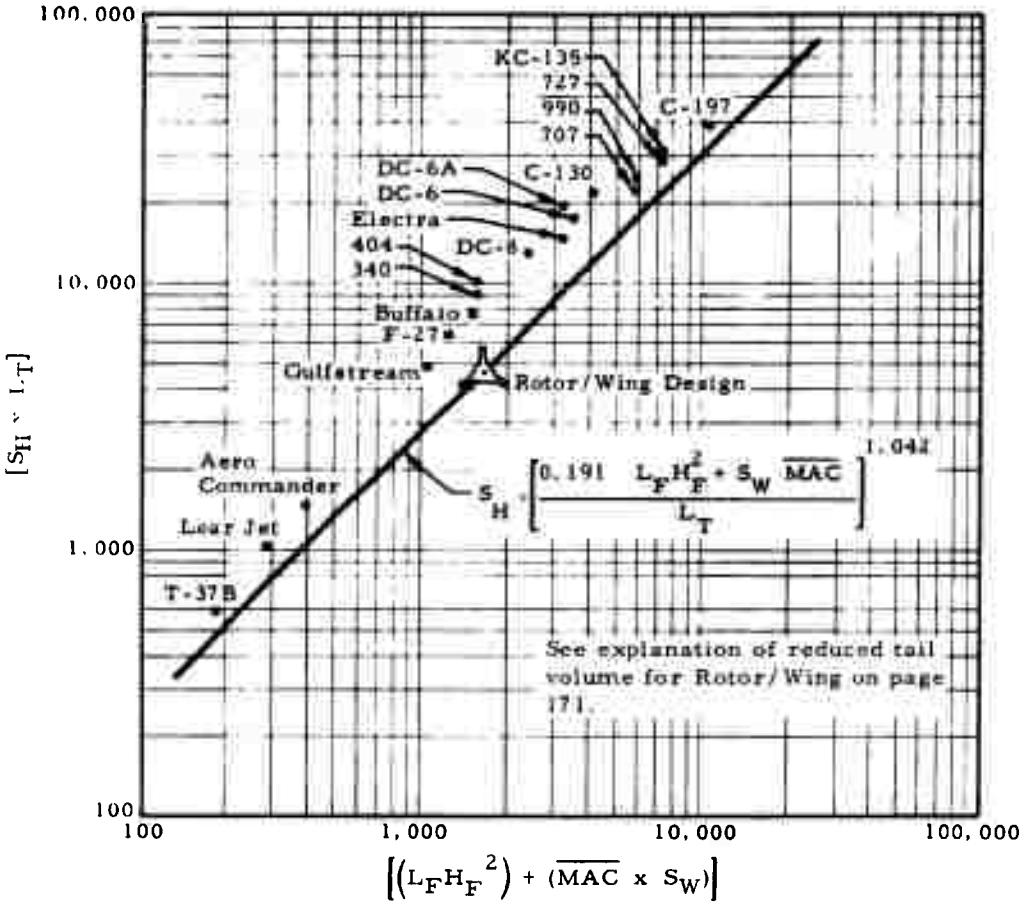

L_F = Fuselage Length - Ft

H_F = Fuselage Height - Ft

S_W = Wing Area - Ft^2

$\overline{MAC}$ = Mean Aero Chord - Ft

L_T = Tail Length - Ft (0.25C to 0.50C)

S_H = Horizontal Tail Area - Ft^2

Figure 105. Horizontal Tail Size Statistical Survey

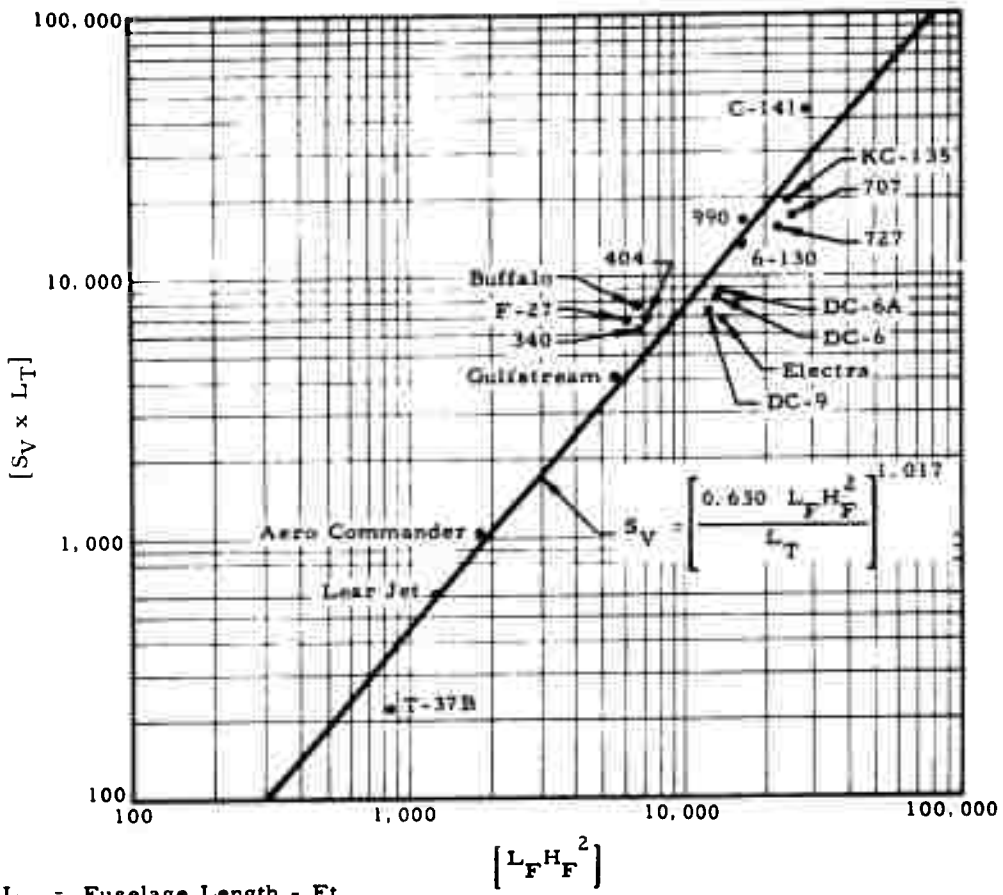

L_F = Fuselage Length - Ft

H_F = Fuselage Height - Ft

L_T = Tail Length - Ft (0.25 to 0.50C)

S_V = Vertical Tail Area - Ft^2

Figure 106. Vertical Tail Size Statistical Survey

BLANK PAGE

RESULTS AND CONCLUSIONS

DATA COMPARISON BETWEEN TUNNELS

The principal purpose of the Series VI tests was to compare the test results of the 7-foot diameter Rotor/Wing model, as measured in the 8-by-10-foot subsonic tunnel at Navy Ship Research and Development Center Aerodynamics Laboratory with those measured in the 30-by-60-foot full-scale tunnel at the NASA Langley Research Center. All across the flight spectrum where comparable conditions were tested, good agreement was shown between the data from both tunnels, when conventional airplane-type tunnel-wall or jet-boundary corrections were made. This indicates that at least this particular rotary-wing model may be tested in the 8-by-10-foot NSRDC tunnel with confidence in the rotor advance-ratio range from 0.15 upward.

ROTOR/WING CONFIGURATION COMPARISONS

The basic Rotor/Wing model configuration for the tests was the trisector wing, plus constant-chord blades. Other configurations with tapered blades, and with triangle and tricusp wing planforms, were compared. The hover efficiency of the tricusp configuration was best, followed by the triangle and trisector, in that order. In the forward-flight helicopter regime and in the autogyro flight regime, there was little to choose between the three configurations.

CONVERSION

The overall characteristics of the three Rotor/Wings during conversion -- that is, the control positions required and the mean forces and moments --

are all very nearly the same, and include none that should make conversion critical. Special tests in the final stages of conversion, at the very low rotor speeds from 100 rpm (17 percent of the design rpm) down to zero, showed that three times per revolution the center of pressure circled around an ellipse located forward of the rotor center in the fuselage-oriented, nonrotating coordinate system. This center of pressure excursion is of very nearly the same magnitude (for the triangle and for trisector rotor) and is independent of whether the rotor is starting or stopping. Vibrations that arise at the pilot's location in a typical Rotor/Wing aircraft as a result of this center-of-pressure travel would be on the order of ±0.30 g vertically and ±0.15 g laterally. Both are well within the short time allowance of military specifications. The tricusp Rotor/Wing experiences a center-of-pressure ellipse travel approximately three times as great as do the other Rotor/Wing configurations.

At the very lowest rotor speeds, as the rotor first starts or as it comes to a stop, pitching and rolling moments are developed that, if uncorrected, could result in fairly large pitching and rolling amplitudes; however, the pilot (or autopilot) has the capability of trimming these moments through control of the elevons. (Note: Recent investigations have indicated that the use of about 15 degrees of B_1 cyclic pitch can substantially reduce these oscillating pitching and rolling moments.)

ANALYTICAL PROCEDURES

Analytical procedures for predicting Rotor/Wing performance and flying qualities that are based on the classical methods established for conventional airplanes, helicopters, and autogyros, but with special consideration given to the unique features of the Rotor/Wing, are shown to be applicable by substantiation with model test data.

PROPOSED AREAS FOR FURTHER INVESTIGATION

The proposed areas for further investigation include:

1. A study of wing planform shape to minimize second and higher harmonic shaft bending at the high angles of attack encountered in autorotation and conversion
2. A study of wing camber effect to minimize the first harmonic shaft bending moments and fuselage pitching and rolling moments during conversion.

REFERENCES

1. Rotor/Wing Series I Wind Tunnel Tests, David Taylor Model Basin, Report TR AL 23, October 1964.

2. R. E. Head, Summary Technical Report, Rotor/Wing Concept Study, HTC-AD 65-15, Hughes Tool Company - Aircraft Division, Culver City, California, September 1965.

3. R. E. Head, Supplementary Study Report, Rotor/Wing Concept Study, HTC-AD 65-37, Hughes Tool Company - Aircraft Division, Culver City, California, February 1966.

4. S. J. DeFrance, NACA Full Scale Wind Tunnel, NACA TR 459, 1933.

5. V. M. Ganzer and W. H. Rae, Jr., An Experimental Investigation of the Effect of Wind Tunnel Walls on the Aerodynamic Performance of a Helicopter Rotor, NASA TN D-415, May 1960.

6. A. Gessow and G. Myers, Aerodynamics of the Helicopter, MacMillan Company, New York, 1952.

7. N. K. Delany and N. E. Sorensen, Low-Speed Drag of Cylinders of Various Shapes, NACA TN 3038, November 1953.

8. J. P. Shivers and P. J. Carpenter, Effects of Compressibility on Rotor Hovering Performance and Synthesized Blade-Section Characteristics Derived from Measured Rotor Performance of Blades Using NACA 0015 Airfoil Tip Sections, NACA TN 4356, 1958.

9. Theodorsen and Regier, Experiments on Drag of Revolving Disks, Cylinders, and Streamlined Rods at High Speeds, NACA TR 793.

10. S. F. Hoerner, Aerodynamic Drag, Oberbein Press, Dayton, Ohio, 1951.

11. C. D. Perkins and R. E. Hage, Airplane Performance, Stability, and Control, John Wiley and Sons, New York, New York.

12. R. C. Frost and R. Rutherford, "Subsonic Wing Span Efficiency", AIAA Journal, April 1963.

13. A. Gessow and R. Tapscott, Charts for Estimating Performance of High-Performance Helicopters, NACA TN 3323, 1955.

14. Aerodynamic Characteristics of NACA 0012 Airfoil Sections at Angles of Attack from 0° to 180°, NACA TN 3361, January 1955.

15. W. H. Turner, Charts for Estimating Rotary Wing Performance in Hover and at High Forward Speeds, NASA CR-114, November 1964.

16. I. Abbott and A. von Doenhoff, Theory of Wing Sections, Dover Publications, New York, New York.

17. F. J. Briardy, Rotor/Wing Series II Whirlstand Tests, 7-Foot-Diameter Model, HTC-AD 66-8, Hughes Tool Company - Aircraft Division, Culver City, California, April 1966.

APPENDIX

DETAIL TEST RUN SHEETS FOR SERIES VI TESTS

APPENDIX

DETAIL TEST RUN SHEETS FOR SERIES VI TESTS

Detailed test run sheets for the Series VI Rotor/Wing tests may be found in this Appendix. These supplement the summary of tests given in Table 1.

TPN	RUN NO.	ROLL NO.	α	θ	A_1	B_1	RPM	TP/V	μ	CONFIGURATION	COMMENTS
86-90	4	5	0	0	0	0	600	0	0	TE FLECTOR P_3=5° Symmetric (NASA Cont. 101) Horizontal Tail off	HOVER
91-95				2							
96-100				4							
101-105				6							
106-110				8							
111-115		6		10							
116-120				12							
121-125				14							
126-130				16							
131-135				18							
136-140				20							
141-145				0							— DATA N.G.
146-150				0							
151-155				10	0	0					
156-160					-5	0					Sign on Cyclic Control Questionable.
161-165					+5	0					
166-170					0	-5					
171-175					0	+5					
											Pts 111 to 176 Re-run as pts 177-250

TPN	RUN NO.	ROLL NO.	α	θ	A_1	B_1	RPM	TP/V	μ	CONFIGURATION	COMMENTS
176-220	SYSTEM ZEROS & CALIBRATIONS									TRISECTOR, A_2=5° (NASA Conf. 101)	HOVER
220-225	4	7	0	0	0	0	600	0	0		
226-230				2.5						HORIZONTAL TAIL OFF	REPEAT at PTS. 86 to 175
231-235				5							
236-240				7.5							
241-245				10							
246-250				12.5							
251-255				15							
256-260				17.5							
261-265				20.							
266-270				10	0	0					
271-275					-5	0					
276-280					5	0					
281-285					0	5					
286-290					0	-5					

TPN	RUN NO.	ROLL NO.	α	θ	A_1	B_1	RPM	TP/V	μ	CONFIGURATION	COMMENTS
291	5	8	-8	5			600	11 kts	.05	TRISECTOR, A_2=5°	HELICOPTER FLT, A_1 & B_1 READ for TRIM
292			-2								
293			4		-1.3	-2.5				Horizontal Tail off	
294			10		-2.0	-0.2					
295	6		-8	10	-1.0	0.5					
296			-2		-1.2	0.6					
297					3.8	0.6					ΔA_1 = +5°
298					-6.2	0.6					ΔA_1 = -5° Not
299					-1.2	5.6					ΔB_1 = +5° Trimmed
300					-1.2	-4.4					ΔB_1 = -5°
301			4		-1.5	0.4					
302			10		-2.2	0.8					
303	7		-14	15	-1.6	1.3					
304			-8		-2.0	1.4					
305			-2		-2.3	1.4					
306			4		-2.6	1.1					
307	8		-14	20	-3.5	1.6					
308			-8		-3.6	1.9					
309			-2		-3.7	1.6					
310			4		-3.7	1.5					

TPN	RUN NO.	ROLL NO.	α	θ	A_1	B_1	RPM	TP/V	μ	CONFIGURATION	COMMENTS
311	9	9	-8	5	-0.6	0.6	600	22 kts	.10	TRISECTOR, A_2 = 5° (NASA CONF. 103) HORIZONTAL TAIL OFF	HELICOPTER FLT.
312			-2		-0.1	0.2					
313			4		-2.3	0.2					A_1 & B_1 Required for Trim.
314			10		-3.2	0.5					
315	10		-8	10	-1.0	1.4					
316			-2		-1.5	1.5					
317					3.5	1.5					ΔA_1 = +5°
318					-6.5	1.5					ΔA_1 = -5° Not
319					-1.5	6.5					ΔB_1 = +5° Trimmed
320					-1.5	-3.5					ΔB_1 = -5°
321			4		-2.0	1.7					
322			10		-4.0	2.3					
323	11		-14	15	-1.2	2.4					
324			-8		-1.7	2.7					
325			-2		-2.5	2.8					
326			4		-3.7	3.7					
327	12		-14	20	-3.0	4.0					
328			-8		-3.5	4.0					
329			-2		-3.2	4.2					
330			4		-3.7	5.2					

TPN	RUN NO.	ROLL NO.	α	θ	A_1	B_1	RPM	TP/V	μ	CONFIGURATION	COMMENTS
331	13	10	-8	5	-0.1	0.5	600	1/	.15	TRISECTOR, A_2 = 5° (NASA Cont 103) Horizontal Tail 1.04	Helicopter Flt.
332			-2		-1.3	0.5		26 KNM			
333			4		-3.2	0.8		NOMINAL			A_1 & B_1 required for Trim
334			10		-4.1	0.5					
335	14		-8	10	-0.7	2.8					
336			-2		-2.2	2.8					
337					2.8	2.8					ΔA_1 = +5°
338					-7.2	2.8					ΔA_1 = -5° Not
339					-2.2	7.8					ΔB_1 = +5° Trimmed
340					-2.2	-2.2					ΔB_1 = -5°
341			4		-3.8	3.5					
342			10		-5.2	2.8					
343	15		-14	15	0	3.7					
344			-8		-1.1	5.0					
345			-2		-3.0	5.0					
346			4		-5.0	5.4					
347	16		-14	20	-1.1	6.2					
348			-8		-2.5	7.0					
349			-2		-4.0	7.7					
350			4		-5.2	8.1					
351	17	No	4	20	-4.0	7.7					Rerun-No Records
352		Record	-2		-2.5	7.0					Taken
353		Taken	-8		-1.1	6.2					
354			-14		?	?					

TPN	RUN NO.	ROLL NO.	α	θ	A_1	B_1	RPM	TP/V	μ	CONFIGURATION	COMMENTS
355	18	10	-8	5	0	0.5	600	4/	.25	TRISECTOR, A_2=5° (NASA CONF 103)	A_1 & B_1 IN ERROR ON MAG. TAPE, THESE VALUES CORRECTED
356	↓	↓	-2	↓	-2.0	1.2	↓	37.2	↓		
357	↓	↓	4	↓	-3.5	1.6	↓	↓	↓		
358	↓	↓	10	↓	-5.5	2.0	↓	↓	↓	HORIZONTAL TAIL-OFF	
359	19	↓	-8	10	0	3.2	↓	↓	↓		
360	↓	↓	-2	↓	-2.8	4.5	↓	↓	↓		
361	↓	↓	↓	↓	-7.8	4.5	↓	↓	↓		ΔA_1 = 5°
362	↓	↓	↓	↓	2.2	4.5	↓	↓	↓		ΔA_1 = -5°
363	↓	↓	↓	↓	-2.8	9.5	↓	↓	↓		ΔB_1 = 5° NOT TRIMMED
364	↓	↓	↓	↓	-2.8	0.5	↓	↓	↓		ΔB_1 = -5°
365	↓	↓	4	↓	-4.0	5.0	↓	↓	↓		
366	↓	↓	10	↓	-5.5	4.5	↓	↓	↓		
367	20	↓	-14	15	1.5	5.0	↓	↓	↓		
368	↓	↓	-8	↓	-0.5	5.0	↓	↓	↓		
369	↓	↓	-2	↓	-4.0	6.5	↓	↓	↓		
370	↓	↓	4	↓	-6.0	0	↓	↓	↓		
371	21	↓	↓	20	1.0	0.6	↓	↓	↓		θ MAY be in error ON MAG. TAPE; THESE VALUES CORRECTED
372	↓	↓	↓	↓	-1.5	8.0	↓	↓	↓		
373	↓	↓	↓	↓	-4.0	9.5	↓	↓	↓		
374	↓	↓	↓	↓	-7.0	9.5	↓	↓	↓		

TPN	RUN NO.	ROLL NO.	α	θ	A_1	B_1	RPM	TP/V	μ	CONFIGURATION	COMMENTS
375	22	11	-8	5	0.5	1.2	600	8/	.35	TRISECTOR, A_2=5° (NASA Conf. 103)	HELICOPTER FLT.
376	↓	↓	-2	↓	-2.8	2.9	↓	55.4	↓		
377	↓	↓	4	↓	-6.0	3.2	↓	↓	↓		
378	↓	↓	10	↓	?	?	↓	↓	↓		
379	23	↓	-8	10	0.5	5.0	↓	↓	↓		
425	25	↓	-8	10	0	4.5	↓	↓	↓		
426	↓	↓	-2	↓	-3.5	5.7	↓	↓	↓		
427	↓	↓	↓	↓	1.5	5.7	↓	↓	↓		ΔA_1 = 5°
428	↓	↓	↓	↓	-8.5	5.7	↓	↓	↓		ΔA_1 = -5° NOT TRIMMED
429	↓	↓	↓	↓	-3.5	0.7	↓	↓	↓		ΔB_1 = -5° CEL NOS
430	↓	↓	↓	↓	-3.5	10.7	↓	↓	↓		ΔB_1 = 5° OUT OF ORDER
431	↓	↓	4	↓	-5.8	4.3	↓	↓	↓		
432	↓	↓	10	↓	-8.5	5.5	↓	↓	↓		
433	26	↓	-14	15	3.8	5.0	↓	↓	↓		
434	↓	↓	-8	↓	0	7.7	↓	↓	↓		
435	↓	↓	-2	↓	-3.5	8.5	↓	↓	↓		
436	↓	↓	4	↓	-6.0	11.4	↓	↓	↓		
437	27	↓	-8	20	0	11.0	↓	↓	↓		
438	↓	↓	-2	↓	-3.7	13.8	↓	↓	↓		
439	↓	↓	4	↓	-7.0	15.5	↓	↓	↓		
440	28	↓	-2	5	0	0	↓	↓	↓		
441	↓	↓	4	↓	0	1.4	↓	↓	↓		A, NOT TRIMMED
442	↓	↓	10	↓	0	2.7	↓	↓	↓		B, TRIMMED

TPN	RUN NO.	ROLL NO.	α	θ	A_1	B_1	RPM	TP/V	μ	CONFIGURATION	COMMENTS
443	29	11	-8	10	0	4.0	600	8/	.35	TRISECTOR, $A_2 = 5°$	HELICOPTER FLT
444	↓	↓	-2	↓	0	4.2	↓	55.2 MPH	↓	(NASA Conf 102)	A_1 NOT TRIMMED
											TRIM TRICD. 5-SERDS
	30	SYS	TEM	CALIB	RAT	ION					SAFE SIZE LIMITS
555	31	12	-8	10	0	4.8	600	8/	.35		PITCH NOT TRIMMED
556	↓		-2	↓		5.8	↓	55.2 MPH	↓		
557	32		-8	5		0.8	600	4/	.25		PTS. 555 → 564
558			-2			1.5		37.2 MPH			RERUN AS 566-575
559			4			1.7					SEE BELOW
560	↓		10	↓		1.8					
561	33		-8	10		2.8					
562			-2			4.0					
563			4			4.3					
564	↓	↓	10	↓	↓	4.8	↓		↓		
565	VOID,		θ IN	ERROR							
566	34	12	-8	5	0	0.7	600	4/	.25		RERUN OF ABOVE PTS.
567			-2			1.0		37.2 MPH			
568			4			1.4					
569	↓		10	↓		1.4					
570	35		-8	10		3.0					
571			-2			3.7					
572			4			3.7					
573	↓	↓	10	↓	↓	3.5	↓		↓		

TPN	RUN NO.	ROLL NO.	α	θ	A_1	B_1	RPM	TP/V	μ	CONFIGURATION	COMMENTS
574	36	12	-8	10	0	4.1	600	8/	.35	TRISECTOR, $A_2 = 5°$	HELICOPTER FLT.
575	↓		-2	↓	↓	5.4	↓	55.2 MPH	↓	(NASA Conf 102)	PITCH NOT TRIMMED
576	37	12	3	10.8	-4.0	1.8	600	8/	.35	TRISECTOR, $A_2 = 5°$	AUTOGIRO FLT.
577			3	8.0	-5.0	5.3		55.2 MPH		TAIL-OFF	(MAIN OFF)
578		↓	6	4.5	-6.0	4.2				(NASA Conf 104)	LIFT = 50#
579		13	9	2.0	-6.8	2.0					θ, A, & B, AS REQ'D
580			12	-1.6	-8.6	1.5					for Lift & Trim.
581			13	-3.7	-8.7	0					(PSEUDO CONVERSION)
582			14	-5.0	-9.1	-0.5					
583	↓	↓	15	-5.5	-9.2	-0.8	↓		↓		
584	38		0	12.5	0	8.5					PITCH NOT TRIMMED
585			3	8.6		5.2					θ & B, AS REQ'D
586			6	5.4		3.3					
587			9	2.3		2.7					
588			12	-0.5		0.5					
589			13	-3.0		1.3					
590			14	-3.6		-1.5					
591	↓	↓	15	-5.5	↓	-2.2	↓		↓		

TPN	RUN NO.	ROLL NO.	α	θ	A_1	B_1	RPM	TP/V	μ	CONFIGURATION	COMMENTS
592	39	13	3	18.0	-7.0	10.0	500	8/	.42	TRISECTOR, A_2 = 5° (NASA Conf. 104)	AUTOGIRO FLT. (PSEUDO CONVERSION) LIFT = 50# A_1 & B_1 TRIMMED
593			6	10.0	-8.0	10.0		55.2 RPM			
594			9	5.3	-11.0	6.3					
595			12	0	-11.5	2.8					
596			13	0	-11.5	2.3					
597			14	-5.0	-11.8	-1.0					
598			15	-7.5	-13.0	-2.0					
599	40		3	11.7	0	10.0					PITCH NOT TRIMMED θ & B_1 AS REQ'D
600			6	10.0		7.8					
601			9	6.8		7.0					
602			12	0		1.8					
603		14	13	-2.0		-0.1					
604			14	-3.5		-0.5					
605			15	-6.2		-2.8					
606	41		9	12.5	-15.0	16.2	395		*.53		NOMINAL ROTOR SPEED = 400 RPM * NOMINAL μ
607			12	3.0	-15.0	7.8	392				
608			13	-2.5	-15.2	2.7	390				
609			14	-5.5	-15.2	0.3	399				
610			15	-8.0	-15.2	-1.7	395				
611	42		9	13.0	0	15.5	392				PITCH NOT TRIMMED θ & B_1 AS REQ'D
612			12	4.0		8.0	393				
613			13	-1.0		3.4	397				
614			14	-4.0		0.2	418				
615			15	-6.5		-2.0	418				

TPN	RUN NO.	ROLL NO.	α	θ	A_1	B_1	RPM	TP/V	μ	CONFIGURATION	COMMENTS
616	43	14	9	11.7	0	16.2	290	8/	.70	TRISECTOR, A_2 = 5° (NASA CONF 104)	300 AUTOGIRO FLT. (PSEUDO CONV) LIFT = 50# PITCH NOT TRIMMED B_1 for TRIM
617			12	8.2		16.2	301	55.2 RPM			
618			13	5.5		13.5	299				
619			14	-5.0		0.7	351				
620			15	-8.0		-3.1	345				
621	44		12	10.0		16.2	226		1.05		200 NOMINAL ROTOR SPEED
622			13	5.7		16.2	226				
623			14	2.5		11.0	243				
624			15	-8.0		0.5	182				
625	45		14	3.5		16.3	101		2.10		100
626			13	2.6		15.0	95				
627			15	-8.0		-1.5	104				
	46	15		ATTEMPT		AT	AUTOMATIC			& MANUAL CONVERSION	
768	53	16	19.5	2	0	1.8	565	4/			Data not recorded on CEL System
769			16.8			3.6	554	8/			
770			13.0			5.8	600	12/			
771			11.0			7.3	550	16/			
772	54		10.5			7.5	500	16/			
773			12.7			6.8	527	12/			
774			14.5			5.0	522	8/			
775			19.5			3.2	412	4/			

TPN	RUN NO.	ROLL NO.	α	θ	A_1	B_1	RPM	TP/V	μ	CONFIGURATION	COMMENTS
775	55		19.5	2	0		500	4	.25	TRISECTOR, A_2=5	AUTOGYRO FLT.
776			13.5					8	.35		RERUN of 768-771
777		SEE SHEET	13.5			NOT RECORDED		12	.45		BECAUSE CEL SYSTEM
778			10.0					16	.54		WAS INOPERATIVE. No
779	56		11.0				600	16	.54		OSCILLOGRAPHS TAKEN
780			12.5					12	.45		FOR 775-782.
781			15.0					8	.35		SOME CONFUSION ON
782			19.5					4	.25		TPN's
828	57	NONE FED'D	-3.7	0	0	0	0	14/ 71.7mm	∞	TRISECTOR, (NASA CONF 109) TAIL-OFF	AIRPLANE FLT.
829			0								
830			2								
831			4								
832			6								
833			8								
834			12								
835			16								
836			19.5								

TPN	RUN NO.	ROLL NO.	α	θ	A_1	B_1	RPM	TP/V	μ	CONFIGURATION	COMMENTS
~~896~~	CALIBRATION									TRICUSPED (NASA CONF. 209) TAIL-OFF	AIRPLANE FLT.
897	59		-4	0	0	0	0	14/ 71.7mm	0		
898			0								
899		NONE FED'D	2								
900			4								
901			6								
902			8								
903			12								
904			16								
905			19.5								
946	60	17	17.4	2	0	0	593	4/		TRICUSPED, A_2=5° (NASA CONF 208) TAIL-OFF	AUTOGYRO FLT
947			12.3			2.3	600	8/			B, TRIMMED
948			11.3			5.0	583	12/			A_1 = 0
949			12.3			8.3	581	16/			
950	61		11.3			9.4	580	16/			500 RPM NOMINAL
951			11.5			5.3	585	12/			
952			10.9			2.3	585	8/			
953			15.3			1.0	523	4/			

TPN	RUN NO.	ROLL NO.	α	θ	A_1	B_1	RPM	TP/V	μ	CONFIGURATION	COMMENTS
984	62	17	0	0	0	0	600	0	0	TRICUSPED, A_2=5 (NASA CONF 201) TAIL-OFF	HOVER
985				2							
986				4							
987				5							
988				6							
989				8							
990				10							
991				12							
992				14							
993				15							
994				16							
995				18							
996				20							
997				10	0	0					TEST FOR CONTROL POWER AVAIL.
998					-5	0					
999					5	0					
1000					0	5					
1001					0	-5					

TPN	RUN NO.	ROLL NO.	α	θ	A_1	B_1	RPM	TP/V	μ	CONFIGURATION	COMMENTS
1002	63	17	-8	5	-0.5	0	600	11/sec	.05	TRICUSPED, A_2=5° (NASA CONF 202) TAIL-OFF	HELICOPTER FLT.
1003			-2		-0.6	0					
1004			4		-2.5	0					A, & B, TRIMMED
1005			10		-2.5	0					
1006	64		-8	10	-1.0	0.5					
1007			-2		-1.5	0.5					
1008					3.5	0.5					ΔA_1 = 5°
1009					-6.5	0.5					ΔA_1 = -5°
1010					-1.5	5.5					ΔB_1 = 5°
1011					-1.5	-4.5					ΔB_1 = -5°
1012			4		-2.0	0.6					CONTROL POWER AVAIL.
1013			10		-1.8	0.6					
1014	65		-14	15	-1.8	1.0					
1015			-8		-1.8	1.0					
1016			-2		-2.2	1.0					
1017			4		-2.7	1.3					
1018	66		-14	20	-2.3	1.4					
1019			-8		-2.3	1.5					
1020			-2		-2.5	1.5					
1021			4		-3.3	1.5					

TPN	RUN NO.	ROLL NO.	α	θ	A_1	B_1	RPM	TP/V	μ	CONFIGURATION	COMMENTS
1022	67	17	-8	5	-0.5	0	600	/22kts	.10	TRICUSPED, A_2 = 5°	HELICOPTER FLT
1023			-2		-1.5	0.5				(NASA 203)	
1024			4		-2.8	0.5				TAIL-OFF	A_1 & B_1 TRIMMED
1025			10		-3.3	0.5					
1026	68		-8	10	-1.1	1.5					
1027			-2		-2.2	1.4					
1028					2.8	1.4					ΔA_1 = 5° } CONTROL
1029					-7.2	1.4					ΔA_1 = -5° } POWER
1030					-2.2	6.4					ΔB_1 = 5° } AVAIL.
1031					-2.2	-3.6					ΔB_1 = -5° }
1032			4		-3.1	2.3					
1033			10		-4.0	2.0					
1034	69		-14	15	-1.5	2.4					
1035			-8		-2.0	2.0					
1036			-2		-2.5	3.0					
1037			4		-3.3	2.8					
1038	70		-14	20	-2.8	3.3					
1039			-8		-3.4	3.3					
1040			-2		-3.8	4.5					
1041			4		-4.2	5.0					

TPN	RUN NO.	ROLL NO.	α	θ	A_1	B_1	RPM	TP/V	μ	CONFIGURATION	COMMENTS
1087	72	18	-8	5	-1.0	1.3	600	1/	.15	TRICUSPED, A_2=5°	HELICOPTER FLT.
1088			-2		-2.0	1.2		26kts		(NASA CONF. 203.)	
1089			4		-3.0	1.7				TAIL-OFF	A_1 & B_1 TRIMMED
1090			10		-4.0	1.7					
1091	73		-8	10	-1.2	3.0					
1092			-2		-3.0	2.5					
1093					2.0	2.6					ΔA_1 = 5° } CONTROL
1094					-8.0	4.0					ΔA_1 = -5° } POWER
1095					-3.0	7.5					ΔB_1 = 5° } AVAIL
1096					-3.5	-2.5					ΔB_1 = -5° }
1097			4		-4.1	3.0					
1098			10		-5.0	3.1					
1099	74		-14	15	-1.0	4.5					
1100			-8		-2.0	5.1					
1101			-2		-3.5	5.2					
1102			4		4.5	5.6					
1103	75		-14	20	-2.2	6.5					
1104			-8		-3.2	6.1					
1105			-2		-4.7	7.6					
1106			4		-5.5	7.8					

TPN	RUN NO.	ROLL NO.	α	θ	A_1	B_1	RPM	TP/V	μ	CONFIGURATION	COMMENTS
1107	76	18	-8	5	-0.5	1.5	600	61	.35	TRICUSPED, A_2=5° (NASA CONF 203) TAIL-OFF	HELICOPTER FLT. A_1 & B_1 TRIMMED
1108	↓	↓	-2	↓	-2.3	2.6	↓	55.2mm	↓	↓	↓
1109	↓	↓	4	↓	-2.5	2.8	↓	↓	↓	↓	↓
1110	↓	↓	10	↓	-4.7	3.0	↓	↓	↓	↓	↓
1111	77	↓	-8	10	-1.5	4.8	↓	↓	↓	↓	↓
1112	↓	↓	-2	↓	-3.0	4.6	↓	↓	↓	↓	↓
1113	↓	↓	↓	↓	2.0	4.0	↓	↓	↓	↓	↓
1114	↓	↓	↓	↓	-8.0	6.0	↓	↓	↓	↓	↓
1115	↓	↓	↓	↓	-3.0	5.6	↓	↓	↓	↓	↓
1116	↓	↓	↓	↓	-4.0	-4.4	↓	↓	↓	↓	↓
1117	↓	↓	4	↓	-4.1	4.5	↓	↓	↓	↓	↓
1118	↓	↓	10	↓	-5.2	5.2	↓	↓	↓	↓	↓
1119	78	↓	-14	15	0	5.6	↓	↓	↓	↓	↓
1120	↓	↓	-8	↓	-1.5	6.3	↓	↓	↓	↓	↓
1121	↓	↓	-2	↓	-4.0	6.5	↓	↓	↓	↓	↓
1122	↓	↓	4	↓	-5.0	7.3	↓	↓	↓	↓	↓
1123	79	↓	-14	20	-1.3	8.4	↓	↓	↓	↓	↓
1124	↓	↓	-8	↓	-2.5	9.0	↓	↓	↓	↓	↓
1125	↓	↓	-2	↓	-5.0	10.5	↓	↓	↓	↓	↓
1126	↓	↓	4	↓	-5.4	11.5	↓	↓	↓	↓	↓

ΔA_1 = 5°, ΔA_1 = -5°, ΔB_1 = 5°, ΔB_1 = -5° } Control Power Avail.

TPN	RUN NO.	ROLL NO.	α	θ	A_1	B_1	RPM	TP/V	μ	CONFIGURATION	COMMENTS
1127	80	18	-8	5	-0.5	0.2	600	81	.35	TRICUSPED, A_2=5 (NASA Conf 203) TAIL-OFF	HELICOPTER FLT. A_1 & B_1 TRIMMED
1128	↓	↓	-2	↓	-3.0	3.0	↓	55.2mm	↓	↓	↓
1129	↓	↓	4	↓	-4.5	4.4	↓	↓	↓	↓	↓
1130	↓	↓	10	↓	-6.0	5.7	↓	↓	↓	↓	↓
1131	81	↓	-8	10	-0.9	6.0	↓	↓	↓	↓	↓
1132	↓	↓	-2	↓	-3.8	6.7	↓	↓	↓	↓	↓
1133	↓	↓	↓	↓	1.2	6.0	↓	↓	↓	↓	↓
1134	↓	↓	↓	↓	-8.8	7.7	↓	↓	↓	↓	↓
1135	↓	↓	↓	↓	-3.0	9.7	↓	↓	↓	↓	↓
1136	↓	↓	↓	↓	-4.1	-0.3	↓	↓	↓	↓	↓
1137	↓	↓	4	↓	-5.0	8.2	↓	↓	↓	↓	↓
1138	↓	↓	10	↓	-6.3	7.7	↓	↓	↓	↓	↓
1139	82	↓	-14	15	1.0	7.0	↓	↓	↓	↓	↓
1140	↓	↓	-8	↓	-1.0	8.5	↓	↓	↓	↓	↓
1141	↓	↓	-2	↓	-2.5	9.5	↓	↓	↓	↓	↓
1142	↓	↓	4	↓	-5.0	11.7	↓	↓	↓	↓	↓
1143	83	↓	-14	20	0.4	9.8	↓	↓	↓	↓	↓
1144	↓	↓	-8	↓	-1.7	11.6	↓	↓	↓	↓	↓
1145	↓	↓	-2	↓	-4.6	14.2	↓	↓	↓	↓	↓
1146	↓	↓	4	↓	-5.9	15.8	↓	↓	↓	↓	↓

ΔA_1 = 5°, ΔA_1 = -5°, ΔB_1 = 5, ΔB_1 = -5 } Control Power Avail.

TPN	RUN NO.	ROLL NO.	α	θ	A_1	B_1	RPM	TP/V	μ	CONFIGURATION	COMMENTS
1192	B5	18	0	18.0	0	6.0	[illegible]	B/	.35	Trimmed, A_1=5° (Wheel Cond. 304) TPL-[illegible]	Airborne Eff. A_1 = 0 B. Trimmed
1193			3	7.1		4.6		500 rpm			
1194			6	4.0		2.7					
1195			9	2.2		3.8					
1196			12	-1.5		5.5					
1197			13	-2.0		0					
1198	↓		14	-3.0	↓	0	↓		↓		
1199	B6		3	13.0	0	11.5	500		.43		
1200			6	8.7		8.5					
1201			9	5.0		6.0					
1202			12	1.0		3.0					
1203			13	-1.0		2.5	↓		↓		
1204			14	-2.0		0	460		.46		
1205	↓		15	-3.0	↓	1.5	560		.39		
1206	B7		12	11.5	0	11.5	400		.18		Can't Trim Roll at this Point Therefore Values
1207			13	9.0		6.0					
1208			14	-2.0		5.0					
1209	↓		15	-2.5	↓	5.0	↓		↓		
1210	B8		13	7.0	0	16.5	300				See next page for additional data, was [illegible] all [illegible]
1211			14	2.5		12.0	320				
1212			15	0	↓	9.5	350				
1213	B9		14	6.7	0	16.5	200				
1214	↓		15	3.5	↓	14.5	210				
1215	B10	↓	15	5.0	0	16.5	110	↓			

TPN	RUN NO.	ROLL NO.	α	θ	A_1	B_1	RPM	TP/V	μ	CONFIGURATION	COMMENTS
1216A	B8	18	16	-2.5	0	5.0	315	B/		Trimmed, A_1=5° (Wheel Cond. 304) TPL-[illegible]	Airborne A_1 = 0 B. Trimmed
B			17	-2.0		[illegible]	[illegible]	500 rpm			
C			18	-1.5		[illegible]	720				
1216A	B9		16	-2.1	0	6.0	210				
B			17	-1.5		2.5	220				Continued of data from page 24
C			18	-1.0		2.5	210				
1216A	B10	↓	16	-1.0	0	2.5	130	↓			

TPN	RUN NO.	ROLL NO.	α	θ	A_1	B_1	RPM	TP/V	μ	CONFIGURATION	COMMENTS
1337	96	20	0	0	0	0	600	0	0	TRIANGLE, A_2=5 (NASA CONF 301) TAIL-OFF	HOVER FLT.
1338				2							
1339				4							
1340				5							
1341				6							θ RECORDED IN ERROR ON CEL SYSTEM for pts 1338 - 1346
1342				8							
1343				10							
1344				12							
1345				14							
1346				15							
1347				16							
1348				18							
1349				20							
1350				10							
1351					-5	0					CONTROL POWER AVAILABLE
1352					5	0					
1353					0	5					
1354					0	-5					

TPN	RUN NO.	ROLL NO.	α	θ	A_1	B_1	RPM	TP/V	μ	CONFIGURATION	COMMENTS
1355	97	21	-8	5	-0.5	0.2	600	11 kts	.05	TRIANGLE, A_2=5° (NASA CONF 303) TAIL-OFF	HELICOPTER FLT. A & B, TRIMMED
1356			-2		-1.0	0					
1357			4		-1.4	0					
1358			10		-1.8	0					
1359	98		-8	10	-0.8	0.6					
1360			-2		-1.1	0.6					
1361					3.9	3.9					ΔA_1 = 5°
1362					-6.1	0.6					ΔA_1 = -5°
1363					-1.1	5.6					ΔB_1 = 5°
1364					-1.1	-4.4					ΔB_1 = -5° CONTROL POWER AVAIL.
1365			4		-1.5	1.0					
1366			10		-1.4	0.8					
1367	99		-14	15	-1.2	1.5					
1368			-8		-1.5	1.5					
1369			-2		-1.8	1.8					
1370			4		-2.2	1.8					
1371	100		-14	20	-1.6	2.2					
1372			-8		-1.7	2.0					
1373			-2		-2.5	2.0					
1374			4		-2.7	2.3					

TPN	RUN NO.	ROLL NO.	α	θ	A_1	B_1	RPM	TP/V	μ	CONFIGURATION	COMMENTS
1375	101	21	-8	5	-0.1	0.2	600	22 kts	.10	TRIANGLE, A_2 = 5° (NASA Cont 303) TAIL-OFF	HELICOPTER FLT. A & B, TRIMMED
1376	↓		-2	↓	-1.6	0.5					
1377			4		-3.0	0					
1378	102		10	10	-3.6	0					
1379			-8		-1.0	1.5					
1380			-2		-2.2	1.9					
1381					2.8	1.9					ΔA₁ = 5°, ΔA₁ = -5°, ΔB₁ = 5°, ΔB₁ = -5° } CONTROL POWER AVAIL.
1382					-2.2	1.9					
1383					-2.2	6.9					
1384			↓		-2.2	-3.1					
1385			4		-3.7	2.2					
1386	↓		10	↓	-4.0	2.3					
1387	103		-14	15	-1.5	2.5					
1388			-8		-2.0	2.8					
1389			-2		-2.7	3.0					
1390	↓		4	↓	-3.2	3.8					
1391	104		-14	20	-2.8	3.3					
1392			-8		-3.2	4.1					
1393			-2		-3.9	4.0					
1394	↓	↓	4	↓	-4.5	5.8	↓	↓	↓		
1395	——		V-O-I-D								

TPN	RUN NO.	ROLL NO.	α	θ	A_1	B_1	RPM	TP/V	μ	CONFIGURATION	COMMENTS
1396	105	21	-8	5	-0.5	1.0	600	1	.15	TRIANGLE, A_2 = 5° (NASA Cont 303) TAIL-OFF	HELICOPTER FLT. A & B, TRIMMED
1397			-2		-1.6	1.0		26 kts			
1398			4		-3.6	1.0					
1399	↑		10	↓	-4.0	1.0					
1400	106		-8	10	-0.6	2.8					
1401			-2		-3.0	2.8					
1402					2.0	2.8					ΔA₁ = 5°, ΔA₁ = -5°, ΔB₁ = 5°, ΔB₁ = -5° } CONTROL POWER AVAIL.
1403					-5.5	2.8					
1404					-3.0	7.8					
1405			↓		-3.0	-2.2					
1406			4		-4.5	3.2					
1407	↑		10	↓	-5.2	3.2					
1408	107		-14	15	0	3.4					
1409			-8		-1.0	4.5					
1410			-2		-3.2	5.0					
1411	↑		4	↓	-5.3	4.3					
1412	108		-14	20	-0.7	6.4					
1413			-8		-2.0	5.2					
1414			-2		-4.5	8.1					
1415	↓	↓	4	↓	-5.0	8.6	↓		↓		

TPN	RUN NO.	ROLL NO.	α	θ	A_1	B_1	RPM	TP/V	μ	CONFIGURATION	COMMENTS
1416	109	21	-8	5	0.2	1.0	600	4/	.25	TRIANGLE, A_2 = 5°	HELICOPTER, FLT
1417			-2		-2.0	2.0		372 KNM		(NASA Cont 303)	A, & B, TRIMMED
1418			4		-3.8	2.0				TAIL-OFF	
1419			10		-5.0	2.0					
1420	110		-8	10	-2.0	3.2					
1421			-2		-2.7	4.5					
1422					2.3	4.5					
1423					-5.2	4.5					ΔA, = 5°
1424					-2.7	9.5					ΔA, = -2.5 } CONTROL
1425					-2.7	-0.5					ΔB, = 5° } POWER
1426			4		-4.7	4.2					ΔB, = -5° } AVAIL.
1427			10		-5.7	4.2					
1428	111		-14	15	1.2	5.2					
1429			-8		-0.6	6.5					
1430			-2		-3.0	7.0					
1431			4		-5.5	7.8					
1432	112		-14	20	0	8.0					
1433			-8		-1.5	9.3					REPEATED BELOW
1434	113		-14	20	0.2	7.6					
1435			-8		-1.6	9.3					
1436			-2		-4.0	10.7					
1437			4		-5.0	11.5					

TPN	RUN NO.	ROLL NO.	α	θ	A_1	B_1	RPM	TP/V	μ	CONFIGURATION	COMMENTS
1438	114	21	-8	5	0.5	1.7	600	8/	.35	TRIANGLE, A_2 = 5	HELICOPTER FLT.
1439			-2		-2.2	3.8		552 KNM		(NASA Cont 303)	A, & B, TRIMMED
1440			4		-4.5	4.1				TAIL-OFF	
1441			10		-7.0	5.2					
1442	115		-8	10	0.5	5.2					
1443			-2		-2.7	6.2					
1444					2.3	6.2					
1445					-5.2	6.2					ΔA, = 5°
1446					-2.7	11.2					ΔA, = -2.5° } CONTROL
1447					-2.7	1.2					ΔB, = 5° } POWER
1448			4		-5.0	8.2					ΔB, = -5° } AVAIL.
1449			10		-7.5	9.4					
1450	116		-14	15	2.7	6.4					
1451			-8		0	8.6					
1452			-2		-3.0	10.7					
1453			4		-4.9	11.4					
1454	117		-14	20	2.0	9.5					
1455			-8		-0.2	11.8					
1456			-2		-3.4	14.8					
1457			4		-5.0	15.5					

TPN	RUN NO.	ROLL NO.	α	θ	A_1	B_1	RPM	TP/V	μ	CONFIGURATION	COMMENTS
1499	118	22	0	10.0	0	5.5	600	8/	.35	TRIANGLE, A_2 = 5° (NASA CONF 304) TAIL-OFF	AUTOGYRO FLT. (PSEUDO CONVERSION) LIFT = 50 # A_1 = 0 B_1 TRIMMED
1500			3	7.0		4.7		55.2 KN			
1501			6	3.0		2.2					
1502			9	0		0.7					
1503			12	-1.5		0					
1504			13	-3.5		-0.7					
1505			14	-5.0		-2.0					
1506			15	-6.5		-3.0					
1507	119		3	12.0		11.0	500		.47		
1508			6	6.0		5.8					
1509			9	3.0		3.3					
1510			12	-1.5		0.2	490				
1511			13	-4.7		-0.7					
1512			14	-5.2		-1.1					
1513			15	-7.0		-2.0					
1514	120		6	15.1		16.5	400		.60		
1515			9	10.6		15.1	400				
1516			12	1.0		4.5	410				
1518			13	-2.5		3.3	410				
1519			14	-4.5		-0.2	460		?		
1520			15	-7.5		-2.2	465		?		

TPN	RUN NO.	ROLL NO.	α	θ	A_1	B_1	RPM	TP/V	μ	CONFIGURATION	COMMENTS
1521	121	22	9	14.5	0	16.5	290	8/	.85	TRIANGLE, A_2 = 5° (NASA CONF 304) TAIL-OFF	AUTOGYRO FLT. (PSEUDO CONV) LIFT = 50 # A_1 = 0 B_1 TRIMMED *(TPN 1521 NOT TRIMMED)
1522			12	8.0		16.0	300				
1523			13	0		7.0	320				
1524			14	-6.0		4.0	340				
1525			15	-7.5		0	350				
1526	122		12	-1.5	0	5.2	130				
1527			13	-6.0		5.2	140				
1528			14	-10.0		-1.0	190				
1529	123	22	0	12.5	0	7.2	600	8/	.35		LIFT = 70 # A_1 = 0 B_1 TRIMMED
1530			3	9.0		5.0					
1531			6	7.0		3.5					
1532			9	4.7		3.0					
1533			12	0		0.5					
1534			13	0		0.5					
1535			14	-1.5		0					
1536			15	-2.0		-0.2					
15[illegible]7			16	-3.5		0.5	590				
15[illegible]3	124		3	18.0		16.0	490		.42		
15[illegible]			6	16.8		15.5	490				
1540			9	12.0		11.0	500				
1541			12	4.0		4.1	516				
1542			13	2.5		5.2	[illegible]				
1543			14	0		3.5	[illegible]				
1544			15	1.5		2.6	440				

TPN	RUN NO.	ROLL NO.	α	θ	A_1	B_1	RPM	TP/V	μ	CONFIGURATION	COMMENTS
1545	125	22	9	18.5	0	16.5*	380	8/	.6	TRIANGLE, A_2=5° (NASA Conf 304) TAIL-OFF	AUTOGYRO FLT. (PSEUDO CONV.) LIFT= 70# A_1 = 0 B_1 TRIMMED
1546			12	12.6		16.5*	390	55.2mm			
1547			13	9.0		15.1	400				
1548			14	8.0		13.5	410				
1549			15	4.0		10.0	410				
1550			16	1.0		5.5	450				
1551			17	-3.5		0.5	435				
1552	126		15	7.0		16.5	320		.85		*TPN 1545 & 46 NOT TRIMMED
1553			16	6.5		16.2	320				
1554			17	2.5		13.5	330				
1555			18	-1.5		9.0	270				
1556			19.5	-3.5		9.0	260				
1557	127		17	4.0		16.0	170		1.4		
1558			18	-2.0		10.0	150				
1559			19.5	-2.5		3.0	240				

TPN	RUN NO.	ROLL NO.	α	θ	A_1	B_1	RPM	TP/V	μ	CONFIGURATION	COMMENTS
1635	129	23	0	10.5	0	7.0	600	8/	.35	TRIANGLE, A_2=5° (NASA Conf. 304) TAIL-OFF	AUTOGYRO FLT. (PSEUDO CONV.) LIFT= 60 # A_1 = 0 B_1 TRIMMED
1636			3	7.0		5.2		55.2mm			
1637			6	6.5		3.0					
1638			9	3.0		2.5					
1639			12	-1.5		0.5					
1640			13	-2.5		0					
1641			14	-3.5		-0.7					
1642			15	-4.0		-1.2					
1643	130		3	18.5	0	16.5	500		.47		
1644			6	18.2		16.5					
1645			9	7.0		7.5					
1646			12	0		2.2					
1647			13	-2.0		1.0					
1648			14	-2.0		0.7	550				
1649			15	-3.5		0	540				
1650	131		12	7.6	0	12.5	400		.6		
1651			13	2.0		7.2	400				
1652		24	14	0		5.7	420				
1653			15	-3.0		3.0	460				
1654			16	-5.0		0.2	400				
1655			17	-6.5		0.5	400				

TPN	RUN NO.	ROLL NO.	α	θ	A_1	B_1	RPM	TP/V	μ	CONFIGURATION	COMMENTS
1656	132	24	14	0	0	9.0	330	8/	.25	TRIANGLE $A_2 = 0$ (NASA Con't 308) TAIL-OFF	AUTOGYRO FLT. (PSEUDO CONV) LIFT: b_1 $A_1 = 0$ B_1 FREE
1657	↓	↓	15	0	↓	8.0	310	55 RPM	↓		
1658	↓	↓	16	-2.2	↓	7.5	303	↓	↓		
1659	↓	↓	18	-7.5	↓	0	303	↓	↓		
1660	133	↓	16	-8.7	↓	0	200	↓	.105		
1661	↓	↓	17	-9.5	↓	0	200	↓	↓		
1662	↓	↓	18	-11.0	↓	0	200	↓	↓		
1793	140	25	13.0	2.0	0	3.7	579	14/			
1794	↓	↓	13.5	2.0	↓	7.0	577	12/			
1795	↓	↓	11.5	2.0	↓	11.5	468	16/			
1796	↓	↓	11.8	2.0	↓	5.2	556	12/			
1797	↓	↓	11.8	1.0	↓	2.3	723	12/			
1798	↓	↓	11.8	3.0	↓	12.8	313	12/			
1799	141	↓	11.0	1.0	↓	7.7	567	16/			
1800	↓	↓	11.1	1.0	↓	4.0	597	12/			
1801	↓	↓	11.8	1.0	↓	2.3	597	8/			
1802	↓	↓	19.0	1.0	↓	0	600	4/			
1803	142	↓	19.5	0	↓	-0.5	606	4/			
1804	↓	↓	12.3	0	↓	1.8	606	8/			
1805	↓	↓	10.7	0	↓	3.0	606	12/			
1806	↓	↓	9.5	0	↓	3.5	596	16/			

TPN	RUN NO.	ROLL NO.	α	θ	A_1	B_1	RPM	TP/V	μ	CONFIGURATION	COMMENTS
1807	143		-4	0	0	0	0	16/	0	TRISECTOR $A_2 = 5°$ (NASA Conf 309) TAIL-OFF	AIRPLANE FLT. BLADE FAIRINGS REMOVED, SIMILAR to HELICOPTER CONFIGURATION
1808	↓	↓	0	↓	↓	↓	↓	71.7 RPM	↓		
1809	↓	↓	2	↓	↓	↓	↓	↓	↓		
1810	↓	↓	4	↓	↓	↓	↓	↓	↓		
1811	↓	↓	6	↓	↓	↓	↓	↓	↓		
1812	↓	↓	8	↓	↓	↓	↓	↓	↓		
1813	↓	↓	10	↓	↓	↓	↓	↓	↓		
1814	↓	↓	↓	↓	5	↓	↓	↓	↓		CONTROL POWER AVAILABLE
1815	↓	↓	↓	↓	-5	↓	↓	↓	↓		
1816	↓	↓	↓	↓	0	5	↓	↓	↓		
1817	↓	↓	↓	↓	↓	-5	↓	↓	↓		
1818	↓	↓	↓	50	↓	0	↓	↓	↓		
1819	↓	↓	↓	-50	↓	↓	↓	↓	↓		
1820	↓	↓	12	0	↓	↓	↓	↓	↓		
1821	↓	↓	16	↓	↓	↓	↓	↓	↓		
1822	↓	↓	18.9	↓	↓	↓	↓	↓	↓		

TPN	RUN NO.	ROLL NO.	α	θ	A_1	B_1	RPM	TP/V	μ	CONFIGURATION	COMMENTS
1920	151	27	-8	10	-0.6	2.8	600	1/	.15	TRIANGLE, A_2=5 (NASA CONF 311) TAIL-ON δ_t = 0	HELICOPTER FLT. A_1 & B_1 to MATCH NASA CONF 303 See pages 23 to 27
1921	↓	↓	-2	↓	-3.0	2.8	↓				
1922	↓	↓	4	↓	-4.5	3.2	↓				
1923	↓	↓	10	↓	-5.2	3.2	↓				
1924	152	↓	-8	↓	-2.0	3.2	↓	4/	.25		
1925	↓	↓	-2	↓	-2.7	4.5	↓				
1926	↓	↓	4	↓	-4.7	4.2	↓				
1927	↓	↓	10	↓	-5.7	4.2	↓				
1928	153	↓	-8	↓	0.5	5.2	↓	8/	.35		
1929	↓	↓	-2	↓	-2.7	6.2	↓				
1930	↓	↓	4	↓	-5.0	8.2	↓				
1931	↓	↓	10	↓	-7.5	9.4	↓				
1932	154	↓	-8	10	-0.6	2.8	↓	1/	.15	δ_t = -5° (SURFACE NOSE DN)	
1933	↓	↓	-2	↓	-3.0	2.8	↓				
1934	↓	↓	4	↓	-4.5	3.2	↓				
1935	↓	↓	10	↓	-5.2	3.2	↓				
1936	155	↓	-8	↓	-2.0	3.2	↓	4/	.25		
1937	↓	↓	-2	↓	-2.7	4.5	↓				
1938	↓	↓	4	↓	-4.7	4.2	↓				
1939	↓	↓	10	↓	-5.2	4.2	↓				
1940	156	↓	-8	↓	0.5	5.2	↓	8/	.35		
1941	↓	↓	-2	↓	-2.7	6.2	↓				
1942	↓	↓	4	↓	-5.0	8.2	↓				
1943	↓	↓	10	↓	-7.5	9.4	↓				

TPN	RUN NO.	ROLL NO.	α	θ	A_1	B_1	RPM	TP/V	μ	CONFIGURATION	COMMENTS
1944	157	27	-8	10	-0.6	2.8	600	1/	.15	TRIANGLE, A_2=5° (NASA CONF 311) TAIL-ON δ_t = -10° (SURFACE NOSE DN)	HELICOPTER FLT. A_1 & B_1 to MATCH NASA 303 pp 23 to 27
1945	↓	↓	-2	↓	-3.0	2.8	↓		↓		
1946	↓	↓	4	↓	-4.5	3.2	↓		↓		
1947	↓	↓	10	↓	-5.2	3.2	↓		↓		
1948	158	↓	-8	↓	-2.0	3.2	↓	4/	.25		
1949	↓	↓	-2	↓	-2.7	4.5	↓		↓		
1950	↓	↓	4	↓	-4.7	4.2	↓		↓		
1951	↓	↓	10	↓	-5.7	4.2	↓		↓		
1952	159	↓	-8	↓	0.5	5.2	↓	8/	.35		
1953	↓	↓	-2	↓	-2.7	6.2	↓		↓		
1954	↓	↓	4	↓	-5.0	8.2	↓		↓		
1955	↓	↓	10	↓	-7.5	9.4	↓		↓		
1956	160	↓	-8	10	-0.6	2.8	↓	1/	.15	δ_t = 5° (SURFACE NOSE UP)	
1957	↓	↓	-2	↓	-3.0	2.8	↓		↓		
1958	↓	↓	4	↓	-4.5	3.2	↓		↓		
1959	↓	↓	10	↓	-5.2	3.2	↓		↓		
1960	161	↓	-8	↓	-2.0	3.2	↓	4/	.25		
1961	↓	↓	-2	↓	-2.7	4.5	↓		↓		
1962	↓	↓	4	↓	-4.7	4.2	↓		↓		
1963	↓	↓	10	↓	-5.0	4.2	↓		↓		
1964	162	↓	-8	↓	0.5	5.2	↓	8/	.35		
1965	↓	↓	-2	↓	-2.7	6.2	↓		↓		
1966	↓	↓	4	↓	-5.0	8.2	↓		↓		
1967	↓	↓	10	↓	-7.5	9.0	↓		↓		

TPN	RUN NO.	ROLL NO.	α	θ	A_1	B_1	RPM	TP/V	μ	CONFIGURATION	COMMENTS
1968	163	27	-8	10	-0.6	2.8	600	1/	.15	TRIANGLE, A_2 = 5° (NASA. CONF 311) TAIL-ON δ_t = 10°	HELICOPTER FLT A_1 & B_1 to MATCH NASA CONF 303 pp 23 to 27
1969			-2		-3.0	2.8					
1970			4		-4.5	3.2					
1971			10		-5.2	3.2					
1972	164		-8		-2.0	3.2		4/	.25		
1973			-2		-2.7	4.5					
1974			4		-4.7	4.2					
1975			10		-5.0	4.2					
1976	165		-8		0.5	5.2		8/	.35		
1977			-2		-2.7	6.2					
1978			4		-5.0	8.2					
1979			10		-7.5	9.0					
1980	166		-8	10	-0.6	2.8	600	1/	.15	δ_t = ± 5°	
1981			-2		-3.0	2.8					
1982			4		-4.5	3.2				RT. Surface Nose Down, to Produce Rt. Roll	
1983			10		-5.2	3.2					
1984	167		-8		-2.0	3.2		4/	.25		
1985			-2		-2.7	4.5					
1986			4		-4.7	4.2					
1987			10		-5.7	4.2					
1988	168		-8		0.5	5.2		8/	.35		
1989			-2		-2.7	6.2					
1990			4		-5.0	8.2					
1991			10		-7.5	9.4					

TPN	RUN NO.	ROLL NO.	α	θ	A_1	B_1	RPM	TP/V	μ	CONFIGURATION	COMMENTS
2047	169	28	10.7	0	0	3.1	600	4/		TRIANGLE, A_2 = 5 (NASA 312) TAIL-ON ~ δ_t = 0	AUTOGIRO FLT A_1 & B to MATCH NASA CONF 308 pp 32
2048			12.3			1.8		8/			
2049			19.5			-0.5		12/			
2050	170		10.7			3.0		4/		δ_t = -5°	
2051			12.3			1.8		8/			
2052			19.0			-0.5		12/			
2053	171		10.7			3.0		4/		δ_t = -10°	
2054			12.3			1.8		8/			
2055			19.3			-0.5		12/			
2056	172		10.7			3.0		4/		δ_t = 5°	
2057			12.2			1.8		8/			
2058			19.0			-0.5		12/			
2059	173		10.7			3.0		4/		δ_t = 10°	
2060			12.3			1.8		8/			
2061			19.0			-0.5		12/			

TPN	RUN NO.	ROLL NO.	α	θ	A_1	B_1	RPM	TP/V	μ	CONFIGURATION	COMMENTS
2072	174	29	12	5	0	16.2	200	81		TRIANGLE, A_2 = 5° (NASA 304) TAIL-ON, δ_t = 10°	AUTOGYRO FLT
2073					5		200				
2074					-5		200				
2075					0	13.7	200				
2076					0	11.2	202				
2077	175				0	16.2	166				
2078					5		165				
2079					-5		165				
2080					0	13.7	171				
2081	176			10	0	16.2	156				
2082					5		153				
2083					-5		153				
2084					0	13.7	153				
2085					0	11.2	153				
2086					0	16.2	110				
2087					5	16.2	110				
2088					-5	16.2	110				
2089					0	13.7	110				
2090					0	11.2	107				

TPN	RUN NO.	ROLL NO.	α	θ	A_1	B_1	RPM	TP/V	μ	CONFIGURATION	COMMENTS
2151	178		-4	0	0	0	0	13/ 69 MPH		TRIANGLE, A_2 = -5° (NASA 313) TAIL-ON δ_t = 0	AIRPLANE FLT BLADE FAIRINGS IN PLACE
2152			0								
2153			2								
2154			4								
2155			6								
2156			8								
2157			12								
2158		D	16								
2159			19.5								
2160	179	O	-4							δ_t = 5°	
2161		W	0								
2162		N	2								
2163			4								
2164		T	6								
2165		O	8								
2166		N	12								
2167			16								
2168			19.5								

TPN	RUN NO.	ROLL NO.	α	θ	A_1	B_1	RPM	TP/V	μ	CONFIGURATION	COMMENTS
2169	180		-4	0	0	0	0	13/		TRIANGLE, A_2=5°	AIRPLANE FLT.
2170			0					69MPH		(NASA 313)	
2171			2							TAIL-ON, δ_t=10°	
2172			4								
2173			6								
2174			8								
2175			12								
2176		A	16								
2177			19.5								
2178	181	G	-4							δ_t=-5°	
2179		E	0								
2180		N	2								
2181			4								
2182		T	6								
2183		O	8								
2184		Z	12								
2185			16								
2186			19.5								

TPN	RUN NO.	ROLL NO.	α	θ	A_1	B_1	RPM	TP/V	μ	CONFIGURATION	COMMENTS
2187	182		-4	0	0	0	0	13/		TRIANGLE,	AIRPLANE FLT.
2188			0					69MPH		(NASA 313)	
2189			2							TAIL-ON δ_t=-10	
2190			4								
2191			6								
2192			8								
2193			12								
2194		A	16								
2195		G	19.5								
2196	183	E	-4							δ_t=±5° RT. ROLL	
2197		N	0								
2198			2								
2199		T	4								
2200		O	6								
2201		Z	8								
2202			12								
2203			16								
2204			19.5								

TPN	RUN NO.	ROLL NO.	α	θ	A_1	B_1	RPM	TP/V	μ	CONFIGURATION	COMMENTS
2205	184		-4	0	0	0	0	13/		TRIANGLE	AIRPLANE FLT.
2206			0					69 MPH		(NASA 319)	
2207			2							TAIL-ON, $\delta_t = \pm 10°$	
2208			4							(RT. ROLL	
2209			6								
2210			8								
2211			12								
2212		D	16								
2213			19.5								
		B									
2264	186	E	-4							TAIL-OFF	
2265		A	0								
2266			2								
2267		T	4								
2268		O	6								
2269		N	8								
2270			10								
2271			12								
2272			16								
2273			19.5								

TPN	RUN NO.	ROLL NO.	α	θ	A_1	B_1	RPM	TP/V	μ	CONFIGURATION	COMMENTS
2320	187	30	0	0	0	0	600	0	0	TRIANGLE, $A_2=0$	HOVER
2321				2						(NASA CONF 316)	
2322				4						TAIL-OFF	
2323				5							
2324				6							
2325				8							
2326				10							
2327				12							
2328				14							
2329				15							
2330				16							
2331				18							
2332				20							
2333	188	30	-8	5°	-0.5	0.5	600	11 fps	.05	TRIANGLE, $A_2=0$	HELICOPTER
2334			-2		-0.5	0.5				(NASA CONF 314)	A, & B, TRIMMED
2335			4		-1.2	0.2				TAIL-OFF	
2336			10		-2.2	0.2					
2382	190	31	-8	5°	-0.5	0.5	600	11 fps	.05		Repeat of RUN 188
2383			-2		-0.5	1.0					
2384			4		-0.5	1.1					
2385			10		-1.0	1.2					

TPN	RUN NO.	ROLL NO.	α	θ	A_1	B_1	RPM	TP/V	μ	CONFIGURATION	COMMENTS
2386	191	31	-8	10	-1.5	2.0	600	11 fps	05	TRIANGLE, $A_2=0$ (NASA 314) TAIL-OFF	HELICOPTER A. & B. TRIMMED
2387			-2		-1.7	1.8					
2388			4		-1.7	1.7					
2389			10		-1.7	1.7					
2390	192		-8	15	-1.0	0					
2391			-2		-1.8	1.0					
2392			4		-2.0	1.0					
2393			10		-2.2	0					
2394	193		-8	20	-2.0	2.6					
2395			-2		-2.2	2.8					
2396			4		-2.2	2.5					
2397			10		-2.2	2.5					PITCH NOT TRIMMED
2398	194	31	-8	5	0.5	0	600	22 fps	.10		
2399			-2		-0.6	1.2					
2400			4		-1.7	1.1					
2401			10		-3.0	0.9					
2402	195		-8	10	-1.7	2.5					
2403			-2		-2.0	3.0					
2404			4		-2.0	3.0					
2405			10		-3.2	2.5					
2406	196		-14	15	-1.5	1.0					
2407			-8		-3.0	3.5					
2408			-2		-3.2	3.5					
2409			4		-4.0	4.2					

TPN	RUN NO.	ROLL NO.	α	θ	A_1	B_1	RPM	TP/V	μ	CONFIGURATION	COMMENTS
2410	197	31	-14	20	-2.2	5.0	600	22 fps	.10	TRIANGLE, $A_2=0$ (NASA 314) TAIL-OFF	HELICOPTER A. & B. TRIMMED
2411			-8		-2.8	2.5					
2412	198	31	-8	5	0.2	.5	600	1	.15		A. NOT TRIMMED for *TPN 2410 & 2411 2425 & 2426
2413			-2		-1.5	2.0					
2414			4		-3.0	2.5					
2415			10		-4.5	1.6					
2416	199		-8	10	-0.5	3.0					
2417			-2		-2.4	3.6					
2418			4		-4.5	4.7					
2419			10		-5.4	3.0					
2420	200		-14	15	0.5	4.2					
2422			-8		-1.7	5.5					
2423			-2		-4.0	6.0					
2424			4		-4.7	6.0					
2425	201		-14	20	-1.5	7.0					
2426			-8		-2.2	7.0					
2427	202		-8	5	0.5	2.0		4	.25		
2428			-2		-1.5	3.0					
2429			4		-2.3	3.0					
2430			10		-4.5	3.0					
2431	203		-8	10	-0.5	4.5					
2432			-2		-2.5	5.0					
2433			4		-4.5	5.7					
2434			10		-6.0	4.5					

TPN	RUN NO.	ROLL NO.	α	θ	A_1	B_1	RPM	TP/V	μ	CONFIGURATION	COMMENTS
2435	204	31	-14	15	1.0	5.5	600	4/	.25	TRIANGLE, A_2=0 (NASA 314) TAIL-OFF	HELICOPTER A_1 & B_1 TRIMMED*
2436			-8		-1.7	6.7					*
2437			-2		-3.5	8.0					A_1 NOT TRIMMED for TPN 2440, 2441 2456,
2438			4		-5.5	9.4					
2439	205		-14	20	0.7	8.5					
2440			-8		-2.2	10.					
2441			-2		-2.2	11.					
2442	206	31	-8	5	0.5	2.5	600	8/	.35		
2443			-2		-2.0	4.5					
2444			4		-4.5	6.0					
2445			10		-7.0	6.0					
2446	207		-8	10	0.5	5.7					
2447			2		-2.0	7.6					
2448			4		-4.5	8.7					
2449			10		-7.0	9.7					
2450	208		-14	15	2.5	7.0					
2451			-8		0	9.0					
2452			-2		-3	11.0					
2453			4		-5.5	12.5					
2454	209		-14	20	2.0	9.7					
2455			-8		-1.0	13.0					
2456			-2		-2.2	16.7					

TPN	RUN NO.	ROLL NO.	α	θ	A_1	B_1	RPM	TP/V	μ	CONFIGURATION	COMMENTS
2522	210		0							FUSELAGE ALONE (NASA 315) TAIL-OFF (VERTICAL-ON)	FUSELAGE FAIRED
2532			-8								
2537		10	-4								
2542		9	2								
2547		4	4								
2552		2	6								
2557			8								
2562		1	10								
2567		0	12								
2572		2	14								
2577			16								
2582			18								

TPN	RUN NO.	ROLL NO.	α	θ	A_1	B_1	RPM	TP/V	μ	CONFIGURATION	COMMENTS
2632	211	32	-14	~	~	~	600	1/	.15	TRIANGLE BLADES-OFF (NASA 310) TAIL-OFF	HELICOPTER FLT.
2633			-8								
2635			-2								
2636			4								
2637			10								
2638	212		-14	~	~	~	600	4/	.25		
2639			-8								
2640			-2								
2641			4								
2642			10								
2643	213		-14	~	~	~	600	8/	.35		
2644			-8								
2645			-2								
2646			4								
2647			10								
2648			12								
2649	214		12	~	~	~	300	8/	.70		
2650							200		.105		
2651							150		1.4		
2652							100		2.1		

TPN	RUN NO.	ROLL NO.	α	θ	A_1	B_1	RPM	TP/V	μ	CONFIGURATION	COMMENTS
2705	216	33	-14	~	~	~	600	1/	.15	TRICUSPED BLADES-OFF (NASA 210) TAIL-OFF	HELICOPTER FLT.
2706			-8								
2707			-2								
2708			4								
2701			10								
2710	217		-14				600	4/	.25		
2711			-8								
2712			-2								
2713			4								
2714			10								
2715	218		-14				600	8/	.35		
2716			-8								
2717			-2								
2718			4								
2719			10								
2720			12								
2721	219		12				300	8/	.70		
2722							200		.105		
2723							150		1.4		
2724							100		2.1		

Unclassified

Security Classification

DOCUMENT CONTROL DATA - R & D

(Security classification of title, body of abstract and indexing annotation must be entered when the overall report is classified)

1. ORIGINATING ACTIVITY *(Corporate author)* Hughes Tool Company - Aircraft Division Culver City, California	2a. REPORT SECURITY CLASSIFICATION Unclassified 2b. GROUP ---

3. REPORT TITLE

ROTOR/WING SERIES VI WIND TUNNEL TEST -- 7-FOOT DIAMETER MODEL IN THE NASA LANGLEY RESEARCH CENTER 30-BY-60-FOOT WIND TUNNEL

4. DESCRIPTIVE NOTES *(Type of report and inclusive dates)*

Wind Tunnel Test Report

5. AUTHOR(S) *(First name, middle initial, last name)*

Briardy, Frank J.
Head, Robert E.

6. REPORT DATE April 1968	7a. TOTAL NO. OF PAGES 207	7b. NO. OF REFS 16
8a. CONTRACT OR GRANT NO. Nonr-4588(00) b. PROJECT NO. c. NR 212-162/12-8-64 d.	9a. ORIGINATOR'S REPORT NUMBER(S) HTC-AD 67-3 9b. OTHER REPORT NO(S) *(Any other numbers that may be assigned this report)* ---	

10. DISTRIBUTION STATEMENT

Distribution of this document is unlimited.

11. SUPPLEMENTARY NOTES ---	12. SPONSORING MILITARY ACTIVITY U. S. Navy Office of Naval Research

13. ABSTRACT

Wind tunnel tests of a Rotor/Wing model were conducted for three purposes: To compare the results of testing the same model in a small and a large wind tunnel; to investigate Rotor/Wing planform effects on performance and flying qualities; to investigate in detail the low rotor speed range of conversion. The data gathered from testing the 7-foot diameter model in the 8-by-10-foot tunnel and in the 30-by-60-foot tunnel were in good agreement for rotor advance ratios greater than 0.15. There was little difference in the aerodynamic characteristics of the three Rotor/Wing planforms (trisector, triangle, and tricusp); however, the tricusp was inferior for the helicopter flight mode. The low rotor speed range of conversion shows that the mean lift, rolling, and pitching moments are constant, and that the oscillating components are of low magnitude.

DD FORM 1 NOV 65 1473

Unclassified

Security Classification

Unclassified
Security Classification

14 KEY WORDS	LINK A ROLE	LINK A WT	LINK B ROLE	LINK B WT	LINK C ROLE	LINK C WT
Rotor						
Wing						
Stopped-rotor						
Conversion						
Helicopter						
Autogyro						
Airplane						
Wind tunnel test						

Unclassified
Security Classification